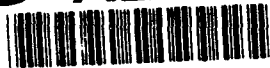


AD-A250 284



DTIC
ELECTE
MAY 18 1992
S C D

(2)

CALSPAN-UB

RESEARCH CENTER

FUNDAMENTAL STUDIES OF THE STRUCTURE
OF HYPERSONIC ATTACHED AND SEPARATED
BOUNDARY LAYERS OVER SMOOTH, ROUGH
AND TRANSPIRATION-COOLED SURFACES

TECHNICAL REPORT

DISTRIBUTION STATEMENT A

Approved for public release;
Distribution Unlimited

CALSPAN
UB
RESEARCH CENTER

CALSPAN-UB RESEARCH CENTER

P.O. BOX 400 BUFFALO, NEW YORK 14225

Technical Report Number

Not reviewed and is
not law AFR 190-12

REPORT DOCUMENTATION PAGE

Form Approved
OMB No. 0704-0188

Public reporting burden for this collection of information is estimated to average 1 hour per response, including the time for reviewing instructions, searching existing data sources, gathering and maintaining the data needed, and completing and reviewing the collection of information. Send comments regarding this burden estimate or any other aspect of this collection of information, including suggestions for reducing the burden, to Washington Headquarters Services, Directorate for Information Operations and Reports, 1215 Jefferson Davis Highway, Suite 1204 Arlington, VA 22202-4302, and to the Office of Management and Budget, Paperwork Reduction Project (0704-0188), Washington, DC 20503.

1. AGENCY USE ONLY (Leave blank) 2. REPORT DATE November 1991 3. REPORT TYPE AND DATES COVERED 15MAY88- Final Technical Report 29AUG91

4. TITLE AND SUBTITLE FUNDAMENTAL STUDIES OF THE STRUCTURE OF HYPERSONIC ATTACHED AND SEPARATED BOUNDARY LAYERS OVER SMOOTH, ROUGH, AND TRANSPIRATION-COOLED SURFACES 5. FUNDING NUMBERS PE 61102F 2307/AS

6. AUTHOR(S) DR. MICHAEL S. HOLDEN AFOSR-88-0223

7. PERFORMING ORGANIZATION NAME(S) AND ADDRESS(ES) CALSPAN-UB RESEARCH CENTER P.O. BOX 400 BUFFALO, NEW YORK 14225 AFOSR-TR-92 0394 8. PERFORMING ORGANIZATION REPORT NUMBER

9. SPONSORING/MONITORING AGENCY NAME(S) AND ADDRESS(ES) AIR FORCE OFFICE OF SCIENTIFIC RESEARCH DIRECTORATE OF AEROSPACE SCIENCES BOLLING AIR FORCE BASE 10. SPONSORING/MONITORING AGENCY REPORT NUMBER AFOSR-88-0223

11. SUPPLEMENTARY NOTES

12a. DISTRIBUTION / AVAILABILITY STATEMENT UNLIMITED 12b. DISTRIBUTION CODE

13. ABSTRACT (Maximum 200 words) A program of fundamental experimental research and analysis has been conducted to examine two key areas associated with the design of hypersonic vehicles for re-entry and sustained hypervelocity flight. In the first, and major segment of the program, detailed measurements were obtained to examine the thermo-fluid dynamics of transpiration-cooling and the separate and combined effects of surface roughness and blowing on the fluid mechanics of transpiration and ablative thermal protection systems. In the second segment of the program, we embarked in a detailed experimental examination of turbulent compressibility effects in regions of attached and separated flows. The first phase of this program was devoted to studies associated with developing the models and instrumentation to obtain highly resolved high frequency measurements in fully turbulent boundary layer at Mach 11, 13, and 15. While in the second phase of this program, segments were concentrated on the development of the direct measurement of density fluctuations using high pressure electron beam techniques. During this contract we also took the opportunity to analyze and publish important measurements made in an earlier program demonstrating compressibility effects in hypersonic turbulent wakes.

14. SUBJECT TERMS Experimental Research, Hypersonic Vehicles, Attached, Separated, Transpiration Cooling, Surface Roughness and Blowing, Ablative Thermal Protection Systems, Compressibility Effects, Heat Transfer, Skin Friction, Electron Beam Technique, Density Measurements 15. NUMBER OF PAGES 61 16. PRICE CODE

17. SECURITY CLASSIFICATION OF REPORT U 18. SECURITY CLASSIFICATION OF THIS PAGE U 19. SECURITY CLASSIFICATION OF ABSTRACT U 20. LIMITATION OF ABSTRACT



**FUNDAMENTAL STUDIES OF THE STRUCTURE
OF HYPERSONIC ATTACHED AND SEPARATED
BOUNDARY LAYERS OVER SMOOTH, ROUGH
AND TRANSPIRATION-COOLED SURFACES**

Final Report

November 1991

92-12933



Prepared for:

**Air Force Office of Scientific Research
Directorate of Aerospace Sciences
Bolling Air Force Base**

Principal Investigator:

**Michael S. Holden
Physical Sciences Department
Telephone No. (716) 631-6853**

Accession For	
NTIS	<input checked="" type="checkbox"/>
DTIC TAB	<input type="checkbox"/>
Unannounced	<input type="checkbox"/>
Justification	
By	
Distribution/	
Availability Codes	
Dist	Avail and/or Special
A-1	



92 5 14 065

(9-ft.) slender cone model, with a flare at the base, as reported in *Appendix 5*. Experimental studies of the compressibility effects on the diffusion of hypersonic wakes are reported in *Appendix 6*.

SUMMARY

A program of fundamental experimental research and analysis has been conducted to examine two key areas associated with the design of hypersonic vehicles for re-entry and sustained hypervelocity flight. In the first, and major segment of the program, detailed measurements were obtained to examine the thermo-fluid dynamics of transpiration cooling and the separate and combined effects of surface roughness and blowing on the fluid mechanics of transpiration and ablative thermal protection systems. In the second segment of the program, we embarked in a detailed experimental examination of compressibility effects in regions of attached and separated flows. The first phase of this program was devoted to studies associated with developing the models and instrumentation to obtain highly resolved high frequency measurements in fully turbulent boundary layer at Mach 11, 13, and 15. While in the second phase of this program, segments were concentrated on the development of the direct measurement of density fluctuations using high pressure electron beam techniques. During this contract we also took the opportunity to analyze and publish important measurements made in an earlier program demonstrating compressibility effects in hypersonic turbulent wakes. A new high pressure reservoir was designed and fabricated during the course of the program to increase the performance of the experimental facility.

During the past five years under AFOSR's sponsorship, we have conducted detailed experimental studies of (1) the effects of surface roughness only on the aerothermal characteristics of ablated noseshapes and slender re-entry vehicles (*Appendix 1*); (2) the effects of combined roughness and blowing on the heat transfer and skin friction to slender MRV's (*Appendix 2*); (3) the effects of surface blowing on the distribution of heat transfer and skin friction together with flowfield properties on slender transpiration-cooled re-entry vehicles; and (4) the effects of the properties of the injectant on the aerothermal characteristics of transpiration-cooled slender re-entry vehicles (*Appendix 3*).

During the latter part of the program, our efforts were focussed toward the examination of the dynamics turbulent structure of attached and separated regions of shock wave/turbulent boundary layer interaction hypersonic flow. The results of our initial studies employing the electron beam technique to obtain mean density measurements through the turbulent boundary layer over the cone were reported in *Appendix 4*. These studies demonstrated that to obtain the resolution necessary to determine the structure of wall regions of the turbulent boundary layer, it is necessary to obtain very thick interaction regions. During the latter part of this program, we accomplished this by using a very large

1.0 INTRODUCTION

Recently, intense use of numerical solutions of full or reduced time-averaged Navier-Stokes equations has resulted in significant progress in the development of efficient and stable numerical algorithms and a greater understanding of gridding techniques. However, little progress has been made in developing fluid mechanical models required for these codes. In many instances, the phenomena of greatest importance in the aerothermal design of advanced vehicles are also the most difficult to model in the codes. These modeling problems include non-equilibrium chemistry and catalytic wall effects, boundary layer transition, and non-equilibrium development of turbulent boundary layers in regions of strong pressure gradients and separated flow and mass addition and combustion. Meaningful advances must be made in the prediction of flow phenomena so that the imbalance in research, particularly in hypersonic flows, may be redressed and experimental studies conducted to examine these problems in depth. In the development of advanced prediction techniques required to design and predict the aerothermal loads on sophisticated, airbreathing maneuverable hypersonic vehicles, there are a number of key flow/field and flow/surface interaction phenomena that must be modeled which require the insight and measurements of detailed experimental study. The modeling of the turbulent flow structure over transpiration-cooled and rough ablating surfaces requires a detailed understanding of the mixing process between the injected fluid, the roughness elements, and the fluids at the base of the turbulent boundary layer. Large surface ablation resulting from heat transfer rates generated on the windward ray of the ablative heat shield close to the nosetip and on the control surfaces of vehicles flying at high angles of attack are of critical concern to the designers of missiles that maneuver during re-entry. To develop an accurate predictive capability to describe the ablation rates of the nosetip, heat shield, and control surfaces, it is necessary to understand and model the separate and combined effects of surface blowing and surface roughness.

To develop and evaluate prediction schemes that will accurately describe the effects of combined roughness, blowing, and entropy layer on the aerothermal performance of slender, rough ablating cones, we conducted experimental studies under hypersonic, high Reynolds number, and highly cooled wall conditions. The models were constructed with well-defined roughness and blowing characteristics. The correlations of the measurements from these studies can be used to directly evaluate the accuracy of aerothermal models currently in use in "shape change" codes, while individual sets of measurements can be

compared with more detailed calculations of combined roughness and blowing on sharp slender cones.

In the second part of the program, an experimental study was conducted in which an electron beam, and pitot and total temperature probes were used to measure the mean and fluctuating density, and mean static temperature across a Mach 7.5 turbulent boundary layer over a 4-ft long 6° sharp cone. The experimental studies were conducted in the Calspan 96" Tunnel at a freestream Mach number of 8.5 and unit Reynolds number of 5×10^6 . Our initial use of this technique has demonstrated a potential to obtain fluctuation measurements up to frequencies approaching 1 MHz. Additional improvement is expected when more advanced optics are used. The mean rotational temperature through the boundary layer were determined from spectra obtained using an Optical Multichannel Analyzer. The electron gun has proven highly reliable and has the potential to work at equivalent densities up to over 100 torr. Further developments are anticipated employing an electron beam to stimulate a gas which is examined using a resonant laser technique.

During the final phases of this program, an opportunity was presented to complete the analysis of and publish measurements made in an earlier program which could shed light on turbulent compressibility effects in hypersonic flow. Specifically, the turbulent diffusion of a hypersonic turbulent wake show significant compressibility effects which manifest themselves as dramatic changes in wake growth. In the experimental program presented in *Appendix 5*, measurements were made to examine the effects of Mach number and Reynolds number on the structure and growth of the wake behind a slender cone.

As a part of the overall experimental effort to obtain fully turbulent flows at the highest Mach numbers and Reynolds numbers, additional experimental hardware and associated instrumentation has been constructed and assembled to enhance the unit Reynolds number and run times for current and future AFOSR experimental programs. These modifications are centered around the construction of a new high pressure driver reservoir. This high pressure driver reservoir was designed and successfully tested and is being now incorporated into the tunnel.

2.0 REVIEW OF RESULTS FROM RESEARCH PROGRAM

2.1 STUDIES OF THE AEROTHERMODYNAMICS OF TRANSPIRATION-COOLED AND ROUGH AND ABLATING HYPERSONIC VEHICLES

The development of design codes for transpiration and ablatively-cooled re-entry vehicles is of significant importance to the Air Force. The codes currently in use for this purpose are, in general, based on technology developed over fifteen years ago and was based on a very weak experimental database. In fact, most codes were "tuned" to match flight measurements of nosetip recession which were not only relatively inaccurate but also were for a specific set of vehicle materials and flight conditions. Also, the predictive codes employed empirical correlations to describe the enhanced stagnation point heating. However, the major problem in these codes is they employ an effective roughness (basically determined from flight data) which in effect controls the level of heating and ablation of the nosetip. However, our experimental studies have indicated that for relatively low levels of blowing, the coolant layer effectively covers the roughness presenting an effectively smooth surface to the flows.

In the studies to examine the effects of transpiration cooling and surface roughness and blowing on the aerothermal characteristics of turbulent hypersonic boundary layers over transpiration-cooled, rough hypersonic vehicles, detailed surface measurements were made that provide a basis for the direct evaluation of the basic modeling of key phenomena in advanced computational codes. Experimental studies were conducted at Mach numbers of 11, 13, and 15 for turbulent flows over transpiration-cooled and rough and smooth blowing models in which the blowing parameter B' was varied from 0.01 to 5. During this program three new and unique transducers were developed and successfully used to measure skin friction and local and average heating on the rough transpiration-cooled surfaces. Two types of heat transfer gages were developed, a calorimeter gage and a multi-element thin-film gage. These gages were used to obtain both average and local heating measurements to determine the effects of mass addition on cone heating. The distribution of heating over and between the roughness elements was determined for a range of blowing rates and freestream conditions with the multi-element thin-film gage. The thin-film elements were distributed over the roughness elements and on the base between the roughness elements and the injection passages. A new skin friction gage, in which there was blowing through the floating sensing element, was used to measure the effects of blowing and roughness on surface shear. The results of the measurements with these

gages are presented together with comparisons with earlier measurements at lower Mach numbers and with the results of semi-empirical prediction techniques. These studies are described in detail in *Appendix 1*.

Heat transfer, skin friction, and pressure measurements were obtained along the models for a range value of the blowing parameter $m/Q_e U_e C_{H_0}$ from 0.10 to 5, using a nitrogen injectant. Holographic interferometry was used to examine the characteristics of the hypersonic flowfield around the MRV model. The measurements were correlated, in terms of the major scaling parameters, and are also compared with earlier measurements at lower Mach numbers. Comparisons are presented with computations made with the BLIMP code, which demonstrate that this code is in relatively good agreement with the experimental data for small blowing rates. However, for $B' > 0.5$, the code significantly under-predicts the effectiveness of transpiration cooling. For these high blowing levels, where (in the extremes) boundary layer blowoff occurs, boundary layer theory (BLIMP code) is inadequate, and solutions to the full or reduced time-averaged Navier-Stokes equations are required. These studies are reported in *Appendix 2*.

The effects of molecular weight and specific heat of the injectant on the turbulent heat transfer to and skin friction of to a sharp slender transpiration-cooled cone in hypersonic flow were then investigated; this study was conducted at Mach numbers of 11 and 13 for local Reynolds numbers of 100×10^6 and 50×10^6 , respectively. Measurements of heat transfer, skin friction, and pressure were obtained along the cone for blowing rates ($m/Q_e U_e C_{H_0}$) from 0.10 to 5, using helium, nitrogen, and freon injectants. The characteristics of the hypersonic turbulent boundary layer were determined with holographic interferometry. Miniature heat transfer instrumentation was used to obtain the detailed distribution around each injection port. Calculations using the BLIMP code and the HEARTS Navier-Stokes code were compared with the experimental measurements. Correlations involving the effects of injection rates and gas properties on the heat transfer and skin friction are presented in terms of the relevant non-dimensional parameters. These studies are described in detail in *Appendix 3*.

2.2 STUDIES OF COMPRESSIBILITY EFFECTS IN REGIONS OF SHOCK WAVE/TURBULENT BOUNDARY LAYER INTERACTION IN HYPERSONIC FLOWS

Powerful numerical techniques based on the Navier-Stokes equations are available for the prediction of hypersonic viscous flows. Providing these flows are laminar the

accuracy of the results of the computations is impressive [Rudy et al (1989)] (*Appendix 7*). However, if the hypersonic boundary layers or shear layers are turbulent, agreement with measured data is often unsatisfactory as a result of serious shortcomings in the time-averaged models used to represent the turbulence. The structure of turbulent boundary layers hypersonic speeds is poorly understood. This in part results from the paucity of measurements to define the fluctuatory characteristics of the turbulence which is in turn related to the severe difficulties in developing suitable instrumentation to make accurate measurements in high Mach number flows. However, without a better physical understanding of the characteristics of the time dependent properties of these flows, the validity of turbulence models cannot be meaningfully evaluated.

Most models of turbulence used to describe compressible flows have been derived from concepts developed from low Mach number or other incompressible flows where fluctuations in thermodynamic quantities (density, temperature, etc.) are small enough to be neglected. As the Mach number increases these fluctuations become more important and at hypersonic speeds, they can be the most significant varying quantities. Furthermore, in many important flows there are features which pose difficulties in modeling. For example, in regions shock/boundary layer interactions, which are regions of intense heating. The way in which the turbulence responds to the rapid changes in flow conditions presently poorly understood.

During this part of the program our efforts were focussed toward the examination of the dynamics turbulent structure of attached and separated regions of shock wave/turbulent boundary layer interaction hypersonic flow. The results of our initial studies employing the electron beam technique to obtain mean density measurements through the turbulent boundary layer over the cone were reported in *Appendix 4*. These studies demonstrated that to obtain the resolution necessary to determine the structure of wall regions of the turbulent boundary layer, it is necessary to obtain very thick interaction regions. During the latter part of this program, we accomplished this by using a very large (9-ft.) slender cone model, with a flare at the base, as reported in *Appendix 5*. These studies were conducted in the Calspan 48-inch and 96-inch shock tunnels at Mach numbers of 11 and 13 and local Reynolds numbers up to 200×10^6 . The analysis of the results from the earlier studies together with further bench tests demonstrated that, while the new system could be used to obtain good mean density measurements, the optical and electronic systems were not fast enough to process frequencies approaching 1 MHz, which are required to follow the turbulent fluctuations in these hypersonic flows. We have been

performing studies to enable us to record and analyze turbulent density fluctuation measurements for frequencies approaching 1 MHz. To capture sufficient light to provide enough photons to fall on the detectors to respond in 2 microseconds, we have had to redesign the optical system. Here, in addition to the large aperture custom-designed lens and mirror system, we have installed the detectors on vibration mountings inside the model. These optics give us the ability to obtain a 0.010 inch resolution across a 1.5 inch thick viscous layer. The 10-channel photodetector system will have a frequency response of 1 MHz and its output will be recorded on a solid state recorder with a sampling rate of 5 MHz. This program is being continued under a current AFOSR grant.

2.3 EXPERIMENTAL STUDIES OF TURBULENT WAKES BEHIND SHARP SLENDER CONES

At the end of this program we completed the analysis of an experimental program, conducted in the Calspan 96-inch Shock Tunnel, in which studies were made of the effect of controlled mass addition from the conical surface of a slender cone on the structure and development of the "low-altitude" turbulent wake. The studies were conducted at Mach 11 and 13 and at Reynolds numbers based on the wetted length of the cone from 15×10^6 to 30×10^6 . Measurements of pitot and static pressure, total temperature, heat transfer, and mass concentration were made for $10 < X/\sqrt{C_D A} < 80$ for three rates of mass addition. From these studies, we have determined a quantitative relationship between the rate of mass addition and the wake velocity for conditions where the boundary layer over the cone is fully turbulent. The profile measurements demonstrated that the viscous wake did not increase significantly in size with mass addition, and that "wake narrowing" may result from fluid dynamic as well as electromagnetic phenomena.

2.4 FABRICATION OF HIGH PRESSURE RESERVOIR

As a part of the overall experimental effort to obtain fully turbulent flows at the highest Mach numbers and Reynolds numbers, additional experimental hardware and associated instrumentation has been constructed and assembled to enhance the unit Reynolds number and run times for current and future AFOSR experimental programs. These modifications are centered around the construction of a new high pressure driver reservoir. This high pressure driver reservoir was designed and successfully tested and is being now incorporated into the tunnel.

APPENDIX 1

**STUDIES OF SURFACE ROUGHNESS AND BLOWING EFFECTS ON
HYPERSONIC TURBULENT BOUNDARY LAYERS OVER
SLENDER CONES**

AIAA '89

AIAA-89-0458

**Studies of Surface Roughness and Blowing
Effects on Hypersonic Turbulent Boundary
Layers Over Slender Cones**

M.S. Holden, Calspan-UB Research Center (CUBRC)
Buffalo, New York 14225

27th Aerospace Sciences Meeting

January 9-12, 1989/Reno, Nevada

STUDIES OF SURFACE ROUGHNESS AND BLOWING EFFECTS ON HYPERSONIC TURBULENT BOUNDARY LAYERS OVER SLENDER CONES

M.S. Holden*

Abstract

Studies are presented of the effects of surface roughness and blowing on the aerothermal characteristics of turbulent hypersonic boundary layers over rough transpiration-cooled slender cones. These detailed surface measurements provide the basis for the direct evaluation of the basic modeling of these phenomena in advanced codes. Experimental studies were conducted at Mach numbers of 11, 13 and 15 for turbulent flows over rough blowing models in which the blowing parameter B' was varied from .01 to 5. Three new and unique transducers were developed and successfully used to measure skin friction and local and average heating on the rough transpiration cooled surfaces. Two types of "roughness and blowing" heat transfer gages were developed, a calorimeter gage and a multi-element thin film gage. The calorimeter gage was constructed with a silver calorimeter element containing two roughness elements and insulated injection passages molded into it. A nickel thin film resistance thermometer is to sense the temperature of the calorimeter element. This gage was used successfully to obtain average local heating measurements to determine the effects of mass addition on cone heating. The distribution of heating over and between the roughness elements was determined for a range of blowing rates and freestream conditions with the multi-element thin film gage. The thin film elements were distributed over the roughness elements and on the base between the roughness elements and the injection passages. A new skin friction gage, in which there was blowing through the floating sensing element, was used successfully to measure the effects of blowing and roughness on surface shear. Two roughness elements were molded into the surface of the transducer and injection passages are incorporated into the gage. The results of the measurements with these gages are presented together with comparisons with earlier measurements at lower Mach numbers and semi-empirical prediction techniques.

1. Introduction

In the development of advanced prediction techniques required to design and predict the aerothermal loads, on sophisticated maneuverable airbreathing hypersonic vehicles, there are a number of key flow/field and flow/surface interaction phenomena that must be modeled which require the insight and measurement of detailed experimental study. The modelling of the turbulent flow structure, of the flow over transpiration-cooled and rough ablating surfaces, is an area where a detailed understanding of the mixing process between the injected fluid, the roughness elements, and the fluids at the base of the turbulent boundary layer is required. Large surface ablation resulting from heat transfer rates generated on the windward ray of the ablative heat shield

close to the nosetip and on the control surfaces of vehicles flying at high angles of attack will be of critical concern to the designer of missiles that maneuver during re-entry. To develop an accurate predictive capability to describe the ablation rates of the nosetip, heat shield, and control surfaces, it is necessary to understand and model the separate and combined effects of surface blowing and surface roughness. Our recent studies of roughness shape and spacing effects on ablating and non-ablating slender cones (Ref. 1) suggest not only that the subsonic studies are inapplicable to the heating of heat shields in hypersonic flow, but also that the basic modeling of the roughness drag and mechanisms of heating in the theoretical models is highly questionable.

The measurements made in earlier studies of transpiration cooling conducted with transpiration cooled nosetips¹ were designed principally to determine whether blockage effects of mass injection are as large as predicted by the current codes. The measurements on the model with zero blowing, presented in Figure 1, clearly show that the intrinsic roughness of the surface causes heating enhancement factors of over 1.7. In fact, it can be seen by comparing Figures 1 and 2 that the heat transfer measurements on the conically rough hemisphere are in good agreement with those obtained on the non-blowing transpiration-cooled nosetip. However, when a small amount of blowing ($\dot{m}/\rho_e u_{CH} = 0.032$) was introduced, the heating rates over a major part of the transpiration-cooled model dropped to levels close to those recorded on the smooth model, as shown in Figures 2 and 3. It could be postulated on the basis of these measurements that the initial effect of mass addition from a rough ablating nosetip is to modify the flow around the roughness elements by eliminating the cavity flows between them in such a way that the momentum defect is small. If the effect of mass addition is to remove surface roughness as an important characteristic parameter, a series of questions are posed for the correlation of flight measurements in terms of an effective surface roughness and the computational procedures in which the ablation rate is determined from heating levels enhanced by surface-roughness effects.

Mass addition at the base of the boundary layer results in a reduction in momentum in the wall layer, which, like roughness, will make the boundary layer more susceptible to separation. However, injecting mass into the boundary layer will also severely distort the temperature and velocity distribution at the base of the boundary layer, which has the potential to cause a reduction in heat transfer and skin friction to the wall. Because momentum reduction on rough walls at the base of the boundary layer results principally from the form drag of the roughness elements, the introduction of

* Calspan-UB Research Center (CUBRC), Buffalo, NY 14225, Associate Fellow AIAA

This work was conducted for AFWAL and AFOSR under Contract Nos. F49620-85-C-0130 and AFOSR-88-0223.

This paper is declared a work of the U.S. Government and is not subject to copyright protection in the United States.

additional mass at the rough wall could significantly change the basic mechanisms that control momentum and energy exchange. Our experience with transpiration-cooled nosetips¹ as well as those of Voisin² on wind tunnel walls suggests that calculating the combined effects of mass addition and surface roughness (as is done in most prediction techniques) by using the product of the 'influence factors', based on measurements of the separate effects of roughness and blowing, is invalid.

To develop and evaluate prediction schemes that will accurately describe the effects of combined roughness, blowing and entropy layer on the aerothermal performance of slender rough ablating cones, we must conduct experimental studies under hypersonic, high-Reynolds-number, and highly cooled-wall conditions. The models should be constructed with well-defined roughness and blowing characteristics. The correlations of the measurements from these studies can then be used to directly evaluate the accuracy of aerothermal models currently in use in "shape change" codes, while individual sets of measurements should be compared with more detailed calculations of combined roughness and blowing on sharp slender cones.

II. Review of Related Studies

Studies of Surface Roughness Effects in Hypersonic Flows

Because most predictive techniques employ an effective sand-grain roughness as the single length scale characterizing roughness size, there continues to remain a key problem in relating the topography of a given surface to a sand-grain height. The experimental studies of Nikuradse⁶ and Schlichting⁷, both hydraulic pipe flow studies, were principally responsible for the selection of sand-grain roughness as the standard against which to measure relative effects of other types of roughness. Although this standard has been frequently employed, the topographical characteristics of a sand-grain surface have yet to be defined. In fact, because of the experimental difficulties involved in the preparation and inspection of rough surfaces inside a small-diameter pipe, it is surprising that Nikuradse's results are as consistent as reported. For fully developed pipe flows, Nikuradse established that the parameter controlling the similitude of the flows is the roughness Reynolds number ($u_\tau K/\nu_w$). This parameter (\bar{R}_{ek}) was selected in many subsequent studies to characterize boundary layer flows where other non-dimensional groupings (such as R_δ/δ , R_θ/θ , etc.) might have been considered more valid.

The Schlichting studies, conducted with roughness of well-defined geometric shapes, provided the first set of measurements which could be reproduced in both experimental and theoretical studies. The results from these studies, together with those from a number of subsequent investigations in subsonic adiabatic flows, were correlated by researchers to yield relationship between an "effective sand-grain height" and parameters which describe the geometric features of the surface. This further perpetuated the use of sand-grain roughness as a standard. The Dirling⁸ correlation, which is shown in Figure 4, is one such plot, from which an effective sand-grain roughness height can be determined from knowledge of peak-to-valley roughness height together with the shape and spacing of the roughness elements. While there is little direct supporting experimental evidence, the "lambda" form of the correlating curve is assumed to reflect a sudden change in flow structure from an "open" to a "closed" cavity flow around (between) the roughness elements as the spacing between the roughness elements is varied. Do open and closed cavity

flows really exist on rough surfaces constructed from three-dimensional roughness elements? Is the structure of the flow around the elements also dependent upon the local Reynolds number, a parameter not taken into account in any such correlations? If an effective roughness height can be accurately determined from a 'bump curve', this dimension must be combined with key fluid dynamic properties to yield a non-dimensional parameter or groups of parameters with which to characterize the flow. The roughness Reynolds number $\bar{R}_{ek} (= \frac{u_\tau K}{\nu_w})$ originally used by Nikuradse, and the non-dimensional roughness heights K/δ^* , K/θ_m and K/θ_c (where δ^* , θ_m , and θ_c are the displacement, momentum, and thermal energy thickness respectively), have all been used to correlate the aerothermal effects associated with boundary layers over rough re-entry vehicles. To date, however, no single parameter or combinations of parameters (e.g., \bar{R}_{ek} , $\frac{K}{\theta_m}$) has been used with any great success to describe the general similitude of turbulent boundary layers in supersonic and hypersonic flows over rough, highly cooled walls.

The studies of Dirling⁸, ettermann⁹, Dvorak¹⁰, Simpson¹¹ and more recently Lin¹² and Finson¹³ have provided further insight into the basic effects of roughness shape and spacing on the characteristics of the rough wall boundary layer and skin friction and heating to a rough surface. Dvorak combined the effects of roughness shape and spacing into a single parameter λ (the roughness density), defined as shown in Figure 5. He linked the downward shift in the velocity profile $\Delta U/u_\tau$ to a combination of roughness Reynolds number $\bar{R}_{ek} (= u_\tau K/\nu_w)$ and λ through the relationship

$$\frac{U}{u_\tau} = \frac{1}{K} \ln \left(\frac{U u_\tau}{\nu_w} \right) + A - \frac{\Delta U}{u_\tau} \left(\frac{K u_\tau}{\nu_w}, \lambda \right) \quad (1)$$

In incompressible flows the smooth regime, where the surface shear is entirely due to viscous shear, is defined by $\bar{R}_{ek} < 5$. For $\bar{R}_{ek} > 30$, the surface shear is composed of form drag on the roughness elements combined with viscous shear. When $\bar{R}_{ek} > 70$, the surface shear results principally from drag, and viscosity is no longer a factor in controlling the velocity profile. For fully rough flows, Equation 1 can be rewritten

$$\frac{U}{u_\tau} = \frac{1}{K} \ln \left(\frac{U u_\tau}{\nu_w} \right) + A - \left[\frac{\Delta U}{u_\tau} - \frac{1}{K} \ln \left(\frac{U u_\tau}{\nu_w} \right) \right] \quad (2)$$

where

$$\frac{\Delta U}{u_\tau} - \frac{1}{K} \ln \left(\frac{K U u_\tau}{\nu_w} \right) = f(\lambda) \quad (3)$$

which is a function of the roughness density. Here it should be noted that $f(\lambda) = A - U_R^+$ where U_R^+ is the velocity close to the top of the roughness elements and A ($= 5$) is the smooth wall constant. Now the definition of Nikuradse's sand-grain roughness is basically

$$\frac{U}{u_\tau} = \frac{1}{K} \ln \left(\frac{U u_\tau}{\nu_w} \right) + B.5$$

Hence, combining equations 2 and 3 we obtain

$$f(\lambda) = - \left[3 + \frac{1}{K} \ln \left(\frac{K}{K_5} \right) \right] \quad (4)$$

Betterman and Dvorak suggest that the subsonic measurements should be correlated by two relationships:

For

$$1 < \lambda < 4.68, f(\lambda) = 17.35 (1.625 \log_{10} \lambda - 1) \quad (5)$$

And for

$$\lambda > 4.68, f(\lambda) = -5.95 (1.103 \log_{10} \lambda - 1) \quad (6)$$

The existence of two regions has been rationalized on physical grounds, supported by experimental studies in two-dimensional flows. There is serious debate about whether a significant change in flow structure occurs as three-dimensional roughness elements are drawn together. Certainly the measurements with stone roughness do not exhibit such a trend. This is particularly unfortunate, since Nikuradse's data falls on the line constructed principally from data obtained on roughness constructed by two-dimensional machined grooves.

Finson's engineering model based on the early concepts of Liepmann and Goddard¹⁴ and his (Finson's) detailed numerical calculations provides a good basis for interpreting the physical phenomena of key importance in rough wall heating, as well as a relatively simple prediction technique. The shear on a rough wall can be expressed as the sum of the viscous and form drag of the rough surface:

$$C_f = C_{f_{base}} + \int_0^T \frac{\rho u^2}{\rho_e u_e^2} \cdot C_D \cdot B(y) \cdot \frac{d(y)}{D^2} dy \quad (7)$$

where $B(y)$ is the blockage factor, and $d(y)$ and D are the diameter of the roughness element and the spacing between elements, respectively. From his detailed numerical solutions, Finson showed that ρ and u were relatively constant between the base and top of the roughness element at values ρ_R, u_R close to the top of the roughness. Equation (7) becomes

$$C_f = C_{f_{base}} + \frac{\rho_R u_R^2}{\rho_e u_e^2} \cdot C_D \cdot B\left(\frac{K}{2}\right) \frac{A_P}{A_S} \quad (8)$$

where A_P/A_S is the ratio of projected area of the roughness element in the direction of the flow to total area of the flow on which they stand, and $B(K/2)$ is the average value of $B(y)$.

For compressible flows Finson found that

$$U_R/U_e = 0.247 + .234 \log \left(\frac{\rho_R}{\rho_e} \frac{A_S}{A_P} \right)$$

where

$$\frac{\rho_R}{\rho_e} = \left[\frac{T_w}{T_e} + \left(1 + \frac{\gamma-1}{2} M_e^2 - \frac{T_w}{T_e}\right) \cdot \left(\frac{U_R}{U_e}\right) - \left(\frac{\gamma-1}{2}\right) M_e^2 \frac{U_R^2}{U_e^2} \right]$$

Therefore, assuming C_{f_B} is the smooth wall heating level, it is possible to relate the rough wall skin friction to the smooth wall value in the generalized form

$$\frac{C_{f_{ROUGH}}}{C_{f_{SMOOTH}}} = 1 + f_1 \left(M_e, \frac{T_w}{T_e}, \frac{K}{\theta} \right) \cdot f_2 \left(\lambda, B, \left(\frac{K}{D} \right), C_D \right)$$

The relationship for heat transfer is assumed of the same form

$$\frac{C_{H_{ROUGH}}}{C_{H_{SMOOTH}}} = f'_1 \left(M_e, \frac{T_w}{T_e}, \frac{K}{\theta} \right) \cdot f'_2 \left(\lambda, B, \frac{K}{D}, C_D \right)$$

If we assume that the product of the blockage factor and C_D are invariant with rough shape and space, then for constant local free stream condition, we get the Dvorak-Simpson Parameter:

$$\frac{C_{H_{ROUGH}}}{C_{H_{SMOOTH}}} = f \left(\frac{A_P}{A_S} \right)$$

A slightly different form can be obtained by the subsonic blunt body approximation

$$C_D = C_{D_{REF}} (A_P/A_{WS})$$

and using D/K rather than A_S/A_P to obtain the correlation in terms of the Dirling¹⁵ parameter,

$$\frac{C_{H_{ROUGH}}}{C_{H_{SMOOTH}}} = f \left(\frac{D}{K} \cdot \left(\frac{A_{WS}}{A_P} \right)^{4/3} \right)$$

where the various areas are illustrated in Figure 36.

In recent studies of the effects of roughness shape and spacing on the heat transfer and skin friction to the roughness, nosetips, frusta and flaps of a typical MRV configuration, Holden used both the Dvorak/Simpson parameter A_S/A_P and the Dirling parameter $\frac{D}{K} \left(\frac{A_{WS}}{A_P} \right)^{4/3}$, and achieved reasonable success in correlations. In these studies, the effects of roughness shape and spacing on the heat transfer and skin friction both for surfaces with sand-grain roughness and those constructed with geometrically well-defined hemispherical and conical roughness elements were examined. Also, heat transfer, skin-friction, and pressure-distribution measurements were obtained on spherical and ablated noseshapes, conical frusta, and control surfaces in hypersonic flow. The results of this work have demonstrated that the low-speed measurements of Nikuradse¹⁶, Schlichting¹⁷, and others, and the correlations of Dirling¹⁸/Simpson¹⁹, cannot be used directly to predict rough-wall heating and skin friction in supersonic and hypersonic flows over non-adiabatic surfaces. Even the more solidly founded prediction scheme developed by Finson²⁰, which is based upon his detailed numerical solutions, consistently overpredicts the roughness-enhanced heating levels in high-speed flows. While direct measurements of the skin friction and heat transfer to geometrically well-defined rough surfaces provide the opportunity to more closely evaluate the accuracy of the current shape-change codes and the more fundamental treatments like that of Finson in high Mach number, high Reynolds number flows, there remains a basic need to define more closely the fundamentals of the fluid dynamics which control momentum and energy exchange in high-speed flows over adiabatic and non-adiabatic rough surfaces.

Combined Blowing and Surface Roughness Effects in High-Speed Flows

The models used in the current codes to describe the effects of surface roughness in the presence of surface blowing unfortunately have little foundation in physical modeling and even less support from experimental measurements. While there have been a series of experimental studies from Nikuradse to Holden to determine the effects of surface roughness, skin friction, and heat transfer, little work has been done to examine the separate and combined effects of surface blowing and surface roughness on the heat transfer and skin friction to rough surfaces. In fact, only two studies are available to substantiate theoretical modelings. One study, conducted in low speed flow ($v = 50$ ft/sec) by

Healzer et al,²¹ and a second by Voisin²² in a wind tunnel wall with Mach 3 airflow in the absence of heat transfer, where the key parameters were orders of magnitude different from those encountered in hypersonic re-entry. In the Healzer studies, the surface was constructed with hemispherical roughness elements while Voisin²² employed a porous surface constructed from wire mesh. In both cases, an effective sand-grain roughness height was selected from Nikuradse²³ or Durling²⁴ correlations of low speed roughness measurements. In the Healzer studies, the skin friction measurements were deduced indirectly from velocity profiles and momentum-integral techniques. While this reduction technique can be relatively accurate for the non-blowing case, when applied to experiments with surface blowing, the accuracy of the technique is poor. Apparently, this was the case because Healzer did not present correlations of his skin friction measurements. One very interesting feature of the results of the Stanford²⁵ study is the form of this expression to correlate the effects of heating on rough walls:

$$\frac{ST_{\text{BLOWING}}}{ST_{\text{UNBLOWN}}} = \left[\ln \left(1 + \frac{\rho_w V_w}{\rho_e u_{eCH}} \right) / \frac{\rho_w V_w}{\rho_e u_{eCH}} \right]^{1.25} \left[1 + \frac{\rho_w V_w}{\rho_e u_{eCH}} \right]^{1/4}$$

This is very similar to the form of the correlation developed at Stanford for smooth walls. Here it should be noted that the non-blowing value of heating coefficient was taken at the same enthalpy thickness as in the blowing case, rather than at a common Reynolds number based on scale length. These measurements were compared with a prediction scheme based on a modified Van Driest method for rough walls. However, because they were tailored to this specific experiment, they have not been used in shape change codes.

Voisin²⁶ studies of the combined effects of roughness and blowing were conducted at Mach 6 under adiabatic wall conditions ($q_w = 0$) on a wind tunnel wall. Only surface skin friction measurements were made during Voisin²⁶ studies. This is unfortunate because while modified Reynolds analogy relationships (however poor) have been developed for rough walls, linking skin friction to heat transfer in the presence of both roughness and blowing is a very difficult theoretical task. However, Voisin²⁶ measurements have clearly demonstrated that the combined effects of flowing and roughness on skin friction cannot be described in a simple manner. First, Voisin²⁶ found that on the tunnel wall, where the experiments were conducted, the effects of surface roughness alone on skin friction could be correlated in terms of the roughness Reynolds number, Re_K . This is a result consistent with earlier measurements on adiabatic walls by Goddard²⁷ and Reda²⁸. In contrast, measurements on models placed in the flow involving significant levels of heating ($T_w/T_o > 0.5$) have in general correlated better with parameters like K/δ , K/θ or $K/\delta^+ \tau$; which, as shown by the theoretical studies of Dvorak and Finson, should have greater relevance to roughness effects on re-entry vehicles. Voisin²⁶ studies demonstrated that the effects of surface roughness and blowing on skin friction cannot be deduced from simple expressions derived from the measurements made of each of the separate effects. Correlations were presented to enable skin friction to be deduced in the presence of combined roughness and blowing. Extrapolating these measurements to flows at higher Mach numbers over highly cooled surfaces, as well as inferring changes in heat transfer from the skin friction measurements, is obviously highly speculative.

A correlation of the measurements on transpiration-cooled "smooth" flat plates and cones at lower Mach numbers are shown in Figure 6. Measurements by Holden¹ on transpiration cooled nosetips and are compared with the earlier measurements in Figure 7. These measurements are compared with the results of current studies in Section IV subheading three.

III. Experimental Program

Objective and Design of the Experimental Study

The objective of this experimental study of blowing and roughness effects in high Reynolds number hypersonic flow was to obtain detailed surface heat transfer and skin friction as well as flow field measurements, to evaluate the models of the surface/flow field interaction. The development of advanced computer codes which, in principal, can be used to describe the macroscopic features at the base of the boundary layer, has basically outmoded the use of surfaces with poorly defined roughness characteristics such as "sand grain" roughness. A review of surface roughness studies suggests that the definition of sand grain roughness is related more to a theoretical criteria based on a measured velocity profile rather than the geometric characteristics of the surface. In fact, Nicuradse³¹, who first introduced sand grained roughness based bonding sand grains "end to end" to a surface, noted that sand of the same size from a different geographic location exhibited different roughness characteristics. From the viewpoint of generating measurements with which to provide a definitive evaluation of predictive techniques, it is important that the roughness geometry is well defined. Schlichting was the first researcher to obtain measurements on surfaces whose geometric roughness could be reproduced in both theoretical and experimental studies. From the results of these and subsequent studies in subsonic, adiabatic flows, an empirical relationship was devised between roughness shape and spacing and an "effective sand-grain roughness height." The correlation of the measurements further perpetuated the use of "sand grain roughness" as a standard.

The single parameter characterization used in many "shape-change" codes designed to predict change in the noseshape of an ablating nosetip as it re-enters the atmosphere is based principally on measurements in low speed, low temperature flows at Mach numbers and Reynolds numbers differing significantly from re-entry conditions. In these studies, the surfaces were characterized by parameters such as K/δ , K/θ and T_w/T_o . The roughness shape parameter (λ), which has been defined in various ways by different investigators, can be generally expressed as the product of the spacing ratio (D/K) and a parameter related to the shape of the roughness element or its drag coefficient. The relationship between K/K_s and the shape parameter λ (the lambda curve shown in Figure 5) exhibits large changes in K_s for small changes in λ . A key question is whether the correlation is sensitive to flow structure between the roughness elements resulting from changes in the local Mach number and Reynolds number. In the present study we elected to use a surface with a spherical roughness characteristic of a sand grain surface with some roughness height.

Experimental Facilities and Test Conditions

The experimental program was conducted in Calspan's 96-inch Shock Tunnel at freestream Mach numbers from 11 to 16, for Reynolds numbers up to 100

$\times 10^6$ and wall-to-freestream stagnation temperature ratios of 0.1 and 0.2. At Mach numbers up to 13, boundary layer transition is complete on the completely smooth models within six inches of the nosetip. For the blowing model at Mach numbers up to 16, transition is within six inches from the nosetip. These studies were conducted at roughness Reynolds numbers (Re_k) from 20 to 300 on the conical forebody, and 200 to 2000 on the flap, thus covering transitional to fully rough regime. Non-dimensional blowing rates, $B'_h = \frac{\rho_w v_w}{\rho_e u_e c_H}$, from 0 to 5 were used in the studies.

Models The slender cone model which was used in the experimental studies is shown in Figure 8. The model has a transpiration cooled surface fed from eight high-pressure reservoirs through eight Valcor fast acting valves. Each section of the model is constructed with six zones that run from the front to the rear of the model. This enabled us to vary the blowing circumferentially to simulate the effects of differential blowing resulting from model incidence. To distribute the gas from the reservoirs uniformly to the surface, each model employs a matrix of distribution passages.

As in our earlier studies of the effects of patterned roughness on the aerothermal characteristics of nonporous slender cones, we used hemispherical roughness elements. A molding technique that was developed at Calspan to produce a number of different roughness patterns was used to obtain the smooth and rough surfaces. The low velocity mass addition between each roughness element occurred from passages molded in the skin between the flow, which was controlled by sonic orifices at their base. This latter technique was employed very successfully in our earlier transpiration-cooled studies where we were able to obtain precisely controlled blowing conditions. The flow from each hole in the model was controlled by eight sonic orifices in the model skin that were fed from plenum chambers in the model. The flow from each orifice was released into a cylindrical passage molded in the rubber skin between each roughness element. The area ratio between the orifice and circular passage allowed injectant flows from the surface at velocities of approximately 100 ft/sec. While this type of model construction is a painstaking task, the end result, which is an experiment where surface roughness and blowing are completely defined, is worth the effort. Because we used choked orifices over the entire model, mass flow from each model zone was precisely controlled by plenum pressures. Mass flows over the model were unaffected by the distribution of surface pressure on transients associated with tunnel starting. Although spherical roughness elements were used in the current studies, this technique can be used to construct rough surfaces that replicate any ablated surface.

Surface Instrumentation The thin film heat transfer instrumentation developed to measure the surface distribution of heat transfer to the roughness is shown in Figures 9 and 10. The two instrumented hemispherical roughness elements can be rotated in the holder to provide measurements on the windward and leeside surfaces of the element. Also, the gage can be rotated in the holder to provide greater details of the heat transfer at the base of the roughness elements. As in the rest of the model, the blowing velocities were in the range of 80 to 300 ft/sec, generating dynamic pressures of less than 1% of the freestream values.

A blowing calorimeter gage developed specifically for this program is shown in Figure 11. The calorimeter element is minted from a high-purity silver billet and drilled to accept the passages for the blowing holes. The

calorimeter element is mounted in a Macor holder and the passages for the coolant are installed with a highly insulating adhesive.

One of the skin friction gages that was designed, developed and constructed is shown in Figure 12. After a number of different approaches were tried, a design was developed with non-metric coolant passages passing through the metric diaphragm with very little clearance. Such tight clearances are allowed because the crystal and rubber support and measuring system on which the diaphragm is mounted is very stiff, so that deflection under load is insignificant. The gage has a linear response up to 0.7 psia and a nominal sensitivity of 20,000 mV/psi.

Pressure measurements were made using flush-mounted Kulite transducers. Pressure gages have been mounted flush with the silicon skin to record the pressure fluctuations, as well as the mean pressure.

Holographic Interferometry

Holographic interferometry was used to make flowfield measurements. Interferograms of complex flowfields provide good qualitative basis for evaluating some of the important phenomena that control the characteristics of these flows. CUBRC's holographic recording system, as shown in Figure 13, was used in this study.³⁸ Both single plate and dual plate techniques are required to record holograms, which are subsequently used in the playback step to obtain shadowgrams, Schlieren photographs, and interferograms of the tests.

IV. Results and Discussion

The experimental studies were conducted at Mach Numbers of 11 and 13 for a range of blowing rates (B' from 0.01 to 5). Both sharp and blunt nosetip configurations were employed in this study, however the principal emphasis was on flows which were not influenced by entropy swallowing effects. The molecular weight of the injectant was varied by diluting the principal injectant nitrogen with helium to provide a gas with a molecular weight similar to that of a typical ablator. A major objective of the current study was to investigate the effects of blowing on boundary layer separation. Measurements were made for a series of flap angles, which in the absence of blowing, the flow was attached. We also studied the effects of blowing and roughness on flows which were well-separated. A matrix of the runs made in the current experimental program is shown in Figure 14, and the test conditions reported in Figure 15.

Performance of New Heat Transfer and Skin Friction Instrumentation

A significant accomplishment in this study was the development three new types of instrumentation to obtain detailed measurements in the presence of roughness and blowing. To provide information which is of direct value to those attempting to model the macroscopic flow mechanics around the roughness elements, we must provide measurements of the heat transfer distribution around and at the base of the roughness elements. These measurements would be of little use if the gages themselves were not an integral part of the blowing surface with the injected gas passing through and flowing over the sensing element. Clearly, such requirements significantly complicate the design and construction of the gage. However, these very difficult problems were overcome, and a series of very unique measurements were obtained.

Design and Measurements with the New Skin Friction Gages

The skin friction gage, shown schematically in Figure 12, is an acceleration compensated single component force balance in which transpiration cooling passages are vented through the surface of the gage. A floating diaphragm, which in this particular design embodies two roughness elements, is supported flush with the surface on a piezoelectric sensing beam through a single fixture. The diaphragm is stabilized around its perimeter silicon posts. The silicon posts are molded into a gasket that contains a rubber boot which is cemented between the diaphragm and the body of the gage to prevent the hot gases from reaching the crystal beam. A second beam and diaphragm combination is incorporated into the body of the gage to provide a signal used for transducer acceleration compensation. The electrical signals from the sensing and compensation beam are added electrically in such a manner that when the gage is "shaken" in the absence of an air load, the net output is zero. The injection flow through the gage is metered through a series of sonic orifices set in the base of the gage. The geometric and mechanical design features of the gages were refined in a series of bench tests and tunnel studies. The developed gage has a frequency response of 20 kHz and a sensitivity of 20,000 mV/psi. A typical output of this skin friction instrumentation during a run with injection through the gage is shown in Figure 16.

New "Roughness and Blowing" Heat Transfer Instrumentation

During the course of these studies we developed two new gages to measure heat transfer in the presence of roughness and blowing. The first was a calorimeter gage which measured the total heat transfer rate to a segment of the surface. The second was a gage which provided the detailed distribution of heat transfer over the roughness elements and on the base of the model between the roughness elements. In each case, the size and geometry of the gage was selected so that it was a representative segment of the roughness and blowing surface. Thus, we selected a rectangular segment which contained two roughness elements and two transpiration cooling ports.

Calorimeter Instrumentation A photograph of the calorimeter gage is shown in Figure 11. The sensing element is a silver calorimeter slug the temperature of which is measured with a nickel resistance thermometer attached to the rear surface. Two roughness elements are molded into the surface of the calorimeter slug as the element is minted from a pure silver billet. The rear surface of the gage is highly polished, and then coated with several different, thin, electrically insulating, but thermally conducting layers upon which the nickel film is deposited. While this gage is significantly more difficult to construct than one employing a thermocouple sensor peened into the base of the silver slug, attaining a sensitivity of almost an order of magnitude larger than the thermocouple gage is well worth the added effort. The calorimeter elements are cemented into a Macor holder with an ultra-low conductivity, polyurethane adhesive which has a thermal diffusion depth of a fraction of a thousand during the 7 millisecond test time. This same adhesive was used to cement the transpiration tubes as they passed through the calorimeter element. Thus, during the test time, there was negligible loss in heating from this source or the evacuated rear surface of the gage. The injectant which passed through the gage was

metered through a series of sonic orifices at the base of the passageway. The design and operation of these gages were refined in a number of bench tests and tunnel studies. While dynamic calibrations have been performed with a high powered laser heat source, we have found that computing the sensitivity on the basis of measuring the mass of the pure silver slug and the temperature coefficient of the nickel resistance thermometer consistently gives the most accurate results. A typical output from the calorimeter gages is shown in Figure 17. The gage has a response time of less than a millisecond. A sliding least-squares technique is used to fit the temperature record, and this curve-fit is differentiated to obtain the temperature rate of change required to calculate the heat transfer rate. Fifteen of the calorimeter gages were constructed and used successfully in this program.

Thin Film Heat Transfer Instrumentation The miniature thin film instrumentation employed in this study enabled, for the first time, detailed distributions of heat transfer to be obtained on the actual roughness elements and on the cone surface adjacent to the injection ports and the roughness elements. Again, the size of the gage was selected to give a representative segment of the surface. Each gage contained 11 individual heat transfer gages. The positioning of the 7 thin films around the base of the roughness elements and around the injection ports was selected to provide distribution of heating in sufficient detail to infer the key aerothermal phenomena (see Figures 9 and 10). Likewise the five measurements over the roughness elements, which could be oriented relative to direction of the free stream, were selected to obtain the heating loads as well as provide evidence to define the micro-structure of the flow. Two injection passages run through the body of the gage, and as in the calorimeter and skin friction gages, the flow through these passages are regulated by sonic orifices at the base of these tubes. The temperature coefficients of the thin film resistance elements are measured in an oil bath. We employ the thermal properties of the pyrex substrate. The heat transfer rate, shown in Figure 18, is derived from the surface temperature/time history using the Rae/Tauble algorithm (Ref. 38).

Interferometer Studies with Blowing and Roughness Model

During the blowing and roughness studies a significant effort was devoted to flow visualization and measurements with holographic interferometry. Both infinite and semi-infinite fringe techniques were used, the first principally for flow visualization, and the second for quantitative flow field measurements. During the course of these studies, measurements were made for a range of compression angles and blowing rates for a rough surface configuration. Both nitrogen and nitrogen/helium mixtures were used as injectant, but clearly, only the interferograms made with the nitrogen can be the subject of quantitative interpretation.

A typical example of an infinite fringe for a small blowing rate and a compression surface angle of 25 degrees is shown in Figure 19. In this photograph, the shock layer and the boundary layer over the cone ahead of the expansion corner are well-defined as is the expansion of the boundary layer around this expansion corner. Boundary layer separation takes place halfway along the flat surfaces ahead of the compression ramp resulting in a well-defined separated region approximately three boundary layer thicknesses in length. The recirculation region is well-defined with holographic interferometry, and in this case there appears to be

multiple bubbles. The separation shock, which is clearly visible when it emerges from the boundary layer, indicates by its changes in curvature that the separation region is unsteady, a feature also observed on smooth non-blowing surfaces. Shown for comparison in Figure 20 is the equivalent non-blowing configuration. Here there is little or no separation and the corner shock is relatively steady. Decreasing the flap angle, again with no blowing, results in a completely attached flow over the model as shown in Figure 21. Increasing the blowing to a level above that used for run 34, we see in Figure 22 that the separation is further extended until the separation for blowing rates of $B' = 3$ has moved forward to the cone/flat junction as shown in Figure 23. Finally for blowing rates boundary layer blow off occurs on the cone and the flow over the entire model is separated as shown in Figure 24. The finite fringe operating mode is the one from which the most accurate measurements of the distribution of density through the boundary layer and shock layer can be obtained. To obtain a quantitative determination of the density, the assumption must of course be made that the flow is either two dimensional or completely axisymmetric and the latter assumption is potentially true only on the conical section of the model. In Figure 25 we show a finite fringe hologram for a flow with very small blowing in which the cone boundary layer shows no visible evidence of injection at its base. The boundary layer appears to remain attached in the compression corner. Tripling the blowing rate results in a definitive change in the structure at the base of the boundary layer on the cone and the formation of a definitive separated region at the flat/compression surface junction, as shown in Figure 26. For large blowing rates, the structure of the shock layer is completely distorted by blowing with the density increasing from the bow shock to the top of the shear layer before dropping rapidly to a relatively constant density region close to the wall, as shown in Figure 27. Here flow separation has moved forward to almost the cone/flat junction and a large portion of the flap is covered with a separated region. Increasing the blowing further begins to move the bow shock away from the body and the structure of the complete shock layer is controlled by surface blowing as shown in Figures 28 and 29. Also shown in Figures 30 and 31 are the holograms with a helium/nitrogen mixture for the blowing gas at low and high injection rates respectively. While only qualitative results can be deduced from these photographs, it is clear that blowing with a gas of low molecular weight has a significantly greater effect on the structure of the flow over the cone and compression surface.

Effects of Transpiration Cooling on Surface Skin Friction and Heating and Pressure

The effects of mass addition on the skin friction and heat transfer to the rough cone/flap configuration were investigated at Mach numbers of 11, 13 and 16 for a range of blowing rates (B') from 0 to 10. A test matrix of these studies is given in Figure 14 and a listing of the run conditions are tabulated in Figure 15.

Figure 32 shows the distribution of heat transfer rate to the surface of the rough cone/flap model for a range of blowing rates at Mach 11. The distribution of heating rate on the cone surface and over the roughness elements are shown for each gage station along the model. Here we observe that in the absence of blowing, the peak heating on the roughness elements is typically 10 times the levels at the base of the roughness elements. At the higher blowing the peak-to-base heating ratios have dropped to values close to 3.

Measurements similar to those described above are shown for the Mach 13 condition in Figure 33 a-f, and those for the Mach 15 condition are shown in Figure 34 a-c. We again see that the peak/base heating levels are between 3 and 10 depending upon the blowing rates.

The distribution of heating rate over the roughness elements for a range of low blowing rates plotted as a fraction of maximum heating rate is shown in Figure 35. Here we see that for the lower blowing rates the shape of the distribution becomes more rounded with increasing blowing. At the larger blowing rates shown in Figure 35, the peak heating is now only three times the base value compared with factors of up to ten times for the weakly blowing case.

The variation of peak heat transfer measured on the roughness elements along the cone for a range of blowing rates for the Mach 11 and 13 conditions are shown in Figures 36a and 36b. Similar distributions are shown for heating levels on the floor between the roughness elements and injectors in Figure 37a and 37b. Measurements from the calorimeter gages plotted in this format are shown in Figure 38a and 38b. Clearly the peak heating levels show a larger variation with λ than those at the base of the roughness elements.

The measurements of heating to the model, normalized by the value for negligible blowing rate, are plotted versus blowing parameter in Figures 39a, 39b, 40a, 40b, 41a and 41b. We observe a rapid decrease in the heat transfer rates with blowing rates for low values of the blowing parameter, and for blowing parameters above 3 there is little decrease in heat transfer with increased blowing.

One of the unique features of this study is that both skin friction and heat transfer measurements were obtained simultaneously for each of the blowing rates and free stream conditions. Thus, we can provide an analogous set of skin friction plots to those presented above for heat transfer. The variations in skin friction along the cone for a range of blowing rates are shown in Figures 42a and 42b for Mach 11, 13, respectively. These measurements are non-dimensionalized by the zero blowing value and re-plotted to show the variation of skin friction with blowing rate parameters in Figure 43. Again, following a rapid decrease in skin friction with a mass addition rate above B' of 1, there is little decrease in skin friction with increased blowing. We speculate that for blowing rates of B' over 2.0, the boundary layer begins to lift from the surface. This contention is supported by the pressure measurements shown in Figure 44 which suggest boundary "lift off" begins at values of blowing close to 1.

Comparisons with Earlier Measurements and Correlation

The experimental study of Voisine² is the only published study which has provided information in supersonic flow on the effects of combined roughness and blowing on the skin friction to a rough porous surface. Since these studies were conducted for adiabatic wall conditions only skin friction measurements were made in this work. Almost all the theoretical approaches have investigated blowing effects on smooth surfaces, the work of Christoph³² and Laganelli, et al³³ being the exceptions. The blowing parameter B'_f has been employed by the major segment of the community to correlate the skin friction data, where

$$B'_f = \frac{\dot{m}}{\rho_e u_e c_{f0}}$$

where the equivalent parameter for heat transfer is

$$B'_h = \frac{\dot{m}}{\rho_e u_e c_{H0}}$$

In the cases where the molecular weight of the injected gas differs from that of the freestream, parameters $(MW_{inj}/MW_{fs})^n$ and $(c_{p, inj}/c_{p, fs})^m$ are used to modify the skin friction and heat transfer parameters B'_f and B'_h respectively. For turbulent flows $n = 2/3$ and $m = 1$ have been selected. For flows over non-porous surfaces the relationship

$$\frac{c_f}{c_{f0}} = \frac{B'_f}{(e^{B'_f} - 1)}$$

has been shown to be in good agreement with measurements in incompressible flows³⁴. Further studies^{35,36} which have included the effects of compressibility suggest that

$$\frac{c_{H0} - c_H}{c_{H0}} = \frac{1}{3} B'_h{}^{1/3}$$

is a better representation of the measurements.

In our studies there was a significant surface roughness effect at all the blowing conditions at Mach number significantly larger than the earlier work, therefore we cannot expect the earlier approaches to be totally valid. A comparison between our skin friction measurements and those of Voisin² are shown in Figure 42 together with the contemporary correlations for compressible flows. Here we see that our measurements fall above those of Voisin² and more in line with the correlations of Walker³⁷ and Langanelli³³. The heat transfer measurements plotted in an analogous format are shown in Figure 43.

Clearly we will have to await our studies on smooth bodies with and in the absence of blowing before we can make definitive statements on the effects of Mach numbers in these flows.

V. Conclusion

In the studies of blowing and roughness effects on the characteristics of turbulent hypersonic boundary layers a unique set of measurements were obtained which provide the basis for the direct evaluation of the basic modeling of these phenomena effects of roughness and blowing on the aerothermal characteristics of flows over cones friction and local and average heating on rough transpiration-cooled surfaces. Experimental studies conducted at Mach numbers of 11, 13 and 16 for turbulent correlations are presented to show the effects of blowing on the distribution of skin friction and heat transfer over the cone/flap model and on the distribution of heating over the individual roughness elements.

References

1. Holden, M.S., "Studies of Boundary Layer Transition and Surface Roughness Effects in Hypersonic Flow," Final Report, AFOSR Contract No. F49620-82-C-0026, October 1983.
2. Voisin, R.L.P., "Combined Influence of Roughness and Mass Transfer on Turbulent Skin Friction at Mach 2.9", AIAA Paper 79-0003, 17th Aerospace Sciences Meeting, January 1979.
3. Holden, M.S., "Boundary Layer Displacement and Leading Edge Bluntness Effects on Attached and Separate Laminar Boundary Layer on a Compression Corner, Part II: Experimental Study," AIAA Journal, Vol. 9, No. 1, pp. 84-93, January 1971.
4. Bin, L.Z. & Harvey, J.K., "The Investigation of the Structure of Hypersonic Turbulent Boundary Layers on a 5° Sharp Cone Using the Electron Beam Fluorescence Technique," I.C. Aero Report, 82-02, January 1986.
5. Holden, M.S., "Shock Wave Turbulent-Boundary Layer Interaction in Hypersonic Flow, AIAA 77-45.
6. Nikuradse, J., "Stromungsgeretze en rauken Rohren," VDI Forshuaq-shift No. 361, 1933, Translated as NACA TM 1292, 1950.
7. Schlichting, H., "Boundary Layer Theory," 4th Edition, McGraw Hill Book Co., New York, 1960.
8. Dvorak, F.A., "Calculation of Turbulent Boundary Layers with Roughness and Heat Transfer," AIAA Journal, 10, pp. 1447-1451, 1969.
9. Betterman, D., "Contribution of L'etude de la Couche Limite Turbulent li Long Plagnes Rugueuse," Rapport 65-5, Centre National de la Recherche Scientifique, Paris, France, 1965.
10. Lewis, M.J., "An Elementary Analysis for Predicting the Momentum- and Heat-Transfer Characteristics of a Hydraulically Rough Surface," Journal of Heat Transfer, 97, pp. 249-254, 1975.
11. Simpson, R.L., "A Generalized Correlation of Roughness Density Effects on the Turbulent Boundary Layer," AIAA Journal, Vol. 11, No. 2, pp. 242-244, 1973.
12. Lin, T.C. and Bywater, R.J., "The Evaluation of Selected Turbulence Models for High-Speed Rough-Wall Boundary Layer Calculations," AIAA Paper-80-0132, Pasadena, California, 1980.
13. Finson, J.L., and Wu, P.K.S., "Analysis of Rough Wall Turbulent Heating with Application to Blunted Flight Vehicles," AIAA Paper No. 79-0008, 17th Aerospace Science Meeting, 1979.
14. Goddard, F.E., Jr., "Effect of Uniformly Distributed Roughness on Turbulent Skin-Friction Drag at Supersonic Speeds," Journal of Aerospace Sciences, 26, pp. 1-15, 1959.
15. Dirling, R.B., Jr., "A Method for Computing Rough-Wall Heat Transfer Rates on Reentry Nosetips," MDAC Paper WD 1778, AIAA 8th Thermophysics Conference, Palm Springs, California, 1973.
16. Nikuradse, J., "Stromungsgeretze en rauken Rohren," VDI Forshuaq-shift No. 361, 1933, Translated as NACA TM 1292, 1950.
17. Schlichting, H., "Boundary Layer Theory," 4th Edition, McGraw Hill Book Co., New York, 1960.

18. Dirling, R.B., Jr., "A Method for Computing Rough-Wall Heat Transfer Rates on Reentry Nosetips," MDAC Paper WD 1778, AIAA 8th Thermophysics Conference, Palm Springs, California, 1973.
19. Simpson, R.L., "A Generalized Correlation of Roughness Density Effects on the Turbulent Boundary Layer," AIAA Journal, Vol. 11, No. 2, pp. 242-244, 1973.
20. Finson, J.L., and Wu, P.K.S., "Analysis of Rough Wall Turbulent Heating with Application to Blunted Flight Vehicles," AIAA Paper No. 79-0008, 17th Aerospace Science Meeting, 1979.
21. Healzer, J.M., Moffat, R.J. and Kays, W.M., "The Turbulent Boundary Layer on a Rough Porous Plate: Experimental Heat Transfer with Uniform Blowing," Report No. HMT-18, Thermosciences Division Dept. of Mech. Eng., Stanford University, 1974.
22. Voisinot, R.L.P., "Influence of Roughness and Blowing on Compressible Turbulent Boundary Layer Flow," Naval Surface Weapons Center, NSWC Report No. TR-79-153, June 1979.
23. Nikuradse, J., "Stromungsgeretze en rauken Rohren," VDI Forshuaq-shift No. 361, 1933, Translated as NACA TM 1292, 1950.
24. Dirling, R.B., Jr., "A Method for Computing Rough-Wall Heat Transfer Rates on Reentry Nosetips," MDAC Paper WD 1778, AIAA 8th Thermophysics Conference, Palm Springs, California, 1973.
25. Healzer, J.M., Moffat, R.J. and Kays, W.M., "The Turbulent Boundary Layer on a Rough Porous Plate: Experimental Heat Transfer with Uniform Blowing," Report No. HMT-18, Thermosciences Division Dept. of Mech. Eng., Stanford University, 1974.
26. Voisinot, R.L.P., "Influence of Roughness and Blowing on Compressible Turbulent Boundary Layer Flow," Naval Surface Weapons Center, NSWC Report No. TR-79-153, June 1979.
27. Goddard, F.E., Jr., "Effect of Uniformly Distributed Roughness on Turbulent Skin-Friction Drag at Supersonic Speeds," Journal of Aerospace Sciences, 26, pp. 1-15.
28. Reda, D.C., "Compressible Turbulent Skin Friction on Rough and Rough/Wavy Walls in Adiabatic Flow," Naval Ordnance Laboratory, Report No. NOLTR 74-34, Silver Springs, MD., 1974.
29. Finson, J.L., and Wu, P.K.S., "Analysis of Rough Wall Turbulent Heating with Application to Blunted Flight Vehicles," AIAA Paper No. 79-0008, 17th Aerospace Science Meeting, 1979.
30. Lin, T.C. and Bywater, R.J., "The Evaluation of Selected Turbulence Models for High-Speed Rough-Wall Boundary Layer Calculations," AIAA Paper-80-0132, Pasadena, California, 1980.
31. Nikuradse, J., "Stromungsgeretze en rauken Rohren," VDI Forshuaq-shift No. 361, 1933, Translated as NACA TM 1292, 1950.
32. Christoph, G.H., "Low-Of-The-Wall Analysis Revisited for Reentry Vehicle Design," AIAA Paper 85-0905, Williamsburg, Virginia, 1985.
33. Laganelli, A.L., Fogano, R.P., and Martellucci, A., "The Effects of Mass Transfer and Angle of Attack on Hypersonic Turbulent Boundary Layer Characteristics," AFFDL-TR 75-35, April 1975.
34. Kays, W.M. and Moffat, R.J., "The Behavior of Transpired Turbulent Boundary Layers," Stanford University, Report No. H MT-20, April 1975.
35. Rubesin, M.W., "An Analytical Estimation of the Effect of Transpiration Cooling on the Heat-Transfer and Skin-Friction Characteristics of a Compressible Turbulent Boundary Layer," NACA TN 3341, December 1954.
36. Dorrance, W.H., and Dore, F.J., "The Effect of Mass Transfer on the Compressible Turbulent Boundary-Layer Skin Friction and Heat Transfer," J. Aeronautical Sciences, June 1954.
37. Walker, G.K., "Turbulent Boundary Layers with Mass Addition," G.E. Document No. TFM-8151-021, November 1963.
38. Holden, M.S., "Studies of Aerothermal Loads Generated in Regions of Shock/Shock Interaction in Hypersonic Flow," CUBRC Report, July 1988.

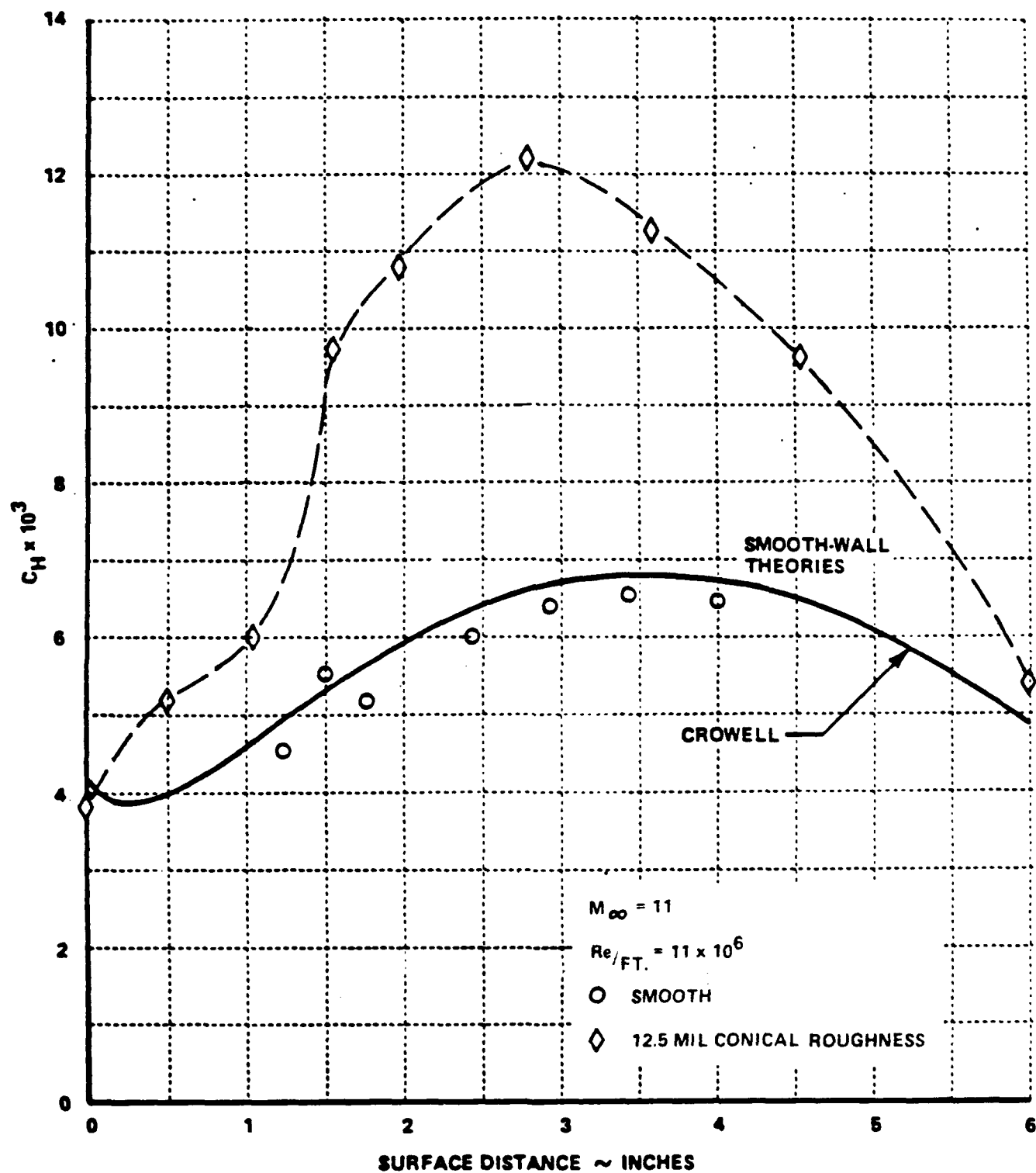


Figure 1 COMPARISON BETWEEN THE TURBULENT THEORIES OF CROWELL, AND SMOOTH-WALL, AND ROUGH-WALL MEASUREMENTS OF HOLDEN ON 12" DIAMETER HEMISPHERE ($M = 11.2$, $Re_D = 11 \times 10^6$, $K = 12.5$)

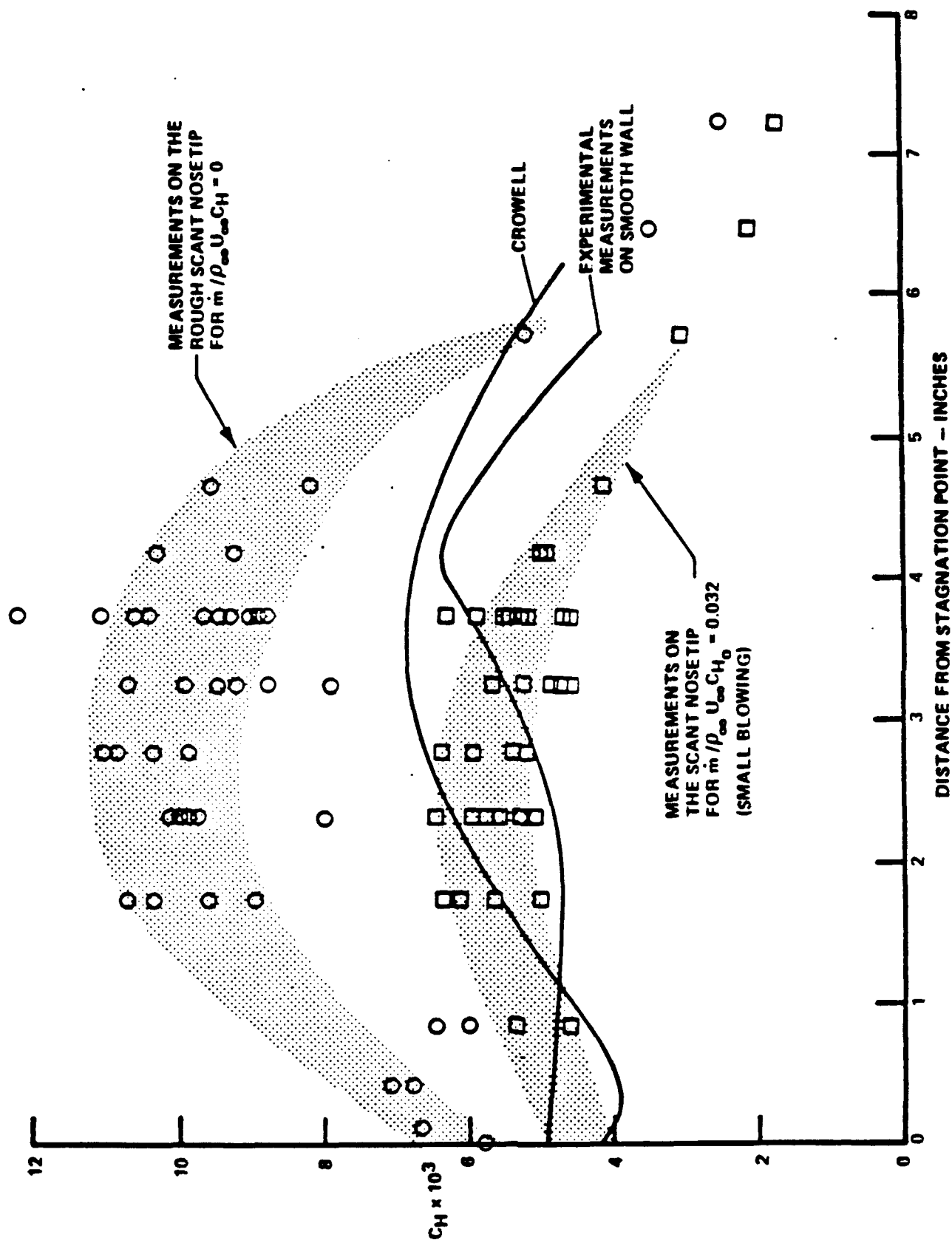


Figure 2 HEAT TRANSFER MEASUREMENTS ON SCANT AND SMOOTH HEMISPHERICAL NOSETIP SHOWING HOW SMALL BLOWING BRINGS DOWN HEATING LEVELS TO SMOOTH-WALL VALUES

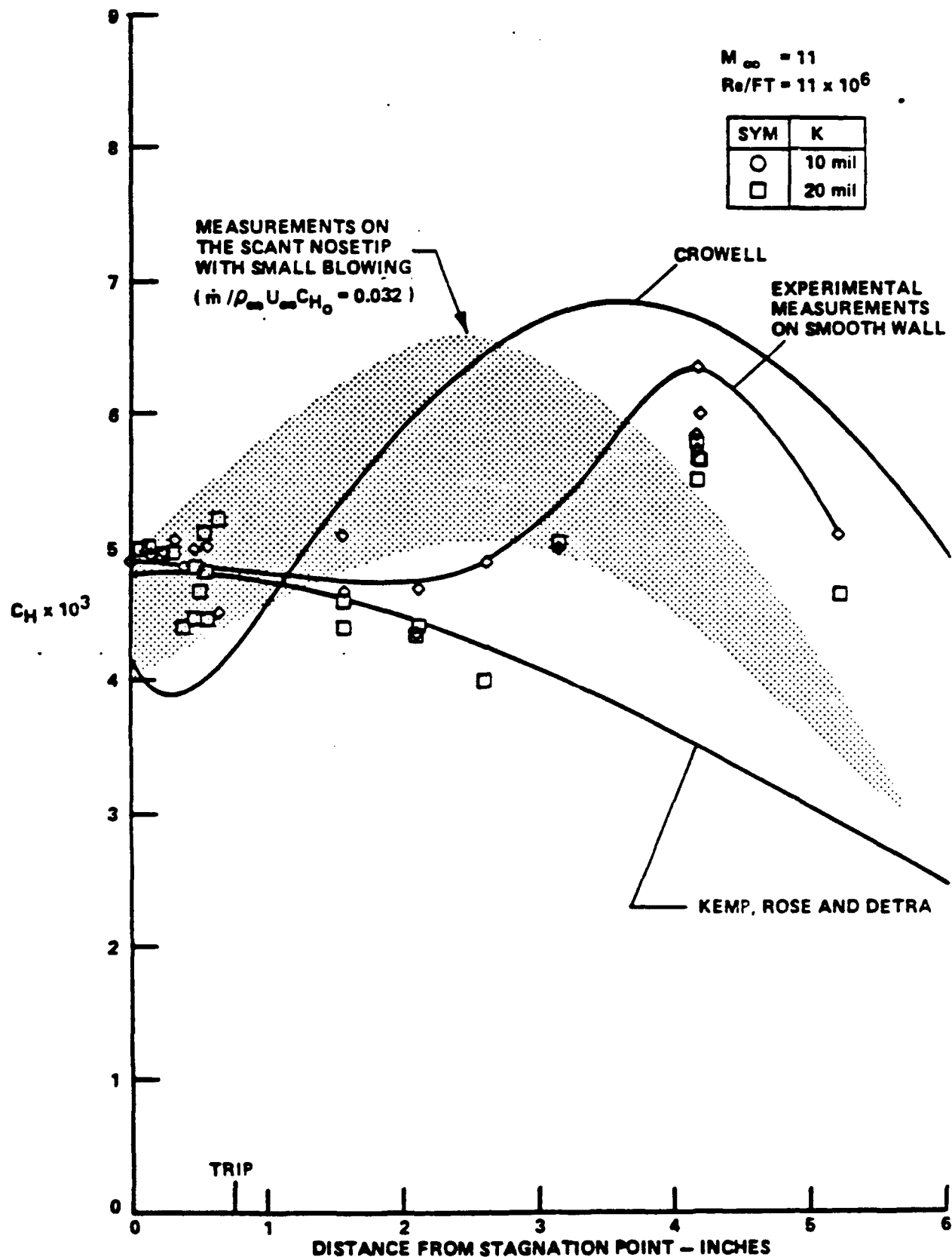


Figure 3 HEAT TRANSFER MEASUREMENTS INDICATING THAT SMALL BLOWING ON ROUGH NOSETIP INITIALLY ACTS TO BRING DOWN HEATING LEVELS TO SMOOTH-WALL VALUES

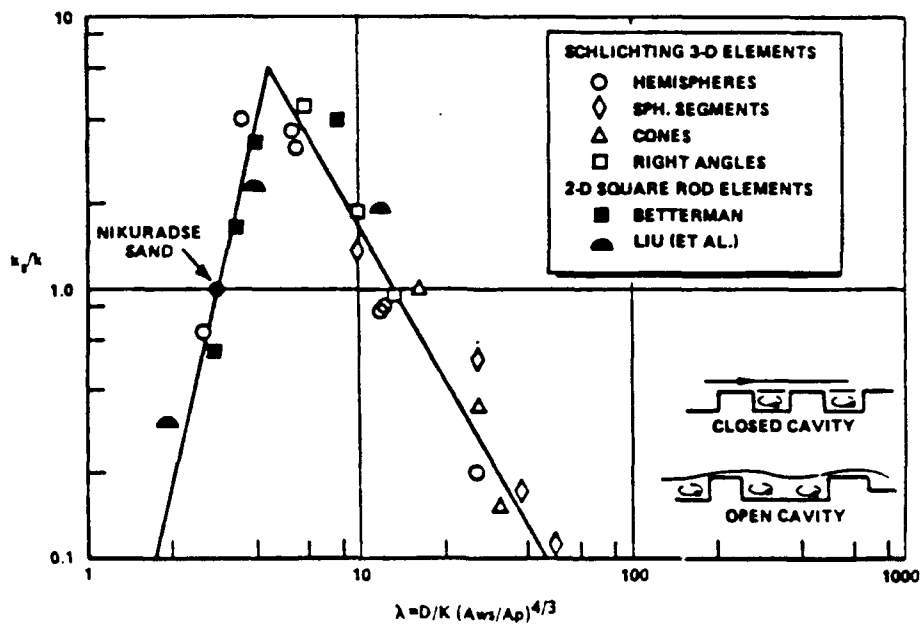


Figure 4 "EFFECTIVE" ROUGHNESS CORRELATIONS FOR DIFFERING ROUGHNESS GEOMETRIES AND SPACINGS

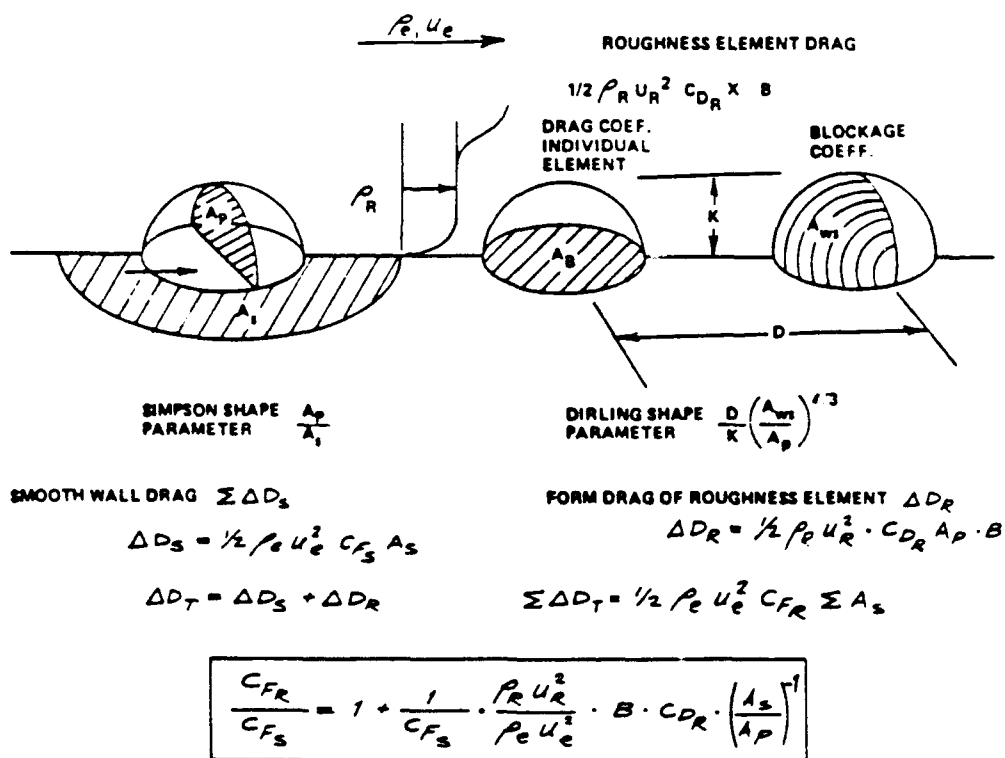


Figure 5 SIMPLIFIED DRAG MODEL FOR ROUGH-WALL SKIN FRICTION

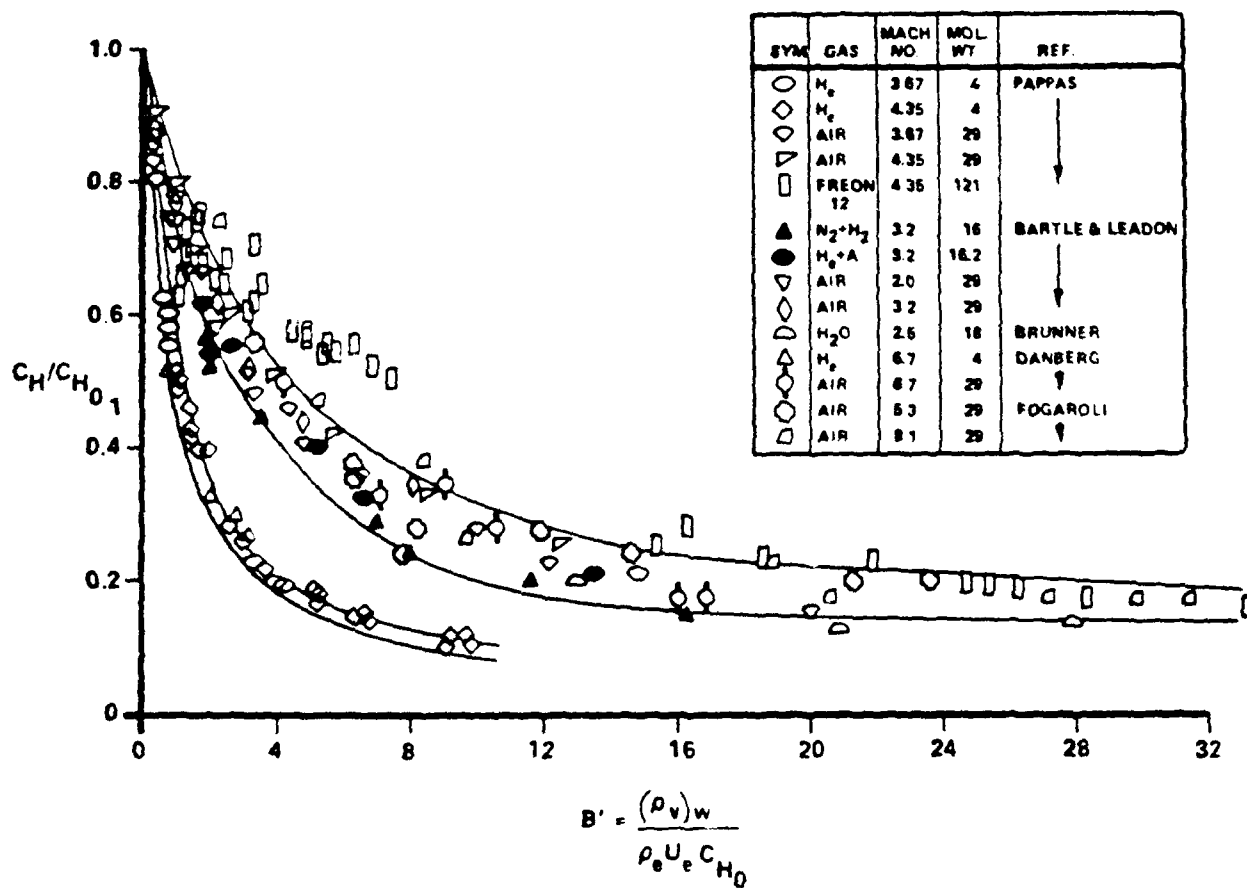


Figure 6 SUMMARY OF BLOCKAGE HEATING FROM EARLIER STUDIES ON FLAT PLATES AND CONES IN TURBULENT FLOW

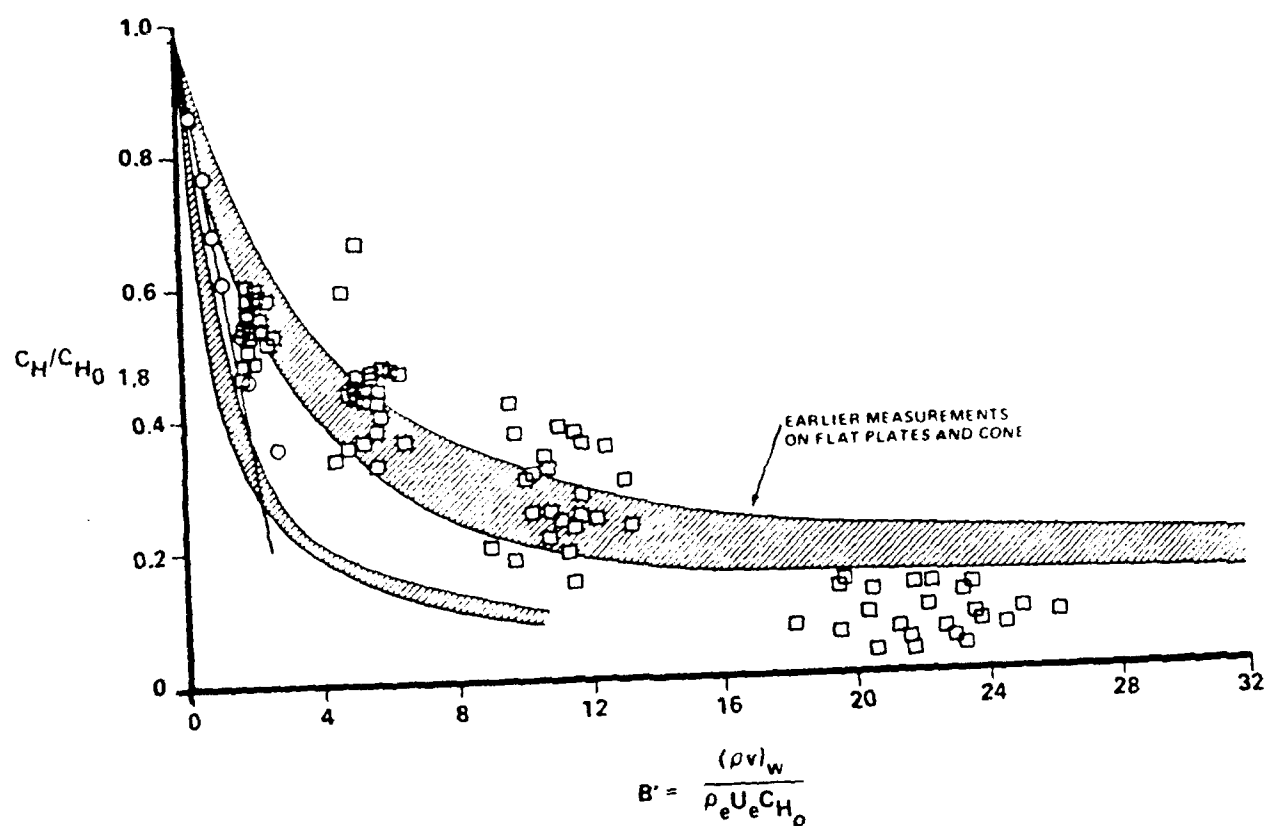


Figure 7 COMPARISON BETWEEN THE MEASUREMENT MADE ON THE
 TRANSPIRATION-COOLED NOSETIPS WITH NITROGEN INJECTANT
 AND THE EARLIER BLOCKAGE DATA

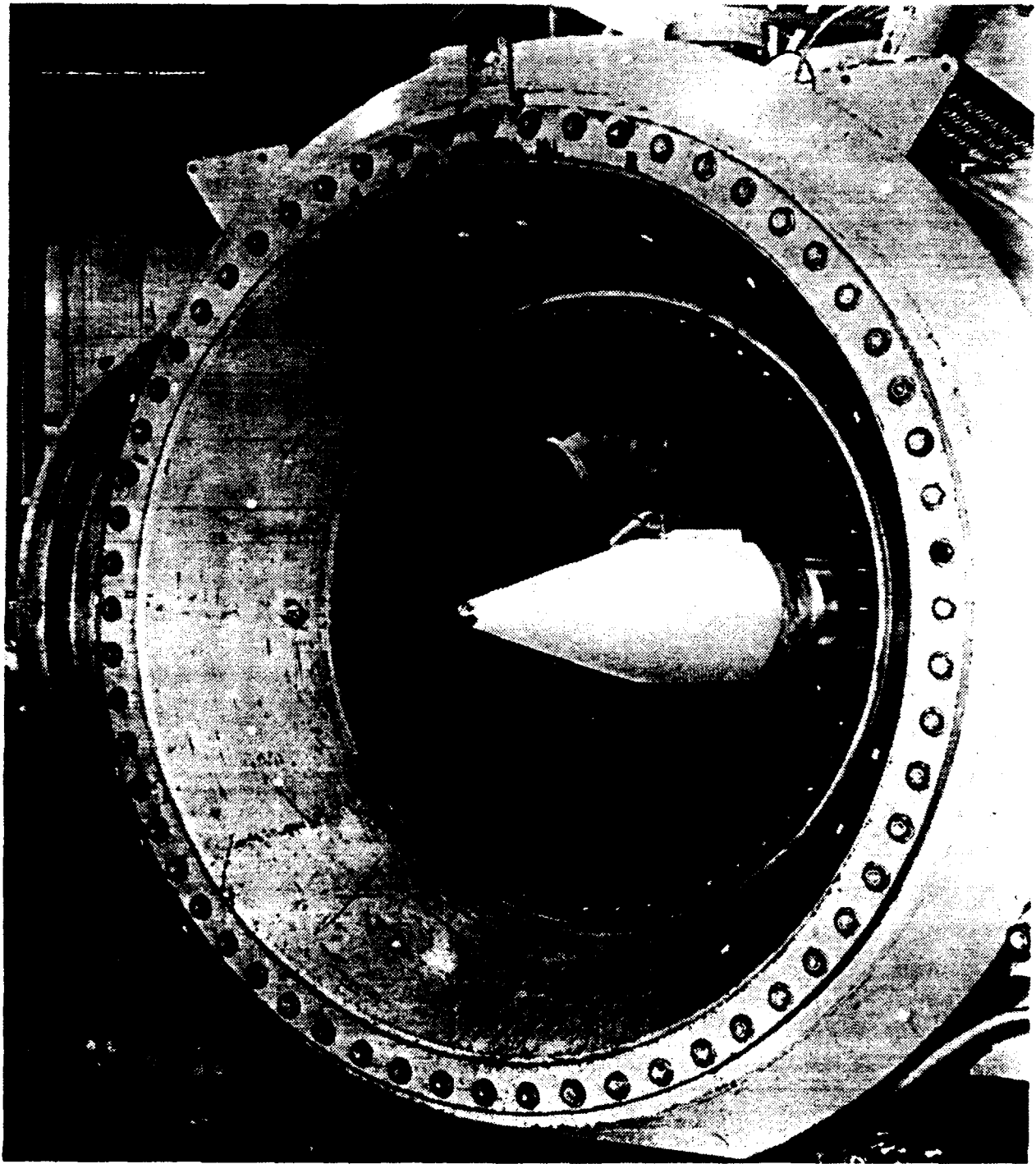


Figure 8 CONE MODEL

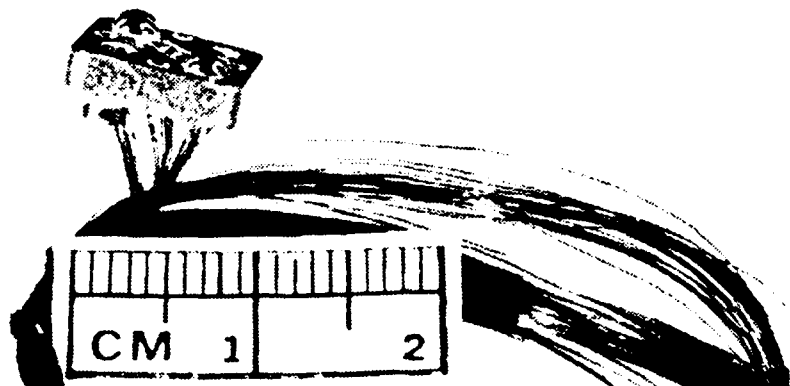


Figure 9 THIN FILM GAGES

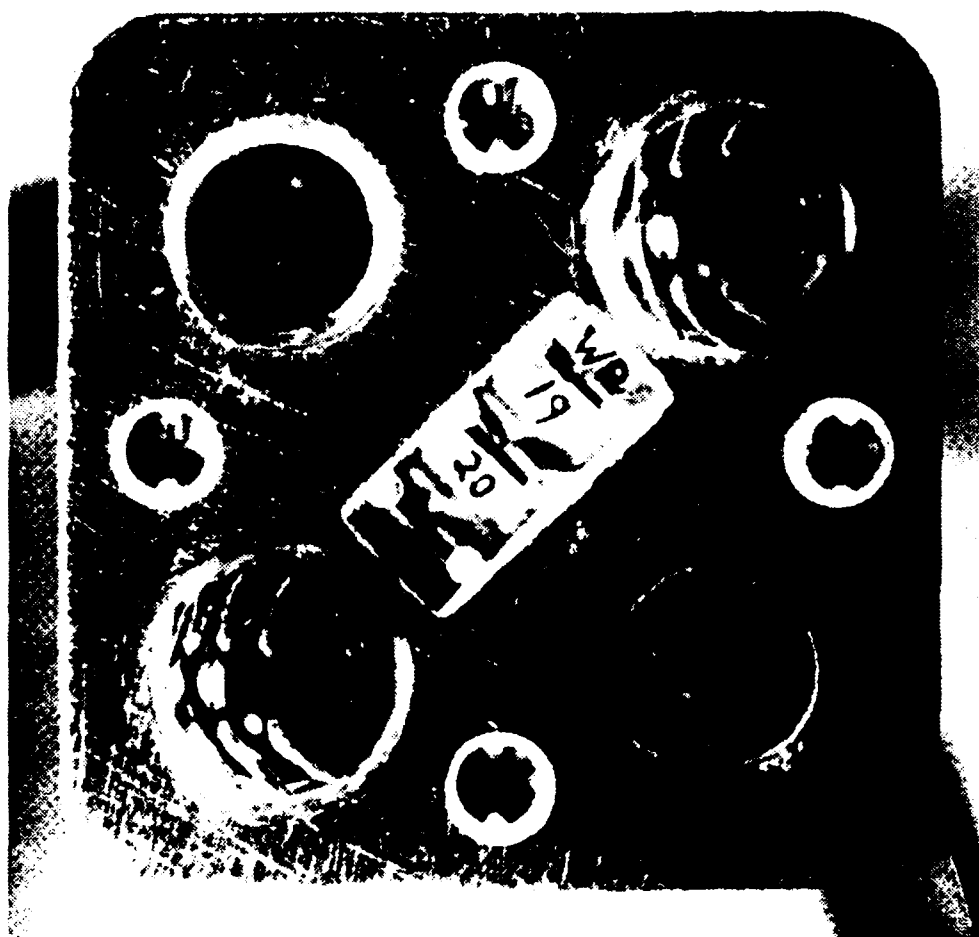


Figure 10 THIN FILM GAGE VIEWED FROM ABOVE

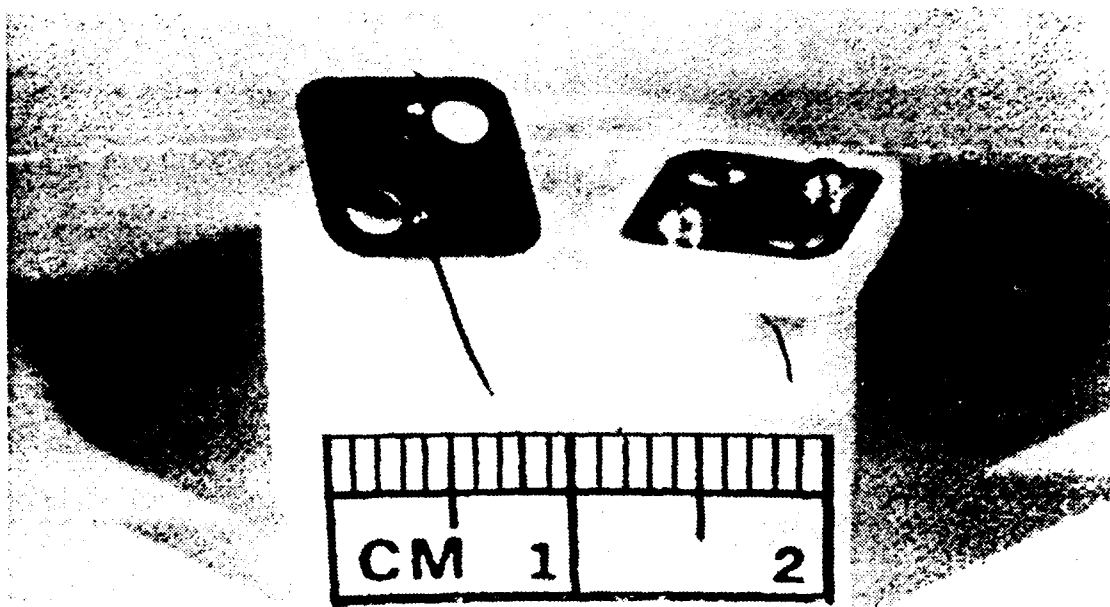


Figure 11 CALORIMETER GAGE

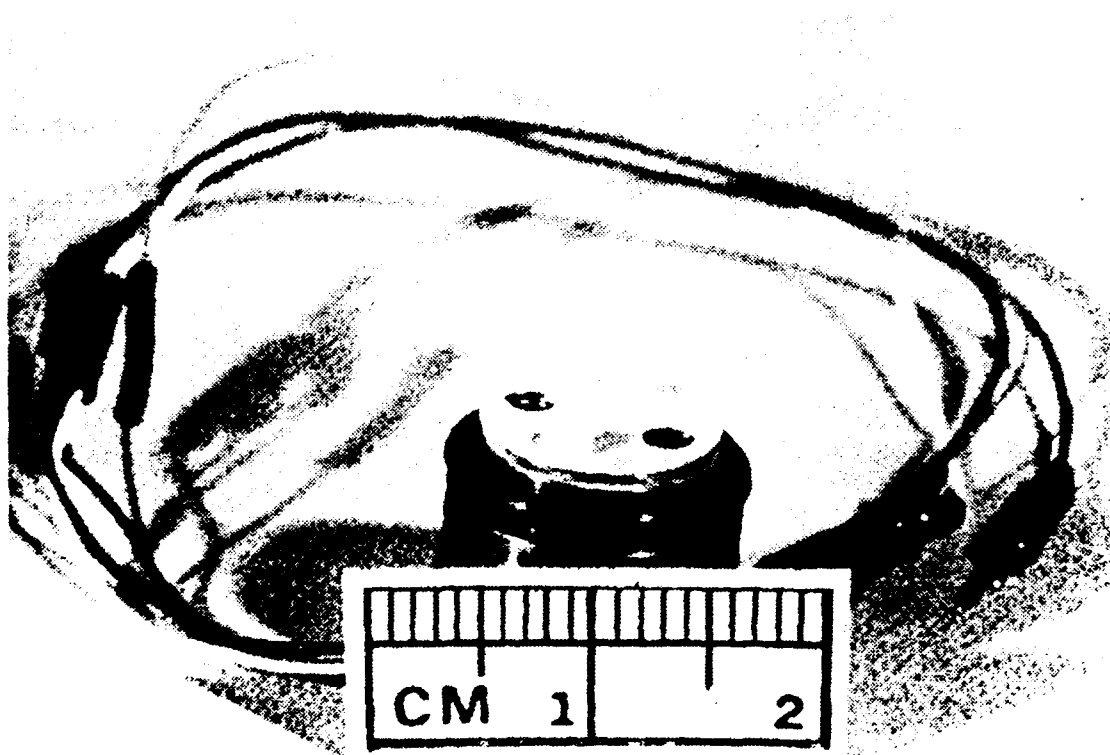
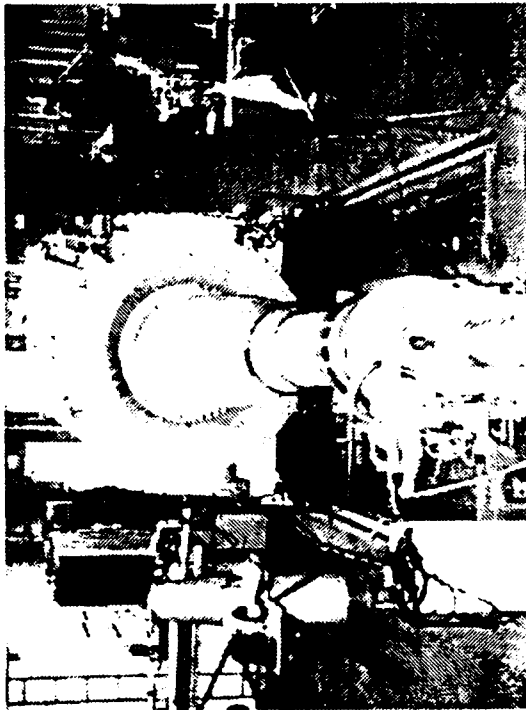
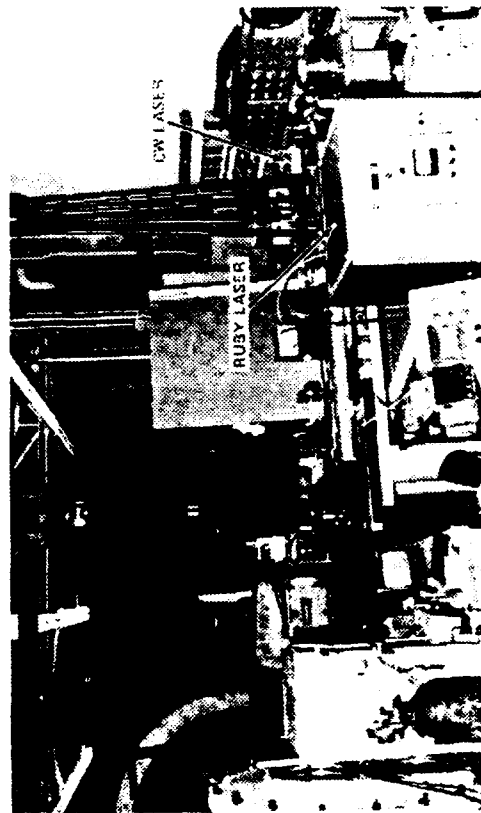


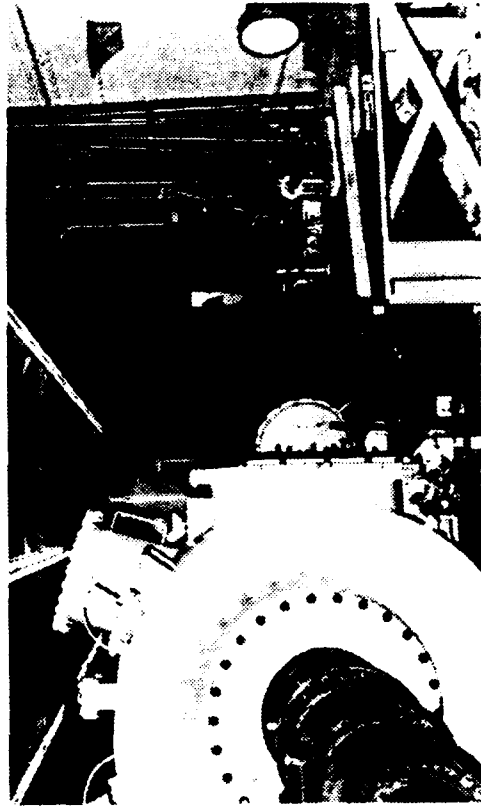
Figure 12 SKIN FRICTION GAGE



96-INCH HYPersonic SHOCK TUNNEL WITH LASER HOLOGRAPHIC SYSTEM INSTALLED



SENDING OPTICS



RECEIVING OPTICS

Figure 13 LASER HOLOGRAPHIC SYSTEM

Run#	Mach#	Reynolds# ($10^6/\text{Ft}$)	Blowing Rate	Injectant	Flap Angle (Deg)	A.O.A. (Deg)	Nose Type
2	13	5.0	0	Nitrogen	15	0	Sharp
3	13	5.0	0	Nitrogen	15	0	Sharp
4	13	5.0	.837	Nitrogen	15	0	Sharp
5	13	5.0	.875	Nitrogen	15	0	Sharp
6	13	5.0	1.650	Nitrogen	15	0	Sharp
7	13	5.0	4.043	Nitrogen	15	0	Sharp
9	13	5.0	.479	Nitrogen	25	0	Sharp
10	13	5.0	1.715	Nitrogen	25	0	Sharp
11	13	5.0	4.218	Nitrogen	25	0	Sharp
12	13	5.0	.862	Nitrogen	25	0	Sharp
13	13	5.0	.677	Nitrogen	25	0	Sharp
14	13	5.0	.106	Nitrogen	25	0	Sharp
15	13	5.0	2.765	Nitrogen	25	0	Sharp
16	13	5.0	.678	N2/He	25	0	Sharp
17	13	5.0	.255	N2/He	25	0	Sharp
18	13	5.0	1.586	N2/He	25	0	Sharp
20	13	5.0	.731	Nitrogen	30	0	Sharp
21	13	5.0	.341	Nitrogen	30	0	Sharp
22	13	5.0	5.382	Nitrogen	30	0	Sharp
23	13	5.0	2.015	Nitrogen	30	0	Blunt
24	13	5.0	.721	Nitrogen	30	0	Blunt
25	13	5.0	.352	Nitrogen	35	0	Sharp
26	13	5.0	.711	Nitrogen	35	0	Sharp
27	13	5.0	2.125	Nitrogen	35	0	Sharp
28	13	5.0	.561	N2/He	35	0	Sharp
29	11	4.0	.526	Nitrogen	25	0	Sharp
30	11	4.0	1.126	Nitrogen	25	0	Sharp
31	11	4.0	0	Nitrogen	25	0	Sharp
32	11	10.0	1.686	Nitrogen	25	0	Sharp
33	11	10.0	.678	Nitrogen	25	0	Sharp
34	11	10.0	.222	Nitrogen	25	0	Sharp
35	11	10.0	3.931	Nitrogen	25	0	Sharp
36	11	10.0	.374	N2/He	25	0	Sharp
37	11	10.0	.870	N2/He	25	0	Sharp
38	11	10.0	.202	N2/He	25	0	Sharp
39	11	10.0	1.329	N2/He	25	0	Sharp
40	15	1.5	.398	Nitrogen	25	0	Sharp
41	15	1.5	.560	Nitrogen	25	0	Sharp
42	15	1.5	1.329	Nitrogen	25	0	Sharp
43	13	7.0	.637	Nitrogen	25	3	Sharp
44	13	7.0	.305	Nitrogen	25	3	Sharp
45	13	7.0	2.102	Nitrogen	25	3	Sharp
46	13	6.0	.681	Nitrogen	25	3	Blunt
47	13	6.0	.652	Nitrogen	25	6	Blunt
48	13	6.0	.305	Nitrogen	25	6	Sharp
49	13	6.0	.679	Nitrogen	25	6	Sharp
50	13	6.0	2.216	Nitrogen	25	6	Sharp

Figure 14 TEST MATRIX FOR THE BLOWING AND ROUGHNESS STUDIES

Run	Po/10 ⁴ PSIA	Ho/10 ⁴ (FT/SEC) ^{1/2}	To °R	Mø	Uø FT/SEC	Tø °R	Pø PSIA	Rhoø SLUGS/FT ³
3	1.7860	2.1181	3063.0	12.968	6417.3	101.820	.076982	6.3447(-5)
4	1.8555	2.0879	3027.2	13.026	6372.1	99.500	.078939	6.6579(-5)
5	1.7671	2.0745	3011.5	13.003	6351.4	99.205	.075545	6.3905(-5)
6	1.8268	2.1142	3051.5	13.019	6412.0	100.870	.077164	6.4199(-5)
7	1.8100	2.0850	3025.8	13.028	6367.8	99.339	.076571	6.4686(-5)
9	1.7010	2.0126	2939.2	13.052	6256.5	95.549	.071542	6.2835(-5)
10	1.7815	2.1206	3073.3	13.031	6421.9	100.990	.074230	6.1681(-5)
11	1.8303	2.2023	3174.1	13.014	6544.2	105.150	.075595	6.0334(-5)
12	1.8320	2.1121	3059.7	13.029	6409.0	100.620	.077089	6.4291(-5)
13	1.8383	2.1364	3091.3	13.034	6445.9	101.710	.076666	6.3259(-5)
14	1.8366	2.1037	3048.2	13.025	6396.1	100.280	.077665	6.4996(-5)
15	1.8235	2.1237	3075.0	13.028	6426.6	101.180	.076408	6.3372(-5)
16	1.7693	2.0641	2997.2	12.997	6335.2	98.793	.076130	6.4669(-5)
17	1.8415	2.1037	3048.2	13.027	6396.1	100.250	.077837	6.5160(-5)
18	1.8528	2.1195	3069.3	13.037	6420.3	100.840	.077633	6.4605(-5)
20	1.7933	2.1111	3059.9	13.025	6407.5	100.630	.075254	6.2760(-5)
21	1.7983	2.1333	3088.5	13.028	6441.0	101.630	.074909	6.1853(-5)
22	1.7878	2.0882	3030.6	13.026	6372.6	99.531	.075458	6.3623(-5)
23	1.8753	2.1386	3092.2	13.032	6449.0	101.830	.078565	6.4745(-5)
24	1.8060	2.0894	3033.7	13.047	6374.8	99.273	.075531	6.3850(-5)
25	1.6813	2.0606	2996.3	12.994	6329.9	98.672	.071683	6.0966(-5)
26	1.8528	2.1216	3073.2	13.048	6423.7	100.790	.077172	6.4254(-5)
27	1.7658	2.0785	3023.0	13.062	6358.3	98.528	.073123	6.2282(-5)
28	1.7993	2.0640	3002.2	13.058	6335.9	97.905	.075321	6.4562(-5)
29	.72940	1.7309	2598.2	11.006	5768.8	114.250	.092331	6.7820(-5)
30	.74835	1.7749	2655.0	10.998	5841.5	117.320	.094527	6.7618(-5)
31	.75930	1.7521	2625.9	11.012	5804.1	115.520	.095770	6.9572(-5)
32	1.7363	1.6998	2575.8	11.347	5723.5	105.800	.207250	1.6439(-4)
33	1.7585	1.7248	2609.1	11.354	5765.6	107.230	.208200	1.6294(-4)
34	1.7423	1.7265	2612.3	11.356	5768.4	107.290	.205350	1.6062(-4)
35	1.7263	1.7357	2624.8	11.353	5783.7	107.930	.202780	1.5767(-4)
36	1.7350	1.7200	2602.3	11.343	5757.4	107.130	.206210	1.6154(-4)
37	1.7435	1.7341	2621.6	11.351	5781.0	107.870	.205710	1.6004(-4)
38	1.6933	1.7223	2607.9	11.348	5761.3	107.180	.199160	1.5593(-4)
39	1.7123	1.6855	2557.2	11.343	5699.2	104.980	.204900	1.6380(-4)
40	1.7995	4.0076	5484.8	15.867	8869.7	129.930	.012272	7.9261(-6)
41	1.8348	2.9248	4028.1	15.414	7572.9	100.370	.019757	1.6519(-5)
42	1.8133	2.9680	4080.7	15.396	7628.5	102.090	.019439	1.5979(-5)
43	2.0123	1.7570	2646.7	13.319	5849.1	80.192	.083197	8.7065(-5)
44	2.0323	1.7925	2693.2	13.326	5908.0	81.733	.082990	8.5211(-5)
45	2.0693	1.8393	2754.4	13.338	5984.8	83.714	.083076	8.3280(-5)
46	1.9748	1.8215	2733.0	13.329	5955.6	83.012	.079161	8.0027(-5)
47	2.0848	1.8666	2788.7	13.326	6020.8	85.111	.083643	8.2473(-5)
48	2.0440	1.8476	2766.1	13.341	5998.3	84.058	.081471	8.1337(-5)
49	2.0260	1.8653	2789.9	13.342	6027.0	84.854	.080084	7.9203(-5)
50	2.0383	1.8941	2827.2	13.343	6073.2	86.142	.079889	7.7829(-5)

Figure 15 EXPERIMENTAL TEST CONDITIONS

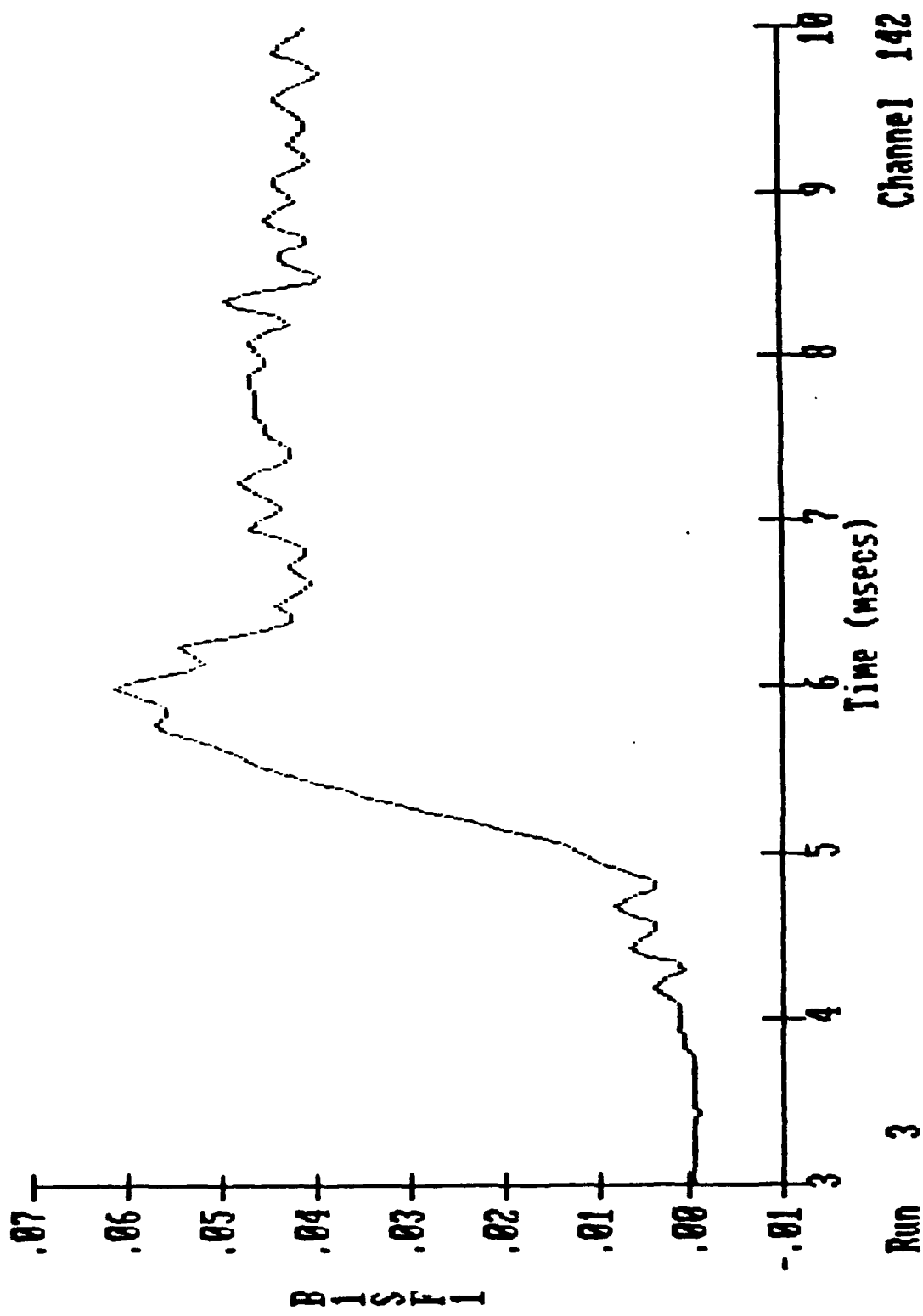


Figure 16 TIME HISTORY TRACE FROM SKIN FRICTION INSTRUMENTATION

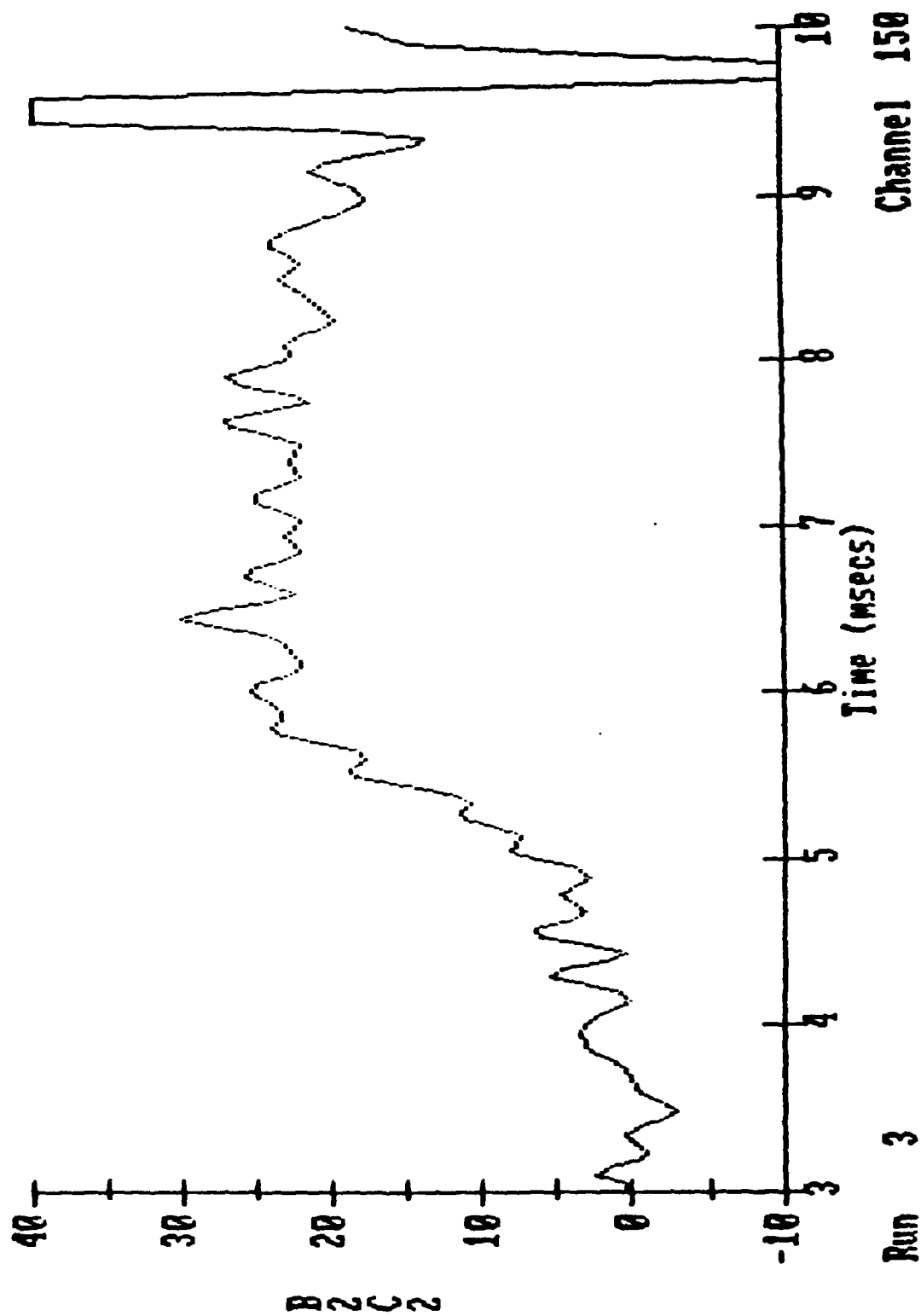


Figure 17 HEAT TRANSFER TIME HISTORY FROM CALORIMETER INSTRUMENTATION

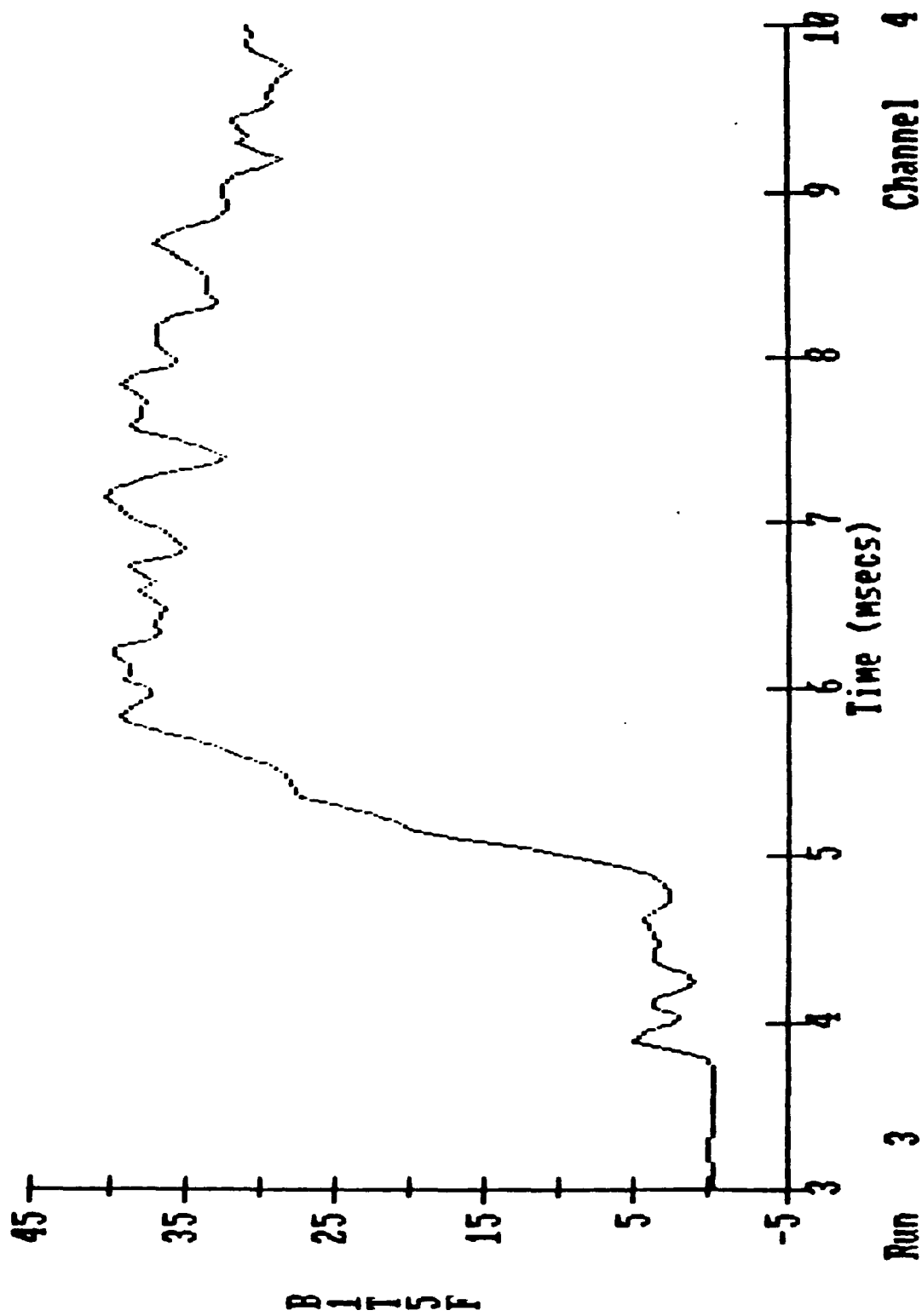


Figure 18 HEAT TRANSFER TIME HISTORY FROM THIN FILM INSTRUMENTATION



Figure 19 INTERFEROMETER PHOTOGRAPH $B' = 0.222$

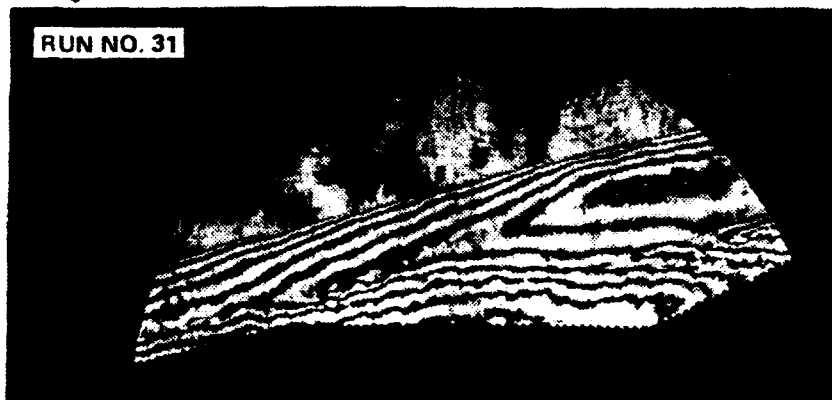


Figure 20 INTERFEROMETER PHOTOGRAPH $B' = 0.0$



Figure 21 INTERFEROMETER PHOTOGRAPH $B' = 0.0$



Figure 22 INTERFEROMETER PHOTOGRAPH $B' = 0.678$



Figure 23 INTERFEROMETER PHOTOGRAPH $B' = 1.686$

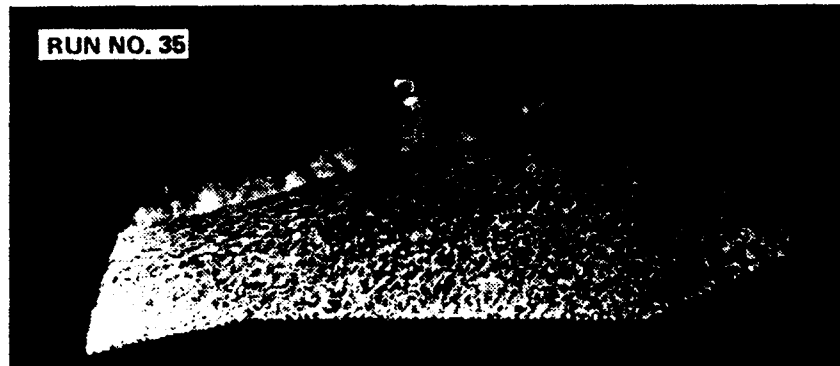


Figure 24 INTERFEROMETER PHOTOGRAPH $B' = 3.931$

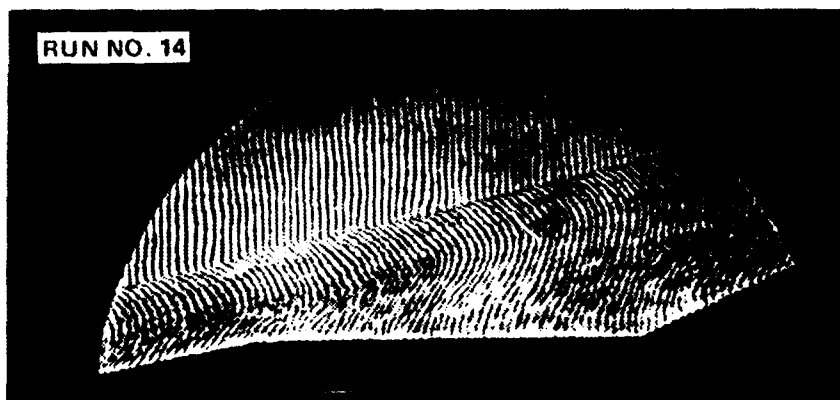


Figure 25 INTERFEROMETER PHOTOGRAPH $B' = 0.106$



Figure 26 INTERFEROMETER PHOTOGRAPH $B' = 0.526$



Figure 27 INTERFEROMETER PHOTOGRAPH $B' = 1.715$

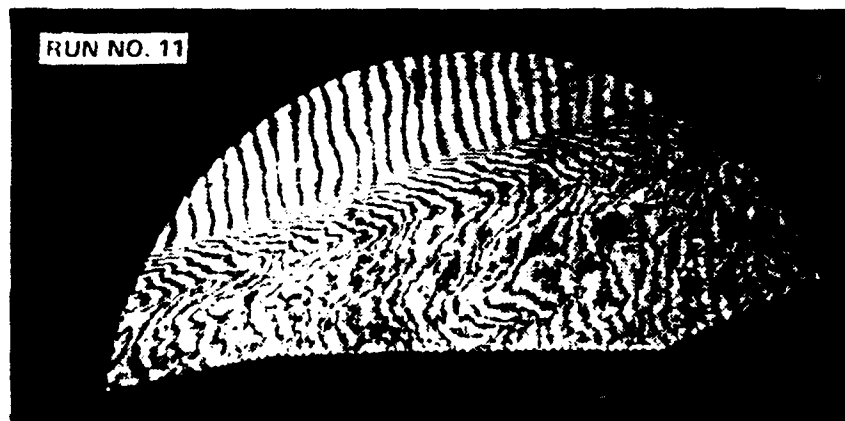


Figure 28 INTERFEROMETER PHOTOGRAPH $B' = 4.218$

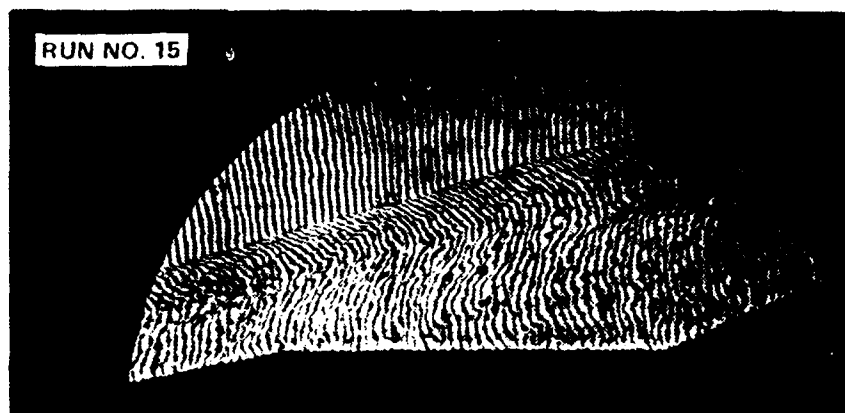


Figure 29 : INTERFEROMETER PHOTOGRAPH $B' = 2.765$

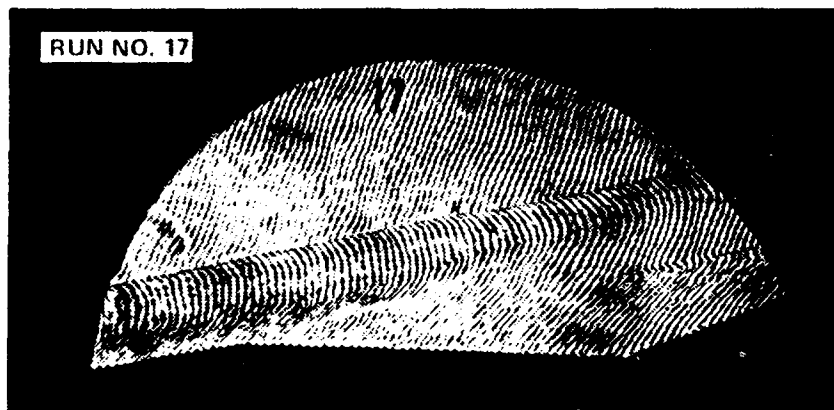


Figure 30 INTERFEROMETER PHOTOGRAPH $B' = 2.549$



Figure 31 INTERFEROMETER PHOTOGRAPH $B' = 1.586$

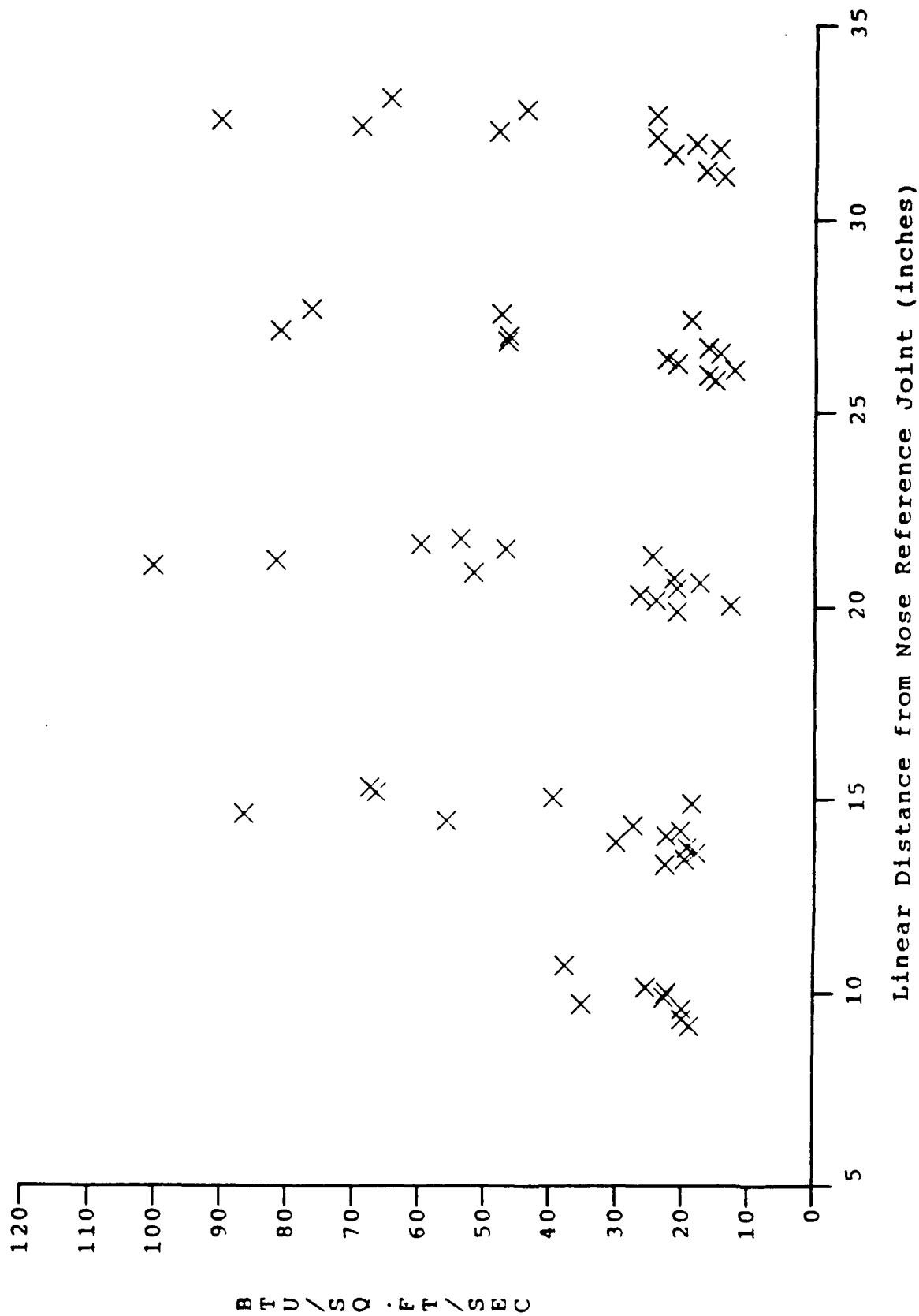


Figure 32a DISTRIBUTION OF HEATING ALONG MODEL SURFACE
(RUN # 34, $B'=0.231$, $M=11$, $Re/FT=1.0 \times 10^{-7}$)

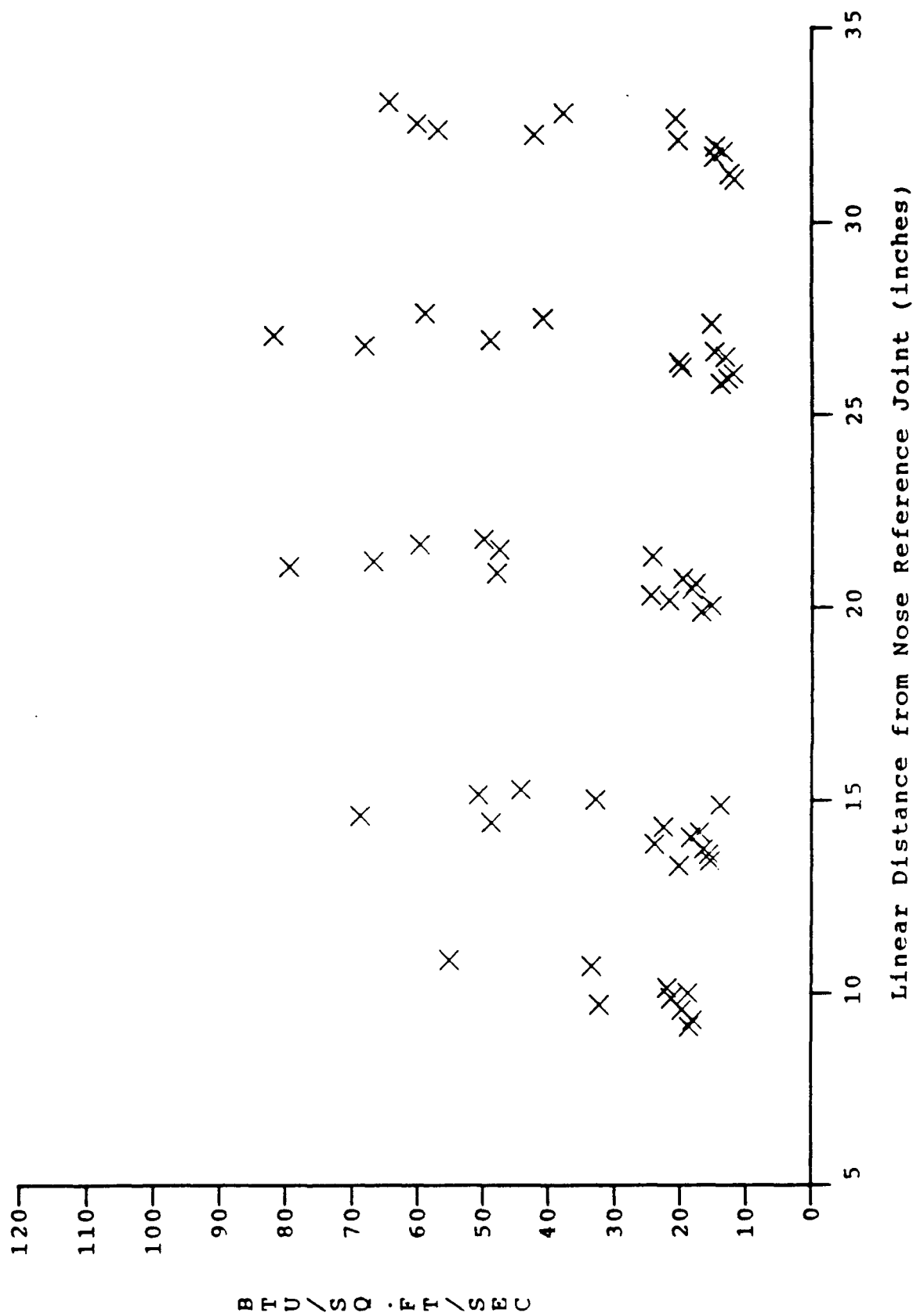


Figure 32b DISTRIBUTION OF HEATING ALONG MODEL SURFACE
(RUN # 33, B'=0.705, M=11, Re/FT=1.0X10⁷)

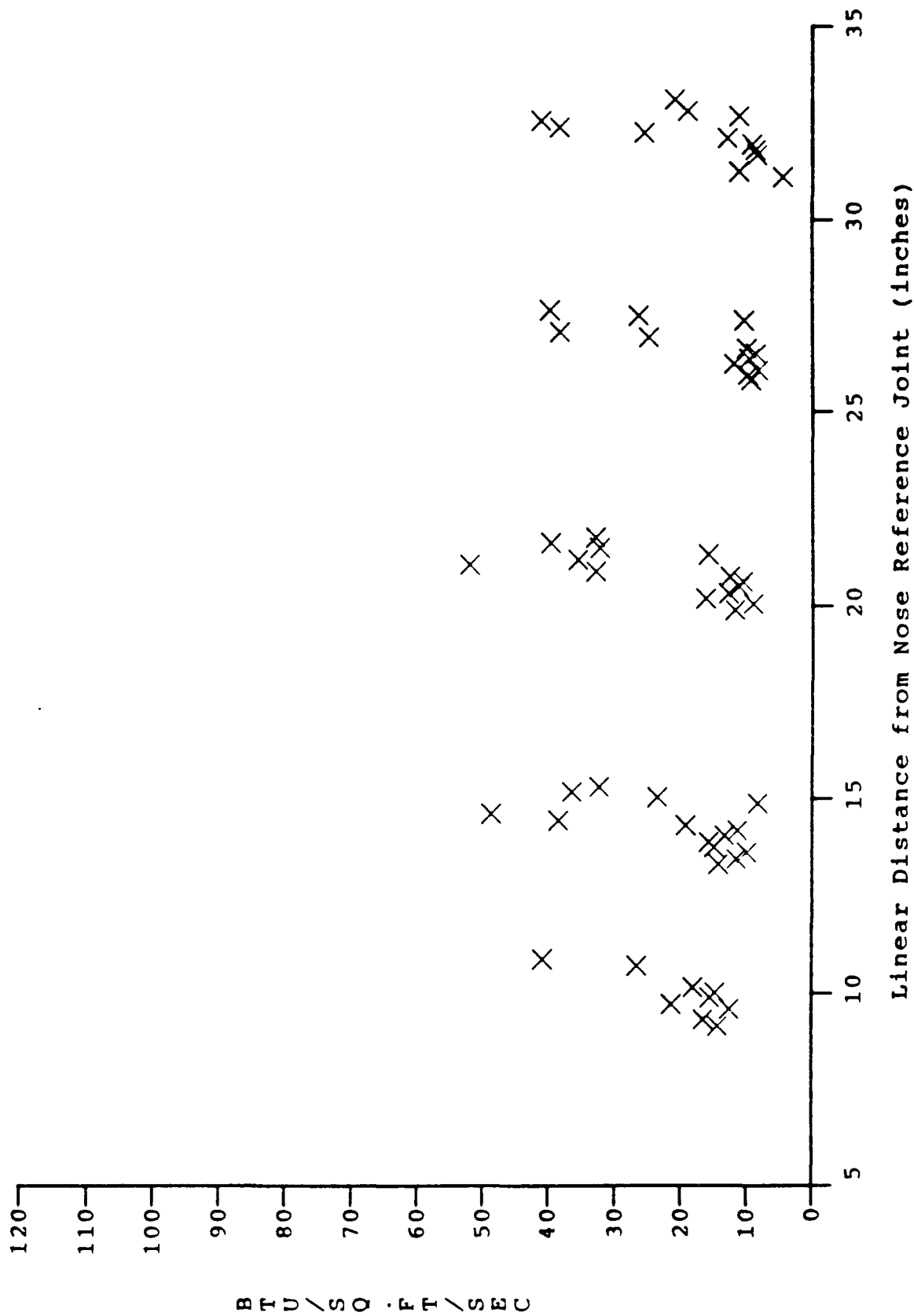


Figure 32c DISTRIBUTION OF HEATING ALONG MODEL SURFACE
(RUN # 32, $B'=1.751$, $M=11$, $Re/FT=1.0 \times 10^{-7}$)

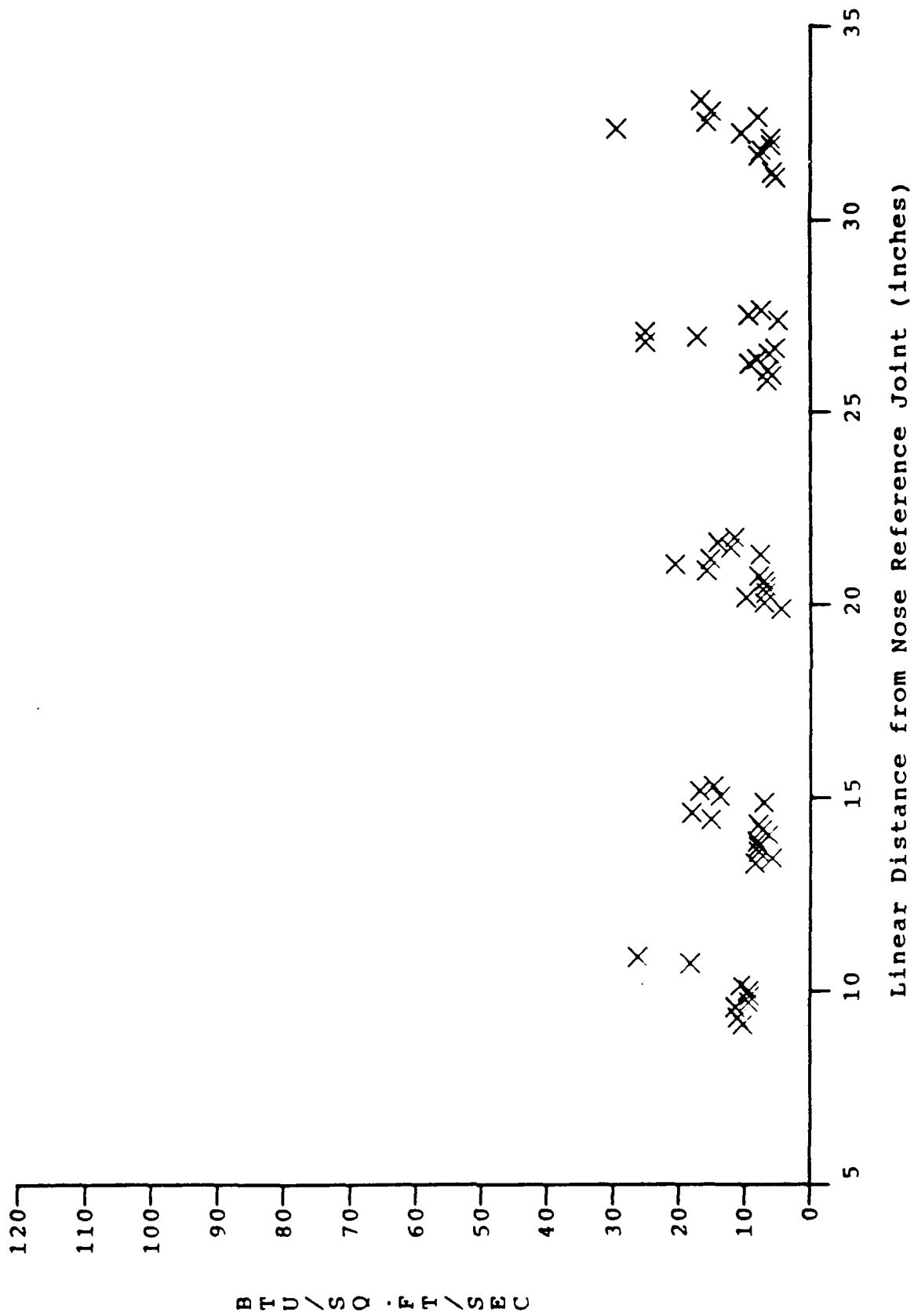


Figure 32d DISTRIBUTION OF HEATING ALONG MODEL SURFACE
(RUN # 35, $B'=4.083$, $M=11$, $Re/FT=1.0 \times 10^{-7}$)

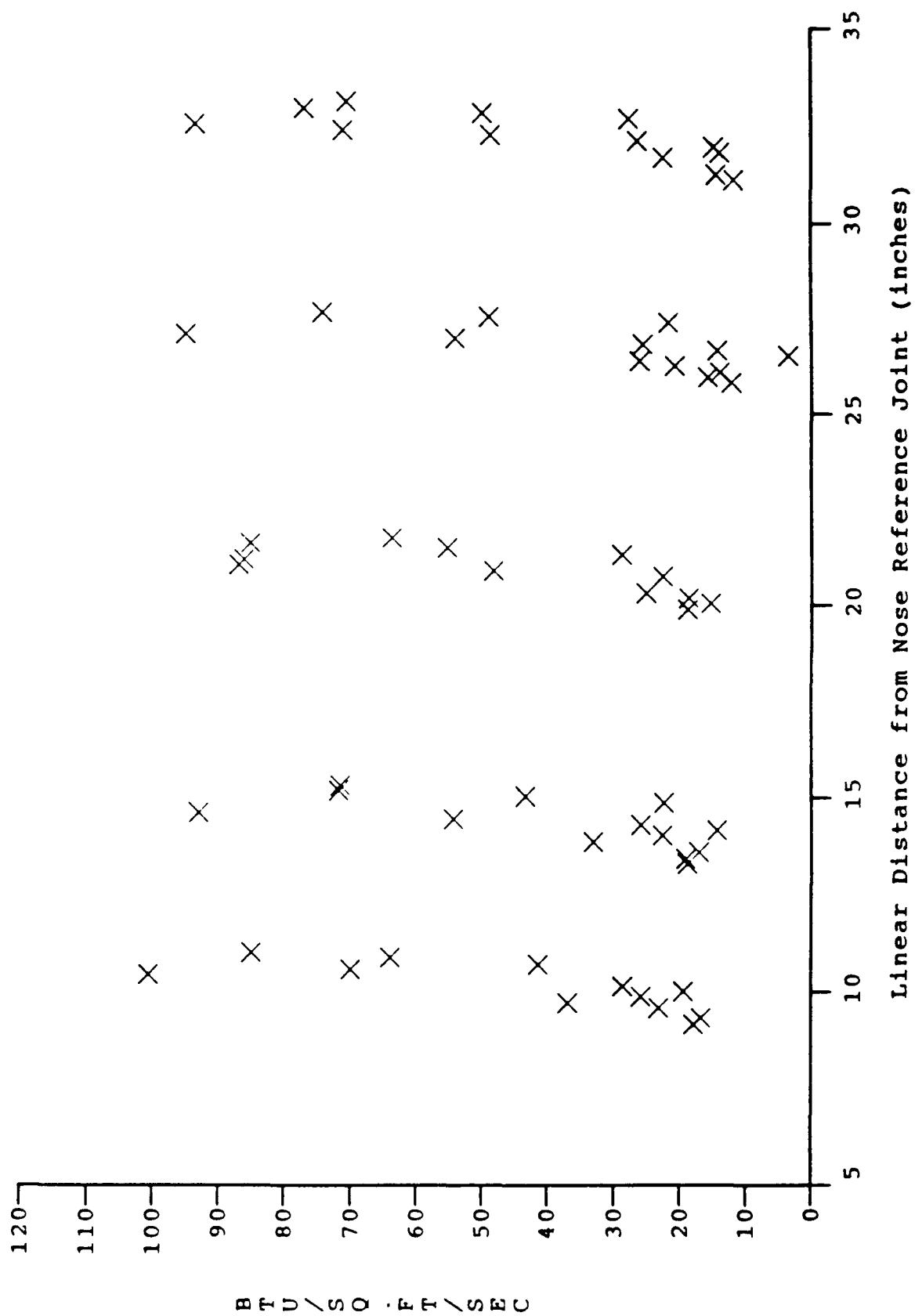


Figure 33a DISTRIBUTION OF HEATING ALONG MODEL SURFACE
(RUN # 3, B'=0.000, M=13, Re/FT=5.0X10⁶)

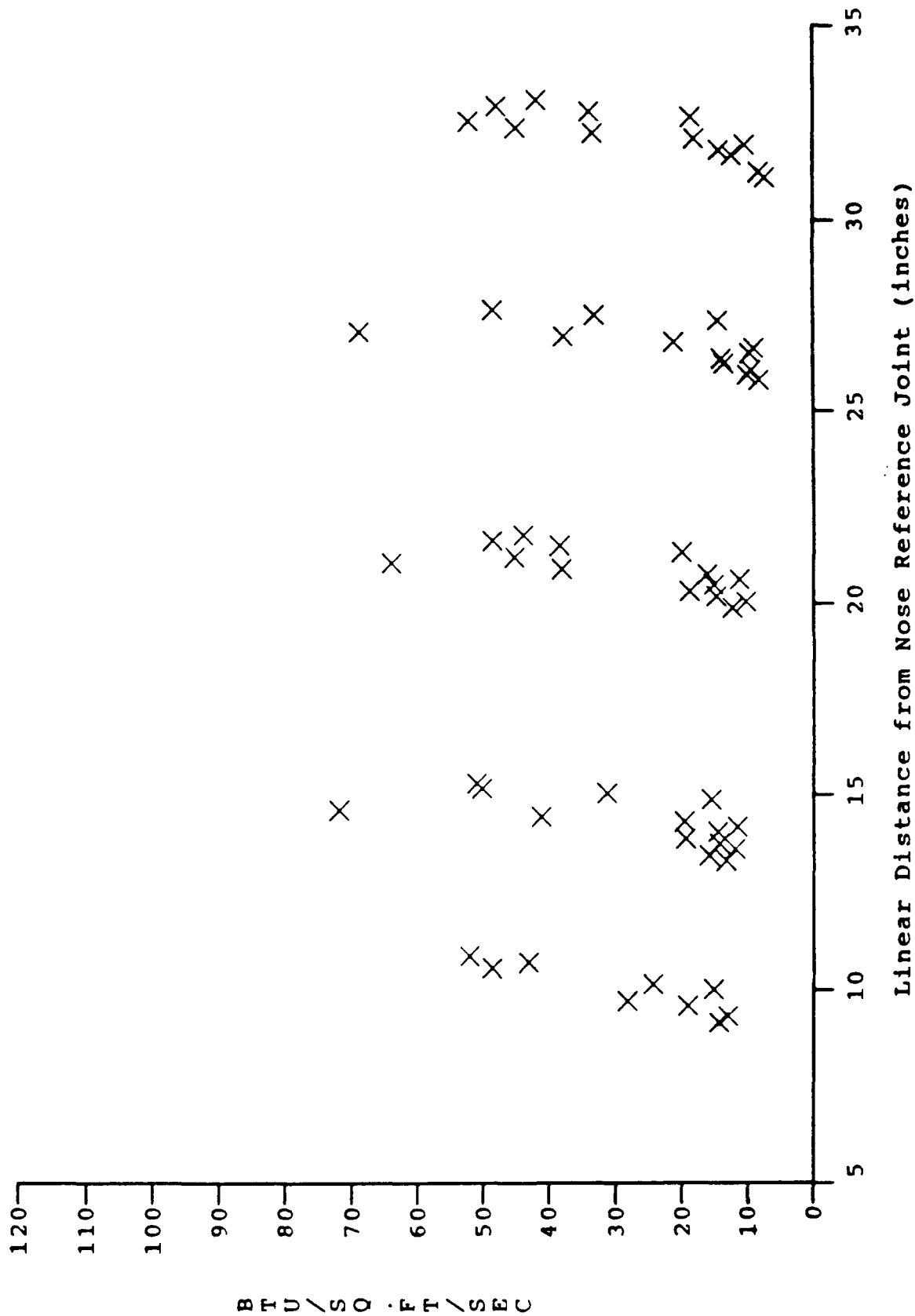
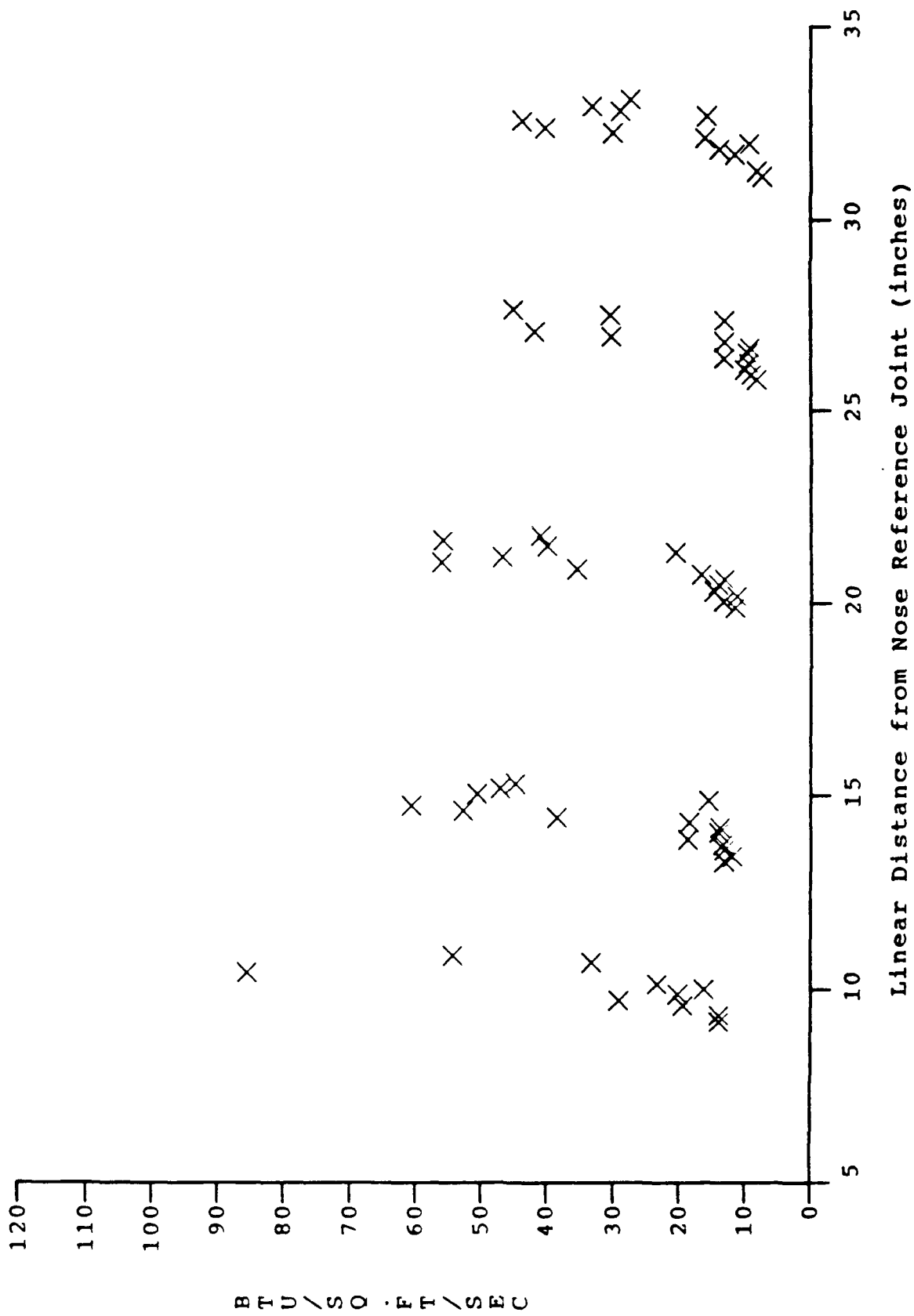


Figure 33b DISTRIBUTION OF HEATING ALONG MODEL SURFACE
(RUN #9, $B'=0.366$, $M=13$, $Re/FT=5.0 \times 10^{-6}$)



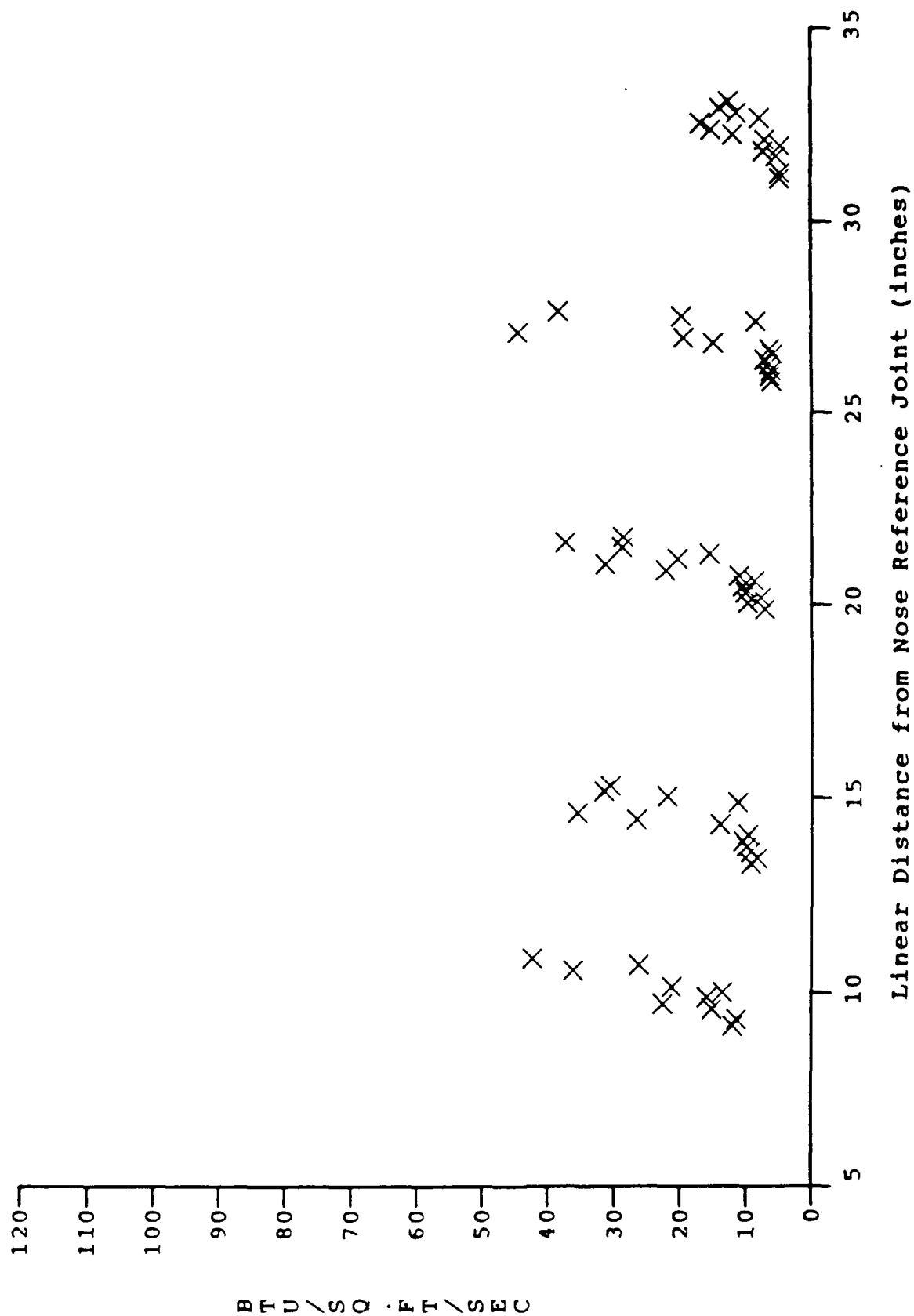
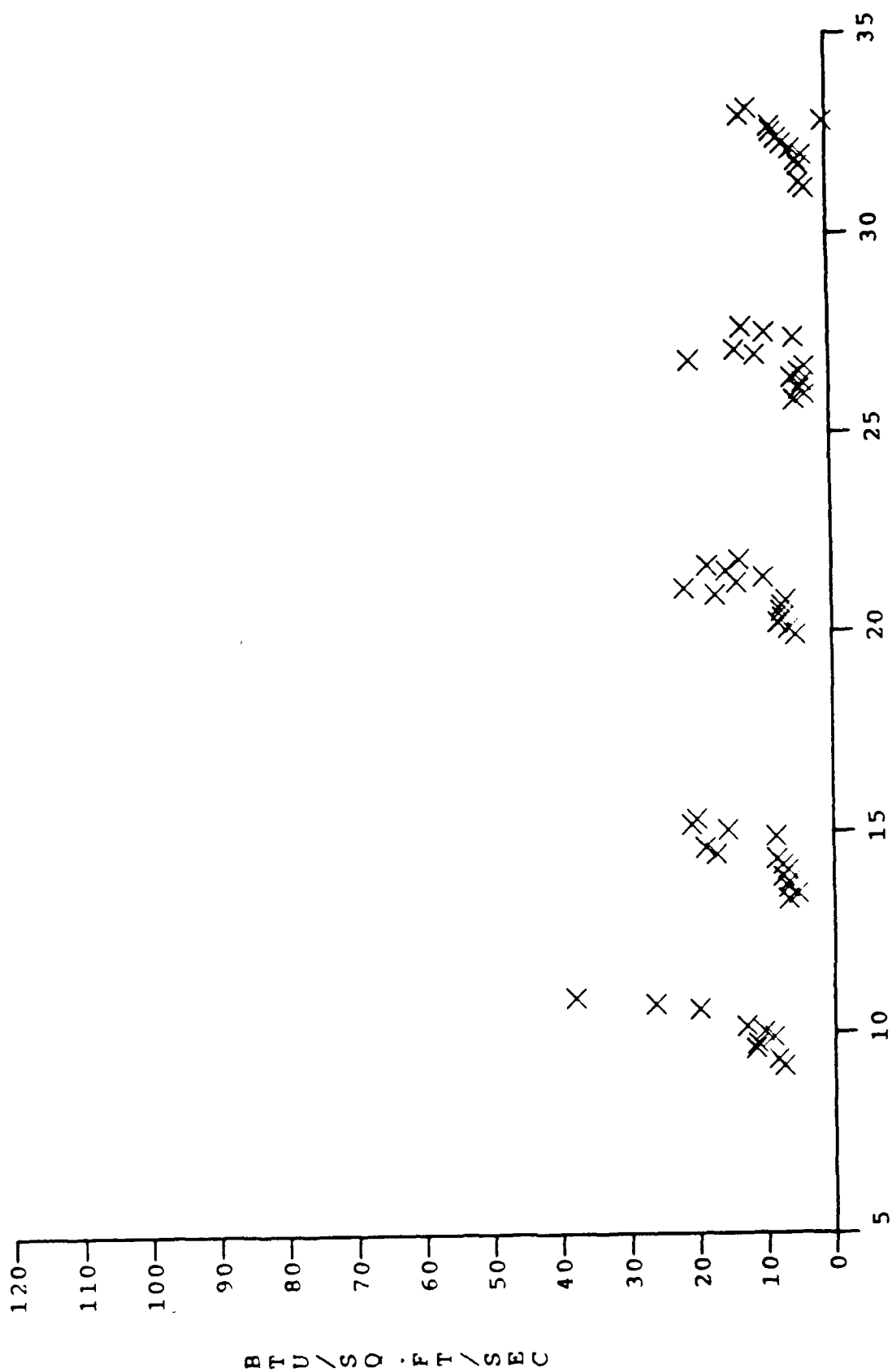


Figure 33d DISTRIBUTION OF HEATING ALONG MODEL SURFACE
(RUN # 6, B'=1.259, M=13, Re/FT=5.0X10⁶)



Linear Distance from Nose Reference Joint (inches)

Figure 33e DISTRIBUTION OF HEATING ALONG MODEL SURFACE
(RUN # 15, $B'=2.111$, $M=13$, $Re/FT=5.0 \times 10^{-6}$)

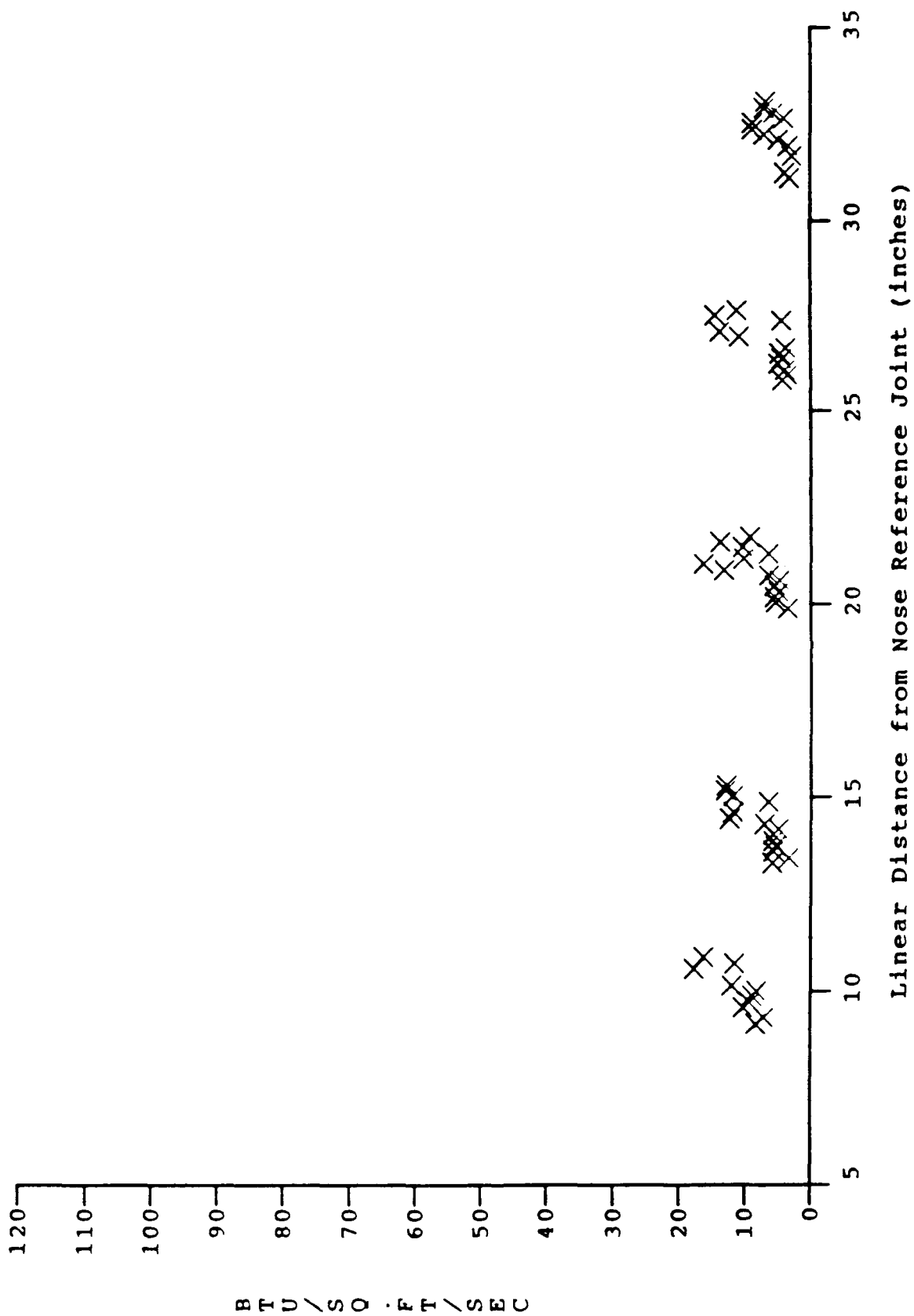
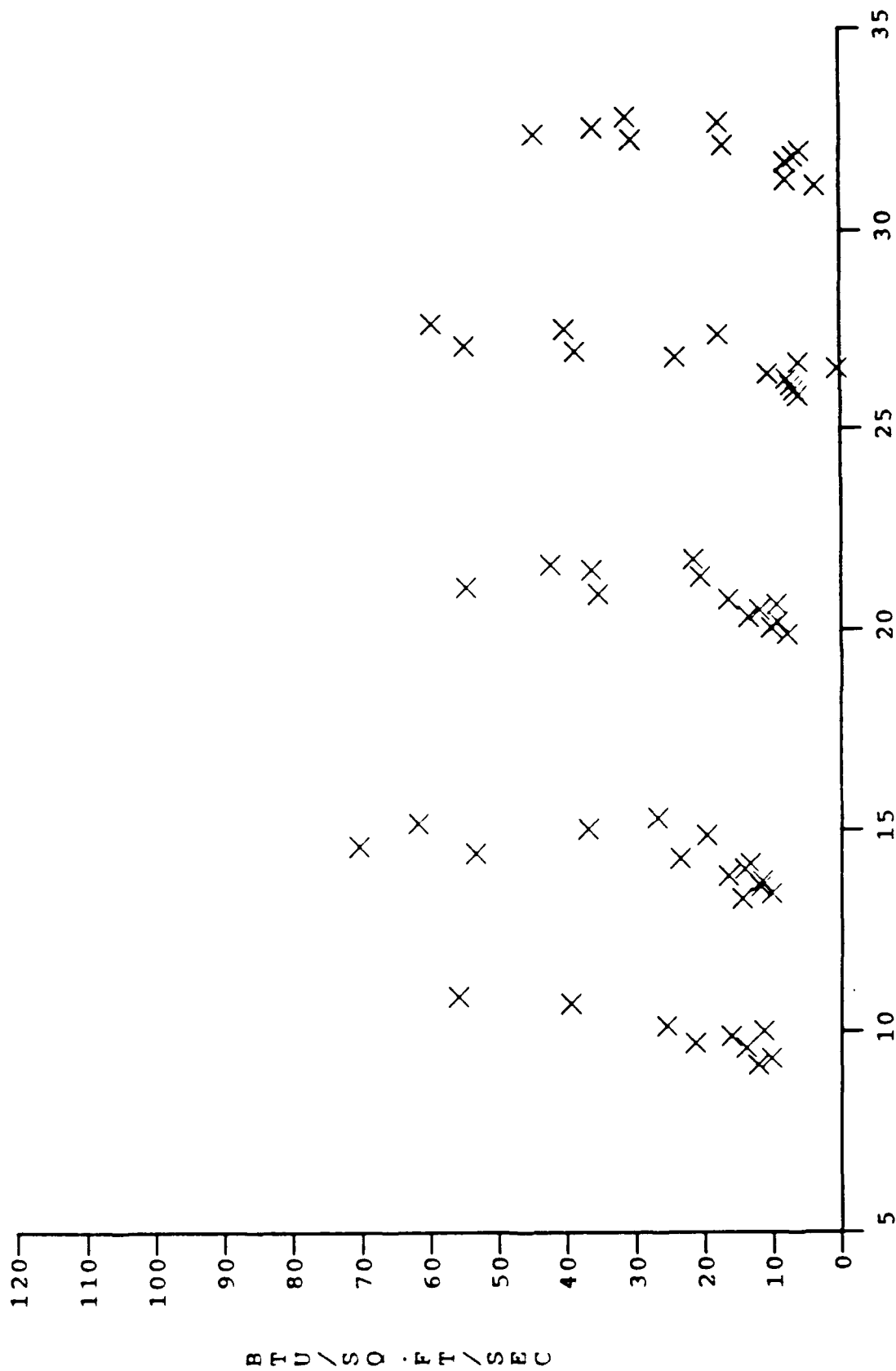


Figure 33f DISTRIBUTION OF HEATING ALONG MODEL SURFACE
(RUN # 7, $B'=3.086$, $M=13$, $Re/FT=5.0 \times 10^{-6}$)



Linear Distance from Nose Reference Joint (inches)

Figure 34a DISTRIBUTION OF HEATING ALONG MODEL SURFACE
(RUN # 40, $B'=0.398$, $M=15$, $Re/FT=1.5 \times 10^6$)

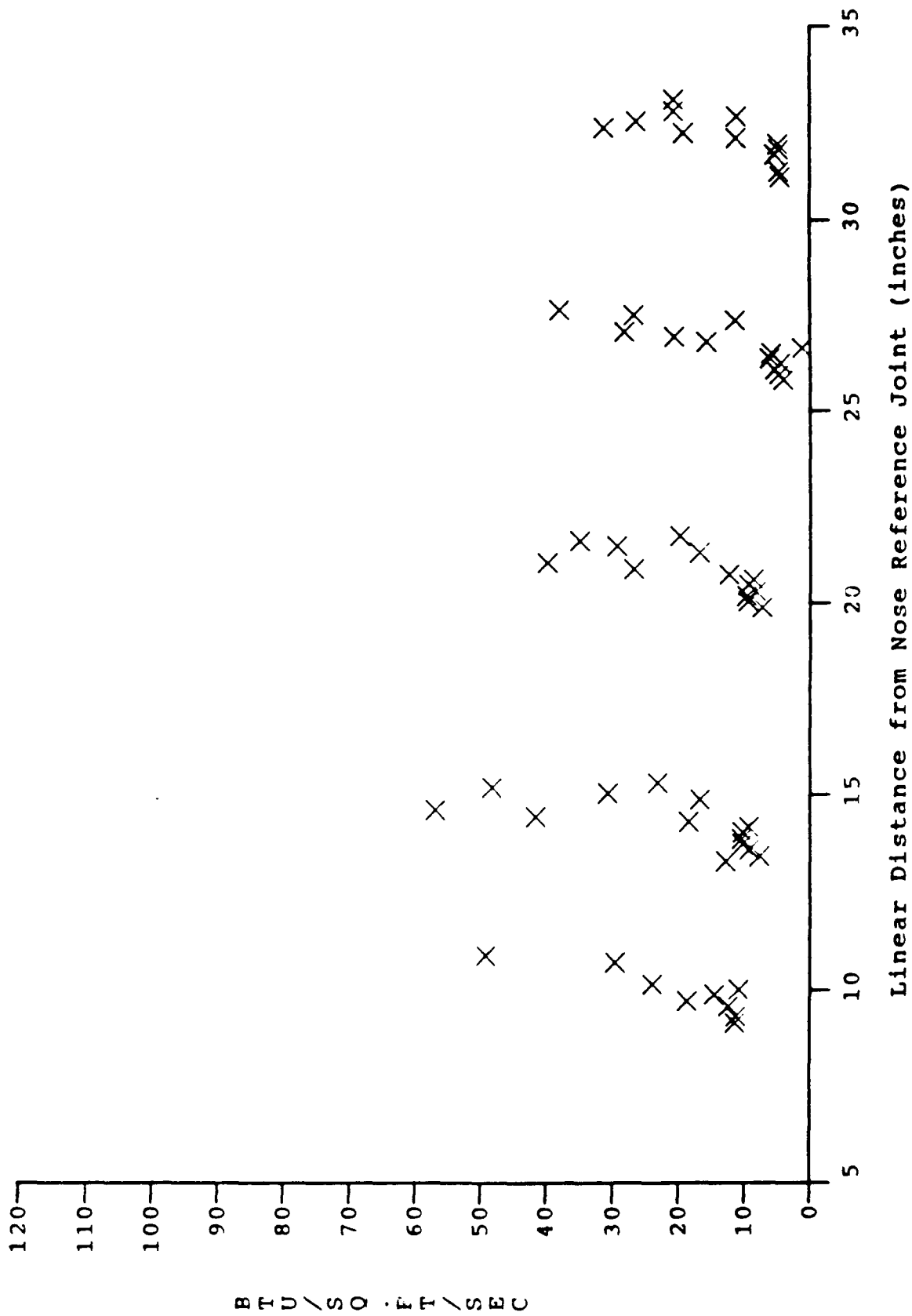


Figure 34b DISTRIBUTION OF HEATING ALONG MODEL SURFACE
(RUN # 41, $B'=0.560$, $M=15$, $Re/FT=1.5 \times 10^6$)

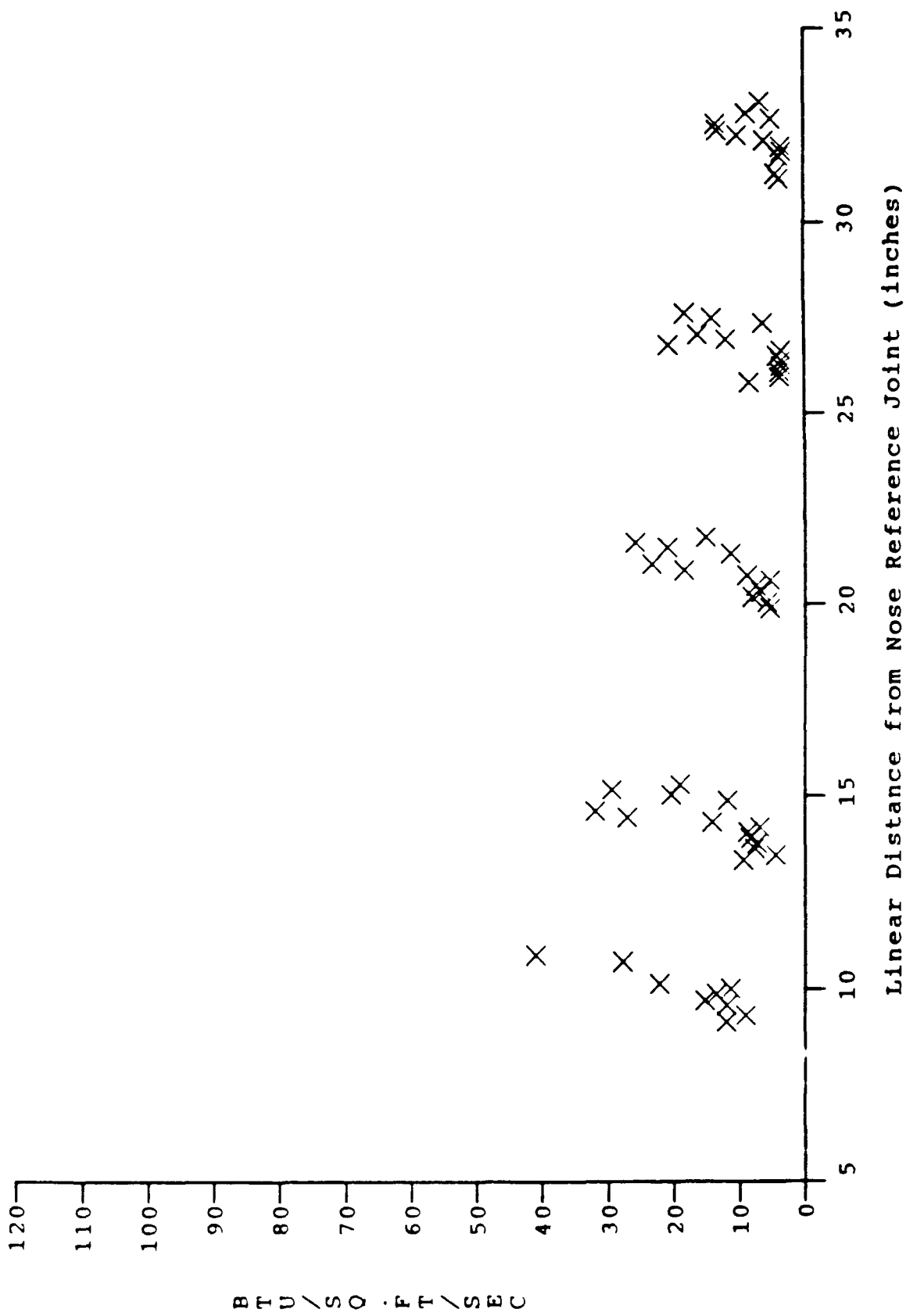
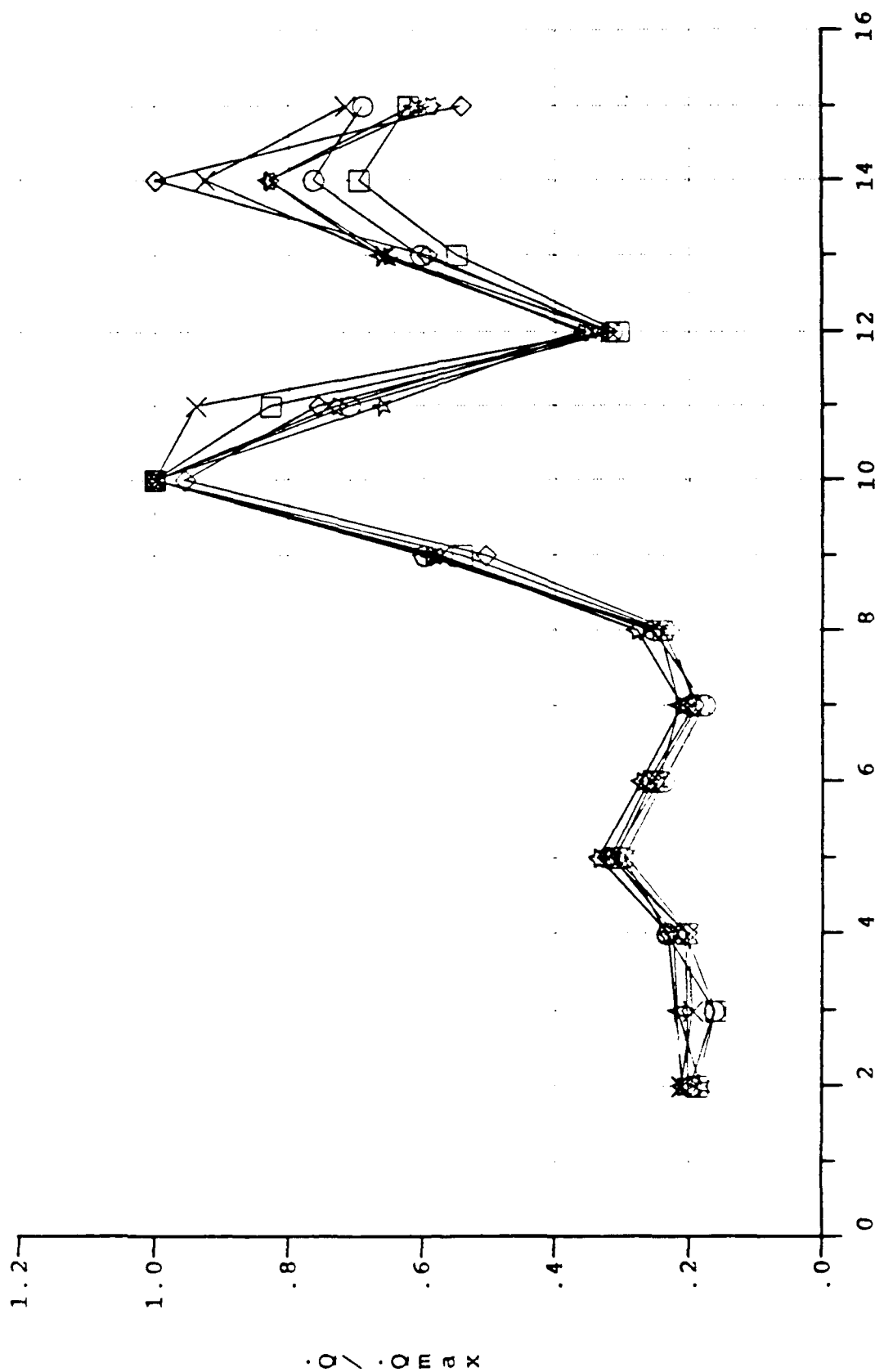


Figure 34c DISTRIBUTION OF HEATING ALONG MODEL SURFACE
(RUN # 42, $B'=1.329$, $M=15$, $Re/FT=1.5 \times 10^6$)

Blowing Rates: X zero □ 0.077 ◇ 0.269 ○ 0.366 ☆ 0.517 ☆ 0.543



Saddle Block 3 Gauges

Figure 35a NORMALIZED HEAT RATE DISTRIBUTIONS FOR VARYING BLOWING RATE
M=13, Re/FT = 5X10⁶, N₂ INJECTANT, SHARP NOSE

Blowing Rates: X 0.639 □ 1.259 ◇ 1.622 ○ 2.111 ☆ 3.086

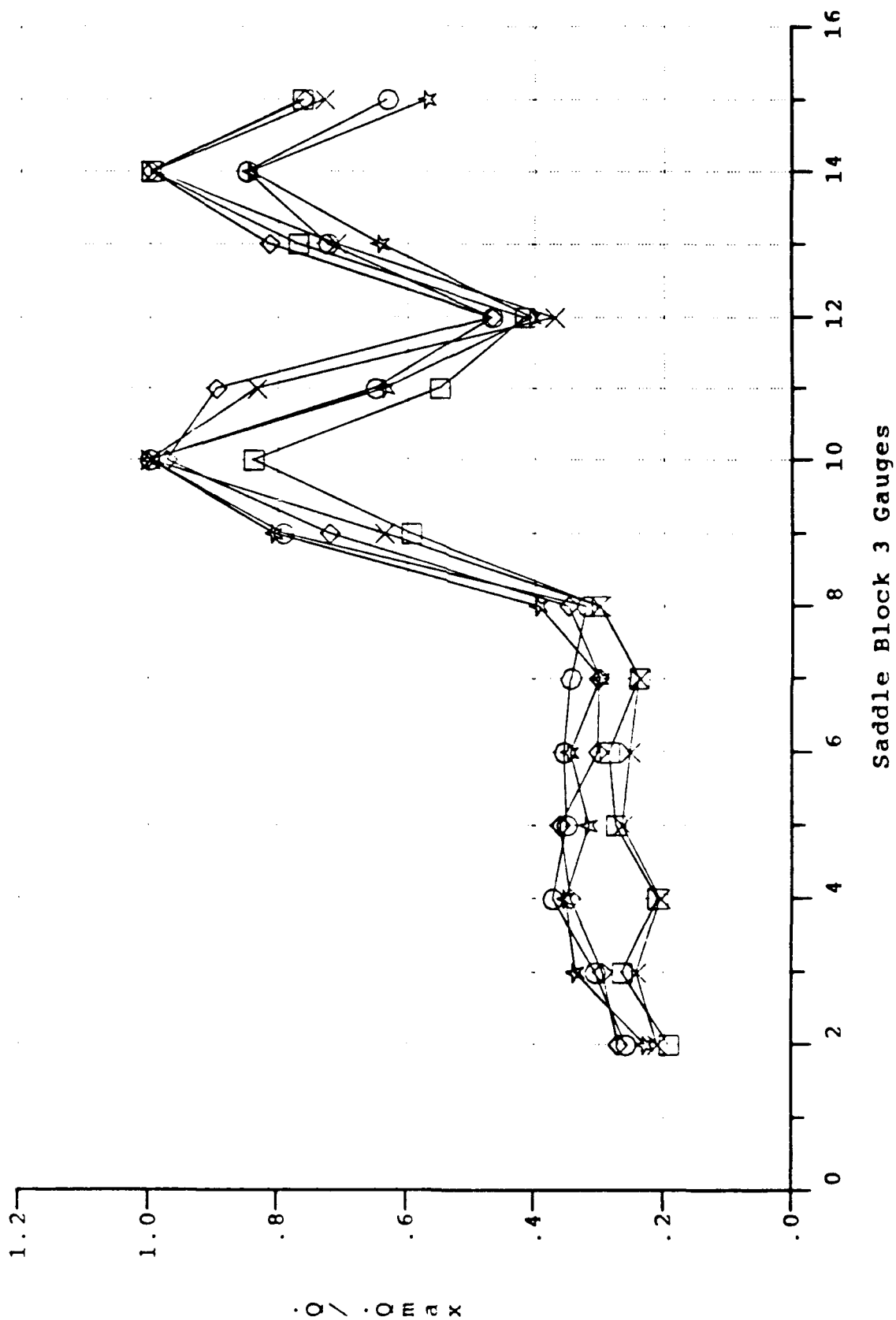
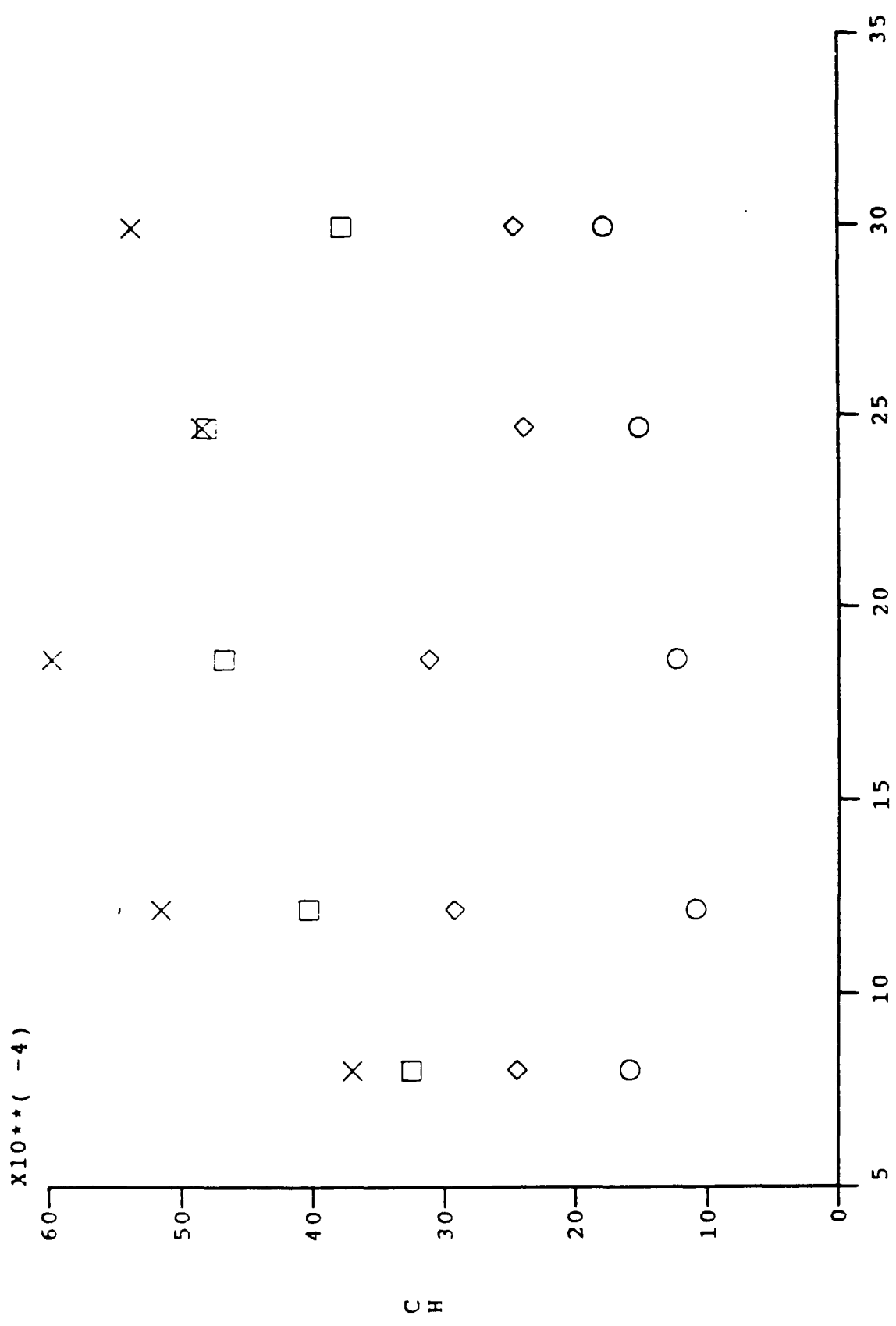


Figure 35h NORMALIZED HEAT RATE DISTRIBUTIONS FOR VARYING BLOWING RATE
M=13, Re/FT = 5X10⁶, N2 INJECTANT, SHARP NOSE

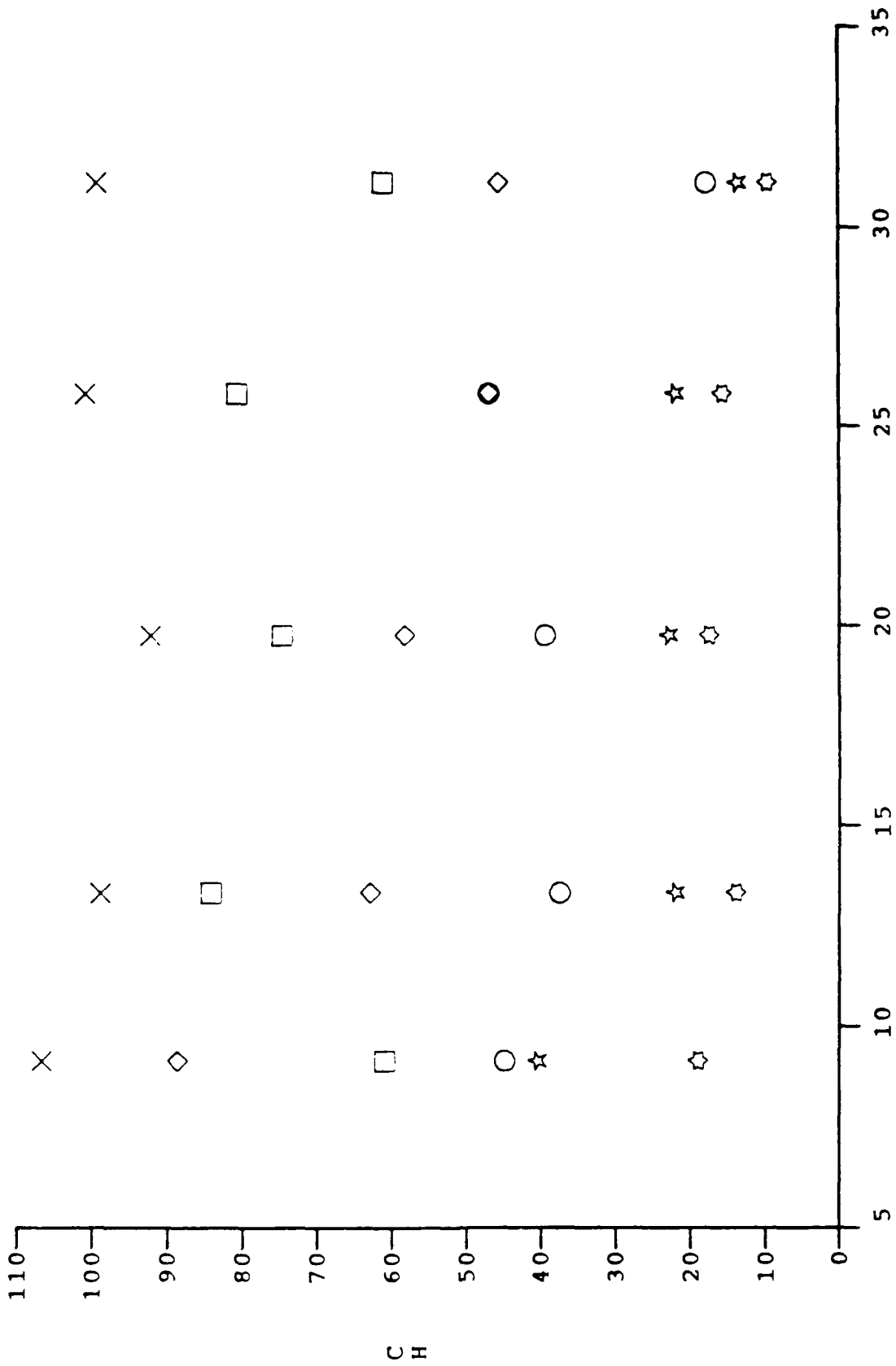
Blowing Rates: X .062 □ .188 ◇ .467 ○ 1.089



Linear Distance from Nose Reference Joint (inches)
 Figure 36a PEAK HEATING RATE ON ROUGHNESS ELEMENTS ALONG MODEL FOR VARIOUS
 BLOWING RATES (MACH # = 11)

Blowing Rates: X Zero □ 0.110 ◇ 0.191 ○ 0.377 ☆ 0.632 ☆ 0.924

$\times 10^{**}(-4)$

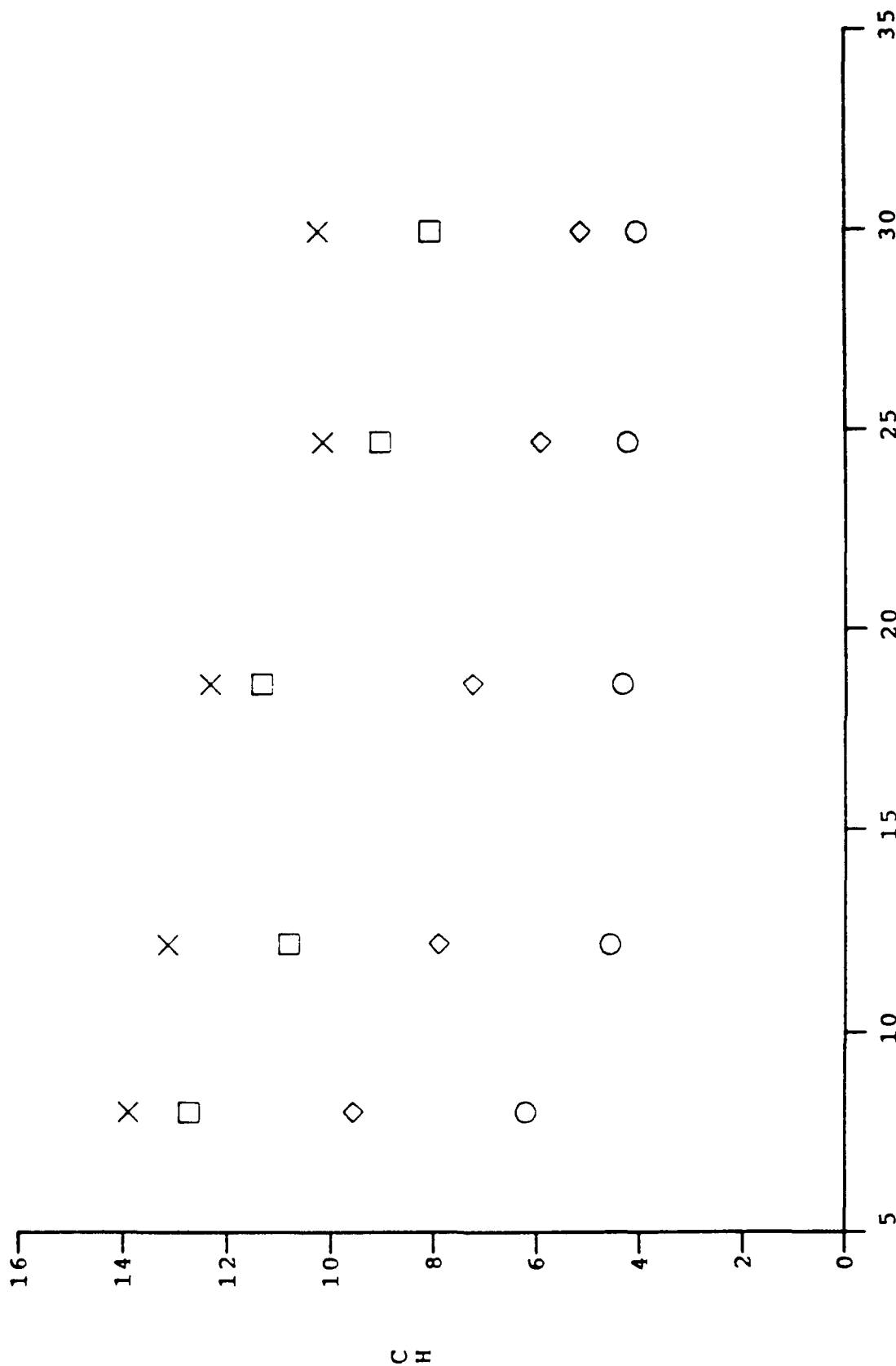


Linear Distance from Nose Reference Joint (inches)

Figure 36b PEAK HEATING RATE ON ROUGHNESS ELEMENTS ALONG MODEL FOR VARIOUS BLOWING RATES (MACH # = 13)

Blowing Rates: X 0.264 □ 0.807 ◇ 2.006 ○ 4.677

$\times 10^{**}(-4)$



Linear Distance from Nose Reference Joint (inches)

Figure 37a HEATING RATE ON BASE ELEMENTS ALONG MODEL FOR VARIOUS BLOWING RATES (MACH # = 11)

Blowing Rates: X Zero □ 0.540 ◇ 0.942 ○ 1.760 ☆ 3.115 ⬠ 4.554

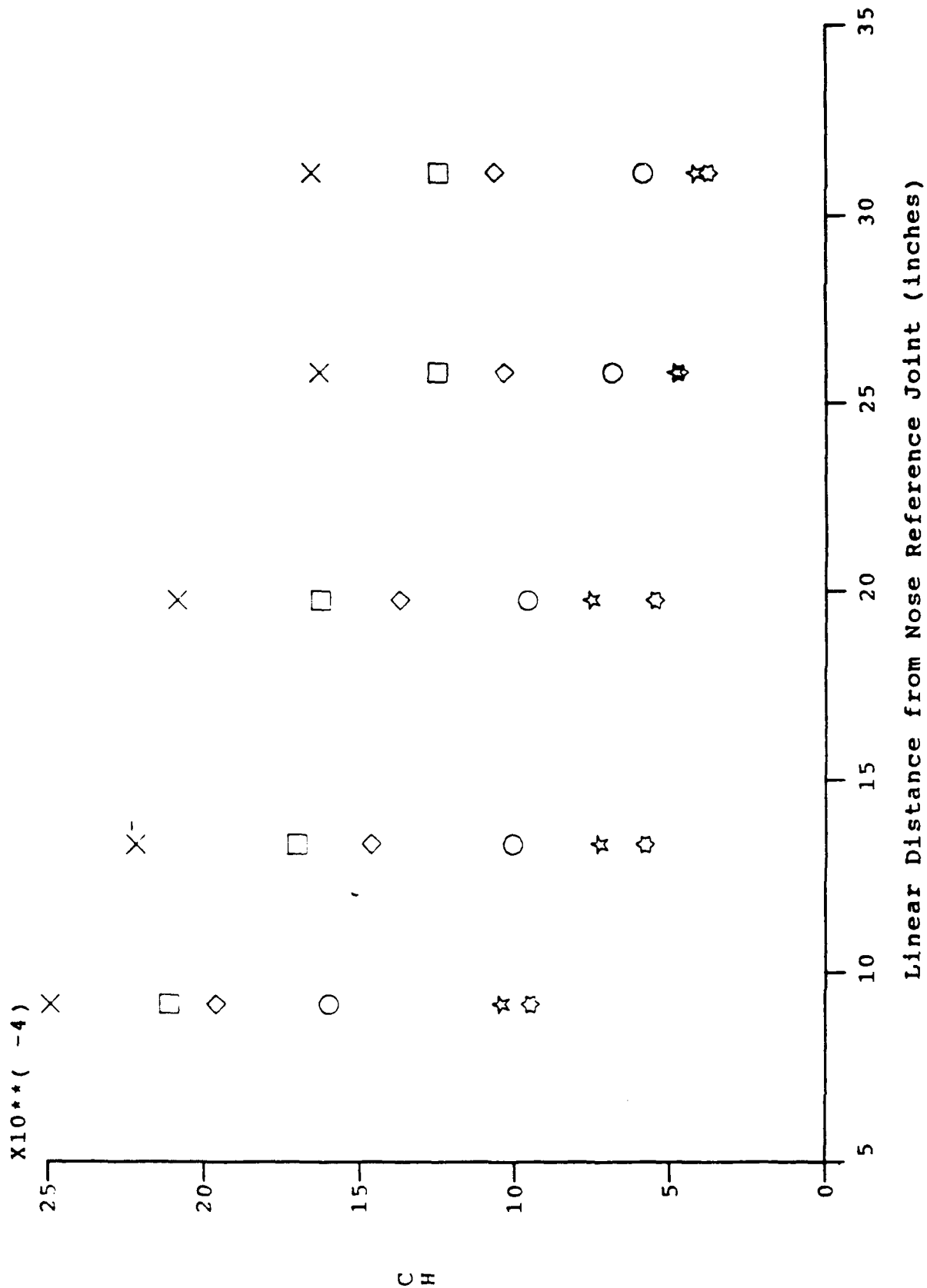


Figure 37b HEATING RATE ON BASE ELEMENTS ALONG MODEL FOR VARIOUS BLOWING RATES (MACH # = 13)

Blowing Rates: X 0.222 □ 0.678 ◇ 1.686 ○ 3.931

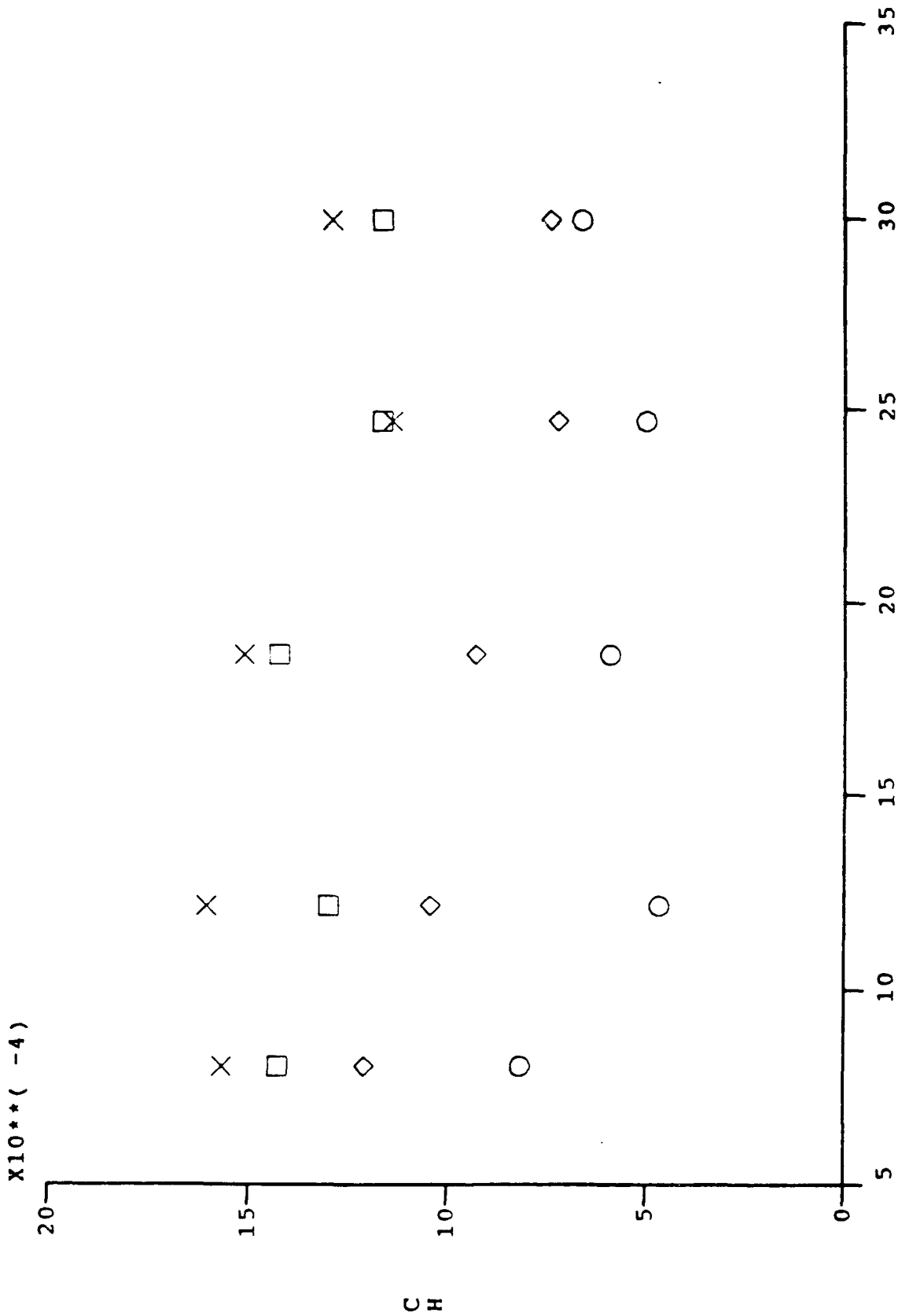
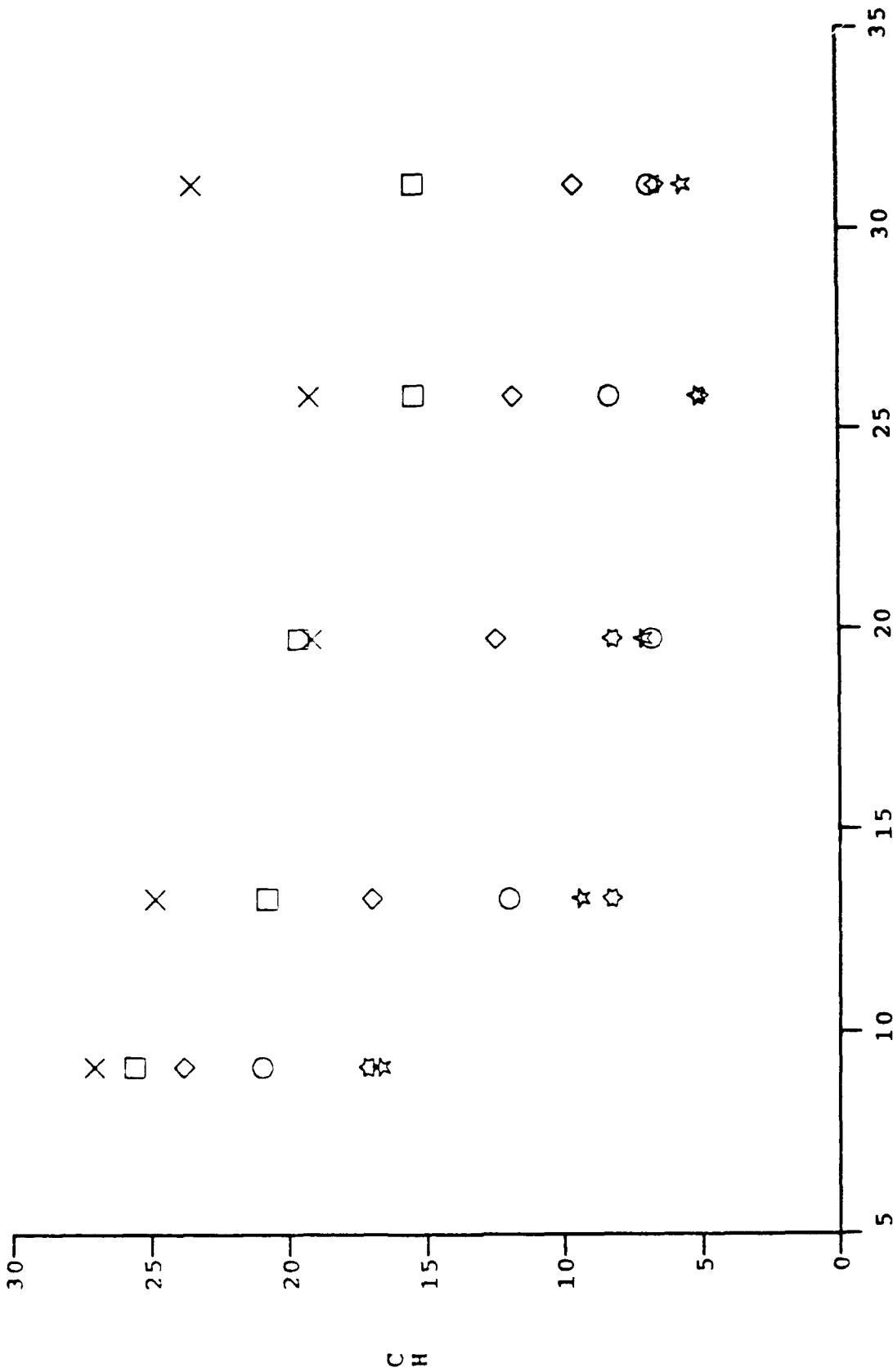


Figure 38a CALORIMETER HEATING RATE ALONG MODEL FOR VARIOUS BLOWING RATES (MACH # = 11)

Blowing Rates: X Zero □ .479 ◇ .837 ○ 1.650 ☆ 2.765 ◊ 4.043

$\times 10^{**} (-4)$



Linear Distance from Nose Reference Joint (inches)

Figure 38b CALORIMETER HEATING RATE ALONG MODEL FOR VARIOUS BLOWING RATES (MACH # = 13)

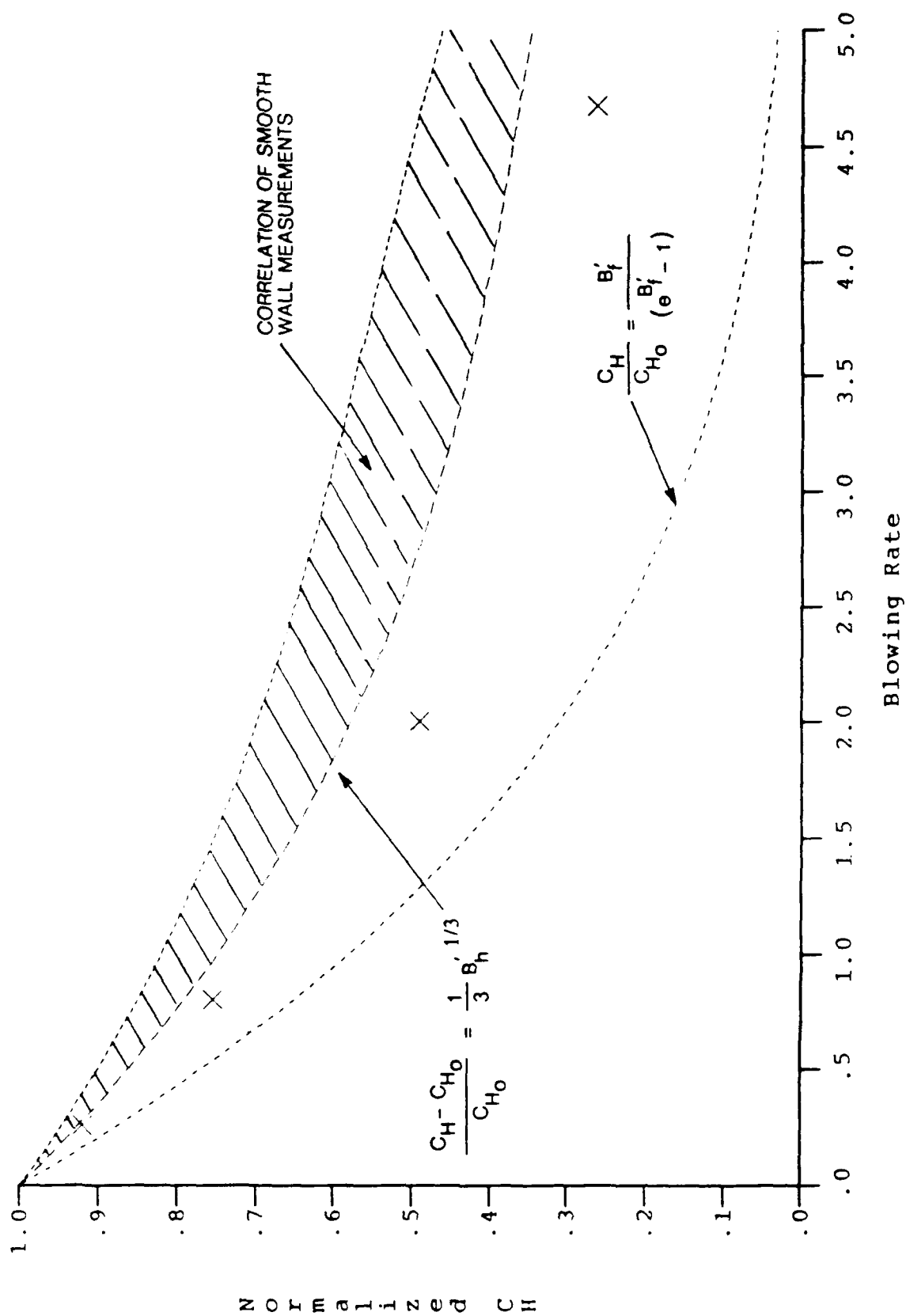


Figure 39a VARIATION OF NORMALIZED PEAK HEATING WITH BLOWING RATE
MACH # = 11 (NORMALIZED $CH = CH/CH_0$)

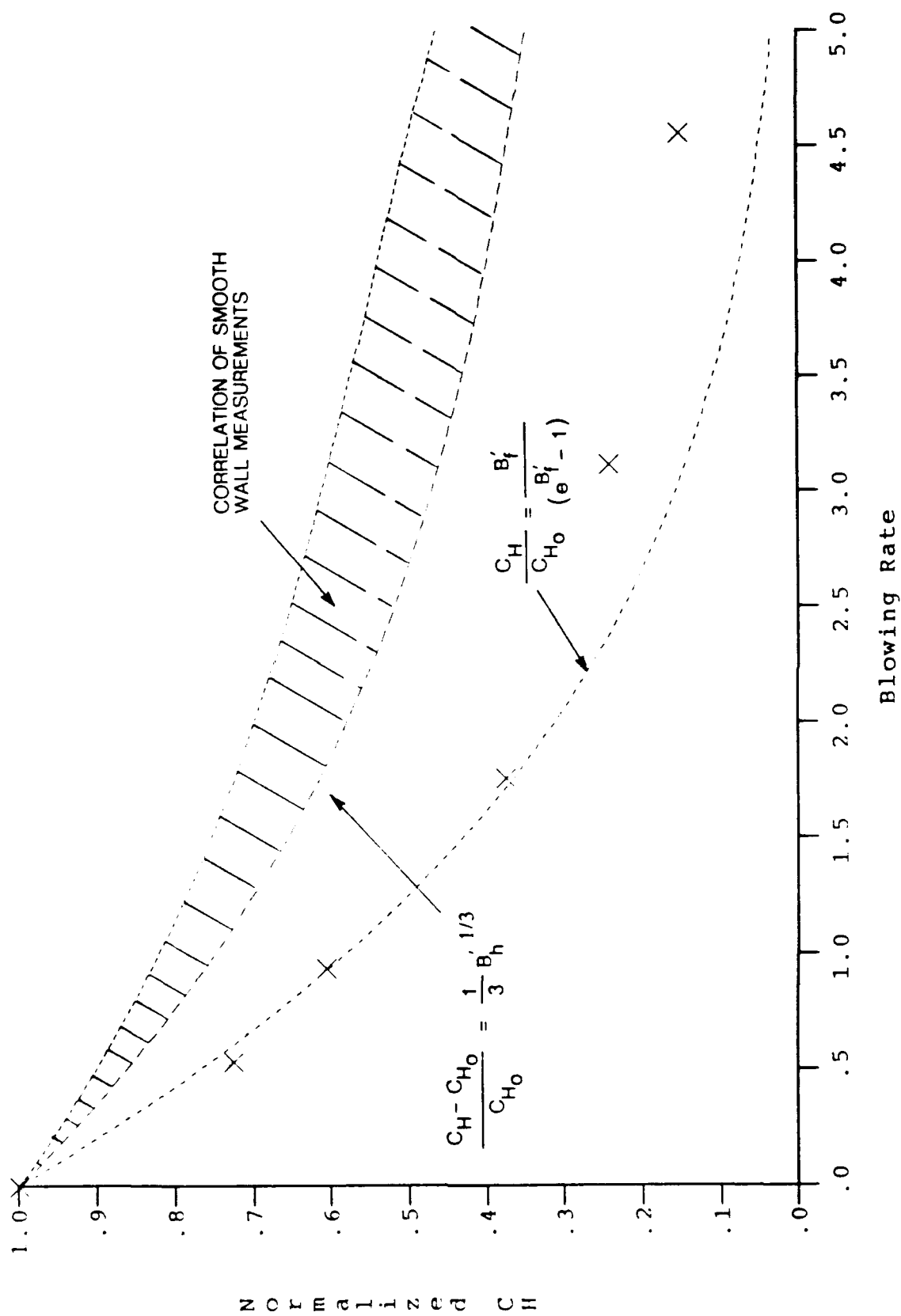


Figure 39b VARIATION OF NORMALIZED PEAK HEATING WITH BLOWING RATE
MACH # = 13 (NORMALIZED $CH = CH/CH_0$)

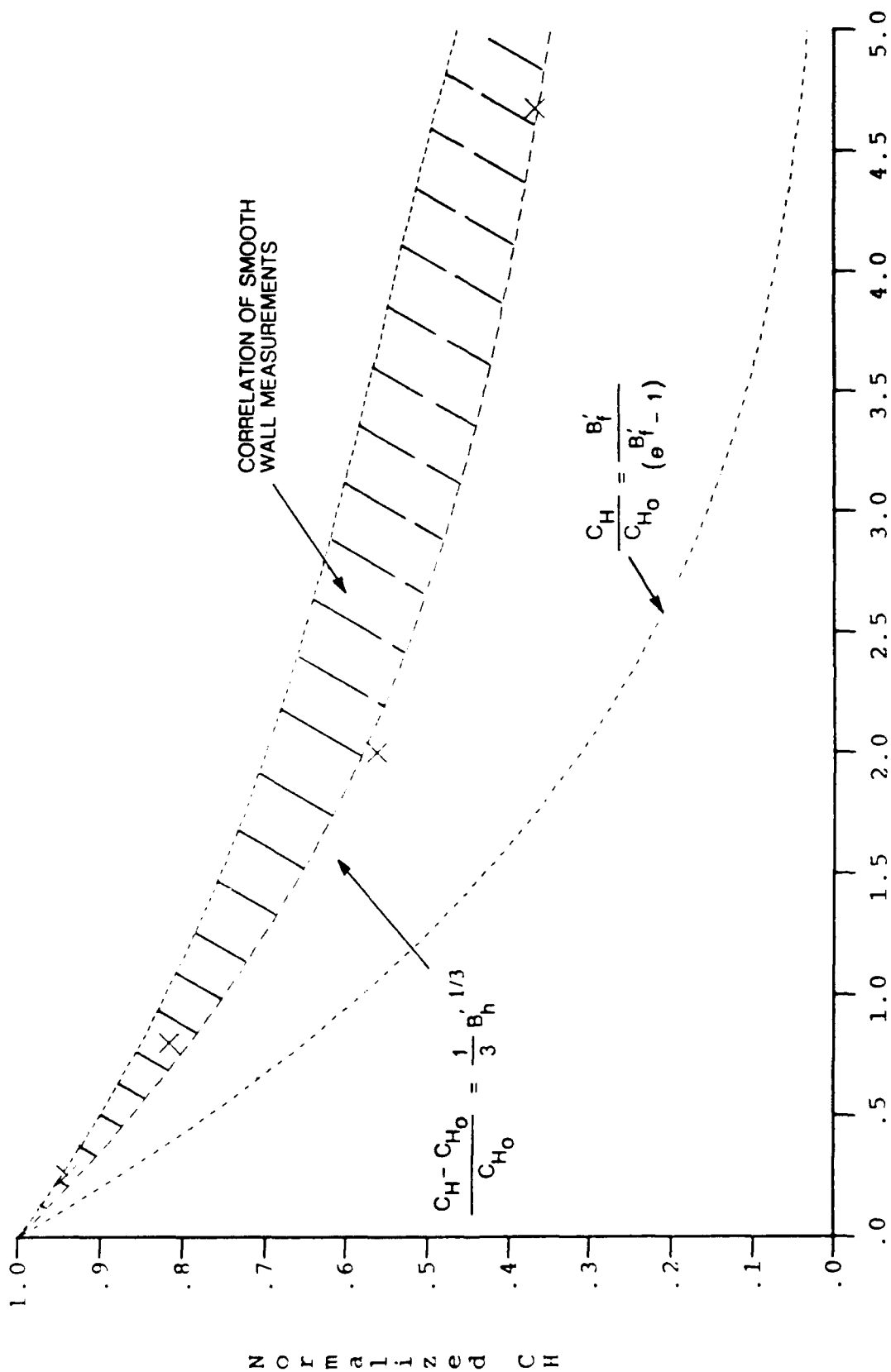


Figure 40a VARIATION OF NORMALIZED BASE HEATING WITH BLOWING RATE
MACH # = 11 (NORMALIZED CH = CH/CH₀)

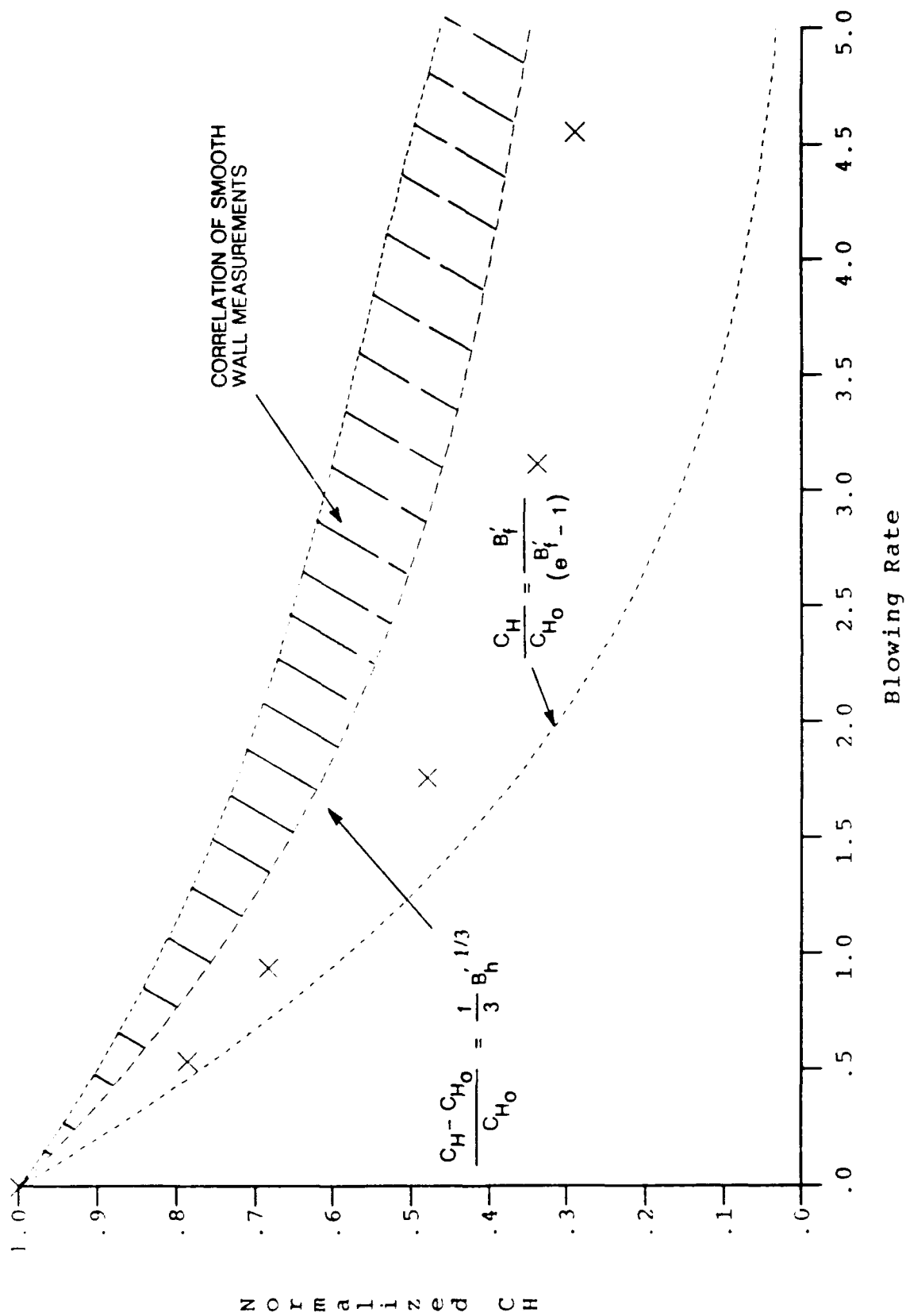


Figure 40b VARIATION OF NORMALIZED BASE HEATING WITH BLOWING RATE
MACH # = 13 (NORMALIZED CH = CH/CH₀)

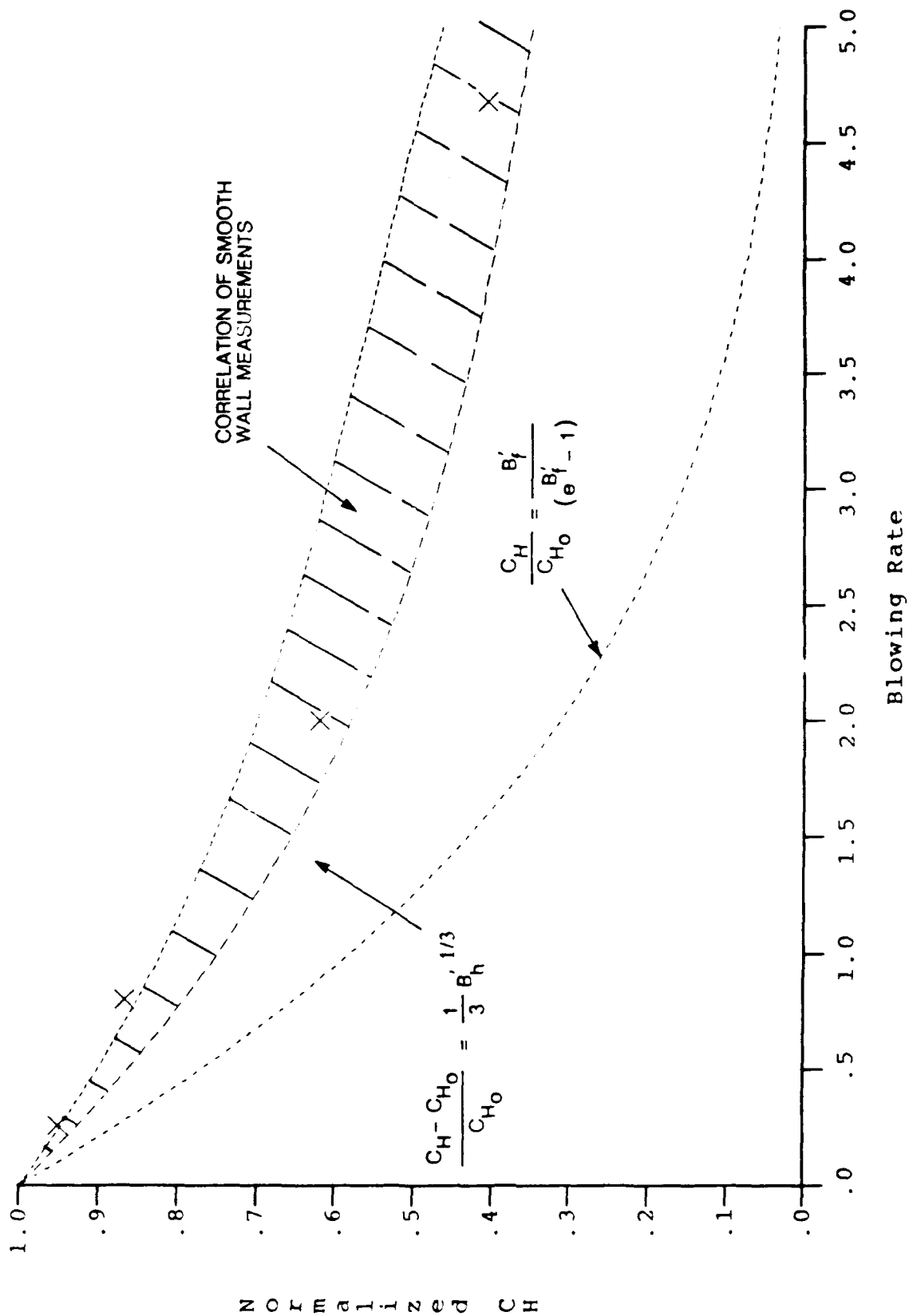


Figure 41a VARIATION OF NORMALIZED CALORIMETER HEATING WITH BLOWING RATE
MACH # = 11 (NORMALIZED CH = CH/CH₀)

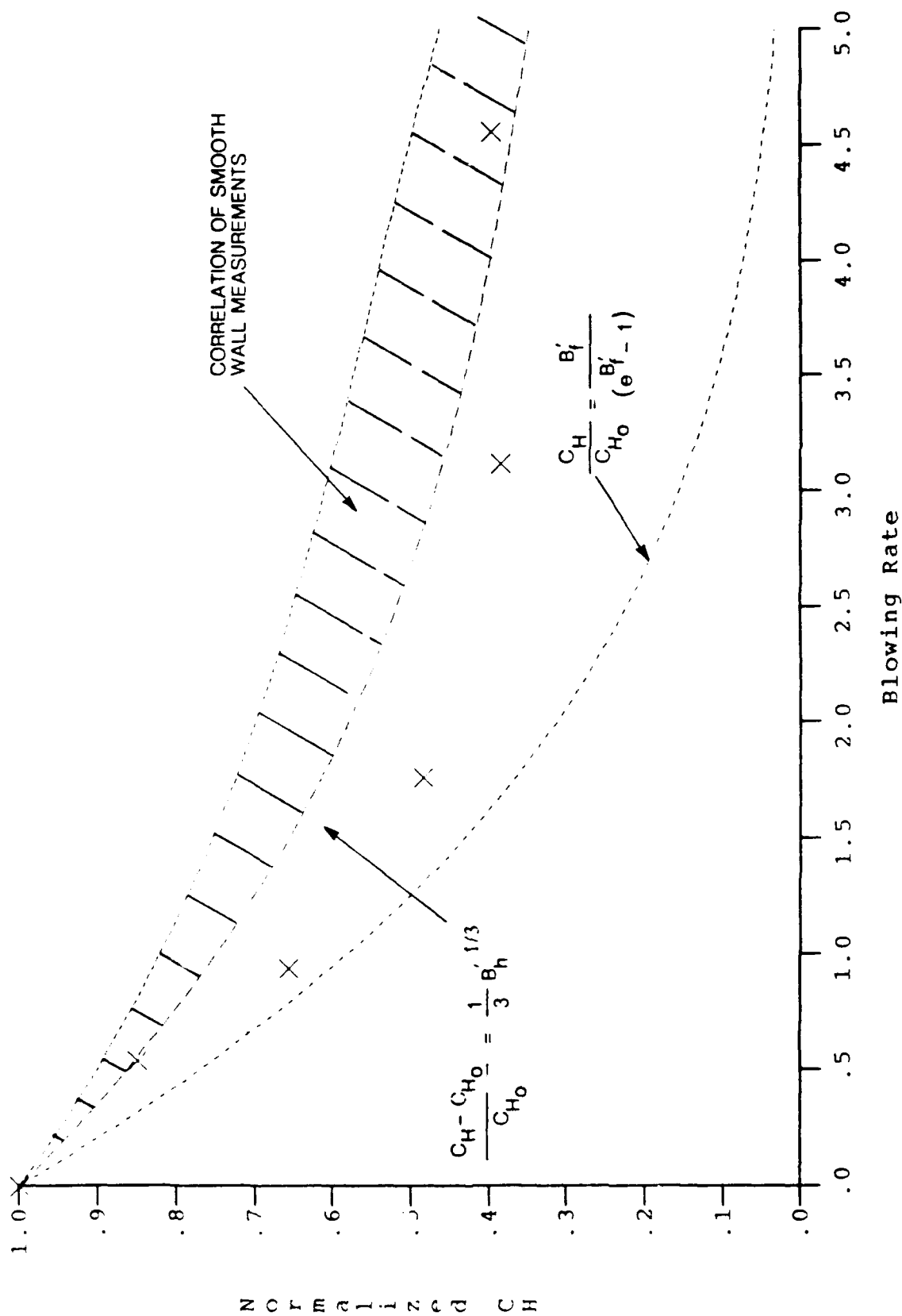


Figure 41b VARIATION OF NORMALIZED CALORIMETER HEATING WITH BLOWING RATE
MACH # = 13 (NORMALIZED CH = CH/CH₀)

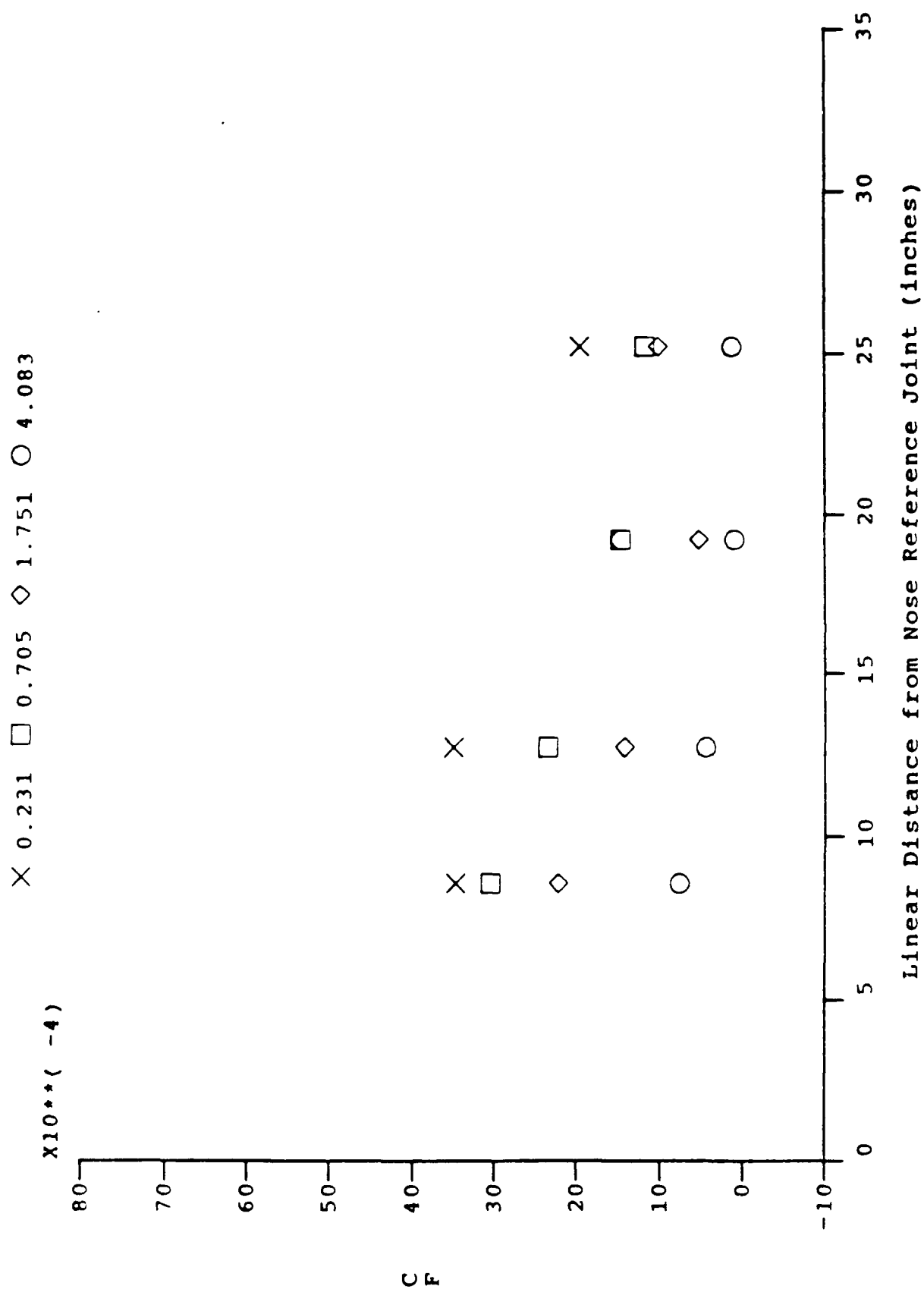


Figure 42a SKIN FRICTION ALONG MODEL FOR VARIOUS BLOWING RATES
 (MACH # = 11)

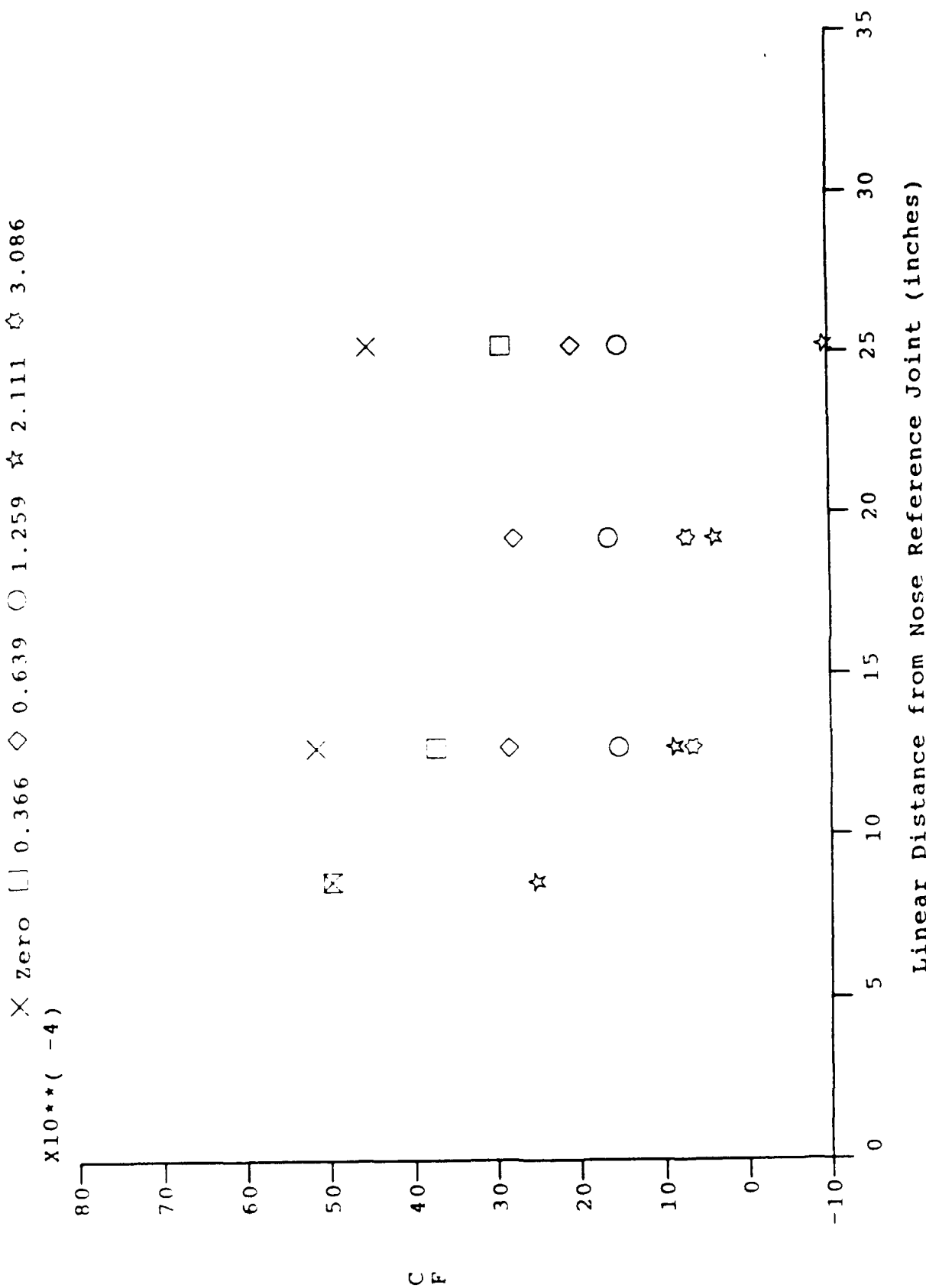


Figure 42h SKIN FRICTION ALONG MODEL FOR VARIOUS BLOWING RATES
(MACH # = 13)

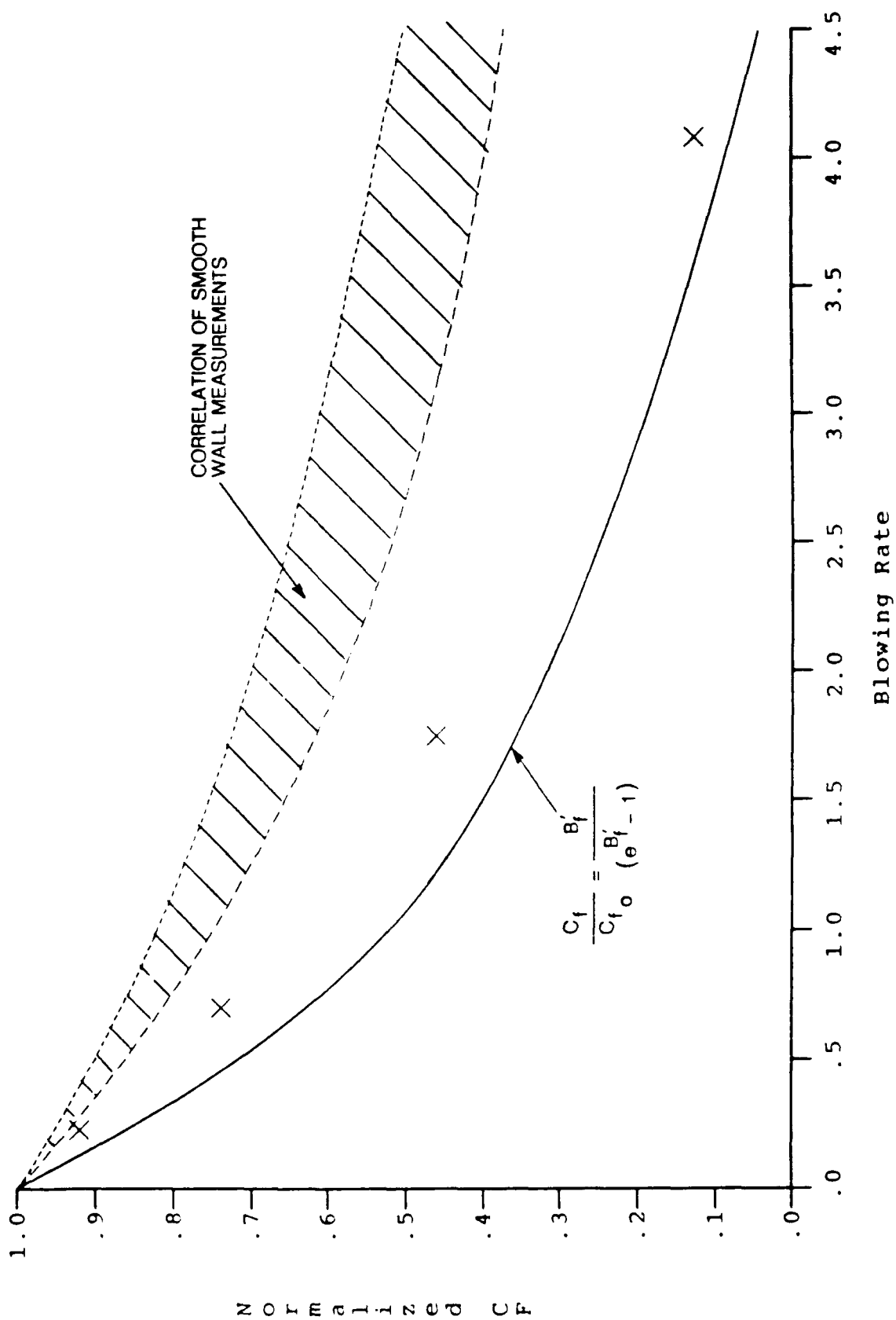


Figure 43a VARIATION OF NORMALIZED SKIN FRICTION WITH BLOWING RATE
MACH # = 11 (NORMALIZED $C_F = C_F/C_{F0}$)

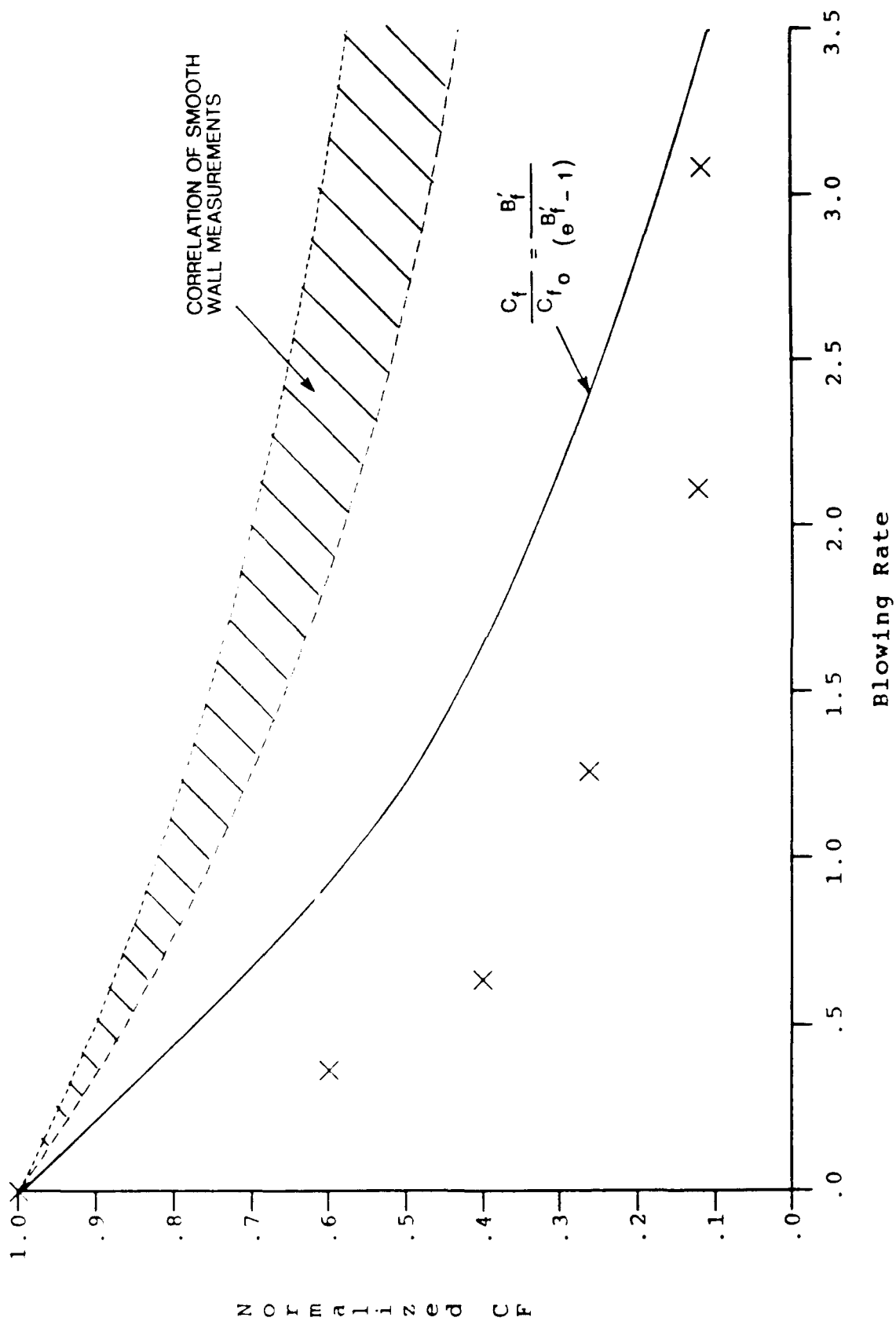


Figure 43b VARIATION OF NORMALIZED SKIN FRICTION WITH BLOWING RATE
MACH # = 13 (NORMALIZED CF = CF/CF₀)

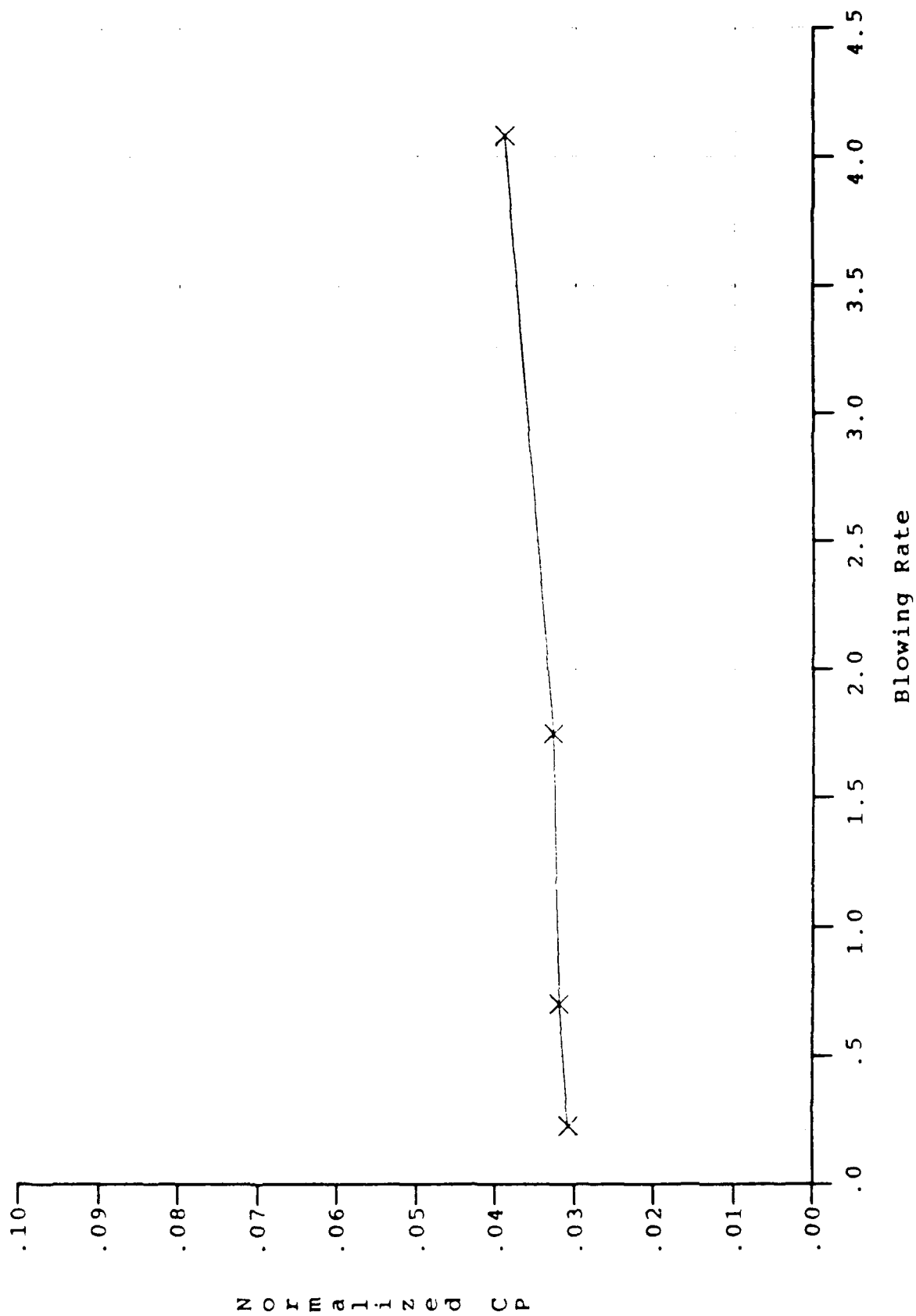


Figure 44a VARIATION OF CP WITH BLOWING RATE (MACH # = 11)

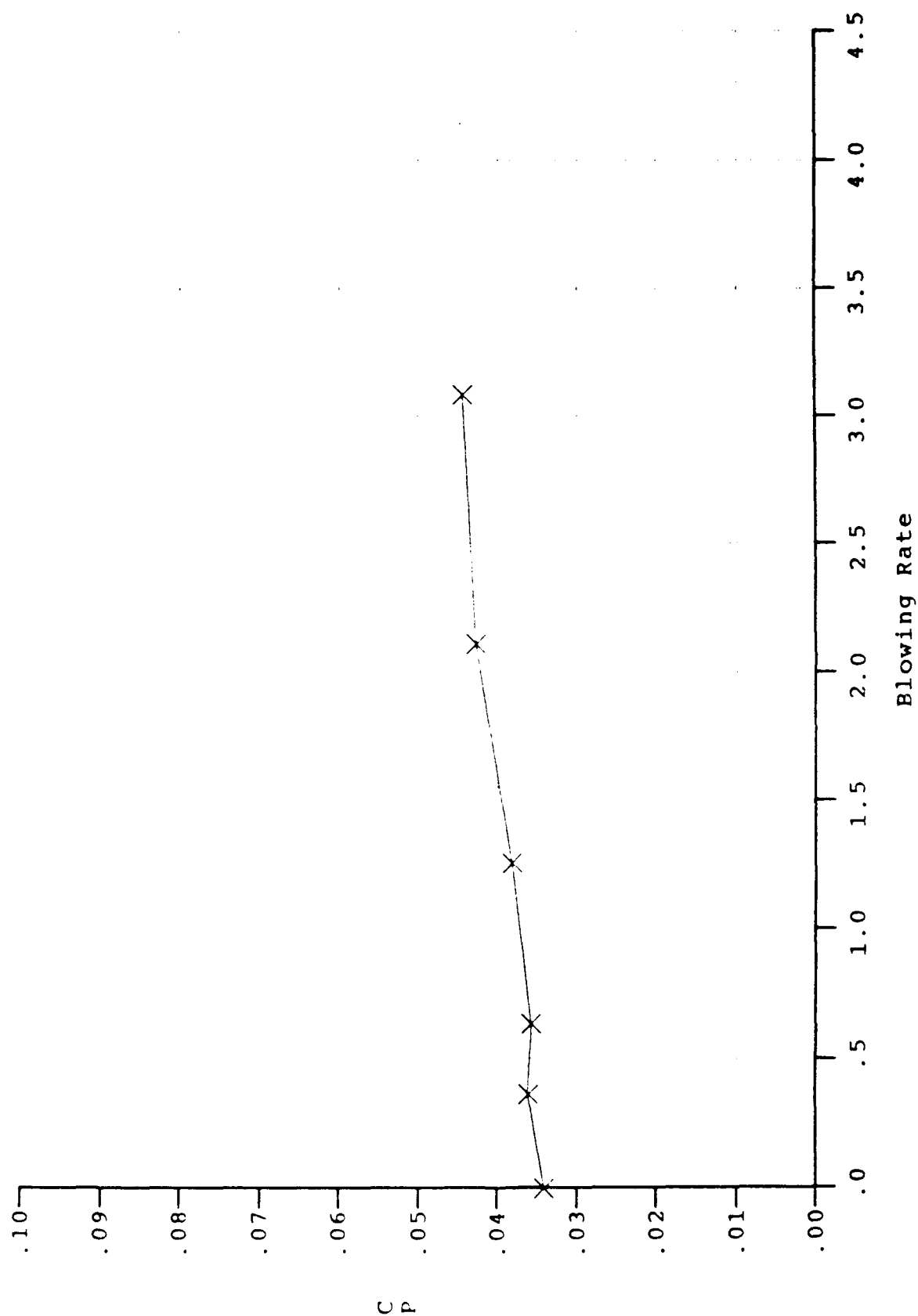


Figure 44b VARIATION OF C_p WITH BLOWING RATE (MACH # = 13)

APPENDIX 2

**AN EXPERIMENTAL STUDY OF THE TRANSPIRATION COOLING ON
THE DISTRIBUTION OF HEAT TRANSFER AND SKIN FRICTION TO A
SHARP SLENDER CONE AT MACH 11 AND 13**



AIAA-90-0308

**An Experimental Study of Transpiration
Cooling on the Distribution of Heat
Transfer and Skin Friction to a Sharp
Slender Cone at Mach 11 and 13**

Michael S. Holden
Calspan/UB Research Center
Buffalo, New York

John Van Osdol
State University of New York
at Buffalo, Buffalo, NY

Kathleen M. Rodriguez
Calspan/UB Research Center
Buffalo, NY

28th Aerospace Sciences Meeting

January 8-11, 1990/Reno, Nevada

AN EXPERIMENTAL STUDY OF TRANSPIRATION COOLING ON THE DISTRIBUTION OF HEAT TRANSFER AND SKIN FRICTION TO A SHARP SLENDER CONE AT MACH 11 AND 13

Michael S. Holden*
John Van Osco!**
Kathleen M. Rodriguez***

ABSTRACT

Experimental studies have been conducted to examine the effects of transpiration cooling on the turbulent heat transfer and skin friction to sharp slender cones in hypersonic flows. These studies were conducted at Mach 11 and 13 for Reynolds numbers, based on local conditions and cone length, of 100×10^6 and 50×10^6 , respectively, in the Calspan 96-inch shock tunnel. Distributions of heat transfer, skin friction and pressure were obtained along the cone for values of the blowing parameter $B' = \frac{q_w}{q_\infty} \sqrt{\frac{\rho_\infty}{\mu_\infty}}$ from 0.10 to 5, using a nitrogen injectant. Holographic interferometry was used to examine the characteristics of the flowfield. A new skin friction transducer was used in these studies, in which the injectant was introduced through the floating sensing element, to obtain meaningful measurements of the reduction of surface shear with surface blowing. Miniature thin-film instrumentation was employed to obtain the detailed distribution of heat transfer around the circular injection ports at each measurement station along the cone. The measurements obtained in this study are correlated with earlier measurements at lower Mach numbers in terms of the major scaling parameters. Comparisons are presented with the computations made with the "BLIMP" code, which demonstrate that for small blowing rates this code is in relatively good agreement with the experimental data. However for $B' > 0.5$ the code significantly underpredicts the effectiveness of transpiration cooling. For these high blowing levels where (in the extremes) boundary layer blowoff occurs, boundary layer theory is inadequate and solutions to the full or reduced time-averaged Navier-Stokes equations are required.

1. INTRODUCTION

The modeling of the turbulent flow structure over transpiration-cooled and rough ablating surfaces requires a detailed understanding of the mixing process between the injected fluid, the roughness elements, and the fluids at the base of the turbulent boundary layer. Large surface ablation, resulting from heat transfer generated on the windward ray of the ablative heat shield close to the nosetip and on the control surfaces of vehicles flying at high angles of attack, will be of critical concern to the designer of vehicles that maneuver during re-entry. To develop an accurate predictive capability to describe the ablation rates of the nosetip, heat shield, and control

surfaces, it is necessary to understand and model the separate and combined effects on ablating and non-ablating slender cones. Based on studies of roughness and blowing on slender cones, Holden¹ suggested that the subsonic studies are inapplicable to the heating of heat shields in hypersonic flow, and also that the basic modeling of the roughness drag and mechanisms of heating used in the theoretical models is highly questionable.

Earlier studies of transpiration cooling techniques were designed principally to evaluate how the blockage heat transfer CH/CH_0 varied with the Mach number, Reynolds number and the physical and chemical properties of the freestream and injectant. The lack of definitive techniques to predict the effectiveness of transpiration/film cooling techniques reflects the lack of fundamental understanding of turbulent mixing in the presence of mass injection and surface roughness. There is a dearth of turbulent data at hypersonic speeds where transpiration cooling is of considerable interest. Experimental studies have been conducted in supersonic flow with flat plates^{2,6,7,8} and cones^{2,3,4}, and there has been some work on the transpiration cooling of blunt nosetips^{9,10}. Based on a survey of the existing experimental data in Reference 9, the correlation shown in Figure 1 was developed. This correlation indicates that for large blowing rates ($B' > 10$), increased blowing does not significantly improve thermal protection. This may well result from a decrease in the stability of the mixing layer and an increase in the scale of turbulence with increasing blowing. However, Holden's measurements on a spherical nosetip, shown in Figures 2 and 3, suggest that heating levels significantly lower than those found on flat plates and cones were obtained for the higher blowing rates. These latter measurements could be correlated in the form $(CH_0 - CH)/CH_0 = 1/3 B'^{1/3}$. However, for blowing rates of greater than one, the flow became highly unstable and violent fluctuations in the surface heating were observed.

The measurements made in earlier studies of transpiration cooling conducted with transpiration cooled nosetips⁹ were designed principally to determine whether blockage effects of mass injection are as large as predicted by the current codes. The measurements on the model with zero blowing, presented in Figure 3, clearly show that the intrinsic roughness of the surface, causes heating enhancement factors of over 1.7. In fact, it can be seen by comparing Figures 3 and 5 that the heat transfer measurements on the conically rough hemisphere are in good agreement with those obtained on the

*Calspan/UB Research Center, Buffalo, NY; Associate Fellow, AIAA

**State University of New York at Buffalo, Buffalo, NY; Student Member, AIAA

***Calspan/UB Research Center, Buffalo, NY

This work has been supported by the Aerospace Sciences Directorate of the U.S. Air Force Office of Scientific Research under contracts F33615-85-3003 and AFOSR-88-0223. This paper is declared a work of the U.S. Government and is not subject to copyright protection in the United States.

non-blowing transpiration-cooled nosetip. However, when a small amount of blowing ($B' = 0.032$) was introduced, the heating rates over a major part of the transpiration-cooled model dropped to levels close to those recorded on the smooth model, as shown in Figures 4 and 5. It could be postulated on the basis of these measurements that the initial effect of mass addition from a rough abiating nosetip is to modify the flow around the roughness elements by eliminating the cavity flows between them in such a way that the momentum defect is small. If the effect of mass addition is to remove surface roughness as an important characteristic parameter, a series of questions are posed for the correlation of flight measurements in terms of an effective surface roughness and the computational procedures in which the ablation rate is determined from heating levels enhanced by surface-roughness effects.

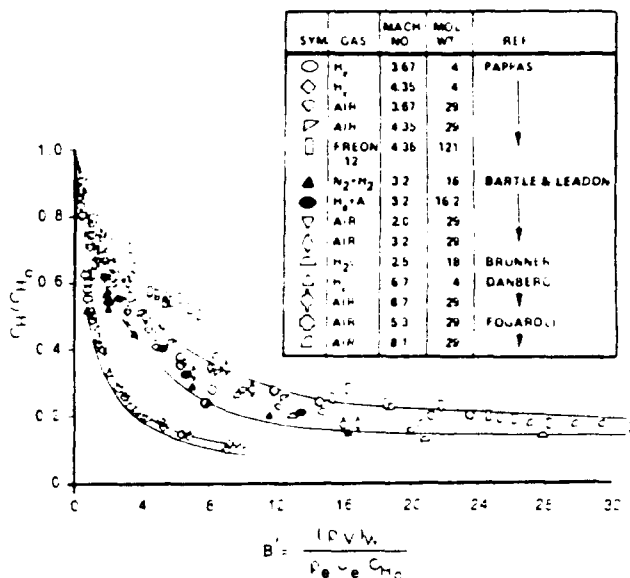


Figure 1 Summary of blockage heating from earlier studies on flat plates and cones in turbulent flow (Holden ref. 9)

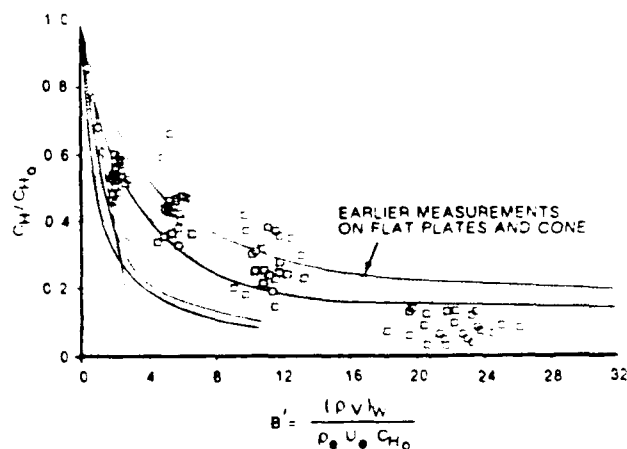


Figure 2 Comparison between the measurement made in the nosetip studies with nitrogen injectant and the earlier blockage data (Holden ref. 9)

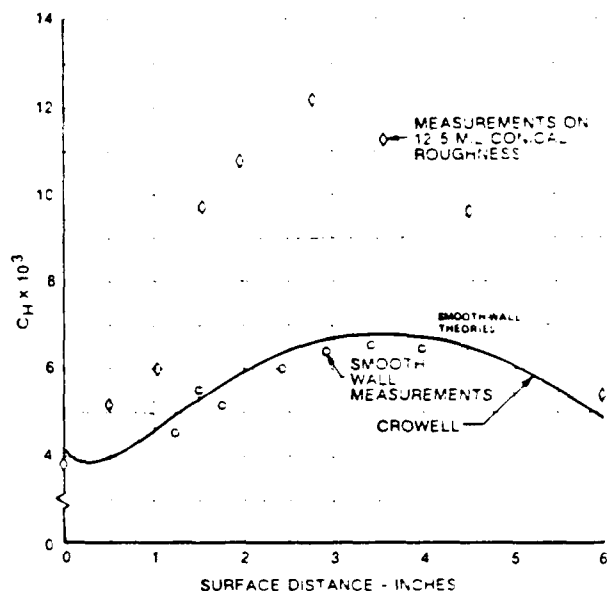


Figure 3 Comparison between the turbulent theories of Lin & Crowell for smooth-wall and rough-wall measurements of Holden on 12 inch diameter hemisphere ($M = 11.2$, $Re_D = 11 \times 10^6$, $k = 12.5$) (Holden ref. 9)

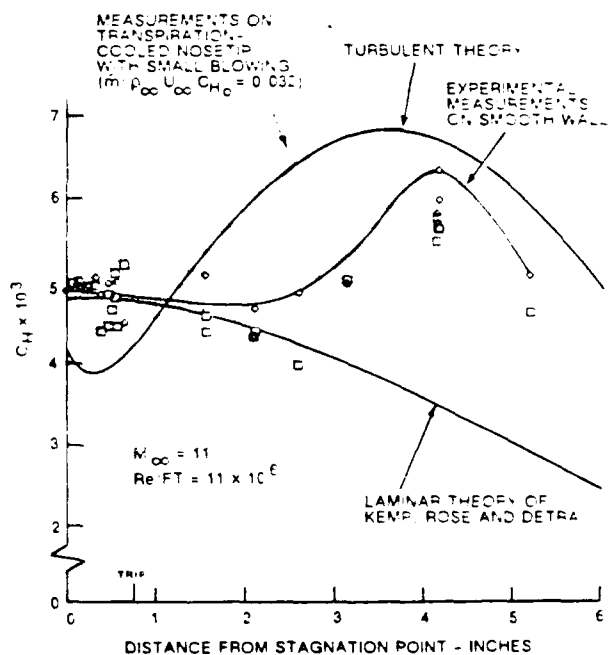


Figure 4 Heat transfer measurements indicating that small blowing on rough nosetip initially acts to bring down heating levels to smooth-wall values

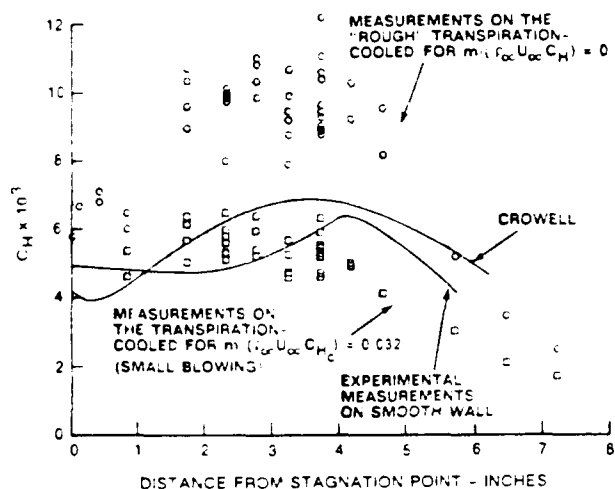


Figure 5 Heat transfer measurements on SCANT and smooth nosetip showing how small blowing brings down heating levels to smooth-wall values (Holden Ref. 9)

The BLIMP¹⁵ code developed by ACCUREX is one of the most commonly used numerical codes for predicting the heat transfer to transpiration-cooled bodies. BLIMP is a boundary layer code employing a mixing length turbulence model. The solution methodology used by BLIMP involves approximating the primary dependent variables of the boundary layer equations using quadratic or cubic polynomials over each of several continuous regions dividing the wall normal coordinate direction. In order to simplify the normal derivative terms, the conservation equations are integrated along the normal direction between the nodes that separate each region. The primary variables and their derivatives at each node are then related by a fourth order Taylor series expansion so that the coefficients in the approximating polynomials can be determined using a technique similar to the Galerkin Method. The solution is propagated forward along the principal flow direction using a two-point or three-point finite difference scheme which is selected by the user. The use of polynomial approximations between the relatively few nodes that define the boundary layer, makes the Boundary Layer Integral Matrix Procedure (BLIMP) a very fast and accurate computational tool, giving it advantages over other finite difference codes when considering flows having large numbers of reacting chemical species in the boundary layer.

The study reported in this paper formed a part of a series of studies to investigate the separate and combined effects of surface roughness and blowing on the heat transfer and skin friction to provide insight into the modeling of aerothermal phenomena associated with the ablative cooling of hypersonic vehicles. Earlier, in the initial phase of these studies, we performed an extensive series of measurements to examine the effects of the shape and spacing of surface roughness on heat transfer and skin friction.¹² Here, the objective was to provide measurements to quantify the relationship between surface geometry and heating to a rough wall without the necessity of introducing a poorly defined parameter associated with sand-grain roughness. We specifically wanted to prevent the manipulation of the results from the prediction techniques by the selection of an "effective sand-grain roughness." These studies were conducted for hemispherical and biconic nosetips, and sharp and blunted slender cones. We then obtained

measurements with hemispherical transpiration-cooled nosetips which demonstrated that roughness heating effects could be significantly reduced or eliminated by surface blowing. Thus, studying roughness effects in the absence of blowing added little to the understanding of heating to rough ablating surfaces. We therefore embarked on a detailed experimental program to examine the combined effects of surface roughness and blowing on the skin friction and heat transfer.¹ To minimize problems associated with transition, these studies were conducted with slender conical configurations under high Reynolds number conditions. We also employed surface configurations with a well-defined surface roughness and blowing geometry to again eliminate the potential selection of an effective sand-grain roughness in comparisons with predictive techniques. This study was also unique because detailed measurements of the distribution of heating over individual roughness elements were made for the first time. Also, skin friction measurements were made on representative segments of the surface. Such measurements provide a direct way of evaluating the accuracy of the macroscopic modeling of these flows. During the third phase of the study, we investigated the surface blowing effects in the absence of surface roughness, and this is the subject of the current paper.

In the following sections of the paper, we discuss the design and objectives of the experimental program, followed by a description of the experimental facilities, the models and instrumentation and the reduction and evaluation of the measurements. The results of the program are then presented and discussed, and compared with measurements from earlier studies. The measurements are compared with simple prediction methods and the results of computations with the BLIMP code.

2. EXPERIMENTAL PROGRAM

2.1 Objective and Design of the Experimental Study

This program was designed as part of a series of studies to investigate the separate and combined effects of surface roughness and blowing on the heat transfer and skin friction to ablative and transpiration-cooled surfaces. A key objective of this work was to obtain measurements which provide insight into the macroscopic modeling of aerothermal phenomena associated with the ablative cooling of hypersonic vehicles. In this third phase of the study, we investigate the surface blowing effects in the absence of surface roughness.

This study of surface blowing effects was designed as a complement to our earlier studies of roughness and blowing.¹ To evaluate the separate and combined effects of surface roughness and blowing, here we obtained measurements at the same freestream conditions of the effects of blowing on a model of identical geometry as the model used in the blowing and roughness studies, but without the hemispherical roughness elements. On the reconfigured model, the miniature heat transfer instrumentation installed in the smooth surface was designed to provide a detailed mapping of the heating around the injection port at each measurement station along the model. Again, we employed unique skin friction instrumentation in which the cooling fluid is introduced through the diaphragm of the floating sensing element.

2.2 Experimental Facilities and Test Conditions

The experimental program was conducted in Calspan's 96-inch shock tunnel¹¹ at freestream Mach numbers of 11 and 13, for local Reynolds numbers up to 100×10^6 and wall-to-freestream stagnation temperature ratios of 0.19 and 0.20. At Mach numbers up to 13, boundary layer transition is complete on the smooth models within 6 inches of the nosetip. As discussed later, the model used was designed so that the transpiration was initiated downstream of the end of boundary layer transition. The conditions at which experimental studies were conducted are shown in Figure 6.

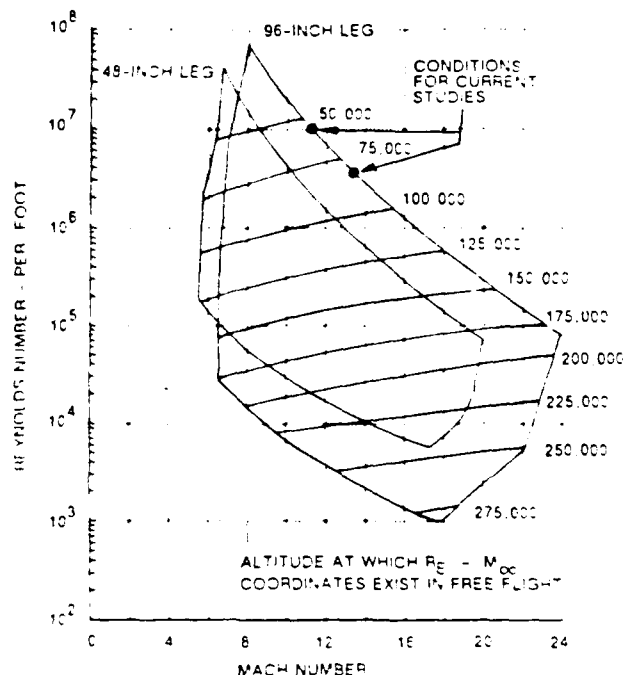


Figure 6 Performance map of Calspan's shock tunnels

The shock tunnel is started by rupturing a double diaphragm that permits high-pressure helium in the driver section to expand into the driven section. This generates a normal shock which propagates through the low pressure air (a wave diagram is shown in Figure 7). A region of high-temperature, high-pressure air is produced between this normal shock front and the gas interface (often referred to as the contact surface) between the driver and driven gas. When the primary or incident shock strikes the end of the driven section, it is reflected, leaving a region of almost stationary, high-pressure, heated air. This air is then expanded through a nozzle to the desired freestream conditions in the test section. The duration of the flow in the test section is controlled by the interactions between the reflected shock, the interface, and the leading expansion wave generated by the nonstationary expansion process occurring in the driver section. We normally control the initial conditions of the gases in the driver and driven sections so the gas interface becomes transparent to the reflected shock interaction. This is known as operating under "tailored-interface" conditions. Under these conditions, the test time is controlled by the time taken for the driver/driven interface to reach the throat, or the leading expansion wave to deplete the reservoir of pressure behind the reflected shock. The flow duration is either driver-gas-limited or expansion-limited, respectively. Figure 8 shows the flow duration in the test section as a function of the

Mach number of the incident shock. Here, it can be seen that for operation at low incident shock Mach number, running times of over 25 milliseconds can be obtained with a long driver section.

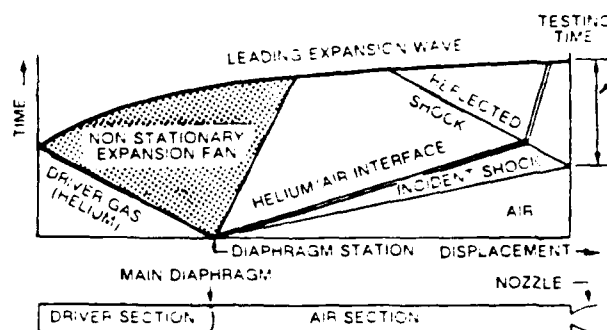


Figure 7 Wave diagram for tailored-interface condition

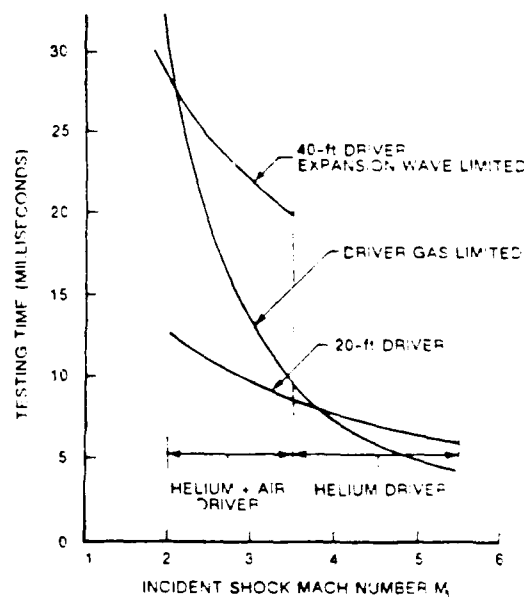


Figure 8 Test time available for tailored interface operation of the shock tunnel

The test conditions at which these studies were conducted are listed in Table 1. For the test conditions at which our studies were conducted the uncertainty in the pitot pressure measurement from errors in calibration and recording is $\pm 2.5\%$. The reservoir pressure can be measured with an uncertainty of $\pm 2\%$, and the total enthalpy (H_0) can be determined from the driven tube pressure and the incident shock Mach number with an uncertainty of $\pm 1.5\%$. These measurements combine to yield an uncertainty in the Mach number and dynamic pressure measurements of $\pm 0.8\%$ and $\pm 3.5\%$ respectively.

Table 1 Test conditions

Run	Po/10 ⁴ PSIA	Mo/10 ⁻⁷ (FT/SEC) ²	To R	Muf	Uinf FT/SEC	Tinf R	Pinf PSIA	Rhoinf SLUGS/FT ³
1	1.7673	2.1545	3071.5	13.072	6478.2	98.674	.07286	5.9895(-5)
2	1.7820	2.1253	3058.0	13.078	6434.4	97.259	.073956	6.1655(-5)
3	1.7643	2.1596	3073.3	13.071	6485.9	98.916	.072673	5.9568(-5)
4	1.7568	2.1174	3066.8	13.055	6422.0	97.217	.073673	6.1444(-5)
5	1.7580	2.1545	3071.5	13.068	6478.2	98.731	.072569	5.9595(-5)
6	1.7755	2.1068	3084.1	13.078	6526.7	100.060	.07249	5.8739(-5)
7	1.7220	1.724	2543.8	11.357	5764.5	103.510	.20516	1.6070(-4)
8	1.7205	1.7482	2560.7	11.359	5861.6	106.260	.20271	1.5444(-4)
9	1.6975	1.787	2552.4	11.355	5864.0	107.140	.19770	1.4944(-4)
10	1.7103	1.7396	2551.5	11.354	5794.4	104.640	.20271	1.5707(-4)
11	1.6986	1.7745	2544.7	11.359	5835.9	106.040	.19853	1.5210(-4)
12	1.7128	1.8.97	2575.9	11.361	5926.6	109.330	.19774	1.6651(-4)

2.3 Models and Instrumentation

2.3.1 Models

The slender cone model used in the experimental studies is shown in Figure 9. The model has a transpiration cooled surface fed from eight high-pressure reservoirs through eight Valcor fast acting valves. Each section of the model is constructed with six zones that run from the front to the rear of the model. This enabled us to vary the blowing circumferentially to simulate the effects of differential blowing resulting from model incidence. To distribute the gas from the reservoirs uniformly to the surface, each model employs a matrix of distribution passages.

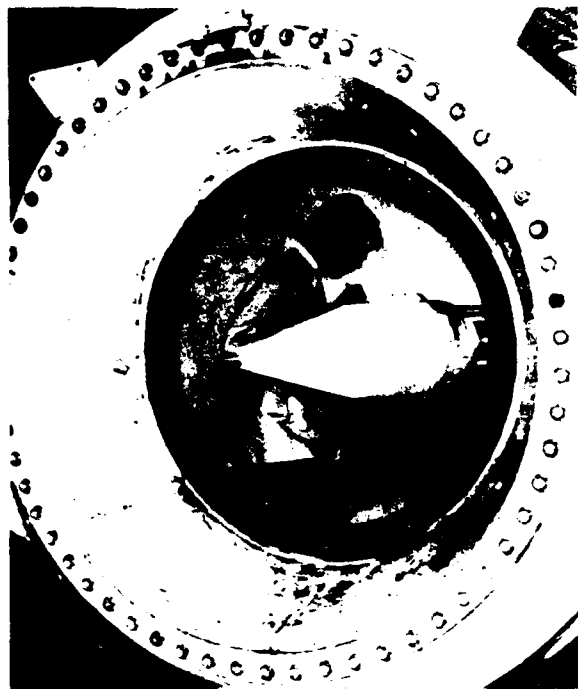


Figure 9 Slender cone model (with sharp nosetip) shown installed in 96-inch shock tunnel (D nozzle removed)

A molding technique¹² that we developed earlier to produce a number of different roughness patterns was used to obtain the smooth and rough surfaces. The low momentum mass addition was injected from passages molded in the model skin into the flow which was controlled by sonic orifices at the base of passage. This latter technique was employed very successfully in our earlier transpiration-cooled studies where we were able to obtain precisely controlled blowing conditions. The flow from each hole in the model was controlled by eight sonic orifices in the model skin that were fed from plenum chambers in the model. The flow from each orifice was released into a cylindrical passage molded in the rubber skin between each roughness element. The area ratio between the orifice and circular passage allowed important flows from the surface at velocities of approximately 100 ft/sec. The painstaking construction of this type of model is worth the effort because it results in an experiment where surface roughness and blowing are completely defined. Because we used choked orifices over the entire model, mass flow from each model zone was precisely controlled by plenum pressures. Mass flows over the model were unaffected by the distribution of surface pressure or transfer associated with tunnel starting. Figure 12 shows the generic schematic with key

dimensions and the locations of the instrumentation blocks containing the heat transfer, pressure and skin friction instrumentation. A typical instrumentation block layout is shown in Figure 11.

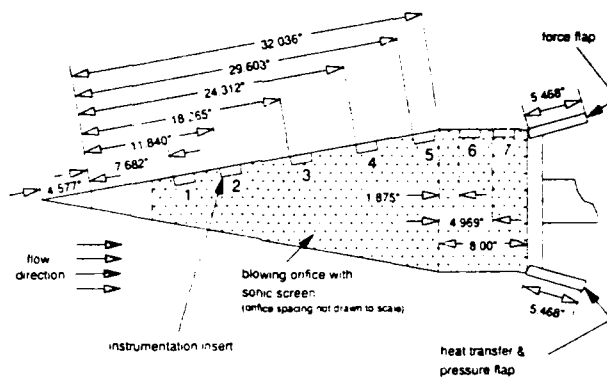


Figure 10 Schematic diagram of 10.5 degree cone model showing blowing configuration and positions of instrumentation inserts

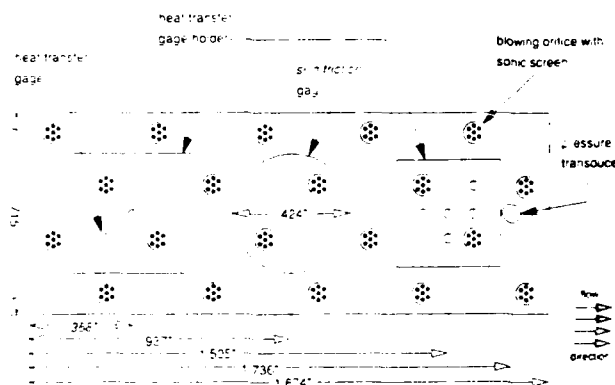


Figure 11 Layout of a typical instrumentation insert

2.3.2 Heat Transfer Instrumentation

The thin-film heat transfer technique is based on sensing the transient surface temperature of a non-conducting model by means of thin-film resistance thermometers. Because the thermal capacity of the gage is negligible, the instantaneous surface temperature of the backing material is related to the heat transfer rate by semi-infinite slab theory. The gages are fabricated on tiny pyrex buttons 0.080 inches in diameter, mounted flush with the model surface. A photograph of the model inserts is shown in Figure 12. As shown in Figures 13a and 13b, these gages were distributed around the injection orifices to provide some insight into the macroscopic flow on these regions.

For the thin-film heat transfer instrumentation, the uncertainties associated with the gage calibration and the recording equipment are estimated to be $\pm 5\%$ for the levels of heating obtained in the current studies.

2.3.3 Skin Friction Instrumentation

The skin friction gage is an acceleration compensated single component force balance in which transpiration cooling passages are vented through the surface of the gage. After a number of different approaches were tried, a design was developed with non-metric coolant passages passing through the metric diaphragm with very little clearance. Such tight

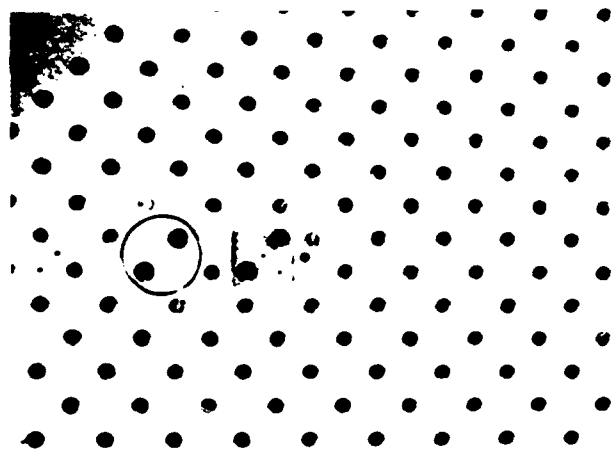


Figure 12 Segment of instrumented surface showing installation of heat transfer, skin friction and pressure instrumentation

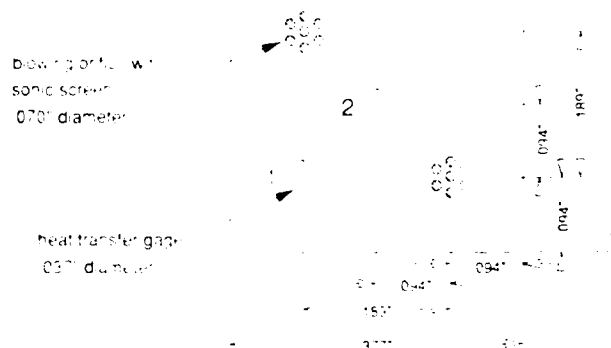


Figure 13a Heat transfer gage positions on gage holder, block A

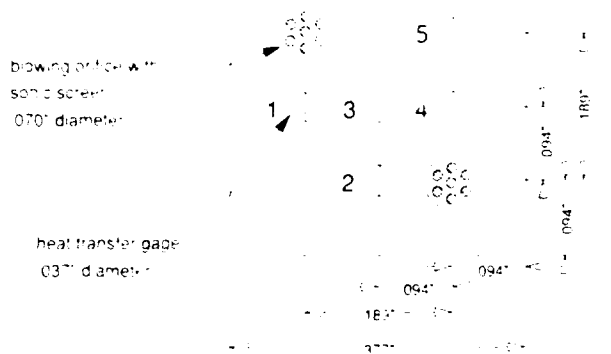


Figure 13b Heat transfer gage positions on gage holder, block B

clearances are allowed because the crystal and rubber support and measuring system on which the diaphragm is mounted is very stiff, so that deflection under load is insignificant. A floating diaphragm, which in this particular design contains the two suction parts, is supported flush with the surface on a piezoelectric sensing beam through a single fixture. The diaphragm is stabilized around its perimeter by four posts. The suction posts are molded into a gasket that contains a rubber boot which is cemented between the diaphragm and the body of the gage to prevent the hot gases from reaching the crystal beam. A second beam and

diaphragm combination is incorporated into the body of the gage to provide a signal used for transducer acceleration compensation. The electrical signals from the sensing and compensation beam are added electrically in such a manner that when the gage is "shaken" in the absence of an air load, the net output is zero. The injection flow through the gage is metered through a series of sonic orifices set in the base of the gage. The geometric and mechanical design features of the gages were refined in a series of bench tests and tunnel studies. The developed gage has a frequency response of 25 kHz, a sensitivity of 25,000 mV/psi, and an overall accuracy of $\pm 4\%$.

2.3.4 Pressure Instrumentation

Pressure measurements were made using flush-mounted Kulite transducers. Pressure gages have been mounted flush with the silicon skin (see Figures 11 and 12) to record the pressure fluctuations, as well as the mean pressure on the flap resulting from the unsteady shock-wave/turbulent boundary layer interaction at the cut/flap junction. Such information is required to specify the vibration environment on the flap as well as to provide insight into the base flow structure. The uncertainties associated with the pressure measurements associated with calibration and recording apparatus are $\pm 3\%$.

2.3.5 Holographic Interferometry

Holographic interferometry was used to make flowfield measurements. Interferograms of complex flowfields provide good qualitative basis for evaluating some of the important phenomena that control the characteristics of these flows. Calspan/University of Buffalo Research Center's (CUBRC) holographic recording system¹³ was used for this study. Both single plate and dual plate techniques are required to record holograms, which are subsequently used in the playback step to obtain shadowgrams, schlieren photographs and interferograms of the tests. Photographs of the flowfield taken with infinite fringe interferometry are shown in Figures 14 and 15.

3. RESULTS AND DISCUSSION

These experimental studies were conducted at Mach 11 and 13 at unit Reynolds numbers of $10 \times 10^6/\text{ft}$ and $9 \times 10^6/\text{ft}$, respectively. A listing of the test conditions at which the studies were conducted are listed in Table 1. All the studies were conducted with a sharp 10.5° conical configuration and a nitrogen injectant. The model orientation and blowing configurations are listed in Table 2.

Table 2 Model and blowing configuration

Run	Mach	Reynolds (x 10 ⁶ /ft)	Angle (deg)	Injection (x 10 ³ /ft)	Flow rate (lb/min)	Flow rate (lb/min)	Flow rate (lb/min)
1	11	10	10.5	1.0	1.0	1.0	1.0
2	11	10	10.5	1.0	1.0	1.0	1.0
3	11	10	10.5	1.0	1.0	1.0	1.0
4	11	10	10.5	1.0	1.0	1.0	1.0
5	11	10	10.5	1.0	1.0	1.0	1.0
6	11	10	10.5	1.0	1.0	1.0	1.0
7	11	10	10.5	1.0	1.0	1.0	1.0
8	11	10	10.5	1.0	1.0	1.0	1.0
9	11	10	10.5	1.0	1.0	1.0	1.0
10	11	10	10.5	1.0	1.0	1.0	1.0
11	11	10	10.5	1.0	1.0	1.0	1.0
12	11	10	10.5	1.0	1.0	1.0	1.0
13	11	10	10.5	1.0	1.0	1.0	1.0
14	11	10	10.5	1.0	1.0	1.0	1.0
15	11	10	10.5	1.0	1.0	1.0	1.0
16	11	10	10.5	1.0	1.0	1.0	1.0
17	11	10	10.5	1.0	1.0	1.0	1.0
18	11	10	10.5	1.0	1.0	1.0	1.0
19	11	10	10.5	1.0	1.0	1.0	1.0
20	11	10	10.5	1.0	1.0	1.0	1.0
21	11	10	10.5	1.0	1.0	1.0	1.0
22	11	10	10.5	1.0	1.0	1.0	1.0
23	11	10	10.5	1.0	1.0	1.0	1.0
24	11	10	10.5	1.0	1.0	1.0	1.0
25	11	10	10.5	1.0	1.0	1.0	1.0
26	11	10	10.5	1.0	1.0	1.0	1.0
27	11	10	10.5	1.0	1.0	1.0	1.0
28	11	10	10.5	1.0	1.0	1.0	1.0
29	11	10	10.5	1.0	1.0	1.0	1.0
30	11	10	10.5	1.0	1.0	1.0	1.0
31	11	10	10.5	1.0	1.0	1.0	1.0
32	11	10	10.5	1.0	1.0	1.0	1.0
33	11	10	10.5	1.0	1.0	1.0	1.0
34	11	10	10.5	1.0	1.0	1.0	1.0
35	11	10	10.5	1.0	1.0	1.0	1.0
36	11	10	10.5	1.0	1.0	1.0	1.0
37	11	10	10.5	1.0	1.0	1.0	1.0
38	11	10	10.5	1.0	1.0	1.0	1.0
39	11	10	10.5	1.0	1.0	1.0	1.0
40	11	10	10.5	1.0	1.0	1.0	1.0
41	11	10	10.5	1.0	1.0	1.0	1.0
42	11	10	10.5	1.0	1.0	1.0	1.0
43	11	10	10.5	1.0	1.0	1.0	1.0
44	11	10	10.5	1.0	1.0	1.0	1.0
45	11	10	10.5	1.0	1.0	1.0	1.0
46	11	10	10.5	1.0	1.0	1.0	1.0
47	11	10	10.5	1.0	1.0	1.0	1.0
48	11	10	10.5	1.0	1.0	1.0	1.0
49	11	10	10.5	1.0	1.0	1.0	1.0
50	11	10	10.5	1.0	1.0	1.0	1.0

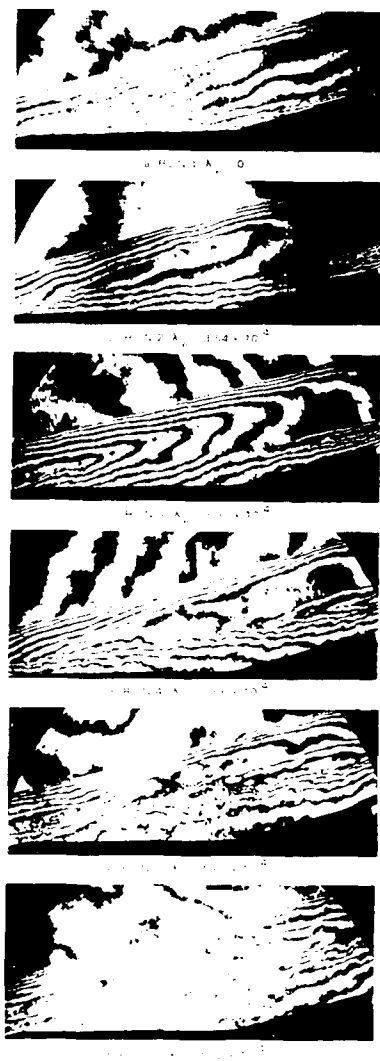


Figure 14 Holographic interferometry photographs for Mach 13 condition

4. $\frac{1}{2} \times \frac{1}{2} = \frac{1}{4}$ (the probability of getting heads on both coins)
 5. $\frac{1}{2} \times \frac{1}{2} = \frac{1}{4}$ (the probability of getting tails on both coins)
 6. $\frac{1}{2} \times \frac{1}{2} = \frac{1}{4}$ (the probability of getting heads on the first coin and tails on the second coin)
 7. $\frac{1}{2} \times \frac{1}{2} = \frac{1}{4}$ (the probability of getting tails on the first coin and heads on the second coin)

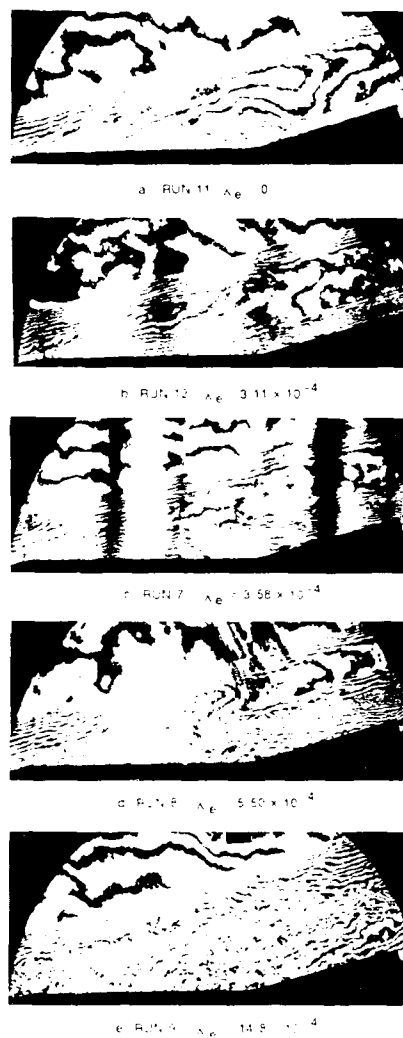
[illegible]

Figure 15 Holographic interferometry photographs for Mach 11 condition

agreement with these measurements. The narrow range of β values, where the law has failed in the quantum theory, presents an effectively smooth boundary to the law.

3.2. Measurements with Transpiration Clogging

For the March 11 and 13 test conditions we varied the area of the wavy region from low values (where the heat transfer and skin friction began to be related to turbulent flow) to the skin friction was reduced to zero as the boundary layer reached the "blow-off" condition. The variation of the heat transfer and skin friction along the surface for the various injection flow rates for the March 11 conditions are shown in Figs. 10a and 10b, respectively. Here we see that skin friction and heat transfer are both dropping rapidly as the injection rate is varied.

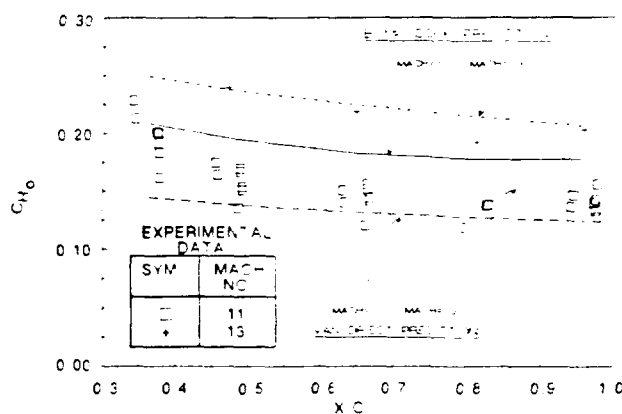


Figure 16 Comparison between predictions and heat transfer measurements for matched pressure (smooth, no blowing) conditions

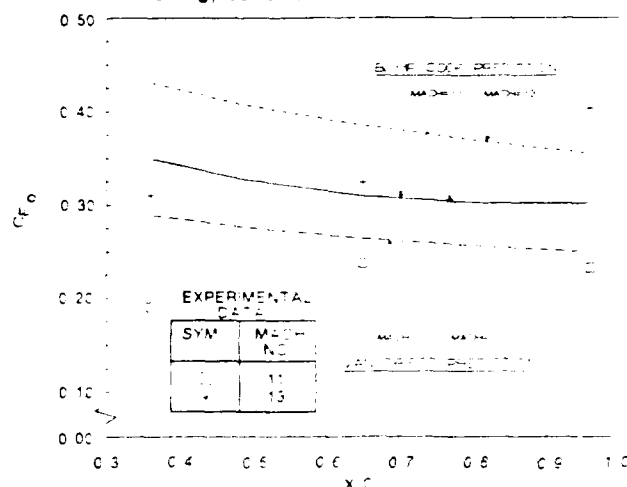


Figure 17 Comparison between predictions and skin friction measurements for matched pressure (smooth, no blowing) conditions

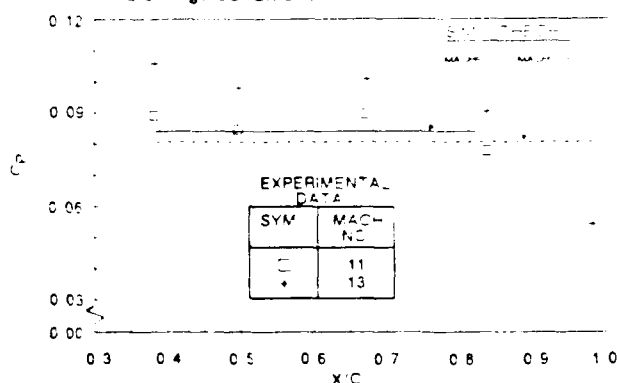


Figure 18 Comparison between pressure measurements and inviscid theory

relatively small. There is almost linear variation in the reduction of heating and skin friction along the cone induced by the injection for all levels of mass injection. At these test conditions the surface shear is reduced to zero for B' of greater than 2. At the Mach 13 conditions the variation of heat transfer and skin friction along the cone (shown in Figures 20a and 20b) for B' from 0.2 to 3 shows the same basic trends as those for the Mach 11 conditions. Again, we observe close to a linear variation of heat transfer and skin friction reduction along the cone, with the gradient of this reduction remaining constant relatively insensitive to the level of blowing for the low rates of injection.

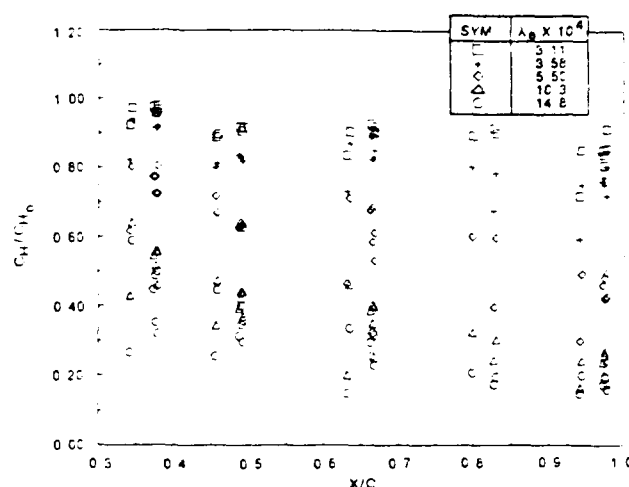


Figure 19a Variation of heat transfer along the cone with mass injection (Mach 11, $Re_{ft} = 10 \times 10^6$)

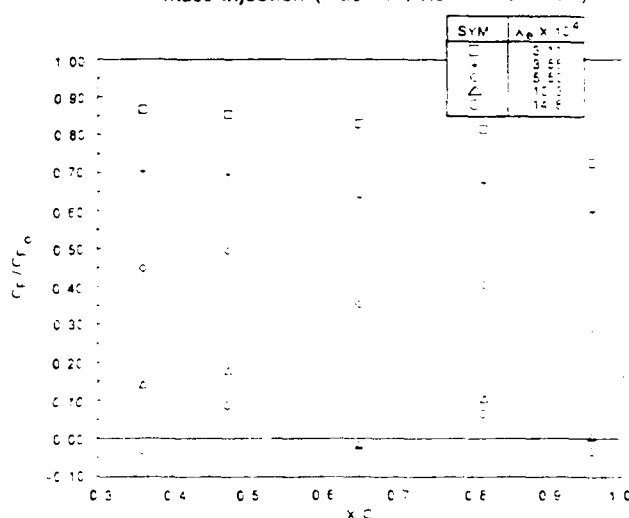


Figure 19b Variation of skin friction along the cone with mass injection (Mach 11, $Re_{ft} = 10 \times 10^6$)

The variation of the reduction in heat transfer and skin friction and pressure with blowing rate parameter B' ($= M/\rho_e c_p C_H$) for the Mach 11 and 13 conditions are shown in Figures 21, 22 and 23, at five streamwise measurement stations along the cone. Here we have averaged the heating levels at each measurement station as shown earlier in Figures 19 and 20. For both the Mach 11 and 13 conditions there is a consistent reduction in heating and skin friction for blowing levels up to B' of between 1 and 2. Above this blowing level the rate of heating reduction is much smaller and the skin friction is reduced to zero as the boundary layer begins to interact with the inviscid flow, as illustrated by the pressure measurements (Figure 23). We also observe that at low blowing rates the heating rates on the cone close to the beginning of blowing are not reduced significantly because the boundary layer is disturbed by the beginning of injection.

3.3 Comparison with Earlier Measurements, Correlations and Calculations with BLIMP Code

The heat transfer measurements obtained in the present study are compared with the measurements made earlier on flat plates and cones at lower freestream Mach numbers (and presented in Figure 24).

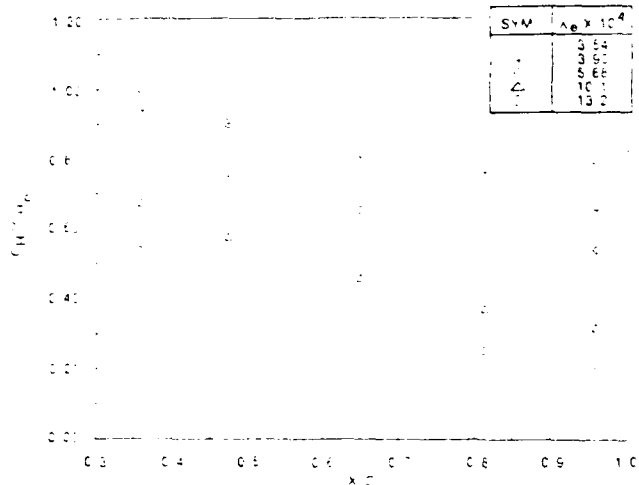


Figure 20a Variation of heat transfer along the cone with mass injection (Mach 13, $Re/ft = 5 \times 10^6$)

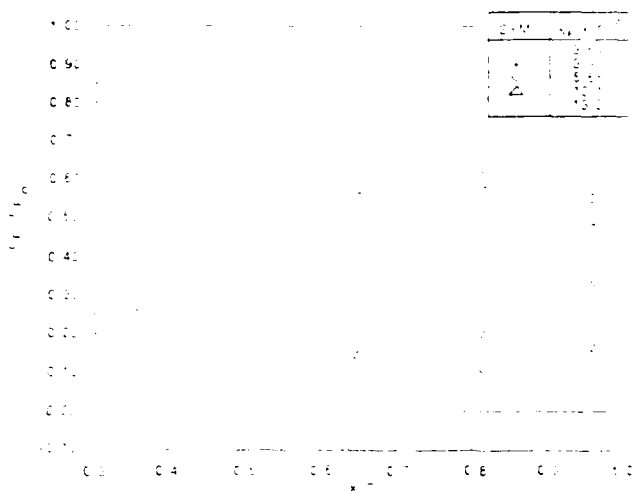


Figure 20b Variation of skin friction along the cone with mass injection (Mach 13, $Re/ft = 5 \times 10^6$)

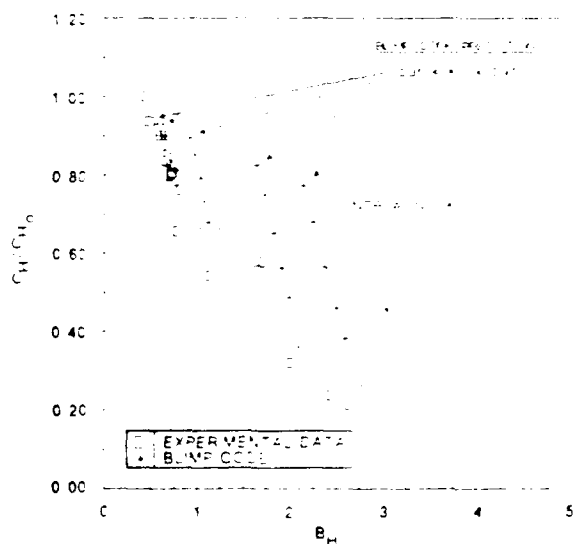


Figure 22a Variation of heat transfer with blowing parameter B_H at Mach 13

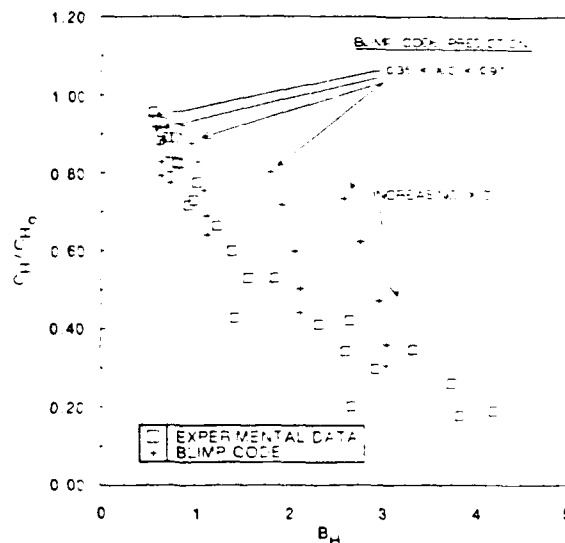


Figure 21a Variation of heat transfer with blowing parameter B_H at Mach 11

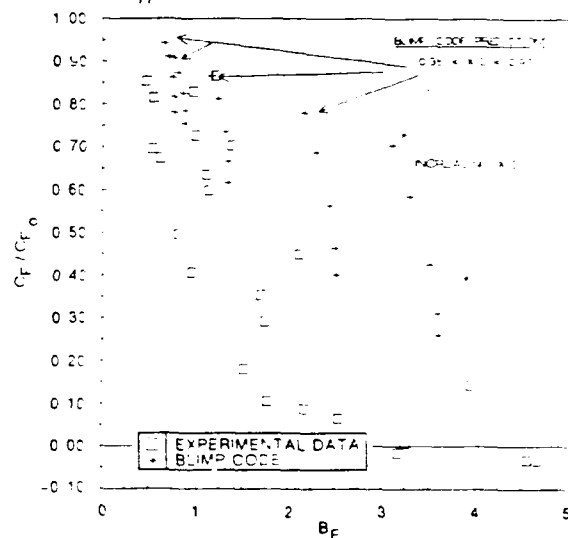


Figure 21b Variation of skin friction with blowing parameter B_F at Mach 11

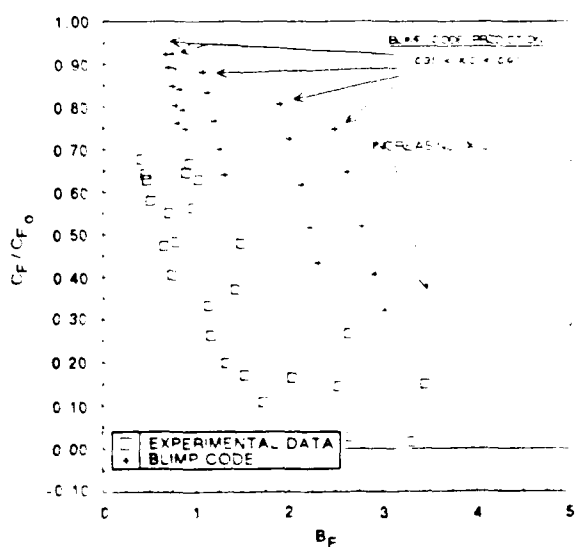


Figure 22b Variation of skin friction with blowing parameter B_F at Mach 13

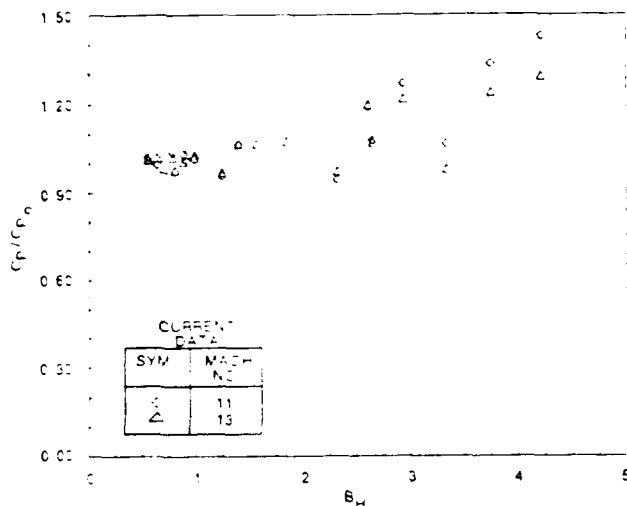


Figure 23 Variation of cone pressure with blowing parameter

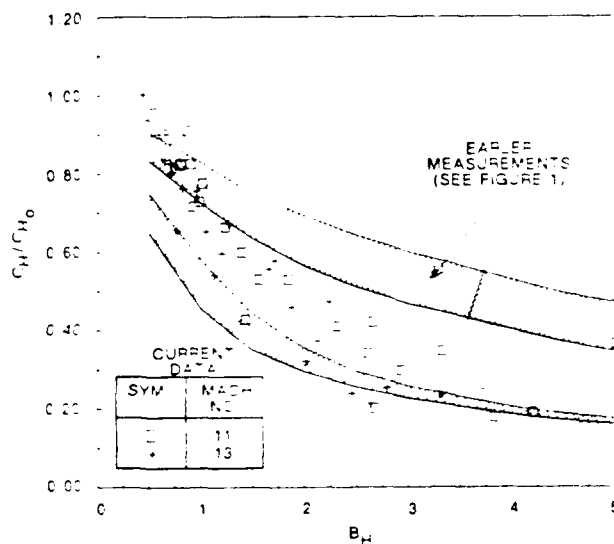


Figure 24 Comparison of current measurements with earlier measurements on cone and flat plates

We see that our measurements show significantly more cooling effectiveness than the earlier measurements at lower Mach numbers for blowing parameters between $0.2 < B_H < 4$. These might be explained as a reduction in the spreading rate with increased Mach numbers, a feature observed in shear flows with large relative Mach numbers.

The input data required by BLIMP was taken from the freestream flow conditions occurring in the test section of each experimental run. This data includes stagnation pressure, stagnation temperature and dynamic pressure. In addition to these the axial distributions of cone surface pressure, surface temperature, and wall transpirant mass flux were input as constants which were consistent with conical flow and the experimental test conditions. The cone surface pressure for each run was calculated using Newtonian Theory and for the zero-blowing cases was checked using the well-known Taylor-Maccoll solution for the supersonic cone. In the case of non-blunt bodies, BLIMP uses a laminar compressible similarity solution at the initial axial station and as the solution progresses along the principal flow direction, the Reynolds number based on momentum thickness

increases until it exceeds a transitional criterion set by the user. At this point, the code computes a turbulent boundary layer and does so for the remainder of the solution. The code was, therefore, run in a fully turbulent mode employing the Cebeci turbulent model with a turbulent Prandtl number of 0.9 and a turbulent Schmidt number of 0.9. The Prandtl mixing length constant was set at 0.4.

Calculations made using the BLIMP code are compared with the measurement of heat transfer and skin friction shown in Figures 25 and 26 for the various injection levels. We see, that for relatively model levels of blowing $B^* < 0.8$, there is relatively good agreement between prediction methods and experiment. However, at Mach 11 and 13 the code consistently and significantly underpredicts the effectiveness of transpiration cooling.

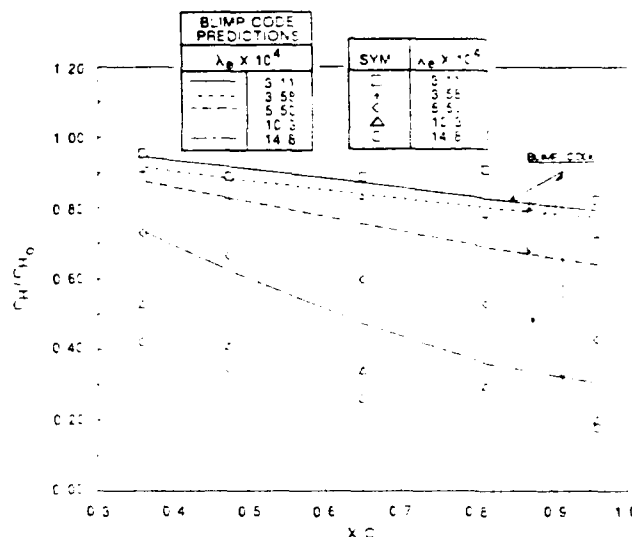


Figure 25a Comparison between heat transfer measurements and BLIMP code calculations (Mach 11, $Re/ft = 10 \times 10^6$)

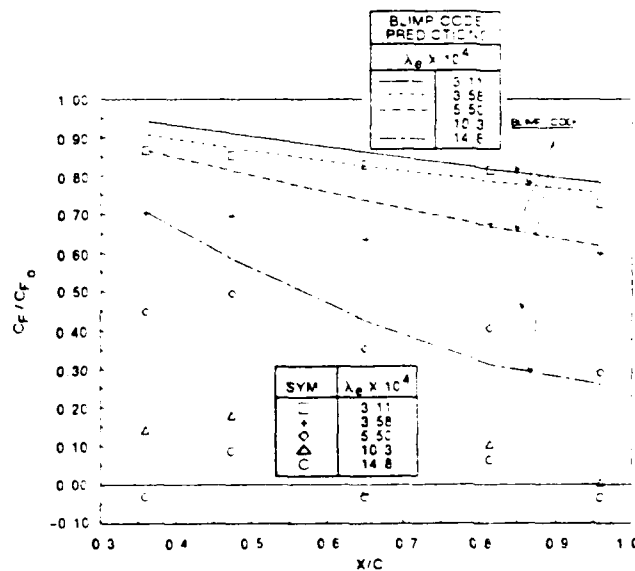


Figure 25b Comparison between skin friction measurements and BLIMP code calculations (Mach 11, $Re/ft = 10 \times 10^6$)

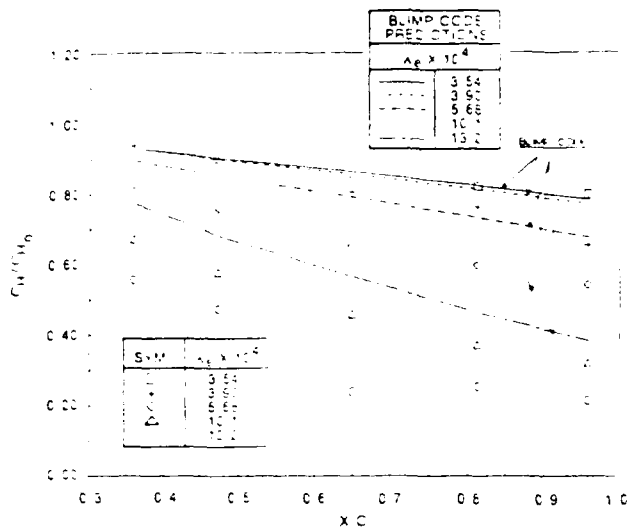


Figure 26a Comparison between heat transfer measurements and BLIMP code calculations (Mach 13, $Re_{ft} = 5 \times 10^6$)

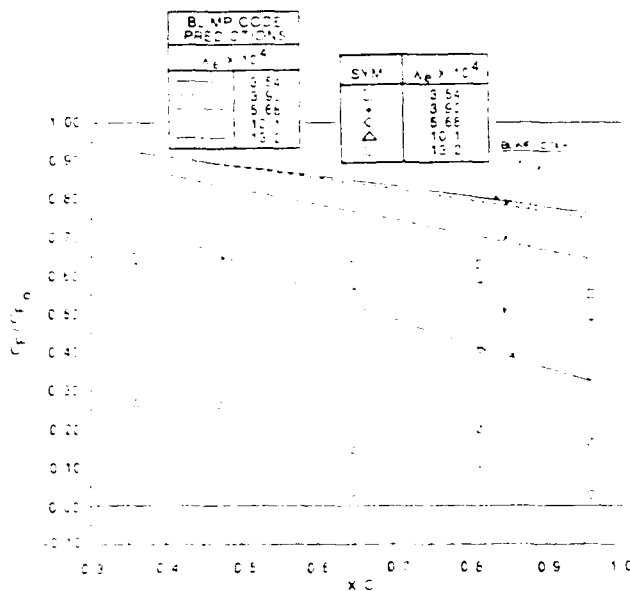


Figure 26b Comparison between skin friction measurements and BLIMP code calculations (Mach 13, $Re_{ft} = 5 \times 10^6$)

In Figures 21 and 22, we have plotted both experiment and BLIMP code predictions in terms of heat transfer and skin prediction versus blowing parameter B' . The BLIMP code predicts reductions in heating of the order of 75% for high levels of blowing while our measurements suggest values of the order of 90% under such conditions. Again, at these high levels of blowing we observe the skin friction to be reduced to zero, as boundary layer blow-off occurs.

We have plotted the measurements from the two Mach numbers together in Figures 27a and 27b together with the BLIMP prediction and a correlation derived from our earlier measurements on transpiration-cooled nosetips and rough blowing cones. While the power law relationship $CH/CH_0 = 1 - 1/3 B'^{1/3}$ works

well for correlating our earlier measurements on nosetips, our current measurements agree better with the relationship $CH/CH_0 = B'/(eB'-1)$ which was in good agreement with our measurements on rough blowing cones with the same geometry as in the current study. Clearly the next effort to predict the current measurement should center on the use of Navier-Stokes codes to overcome the limitations of boundary layer theory.

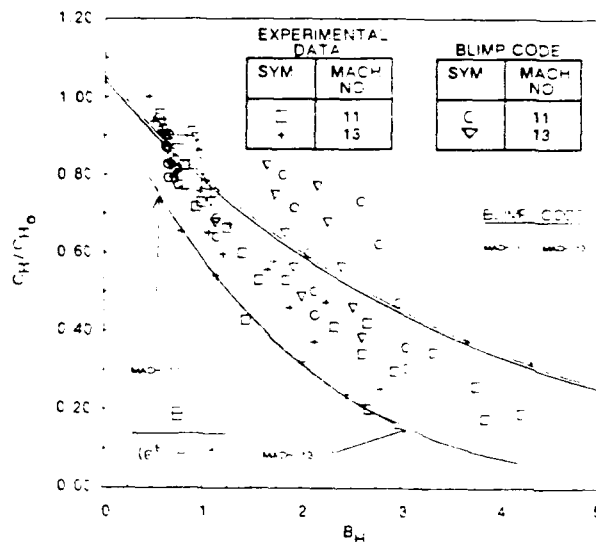


Figure 27a Comparison between calculations with BLIMP code and measurements of heat transfer

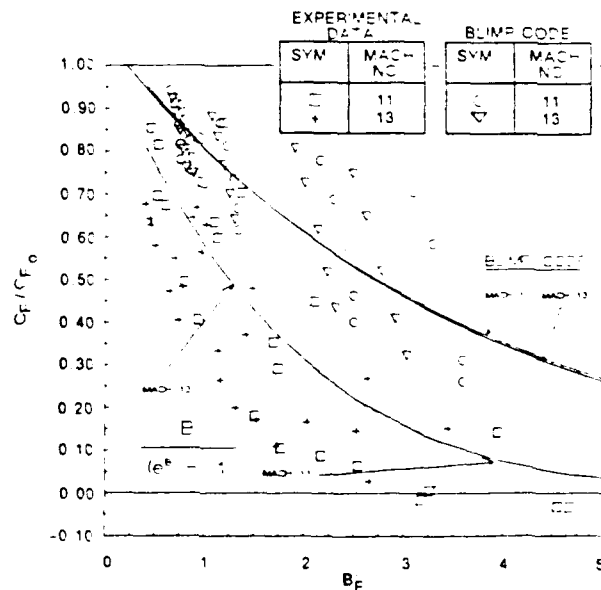


Figure 27b Comparison between calculations with BLIMP code and measurements of skin friction

4. CONCLUSION

An experimental program has been conducted to examine the effects of transpiration cooling on the turbulent heat transfer and skin friction on a sharp slender cone in hypersonic flow. In these studies, conducted at Mach 11 and 13 in the Calspan 96-inch shock tunnel, measurements of heat transfer, skin friction and pressure were obtained along the cone for blowing rates $B' = (\frac{\rho_e u_e c_{f,e}}{2 \rho_w u_{w,e}})$ from 0.10 to 5.0. The measurements of skin friction were obtained using a balance in which the nitrogen injectant was introduced through orifices in the floating element. Detailed heat transfer measurements were made to define the flow around the injection ports. Holographic interferometry was used to examine the structure of the flowfield. Correlations of the heat transfer measurements made in these studies with those obtained earlier on flat plates and cones indicated that we obtained significantly greater cooling effectiveness at the higher Mach numbers at which the present studies were conducted.

Calculations of the distribution of heat transfer and skin friction with the BLIMP code indicated that for small blowing rates the predictions are in relatively good agreement with the measurements. However, for $B' > 0.5$ the code significantly underpredicts the effectiveness of transpiration cooling. For these high blowing rates where the boundary layer is approaching the blow-off condition, boundary layer theory is no longer valid and recourse must be made to solutions based on the full or reduced time-averaged Navier-Stokes equations.

NOMENCLATURE

B'	= B'_e
B_H	= $\frac{\rho_e u_e c_{f,e}}{2 \rho_w u_{w,e}} (h_{e,e} - h_{w,e})$
B_T	= $\frac{2 \rho_w u_{w,e}}{\rho_e u_e} (h_{e,e} - h_{w,e})$
CH	= $\frac{h_{e,e} - h_{w,e}}{h_{e,e} - h_{w,e}} (H_2 - H_w)$; CH_0 zero blowing value
λ	= $\frac{\rho_e u_e c_{f,e}}{\rho_e u_e}$
M	= Mach number
Re_x	= $\frac{\rho_e u_e x}{\mu}$
H	= total enthalpy
C_p	= $P / (2 \rho_e u_e^2)$; C_{p0} zero blowing value
C_f	= $\tau_w / (2 \rho_e u_e^2)$; C_{f0} zero blowing value
P	= static pressure
T	= static temperature
ρ	= density
Subscripts	
O	= stagnation conditions
w	= conditions at wall
e	= local conditions at the edge of boundary layer
∞, ∞	= conditions in the freestream

REFERENCES

1. Holden, M.S., "Studies of Surface Roughness and Blowing Effects on Hypersonic Turbulent Boundary Layers over Slender Cone," AIAA-89-0458, 1989.
2. Brunner, M.J., "Transpiration Cooling Tests at a Sharp Sphere-Cone in a Rocket Exhaust Using N_2 , H_2 and H_2O Coolants," Paper 64-WA/Ht-56 presented at ASME Winter Annual Meeting, New York, 1964.
3. Pappas, C.C. and Okuno, A.F., "Measurements of Heat Transfer and Recovery Factor of a Compressible Turbulent Boundary-Layer on a Sharp Cone with Foreign Gas Injection," NASA TN D-2230, 1964.
4. Fogaroli, R.P., "Measurements of Turbulent Heat Transfer and Skin Friction Reduction on a Porous Cone with Air Injection at High Mach Numbers," General Electric Rep. 64SD5291, 1964.
5. Bartle, E.R. and Leadon, B.M., "The Effectiveness as a Universal Measure of Mass-Transfer Cooling for a Turbulent Boundary-Layer," Proceedings of 1962 Heat Transfer and Fluid Mechanics Institute, Stanford University Press, Stanford, CA 1962.
6. Danberg, J.E., "Characteristics of the Turbulent Boundary-Layer with Heat and Mass Transfer at Mach Number 6.7," Proceedings 5th U.S. Navy Symposium on Aeroballistics, White Oak, MD 1961.
7. Spalding, D.B. and Chi, S.W., "The Drag of a Compressible Turbulent Boundary Layer on a Smooth Flat Plate with and without Heat Transfer," Journal of Fluid Mechanics, Vol. 18, 1964, pp. 117-143.
8. Kays, W.M. and Moffat, R.J., "The Behavior of Transpired Turbulent Boundary Layers," Stanford University, Report No. H MT-26, April 1975.
9. Holden, M.S., "Studies of Transpiration Cooling, Surface Roughness and Entropy Swallowing in Transitional and Turbulent Boundary Layers over Nose Tips," paper presented at IAF-79-F-42, XXX Congress International Astronautical Federation, Sept. 17-22, 1979.
10. Holden, M.S., "An Experimental Simulation of Massive Blowing from a Nosedup During Jovian Entry," Thermophysics of Atmospheric Entry, edited by Thomas E. Horton, Vol. 82, of Progress in Astronautics and Aeronautics, 1982.
11. "Calspan Hypersonic Shock Tunnel, Description and Capabilities Brochure," 1975.
12. Holden, M.S., "Experimental Studies of Surface Roughness Shape and Spalling Effects on Heat Transfer and Skin Friction in Supersonic and Hypersonic Flows," AIAA-84-0016, 1984.
13. Havener, G., Holden, M.S., and Azevedo, D., "Preliminary Applications of Holographic Interferometry to Study Hypersonic Regions of Shock Wave/ Boundary Layer interaction," AIAA-87-1194, 1987.
14. Van Driest, E.R., "Problem of Aerodynamic Heating," Aeronautical Engineering Review, Vol. 15, No. 10, 1956.
15. Murray, A.L., "Facilitation of the BLIMP Computer Code and User's Guide," AFWAL-TR-86-3101, Vol. 1 and Vol. 2, Jan. 1987.

APPENDIX 3

**AN EXPERIMENTAL STUDY OF THE EFFECTS OF INJECTANT
PROPERTIES ON THE AEROTHERMAL CHARACTERISTICS OF
TRANSPIRATION-COOLED CONES IN HYPERSONIC FLOW**



AIAA-90-1487

**An Experimental Study of The Effects of
Injectant Properties on The Aerothermal
Characteristics of Transpiration-Cooled
Cones in Hypersonic Flow**

M. S. Holden

Calspan/UB Research Center
Buffalo, NY

R. D. Neumann, J. Burke

Flight Dynamics Laboratory
Wright-Patterson AFB

K. M. Rodriguez

Calspan/UB Research Center
Buffalo, NY

**AIAA 21st Fluid Dynamics, Plasma Dynamics
and Lasers Conference**

June 18-20, 1990 / Seattle, WA

AN EXPERIMENTAL STUDY OF
THE EFFECTS OF INJECTANT PROPERTIES ON THE
AEROTHERMAL CHARACTERISTICS OF TRANSPIRATION-COOLED
CONES IN HYPERSONIC FLOW

Michael S. Holden*
R.D. Neumann**
G. Burke**
K.M. Rodriguez***
Calspan/UB Research Center
Buffalo, NY

ABSTRACT

An experimental study has been conducted to investigate the effects of molecular weight and specific heat of the injectant on the turbulent heat transfer and skin friction to a sharp slender transpiration-cooled cone in hypersonic flow. The study was conducted in the Calspan 96" Shock Tunnel at Mach numbers of 11 and 13 for local Reynolds' numbers of 100×10^6 and 50×10^6 , respectively. Measurements of heat transfer, skin friction and pressure were obtained along the cone for blowing rates ($\dot{m}/\rho_e u_e C_{H_0}$) from 0.10- to 5, using helium, nitrogen and freon injectants. The characteristics of the flow field were determined with holographic interferometry. Miniature heat transfer instrumentation was used to obtain the detailed distribution around the injection ports. Unique skin friction gages, in which the injectant was introduced through the diaphragm were used in this study. Calculations using the BLIMP code and the Navier-Stokes HEARTS code were made for comparison with the experimental measurements. The effects of the injection rates and gas properties on the heat transfer and skin friction are presented in correlations in terms of the major non-dimensional parameters controlling these flows. Computations using the "BLIMP Code" were in relatively good agreement with the measurement for values of the blowing parameter less than 0.5; however, as boundary layer blow-off begins to occur, the these techniques significantly overpredict the levels of heat transfer and skin friction. However, at these high blowing rates, the HEARTS codes give predictions which are in better agreement with the heat transfer measurements.

1. INTRODUCTION⁴

The use of transpiration cooling on hypersonic vehicles has become of increased interest to designers wishing to look through the boundary layer which would otherwise contain products from the ablative nosetip and frustum. The ablation process itself is one in which transpiration cooling is combined with a flow of a rough surface. To develop methods for ablative cooling, it is important to perform experiments and develop predictive techniques which first address understanding the separate, aerothermal mechanisms associated with surface roughness, and transpiration cooling before attacking the combined effects which occur on an ablative heat shield. In earlier studies, we addressed the effects of surface roughness shape and shaping on the heat transfer and skin friction; and more recently, performed studies to investigate transpiration cooling effects for a nitrogen

injectant. For an ablating body, the specific heat and the molecular weight of the injectant will differ significantly from those of the free stream; thus, it is essential, that we obtain an understanding of how these injectant properties influence the aerothermal loads on the model.

The modeling of the turbulent flow structure over transpiration-cooled and rough ablating surfaces requires a detailed understanding of the mixing process between the injected fluid, the roughness elements, and the fluids at the base of the turbulent boundary layer. To develop an accurate predictive capability to describe the ablation rates of the nosetip, heat shield, and control surfaces, it is necessary to understand and model the separate and combined effects on ablating and non-ablating slender cones. As a result of studies of roughness and blowing on slender cones, Holden¹ suggested that the subsonic studies are inapplicable to the heating of heat shields in hypersonic flow, and also that the basic modeling of the roughness drag and mechanisms of heating used in the theoretical models, which is based on correlations of low speed data, is highly questionable. To obtain the data necessary to perform meaningful code validation it is necessary to obtain measurements under correctly simulated Mach number and Reynolds number conditions.

Review of Earlier Studies

The lack of definitive techniques to predict the effectiveness of transpiration/ablative cooling techniques reflects the lack of fundamental understanding of turbulent mixing in the presence of mass injection and surface roughness. Earlier studies of transpiration cooling techniques were designed principally to evaluate how the blockage heat transfer C_H/C_{H_0} varied with the Mach number, Reynolds number and properties of the freestream and injectant. There is a dearth of turbulent data at hypersonic speeds where transpiration cooling is of considerable interest because it is difficult to generate the test conditions necessary for the correct simulation. Experimental studies have been conducted in supersonic flow with flat plates^{5,6,7,8} and cones^{2,3,4}, and there has been some work on the transpiration cooling of blunt nosetips^{9,10}. Based on a survey of the existing experimental data in Reference 9, the correlation shown in Figure 1 was developed. This correlation indicates that for large blowing rates ($B' > 10$), increased blowing does not significantly improve thermal protection. This may well result from a decrease in the stability of the mixing layer and an increase in the scale of turbulence with increasing blowing. However, Holden's measurements on a spherical nosetip, shown in Figure 2, suggest that heating levels significantly lower than those found on

*Calspan/UB Research Center, Buffalo, NY; Associate Fellow, AIAA

**Flight Dynamics Laboratory, Wright-Patterson AFB.

***Calspan/UB Research Center, Buffalo, NY

This work has been supported by AFWAL and the Aerospace Sciences Directorate of the U.S. Air Force Office of Scientific Research under contracts F33615-85-3003 and AFOSR-88-0223. This paper is declared a work of the U.S. Government and is not subject to copyright protection in the United States.

flat plates and cones were obtained for the higher blowing rates. These latter measurements could be correlated in the form $(\dot{C}_{H_0} - \dot{C}_H)/\dot{C}_{H_0} = 1/3 B^{1/3}$. However, for blowing rates of greater than one, the flow became unstable and violent fluctuations in the surface heating were observed.

The measurements made in earlier studies of transpiration cooling conducted with spherical nose tips suggested that the initial effect of mass addition from a rough ablating nosetip is to modify the flow around the roughness elements by eliminating the cavity flows between them in such a way that the roughness-induced momentum defect is small. If the effect of mass addition is to remove surface roughness as an important characteristic parameter, this throws in question correlations of flight measurements based on an effective surface roughness, and the computational procedures in which the ablation rate is determined from heating levels enhanced by surface-roughness effects.

This program is the fourth part in a series of studies to investigate the separate and combined effects of surface roughness and blowing on the heat transfer and skin friction in hypersonic flow. It was designed to provide insight into the modeling of aerothermal phenomena associated with the ablative and transpiration cooling of hypersonic vehicles. In the earlier phase of this investigation, an extensive series of measurements were performed to examine the effects of the shape and spacing of surface roughness on heat transfer and skin friction.¹² Here, the objective was to provide measurements to quantify the relationship between surface geometry and heating to a rough wall without the necessity of introducing a poorly defined parameter associated with sand-grain roughness. We specifically wanted to prevent the manipulation of the results from the prediction techniques by the selection of an "effective sand-grain roughness." These studies were conducted for hemispherical and biconic nosetips, and sharp and blunted slender cones. Measurements were then obtained with hemispherical transpiration-cooled nosetips which demonstrated that roughness heating effects could be significantly reduced or eliminated by surface blowing. We concluded that, studying roughness effects in the absence of blowing added little to the understanding of heating to rough ablating surfaces. A detailed experimental program was then conducted to examine the combined effects of surface roughness and blowing on the skin friction and heat transfer.¹ To minimize problems associated with transition, these studies were conducted with slender conical configurations under high Reynolds number conditions. We also employed surface configurations with a well-defined surface roughness and blowing geometry to again eliminate the potential selection of an effective sand-grain roughness in comparisons with predictive techniques. A unique feature of this study was the detailed measurements of the distribution of heating over individual roughness elements were made for the first time. Also, skin friction measurements were made on representative segments of the surface. Such measurements provide a direct way of evaluating the accuracy of the macroscopic modeling of these flows. During the third phase of the study, we investigated the surface blowing effects in the absence of surface roughness. The following research forms the fourth segment of this program, designed to investigate the effects on coolant properties on aerothermal performance.

In this paper, we first discuss the design and objectives of the experimental program. A description is then given of the experimental facilities, the models and instrumentation and the reduction and evaluation of the measurements. The results of the program are then presented and discussed, and compared with measurements from earlier studies. The measurements are correlated with those from earlier studies and compared with simple prediction methods and the results of computations with the BLIMP and HEARTS code.

2. EXPERIMENTAL PROGRAM

2.1 Program Objective

This investigation forms the fourth part of a series of studies to investigate the separate and combined effects of surface roughness and blowing on the heat transfer and skin friction to ablative and transpiration-cooled surfaces. A key objective of this work was to obtain measurements which provide insight into the macroscopic modeling of aerothermal phenomena associated with the ablative cooling of hypersonic vehicles. In this phase of the study, we investigated the effects of molecular weight and specific heat of the injectant on the heat transfer and skin friction to the cone surface in the absence of surface roughness.

2.2 Program Design

In order to evaluate the separate and combined effects of surface roughness and blowing, we obtained measurements at the same freestream conditions of the effects of blowing on a model of identical geometry as the model we used earlier in the blowing and roughness studies, but without the hemispherical roughness elements molded into the surface. On the reconfigured model, the miniature heat transfer instrumentation installed in the smooth surface was designed to provide a detailed mapping of the heating around the injection ports at each measurement station along the model. Again, we employed unique skin friction instrumentation in which the cooling fluid is introduced through the diaphragm of the floating sensing element.

2.3 Shock Tunnel Facilities and Free-Stream Conditions

The experimental program was conducted at freestream Mach numbers of 11 and 13, for local Reynolds numbers up to 100×10^6 and wall-to-freestream stagnation temperature ratios of 0.19 and 0.20 in Calspan's 96-inch shock tunnel¹¹. The model used was designed so that at the test conditions at which the studies were conducted, the transpiration was initiated downstream of the end of boundary layer transition. A description of the principles and operation of the shock tunnel are presented in reference 10. The test conditions at which these studies were conducted are listed in Table 1. For the test conditions at which our studies were conducted the uncertainty in the pitot pressure measurement from errors in calibration and recording is $\pm 2.5\%$. The reservoir pressure can be measured with an uncertainty of $\pm 2\%$, and the total enthalpy (H_0) can be determined from the driven tube pressure and the incident shock Mach number with an uncertainty of $\pm 1.5\%$. These measurements combine to yield an uncertainty in the Mach number and dynamic pressure measurements of $\pm 0.8\%$ and $\pm 3.5\%$ respectively.

2.4 Models Design

The transpiration-cooled slender cone model used in the experimental studies is shown in Figure 3. The transpiration cooled surface was fed from eight high-pressure reservoirs through eight Valcor fast acting valves. Each section of the model is constructed with six zones that run from the front to the rear of the model. This enabled us to vary the blowing circumferentially to simulate the effects of differential blowing resulting from model incidence.

We used the surface construction technique developed earlier to produce a number of different roughness patterns to obtain the smooth ablation cooled surface. The low momentum mass addition was injected from passages molded in the model skin into the flow which was controlled by sonic orifices at the base of passage. This latter technique was employed very successfully in our earlier transpiration-cooled studies where we were able to obtain precisely controlled blowing conditions. The flow from each hole in the model was controlled by eight sonic orifices in the model skin that were fed from plenum chambers in the model. The flow from each orifice was released into a cylindrical passage molded in the rubber skin between each roughness element. The area ratio between the orifice and circular passage allowed injectant flows from the surface at velocities of approximately 100 ft/sec. The construction of this type of model is worth the effort because it results in an experiment where surface roughness and blowing are completely defined. Because we used choked orifices over the entire model, mass flow from each model zone was precisely controlled by plenum pressures. Mass flows over the model were unaffected by the distribution of surface pressure on transients associated with tunnel starting. Figure 4 shows the model schematic with key dimensions and the locations of the instrumentation blocks containing the heat transfer, pressure and skin friction instrumentation. A typical instrumentation block layout is shown in Figure 5.

2.5 Surface Instrumentation

The heat transfer instrumentation used in these studies is based on a thin-film heat transfer technique which senses the transient surface temperature of a non-conducting model by means of thin-film resistance thermometers. Because the thermal capacity of the gage is negligible, the instantaneous surface temperature of the backing material is related to the heat transfer rate by semi-infinite slab theory. The gages are fabricated on tiny pyrex buttons 0.080 inches in diameter, mounted flush with the model surface. As shown in Figure 5, these gages were distributed around the injection orifices to provide some insight into the macroscopic flow on these regions. The uncertainties associated with the gage calibration and the recording equipment are estimated to be $\pm 5\%$ for the levels of heating obtained in the current studies.

The skin friction gage is an acceleration compensated single component force balance in which transpiration cooling passages are vented through the surface of the gage. After a number of different approaches were tried, a design was developed with non-metric coolant passages passing through the metric diaphragm with very little clearance. Such tight clearances are allowed because the crystal and rubber support and measuring system on which the diaphragm is mounted is very stiff, so that deflection under load is insignificant. A floating diaphragm, which in this particular design contains the two suction parts is supported flush with the surface on a piezoelectric

sensing beam through a single fixture. The diaphragm is stabilized around its perimeter by silicon posts. The silicon posts are molded into a gasket that contains a rubber boot which is cemented between the diaphragm and the body of the gage to prevent the hot gases from reaching the crystal beam. A second beam and diaphragm combination is incorporated into the body of the gage to provide a signal used for transducer acceleration compensation. The electrical signals from the sensing and compensation beam are added electrically in such a manner that when the gage is "shaken" in the absence of an air load, the net output is zero. The injection flow through the gage is metered through a series of sonic orifices set in the base of the gage. The geometric and mechanical design features of the gages were refined in a series of bench tests and tunnel studies. The developed gage has a frequency response of 20 kHz, a sensitivity of 20,000 mV/psi, and an overall accuracy of $\pm 4\%$.

Pressure measurements were made using flush-mounted Kulite transducers. Pressure gages have been mounted flush with the silicon skin (see Figure 5) to record the pressure fluctuations, as well as the mean pressure on the flap resulting from the unsteady shock-wave/turbulent boundary layer interaction at the cut/flap junction. Such information is required to specify the vibration environment on the flap as well as to provide insight into the base flow structure. The uncertainties associated with the pressure measurements associated with calibration and recording apparatus are $\pm 3\%$.

2.6 Holographic Interferometry

Holographic interferometry was used to make flowfield measurements. Interferograms of complex flowfields provide good qualitative basis for evaluating some of the important phenomena that control the characteristics of these flows. Calspan/University of Buffalo Research Center's (CUBRC) holographic recording system¹³ was used for this study. Both single plate and dual plate techniques are required to record holograms, which are subsequently used in the playback step to obtain shadowgrams, schlieren photographs and interferograms of the tests. Photographs of the flowfield taken with infinite fringe interferometry are shown in Figure 6.

3. RESULTS AND DISCUSSION

These experimental studies were conducted at Mach 11 and 13 at unit Reynolds numbers of $10 \times 10^6/\text{ft}$ and $5 \times 10^6/\text{ft}$, respectively. A listing of the test conditions at which the studies were conducted are presented in Table 1. All the studies were conducted with a sharp 10.5° conical configuration with nitrogen, helium and freon injectants. The model orientation and blowing configurations are listed in Table 2.

3.1 Measurements in the Absence of Transpiration Cooling

Because any transpiration-cooled surfaces must contain orifices through which the injectant is introduced in the absence of blowing the surface will exhibit some degree of roughness to the flow. In our initial studies we explored the influence of the roughness of the surface by matching the pressure in the plenums behind the sonic orifice feeding the surface to the cone pressure; such that there was a minute flow filling the orifices. A comparison between measurements under matched pressure conditions and the heat transfer, skin friction and pressure measurements on the cone at Mach 11 and 13 are shown in Figures 7, 8, and 9. Here we see the

calculations based on the Van Driest¹⁴ method and the BLIMP¹⁵ code for smooth walls are in good agreement with these measurements. The minute values of blowing where the flow has filled in the cavities thereby presents an effectively smooth body to the flow.

3.2 Studies with Nitrogen, Helium, and Freon Injectants

In these studies we investigate the effects of injection rate from very low levels where the heat transfer and skin friction were reduced slightly ($\lambda_e = 3 \times 10^{-4}$) to large blowing rates ($\lambda_e = 1.5 \times 10^{-3}$) where the boundary layer was "blown off" of the surface, for helium, nitrogen or Freon 14 injectants. Here we wished to examine the relative performance of the injectants to quantify the effects of specific heat, and molecular weight on the thermal protection and skin friction reduction of the cooling layer. We anticipated that helium, with its higher C_p than nitrogen, would absorb a greater quantity of heat from the flow; and the lower molecular weight of helium would, for the same mass flow rate of gas, result in a larger volume of gas blocking the heat transfer.

Our initial investigation was with a nitrogen injectant (Reference 2) and we conducted measurements for blowing rates up to boundary layer blow-off. Examples of the interferograms taken during these studies are shown in Figure 6. For $\lambda_e = 1.5 \times 10^{-3}$ boundary layer blow off occurred. This can be observed in the skin friction measurements shown in Figure 10. Figure 10a shows the heat transfer measurements taken in these studies for the different blowing rates. Here we show all the heat transfer data from gases clustered around the injector ports at each downstream station. We observed surprisingly little variation of heating rates around the injectors, and in the remaining plots we have averaged the heating measurements from each instrumental insert. Both the heat transfer and skin friction instrumentation show a rapid decrease in levels with increase in blowing at the lower blowing rates ($B' < 0.5$) while for blowing rates for $B' > 3$ there is relatively little change with increased blowing, as shown in Figures 11a and 11b where the blockage heating is plotted in terms of the blowing parameter B' . Also shown are the calculations with the BLIMP code which illustrate that at the downstream station the code and measurement are in relatively good agreement. This is illustrated in Figure 12 where the heat transfer measurement along the code are compared with the BLIMP code for $\lambda_e = 0.33 \times 10^{-3}$. The results of the HEARTS code for the same flow configuration are shown in Figure 13, together with composites at a lower blowing rate. Again the agreement is good at the back of the cone, well downstream of the transients which are generated as blowing is initiated in the cone.

The measurements of heat transfer and skin friction with the helium injectant are shown in Figures 14a and 14b. It is clear, helium is a far more efficient coolant than nitrogen, with $\lambda_e = 7.5 \times 10^{-4}$ to reduce the heating by 80% rather than the 1.5×10^{-3} required for nitrogen. This we believe results directly from the increased heat absorption of the gas ($C_{pHe}/C_{pNit} = 5.2$) and the increased volume of gas for a given mass flow rate (Mol Wt N_2 /Mol Wt $He = 7$). Boundary layer blow-off occurs for a far lower B' (< 1) for the helium injectant and for B' greater than the heating to the core is reduced. Figures 15a and 15b show correlations of the heat transfer and skin friction blockage factors in terms of the blowing parameter. It can be seen that boundary-layer blowoff occurs for $B's \approx 0.6$, and at these conditions there is a over 80% reduction in the surface heat transfer.

While low molecular weight and high C_p of the helium results in a more effective coolant than nitrogen, freon can be seen in Figure 16 and 17 to be a relatively poor coolant. Even at the largest blowing rates we did not observe boundary layer blow-off and for these high mass addition rates, we were able to achieve no better than a 75% reduction in cone heating. However, the measurements made with freon along the cone correlate reasonably well in terms of blockage factor and blowing parameter as shown in Figure 17.

3.3 Correlations of Experimental Measurements

The measurements for each of the injectants are plotted together in terms of the conventional blockage factors and blowing parameters in Figures 18a and 18b. This figure graphically illustrates the greater effectiveness of the helium injectant in reducing both the momentum and heat transfer flux to the surface. In order to correlate these measurements, we have plotted the blocking parameter in terms of a modified blowing parameter incorporating the specific heat ratio and the molecular weight ratio defined as

$$B'_m = \frac{\dot{m}}{\rho_e u_e c_{H_0}} \left(\frac{C_{p_{INT}}}{C_{p_{FS}}} \right)^{\eta} \left(\frac{M_{FS}}{M_{INT}} \right)^{\eta}$$

We examined correlations based on a number of forms of this expression and selected two forms which give the best correlation of the measurements

$$B'_{mc} = \frac{\dot{m}}{\rho_e u_e c_{H_0}} \left(\frac{C_{p_{INT}}}{C_{p_{FS}}} \right)^{0.7} \text{ or } B'_{mm} = \frac{\dot{m}}{\rho_e u_e c_H} \left(\frac{M_{FS}}{M_{INT}} \right)^{0.5}$$

These correlations are shown in Figures 19 and 20.

Ideally the correlations should contain both the molecular weights and specific heat parameters, however, an additional set of studies with different injectant would be required to justify a more complex form. What is of interest is that both the non-dimensional skin friction and heat transfer correlate well with the same power-law expressions, suggesting that even for large blowing rates the basic mechanisms of heating and momentum transfer are similar. Also in these figures, we have plotted the empirical relationship $C_H/C_{H_0} = B'/(eB'-1)$ which was in relatively good agreement with our earlier measurements on rough blowing cones. We see that this correlation is in good agreement with the skin friction correlations but tends to underpredict the heat transfer to transpiration cooled cones in hypersonic flow. In Figure 21 we show a correlation between the measured cone pressure and the modified blowing parameter. These measurements show that for modified blowing parameters of above 2 there is a significant interaction between the growth of the boundary layer and the inviscid flow. When this occurs the boundary layer is close to the blow-off condition.

The heat transfer measurements made in the current study are compared with those made earlier on flat plates and cones in supersonic flow in Figure 22. In general our measurements in hypersonic flow show increased effectiveness of transpiration cooling with an increase Mach number. This trend is consistent with earlier observations in flows of film cooling.

3.4 Comparison Between BLIMP and HEARTS Code

Calculations made using the HEARTS Code are compared with heat transfer rate measurements of a highly blowing configuration with nitrogen injection, in Figure 23. We see that toward the base of the cone both theory and experiment are in good agreement. Also,

whether the HEARTS Code is employed in a zonal or marching mode it gives consistent results. However, the code (which uses essentially a mixing length model), is unable to predict the behavior of heating just downstream of the point of the initiation of surface blowing. In fact, the calculations show that there is a small upstream influence which results in an extremely rapid decrease to a relatively steady region of reduced heating close to the beginning of injection.

Figures 12 and 13 show comparisons between the BLIMP code and measurements for large surface blowing at Mach 11 and 13. Again, we see that there is relatively good agreement between the code predictions and measurements at the base of the cone. Additional computations for the Mach 13 condition showing the effects of blowing rate on the heat transfer and skin friction distribution are shown in Figure 24. Again we see that for relatively modest levels of blowing $B' < 0.8$, there is relatively good agreement between the prediction methods and experiment on the back of the cone. However, for high blowing rates the BLIMP code significantly overpredicts the skin friction to the cone.

4. CONCLUSIONS

An experimental study has been conducted to examine the effects of coolant properties on the heat transfer and skin friction to a transpiration-cooled sharp cone in hypersonic flow. These studies were conducted in the Calspan 96-Inch Shock Tunnel at a Mach number of 11 and local Reynolds number of 100×10^6 . Measurements of the reduction in heating and skin friction to the cone were made for blowing rates B' from 0.10 to 5.0. The detailed measurement around the injection ports demonstrated that the heating of a given downstream station was not strongly influenced by the injection configuration. A unique skin friction measurement technique, in which the injectant was introduced through the balance was found to work well. The holographic measurements gave definitive indications of boundary layer behavior with blowing.

Correlations of the measurements with those from earlier studies indicate that at hypersonic speeds, we obtain significantly larger cooling effectiveness than at supersonic speeds. Correlations of the heat transfer and skin friction measurements for the different injectants indicate that their relative effectiveness may be expressed in terms of either the effects of specific heat or molecular weight ratio. Prediction with the HEARTS and BLIMP code are in good agreement with the heat transfer and skin friction at the base of the cone for the lower blowing rates. However, close to the initiation of blowing the heating and skin friction levels are under-predicted, presumably because of the simplicity of the turbulence models used in these codes.

NOMENCLATURE

$$\begin{aligned} B' &= \dot{B}_H \\ \dot{B}_H &= (\rho_w v_w) / \rho_e u_e C_H \\ B_F &= 2 \rho_w v_w / \rho_e u_e C_F \\ C_H &= g / \rho_e u_e (H_0 - H_w): C_{H_0} \text{ zero blowing value} \\ \lambda &= \frac{\rho_w v_w}{\rho_e u_e} \\ M &= \text{Mach number} \\ Re_x &= \frac{\rho u x}{\mu} \end{aligned}$$

$$\begin{aligned} H &= \text{total enthalpy} \\ C_p &= P^{1/2} \rho_\infty u_\infty^2 : C_{p_0} \text{ zero blowing value} \\ C_f &= \tau^{1/2} \rho_e u_e^2 : C_{f_0} \text{ zero blowing value} \\ P &= \text{static pressure} \\ T &= \text{static temperature} \\ \rho &= \text{density} \\ \text{Subscripts} & \\ O &= \text{stagnation conditions} \\ W &= \text{conditions at wall} \\ e &= \text{local conditions at the edge of boundary layer} \\ inj &= \text{injectant} \\ \infty, inf, FS &= \text{conditions in the freestream} \end{aligned}$$

REFERENCES

1. Holden, M.S., "Studies of Surface Roughness and Blowing Effects on Hypersonic Turbulent Boundary Layers over Slender Cone," AIAA-89-0458, 1989.
2. Brunner, M.J., "Transpiration Cooling Tests at a Sharp Sphere-Cone in a Rocket Exhaust Using N_2 , H_e and H_2O Coolants," Paper 64-WA/Ht-50 presented at ASME Winter Annual Meeting, New York, 1964.
3. Pappas, C.C. and Okuno, A.F., "Measurements of Heat Transfer and Recovery Factor of a Compressible Turbulent Boundary-Layer on a Sharp Cone with Foreign Gas Injection," NASA TN D-2230, 1964.
4. Fogaroli, R.P., "Measurements of Turbulent Heat Transfer and Skin Friction Reduction on a Porous Cone with Air Injection at High Mach Numbers," General Electric Rep. 64SD5291, 1964.
5. Bartle, E.R. and Leadon, B.M., "The Effectiveness as a Universal Measure of Mass-Transfer Cooling for a Turbulent Boundary-Layer," Proceedings of 1962 Heat Transfer and Fluid Mechanics Institute, Stanford University Press, Stanford, CA 1962.
6. Danberg, J.E., "Characteristics of the Turbulent Boundary-Layer with Heat and Mass Transfer at Mach Number 6.7," Proceedings 5th U.S. Navy Symposium on Aeroballistics, White Oak, MD 1961.
7. Spalding, D.B. and Chi, S.W., "The Drag of a Compressible Turbulent Boundary Layer on a Smooth Flat Plate with and without Heat Transfer," Journal of Fluid Mechanics, Vol. 18, 1964, pp. 117-143.
8. Kays, W.M. and Moffat, R.J., "The Behavior of Transpired Turbulent Boundary Layers," Stanford University, Report No. H MT-20, April 1975.
9. Holden, M.S., "Studies of Transpiration Cooling, Surface Roughness and Entropy Swallowing in Transitional and Turbulent Boundary Layers over Nose Tips," paper presented at IAF-79-F-42, XXX Congress International Astronautical Federation, Sept. 17-22, 1979.

10. Holden, M.S., "An Experimental Simulation of Massive Blowing from a Nosedip During Jovian Entry," Thermophysics of Atmospheric Entry, edited by Thomas E. Horton, Vol. 82, of Progress in Astronautics and Aeronautics, 1982.
11. "Calspan Hypersonic Shock Tunnel, Description and Capabilities Brochure," 1975.
12. Holden, M.S., "Experimental Studies of Surface Roughness Shape and Spacing Effects on Heat Transfer and Skin Friction in Supersonic and Hypersonic Flows," AIAA-84-0016, 1984.
13. Havener, G., Holden, M.S., and Azevedo, D., "Preliminary Applications of Holographic Interferometry to Study Hypersonic Regions of Shock Wave/Boundary Layer Interaction," AIAA-87-1194, 1987.
14. Van Driest, E.R., "Problem of Aerodynamic Heating," Aeronautical Engineering Review, Vol. 15, No. 10, 1956.
15. Murray, A.L., "Facilitation of the BLIMP Computer Code and User's Guide," AFWAL-TR-86-3101, Vol. 1 and Vol. 2, Jan. 1987.

Table I
TEST CONDITIONS

Run	Po/10 ⁻⁴ PSIA	Ho/10 ⁻⁷ (FT/SEC) ²	To R	Minf	Uinf FT/SEC	Tinf R	Pinf PSIA	Rhoinf SLUGS/FT3
1	1.7673	2.1545	3071.5	13.072	6478.2	98.674	.072892	5.9895(-5)
2	1.7820	2.1253	3058.0	13.078	6434.4	97.259	.073958	6.1655(-5)
3	1.7643	2.1596	3073.3	13.071	6485.9	98.916	.072671	5.9568(-5)
4	1.7568	2.1174	3066.8	13.055	6422.0	97.217	.073673	6.1444(-5)
5	1.7580	2.1545	3071.5	13.068	6478.2	98.731	.072569	5.9595(-5)
6	1.7755	2.1868	3084.1	13.078	6526.7	100.060	.072492	5.8739(-5)
7	1.7220	1.7216	2543.8	11.357	5764.5	103.510	.205160	1.6070(-4)
8	1.7205	1.7680	2560.7	11.359	5841.6	106.260	.202000	1.5414(-4)
9	1.6975	1.7827	2552.4	11.359	5866.0	107.140	.197730	1.4964(-4)
10	1.7103	1.7396	2551.5	11.354	5794.4	104.640	.202710	1.5707(-4)
11	1.6988	1.7645	2544.7	11.359	5835.9	106.040	.198930	1.5210(-4)
12	1.7128	1.8197	2575.9	11.361	5926.6	109.330	.197740	1.4665(-4)
16	1.7905	1.7493	2588.6	11.362	5810.7	105.080	.213220	1.6452(-4)
17	1.7855	1.8049	2620.7	11.358	5902.3	108.490	.209640	1.5667(-4)
18	1.7650	1.7584	2568.5	11.366	5825.9	105.550	.208280	1.6000(-4)
19	1.7883	1.7721	2578.4	11.372	5848.7	106.270	.210260	1.6042(-4)
20	1.7613	1.8043	2580.3	11.370	5901.6	108.230	.204600	1.5327(-4)
21	1.7560	1.7882	2575.3	11.367	5875.0	107.320	.205100	1.5496(-4)
22	1.7500	1.8306	2621.5	11.353	5944.1	110.120	.203510	1.4984(-4)
23	1.7100	1.7998	2590.2	11.349	5893.8	108.350	.199830	1.4953(-4)
24	1.7203	1.7978	2611.5	11.341	5890.3	108.370	.202400	1.5143(-4)
25	1.7263	1.8164	2611.4	11.348	5920.8	109.370	.201480	1.4936(-4)
26	1.7163	1.8093	2602.3	11.348	5909.2	108.950	.200430	1.4917(-4)
27	1.7320	1.8375	2614.3	11.353	5955.2	110.540	.200540	1.4709(-4)
28	1.6933	1.8068	2591.2	11.345	5905.1	108.840	.197440	1.4708(-4)
29	1.7160	1.8586	2617.3	11.352	5989.4	111.840	.197240	1.4299(-4)
30	1.6973	1.7928	2581.3	11.348	5882.3	107.950	.198470	1.4907(-4)
31	2.1373	2.2517	3137.6	13.196	6624.5	101.250	.084081	6.7329(-5)
32	2.1837	2.2323	3162.1	13.182	6595.8	100.590	.087343	7.0404(-5)

Table II
MODEL AND BLOWING CONFIGURATION

Run	MACH NO.	Reynolds# (10 ⁶ /ft)	r0/R0 (deg)	lambda-e	Inj.	Force Flap (deg)	HT&P Flap (deg)	AOA (deg)
1	13	4.7	0	0.000E+00	N2	15	15	0
2	13	4.7	0	3.535E-04	N2	15	15	0
3	13	4.7	0	3.898E-04	N2	15	15	0
4	13	4.7	0	5.680E-04	N2	15	15	0
5	13	4.7	0	1.315E-03	N2	15	15	0
6	13	4.7	0	1.010E-03	N2	15	15	0
7	11	10	0	3.577E-04	N2	15	15	0
8	11	10	0	5.502E-04	N2	15	15	0
9	11	10	0	1.478E-03	N2	15	15	0
10	11	10	0	1.031E-03	N2	15	15	0
11	11	10	0	2.321E-04	N2	15	15	0
12	11	10	0	3.111E-04	N2	15	15	0
14	11.4	11	0	5.421E-04	N2	15	15	0
15	11.4	11	0	6.543E-04	N2	15	15	0
16	11.4	11	0	1.027E-04	He	15	15	0
17	11.4	11	0	1.476E-04	He	15	15	0
18	11.4	11	0	2.654E-04	He	15	15	0
19	11.4	11	0	4.382E-04	He	15	15	0
20	11.4	11	0	1.028E-04	He	15	15	0
21	11.4	11	0	9.618E-05	He	15	15	0
22	11.4	10	0	2.198E-04	He	15	15	0
23	11.3	10	0	0.000E+00	-	15	15	0
24	11.3	10	0	3.126E-03	Freon	15	15	0
25	11.3	10	0	2.166E-03	Freon	15	15	0
26	11.3	10	0	1.381E-03	Freon	15	15	0
27	11.4	10	0	9.879E-04	Freon	15	15	0
28	11.3	10	0	6.242E-04	Freon	15	15	0
29	11.4	9.7	0	4.537E-04	Freon	15	15	0
30	11.3	10	0	3.831E-04	Freon	15	15	0
31	13.2	5.6	0	0.000E+00	-	15	15	0
32	13.2	5.8	0	6.761E-04	Freon	15	15	0
33	13.2	5.5	0	0.000E+00	-	15	15	0

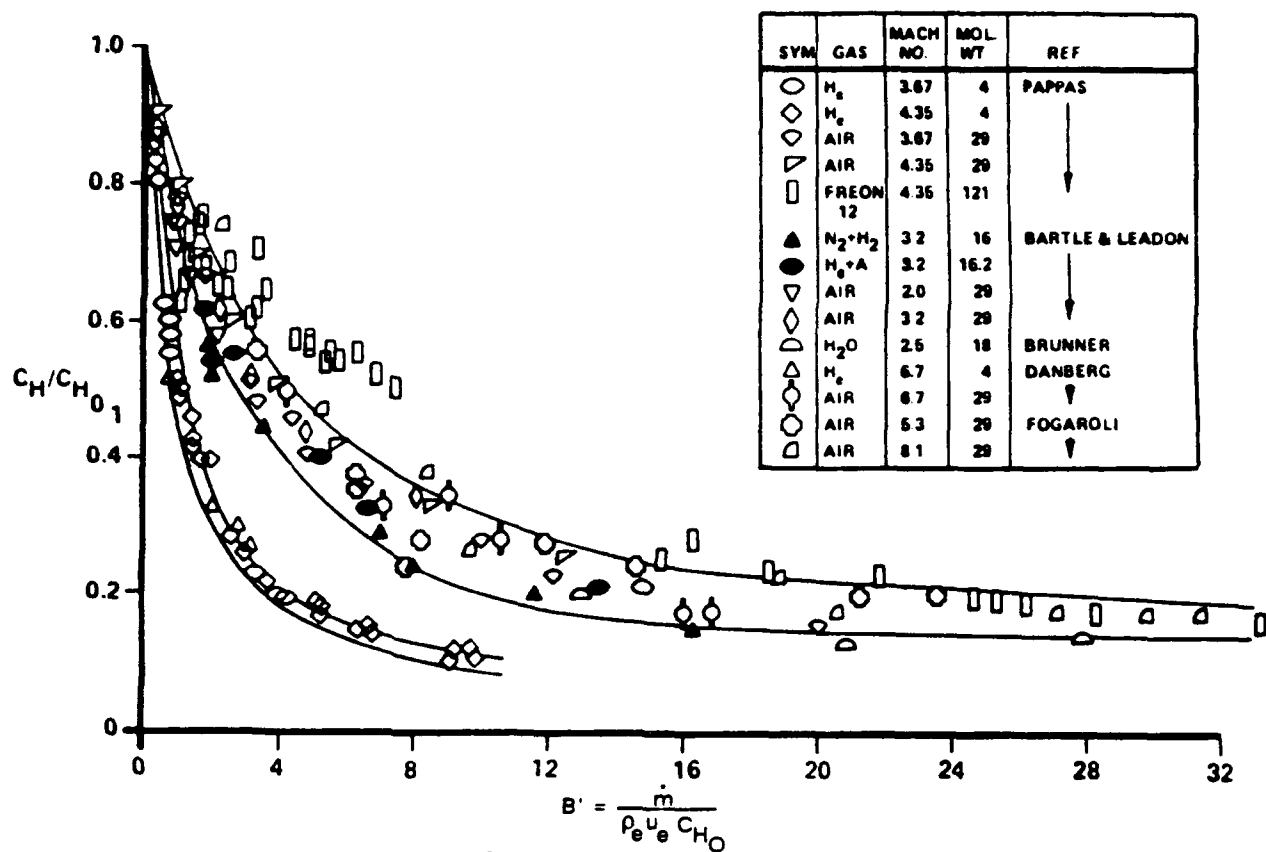


Figure 1 SUMMARY OF BLOCKAGE HEATING FROM EARLIER STUDIES ON FLAT PLATES AND CONES IN TURBULENT FLOW (HOLDEN REF. 1)

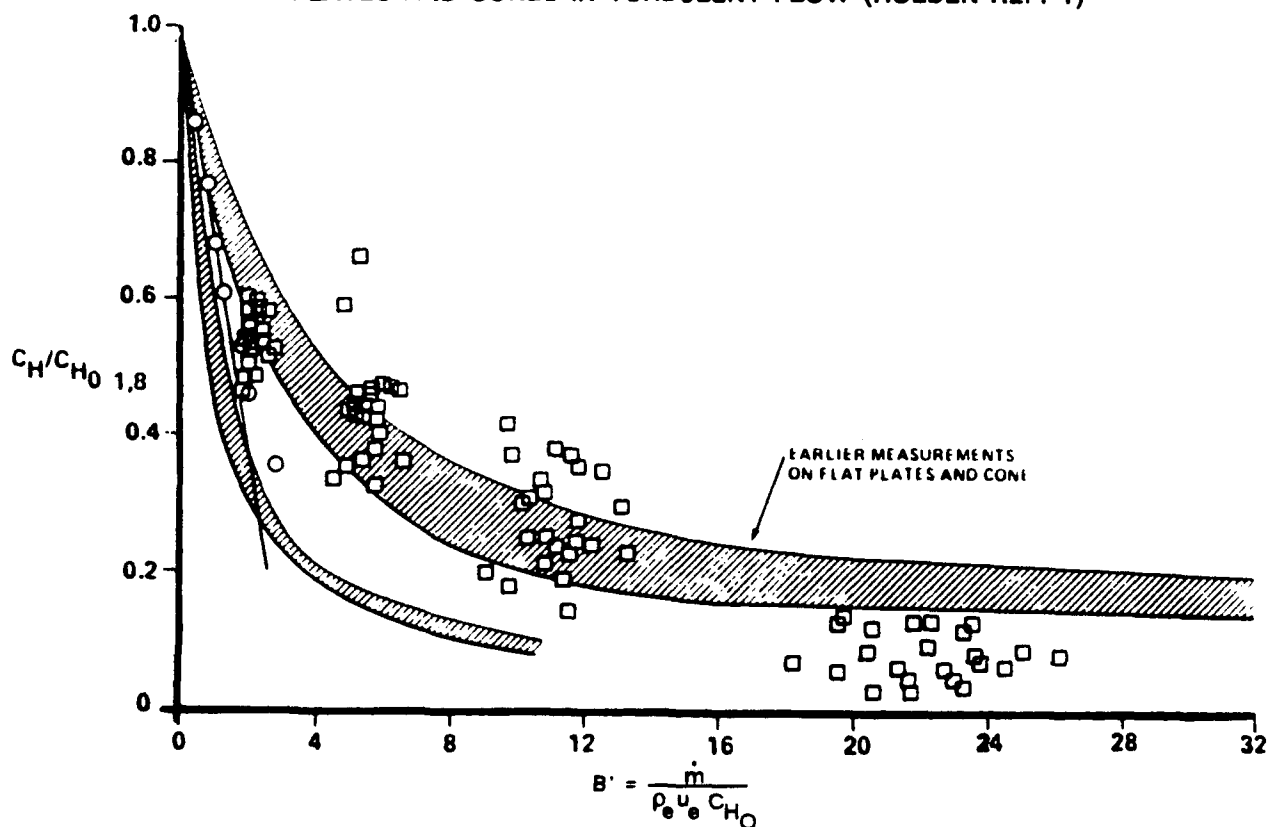


Figure 2 COMPARISON BETWEEN THE MEASUREMENT MADE IN THE NOSETIP STUDIES WITH NITROGEN INJECTANT AND THE EARLIER BLOCKAGE DATA (HOLDEN REF. 1)



Figure 3 SLENDER CONE MODEL (WITH SHARP NOSETIP) SHOWN INSTALLED IN 96-INCH SHOCK TUNNEL (D NOZZLE REMOVED)

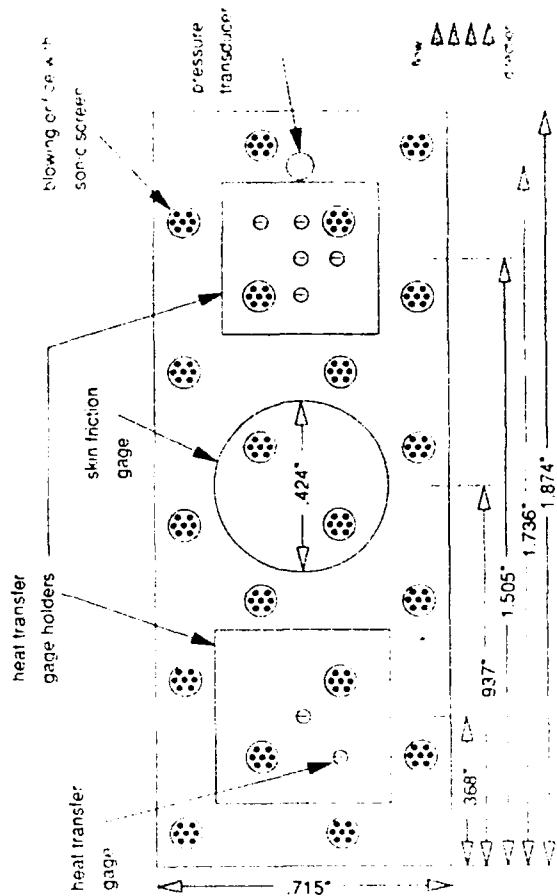


Figure 5 LAYOUT OF A TYPICAL INSTRUMENTATION INSERT

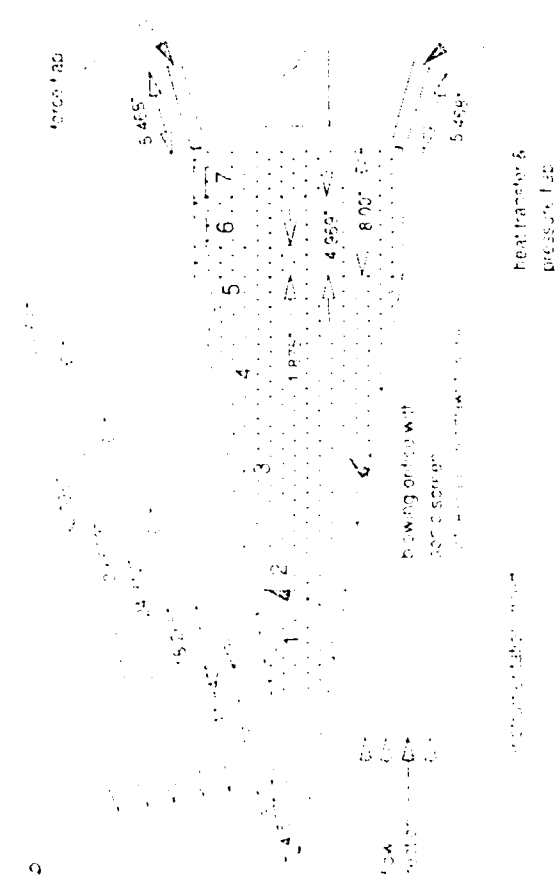
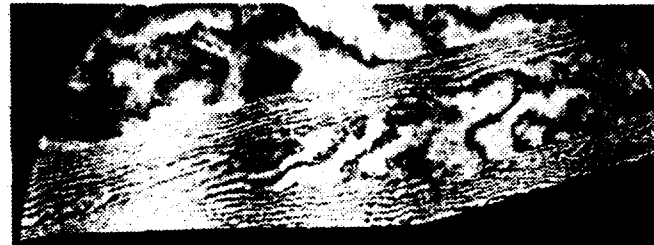


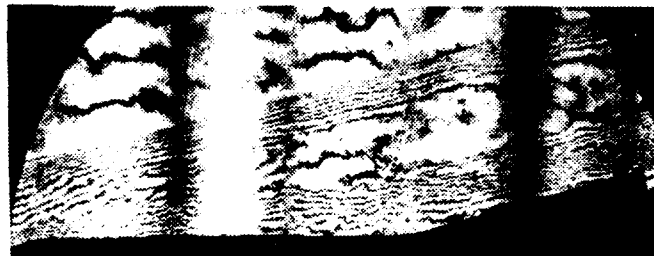
Figure 4 SCHEMATIC DIAGRAM OF 10.5 DEGREE CONE MODEL SHOWING BLOWING CONFIGURATION AND POSITIONS OF INSTRUMENTATION INSERTS



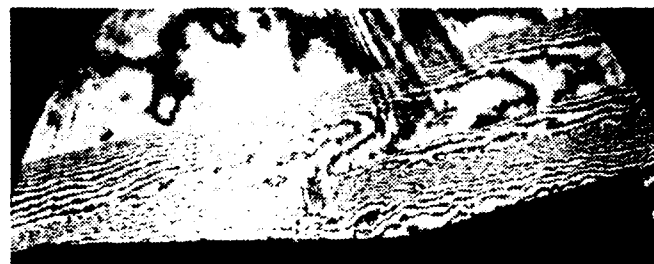
a. RUN 11 $\lambda_e = 0$



b. RUN 12 $\lambda_e = 3.11 \times 10^{-4}$



c. RUN 7 $\lambda_e = 3.58 \times 10^{-4}$



d. RUN 8 $\lambda_e = 5.50 \times 10^{-4}$



e. RUN 9 $\lambda_e = 14.8 \times 10^{-4}$

Figure 6 HOLOGRAPHIC INTERFEROMETRY PHOTOGRAPHS FOR NITROGEN INJECTION AT MACH 11 CONDITION

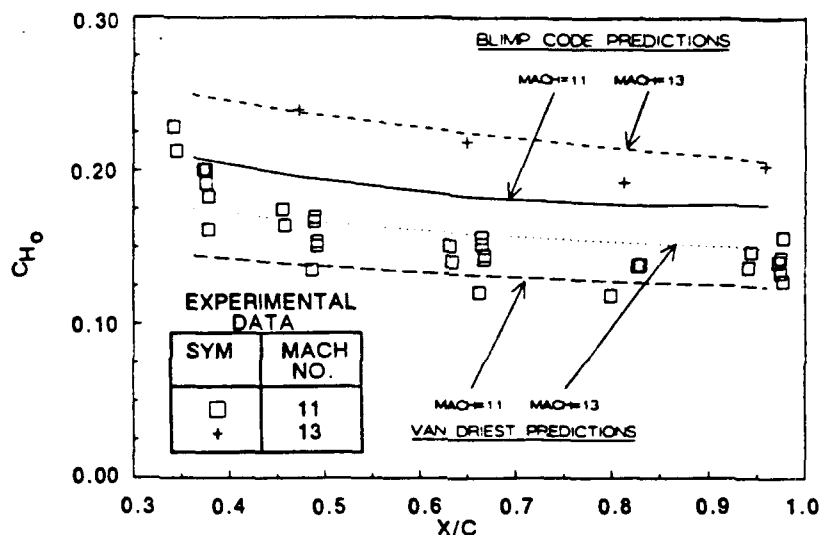


Figure 7 COMPARISON BETWEEN PREDICTIONS AND HEAT TRANSFER MEASUREMENTS FOR MATCHED PRESSURE (SMOOTH, NO BLOWING) CONDITIONS

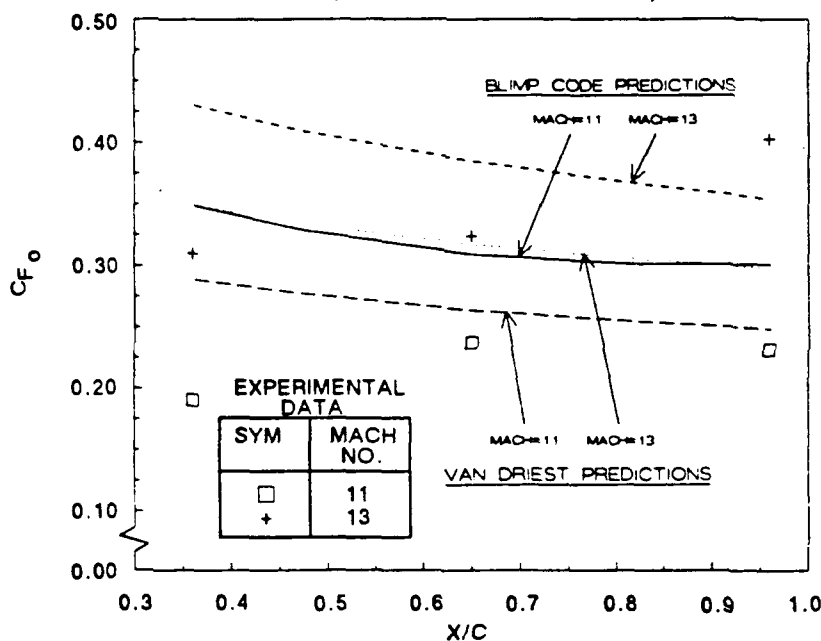


Figure 8 COMPARISON BETWEEN PREDICTIONS AND SKIN FRICTION MEASUREMENTS FOR MATCHED PRESSURE (SMOOTH, NO BLOWING) CONDITIONS

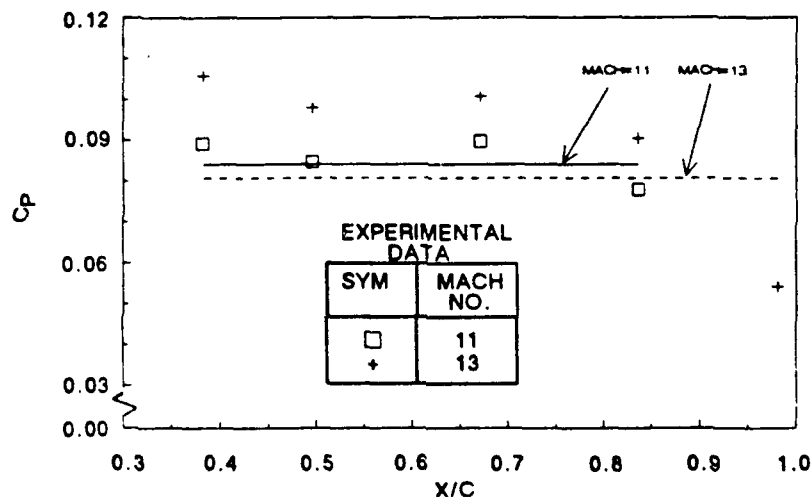


Figure 9 COMPARISON BETWEEN PRESSURE MEASUREMENTS AND INVISCID THEORY

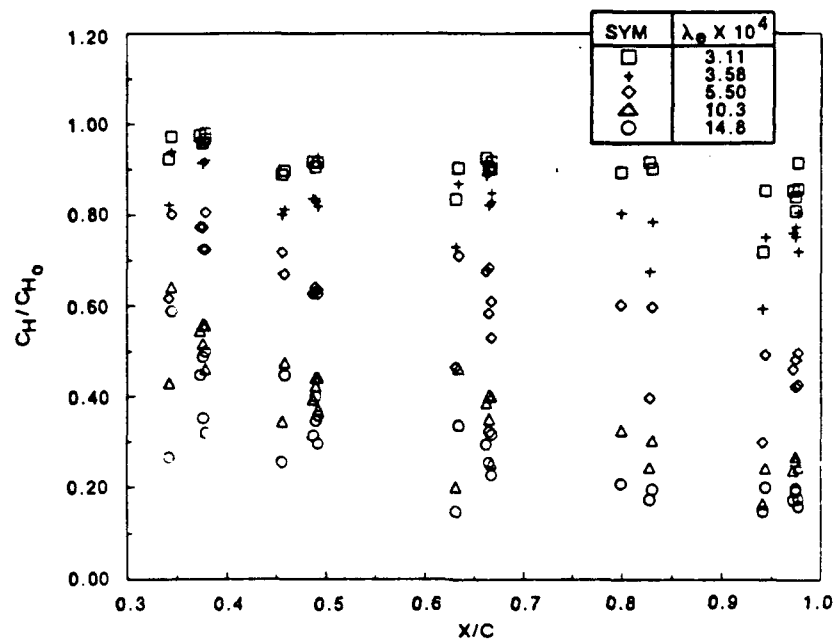


Figure 10a VARIATION OF HEAT TRANSFER ALONG THE CONE WITH NITROGEN INJECTION
(MACH 11, $RE/FT = 10 \times 10^6$)

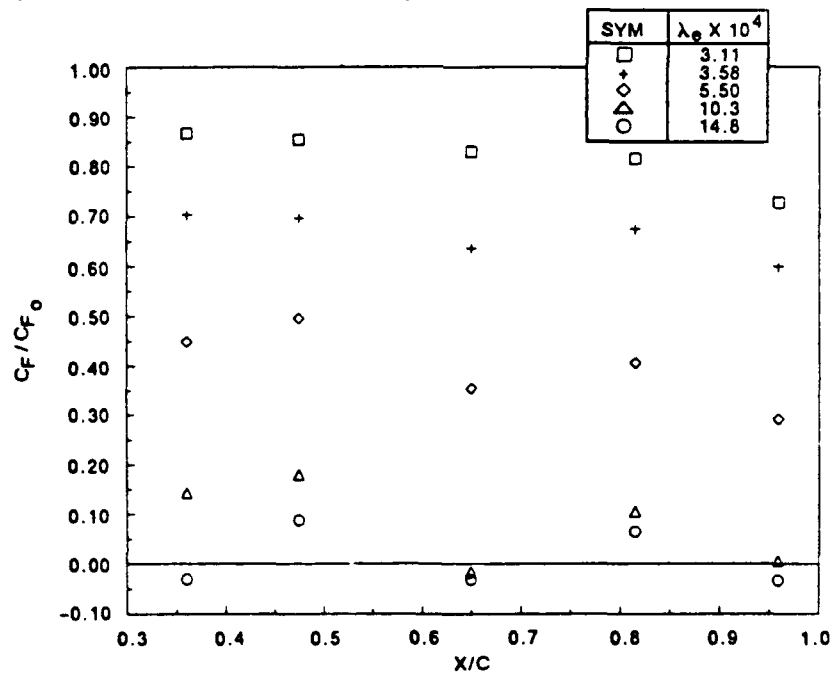


Figure 10b VARIATION OF SKIN FRICTION ALONG THE CONE WITH NITROGEN INJECTION
(MACH 11, $RE/FT = 10 \times 10^6$)

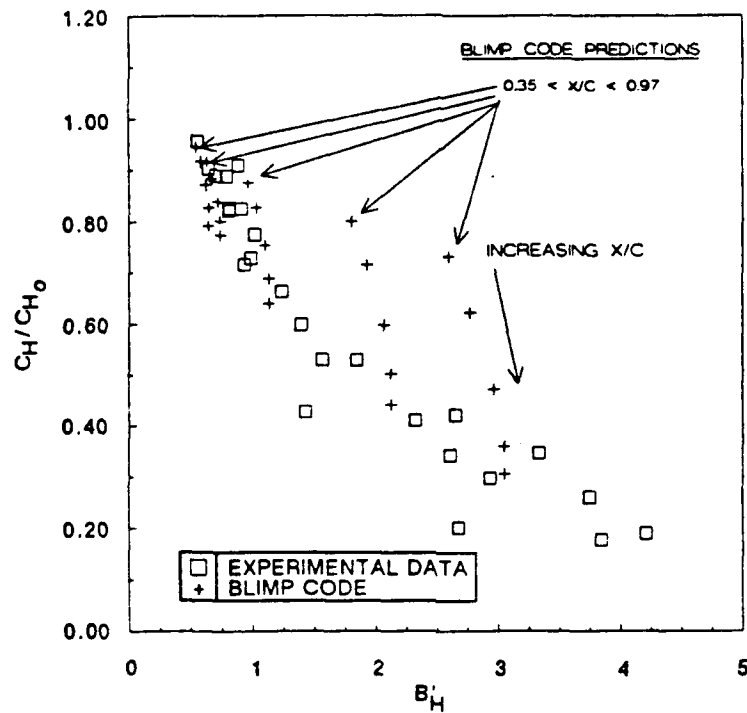


Figure 11a VARIATION OF HEAT TRANSFER WITH BLOWING PARAMETER B'_H AT MACH 11 FOR NITROGEN INJECTION

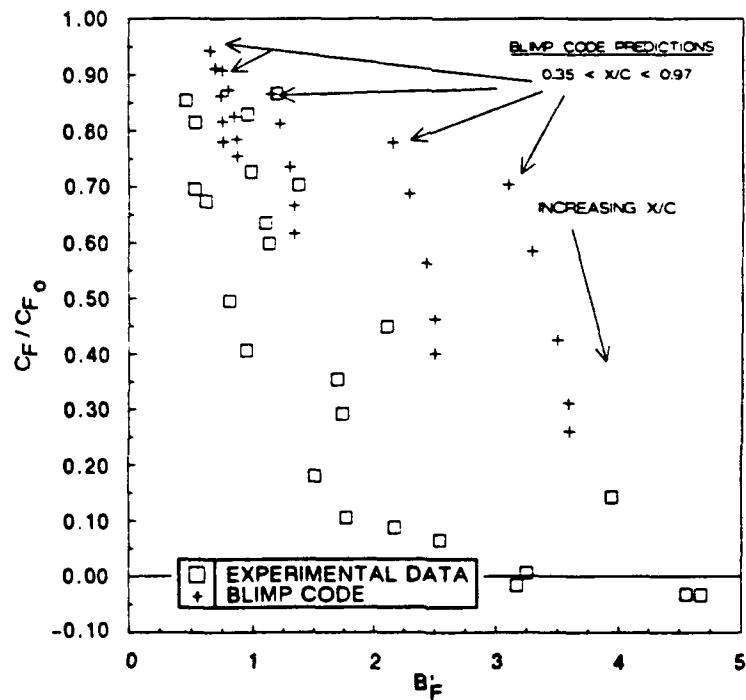


Figure 11b VARIATION OF SKIN FRICTION WITH BLOWING PARAMETER B'_F AT MACH 11 FOR NITROGEN INJECTION

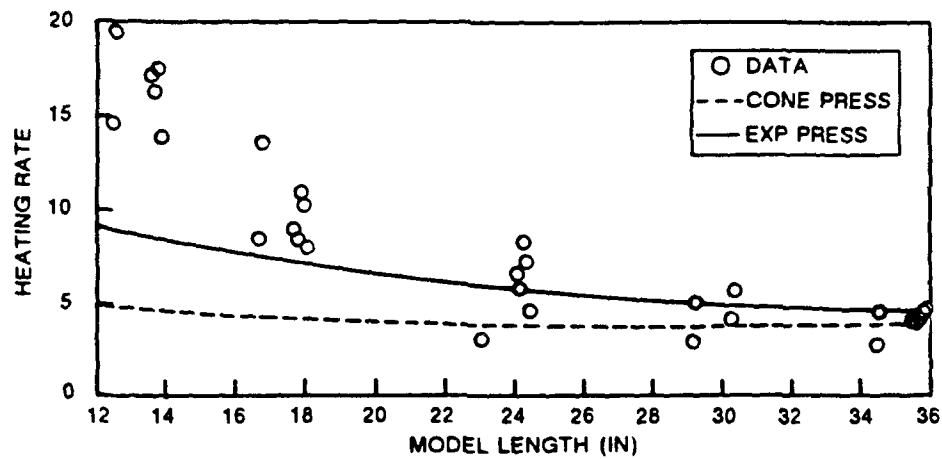


Figure 12 BLIMP COMPARISONS, SMOOTH BLOWING 0.53%

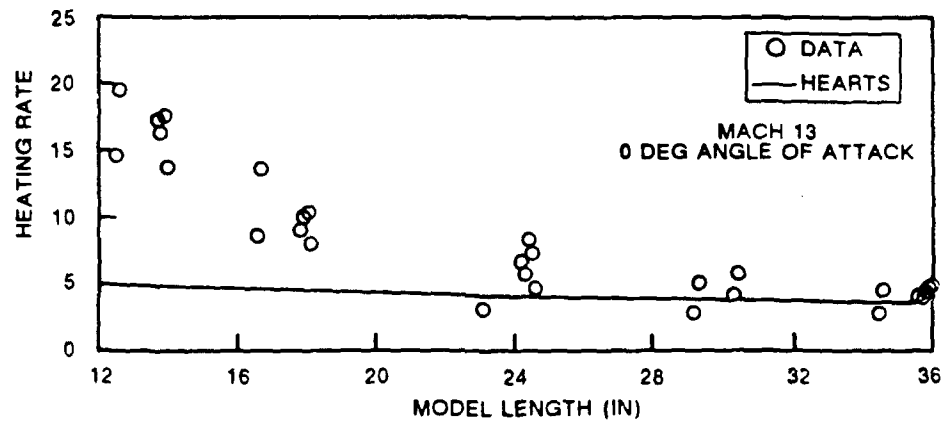


Figure 13a SMOOTH BLOWING DATA, BLOWING RATE = 0.53% FREE STREAM

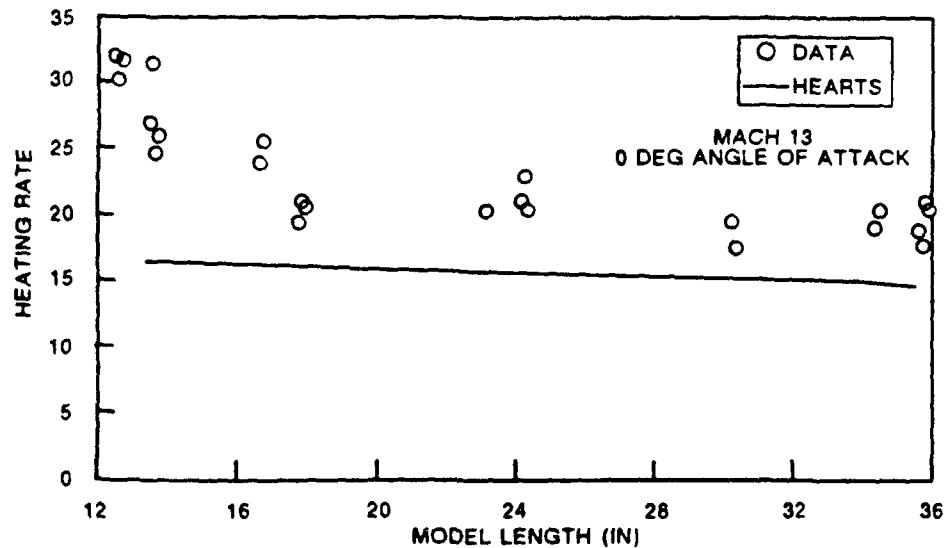


Figure 13b SMOOTH BLOWING DATA, BLOWING RATE = 0.09% FREE STREAM

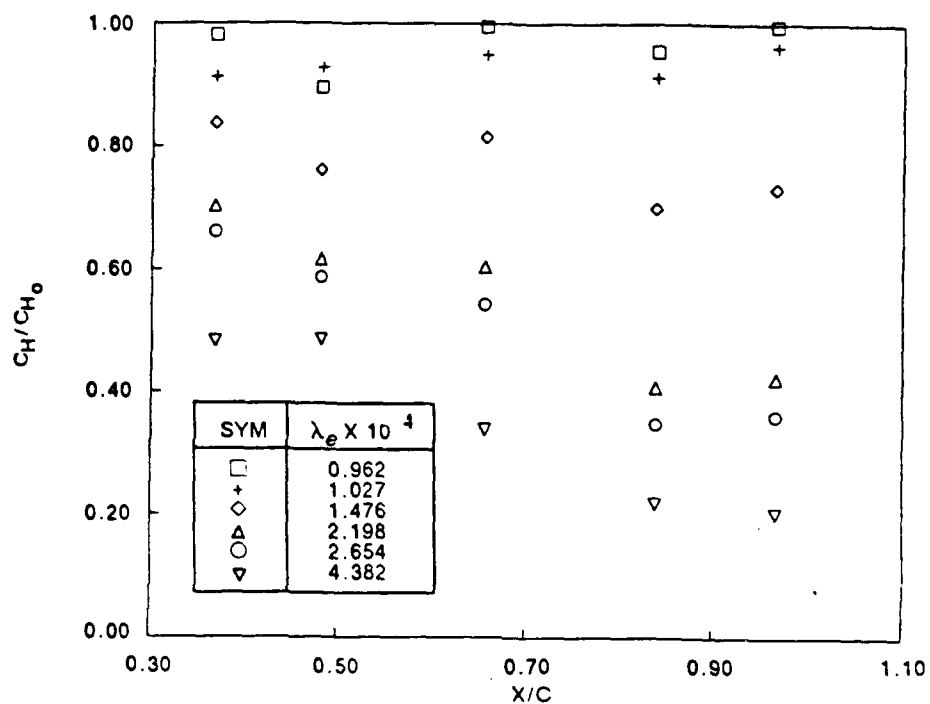


Figure 14a VARIATION OF HEAT TRANSFER MEASUREMENTS WITH BLOWING PARAMETER FOR HELIUM INJECTION

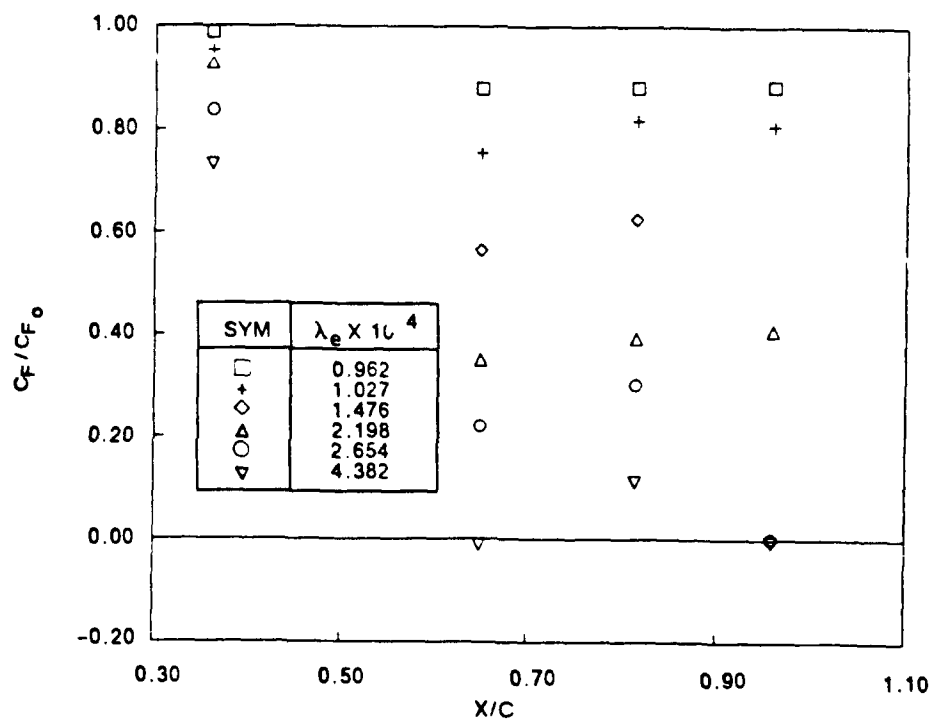


Figure 14b VARIATION OF SKIN FRICTION MEASUREMENTS WITH BLOWING PARAMETER FOR HELIUM INJECTION

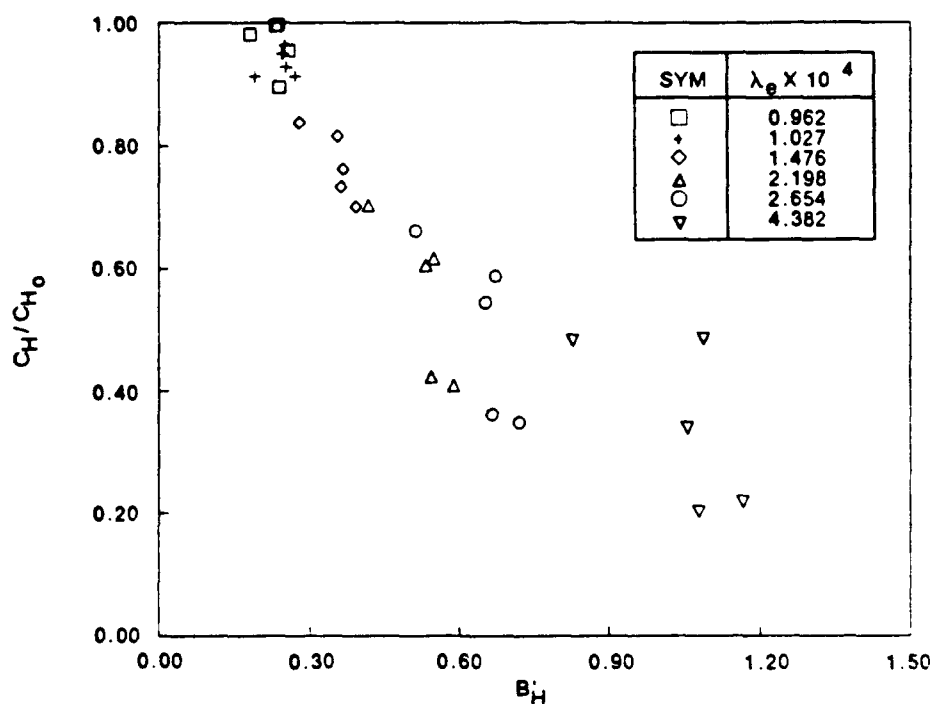


Figure 15a CORRELATION OF HEAT TRANSFER MEASUREMENTS WITH BLOWING PARAMETER FOR HELIUM INJECTION

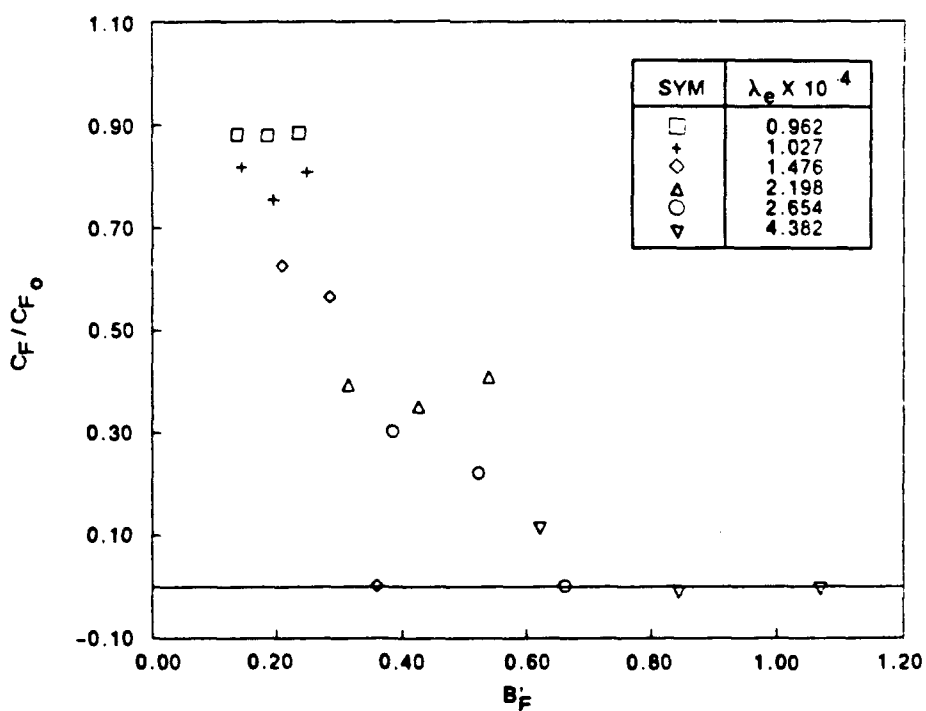


Figure 15b CORRELATION OF SKIN FRICTION MEASUREMENTS WITH BLOWING PARAMETER FOR HELIUM INJECTION

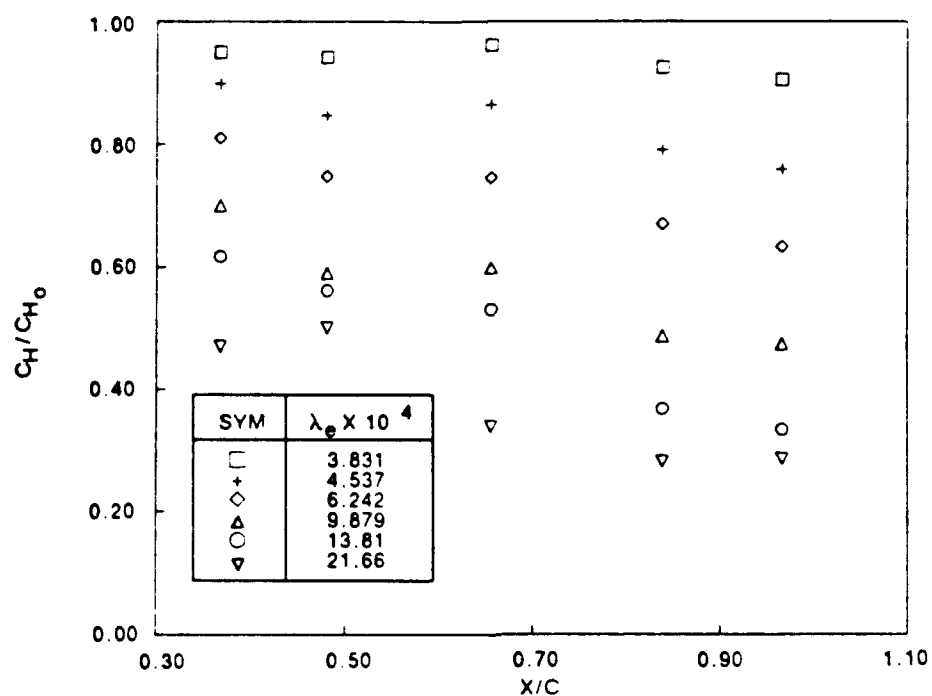


Figure 16a VARIATION OF HEAT TRANSFER MEASUREMENTS FOR FREON INJECTION

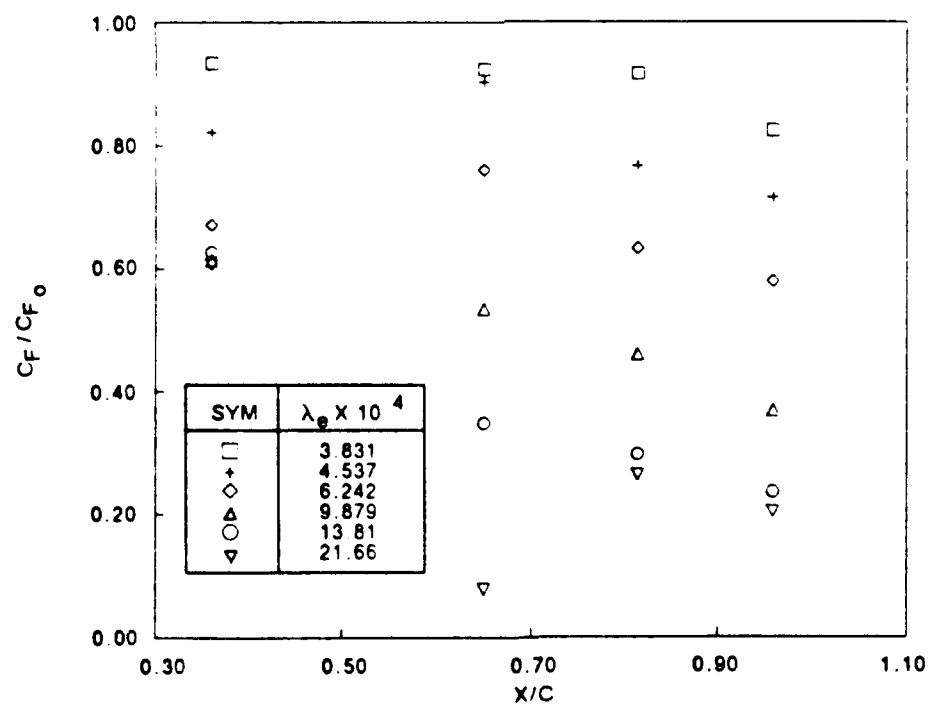


Figure 16b VARIATION OF SKIN FRICTION MEASUREMENTS FOR FREON INJECTION

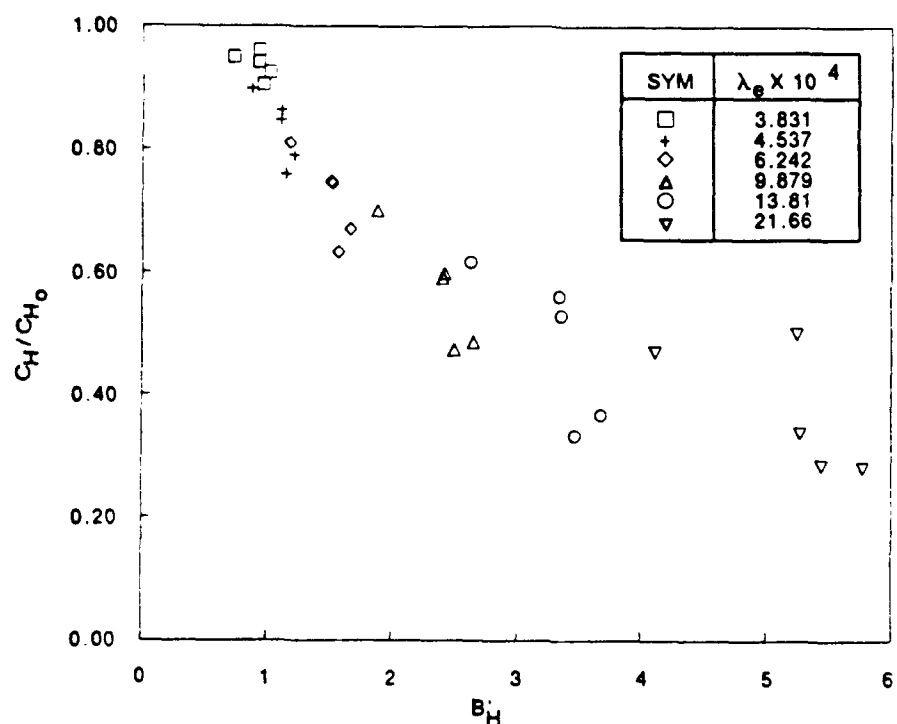


Figure 17a VARIATION OF HEAT TRANSFER WITH BLOWING PARAMETER B'_H FOR FREON INJECTANT

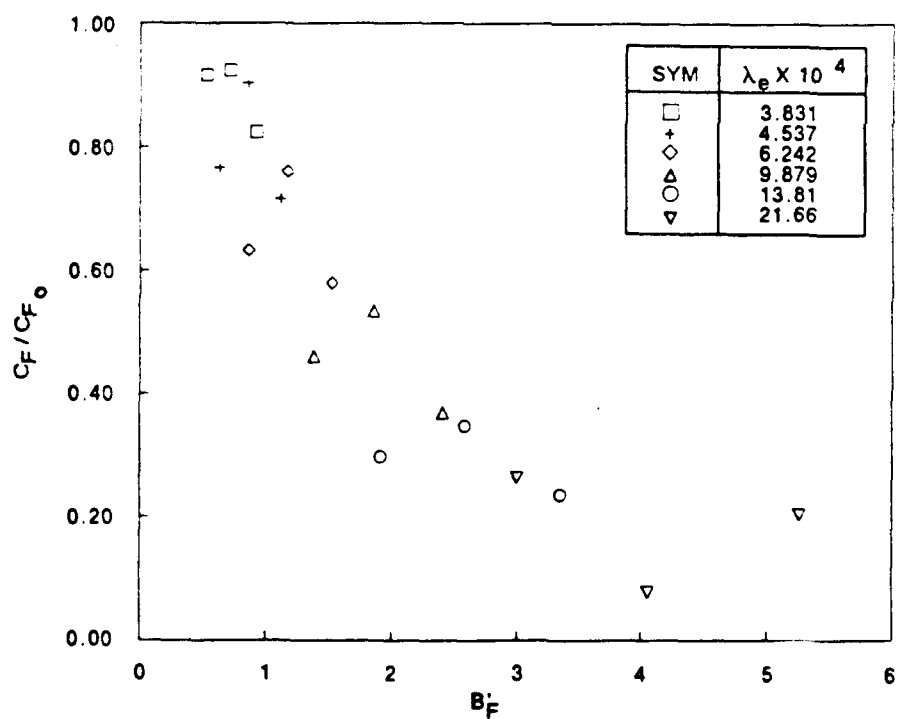


Figure 17b VARIATION OF SKIN FRICTION WITH BLOWING PARAMETER B'_F FOR FREON INJECTANT

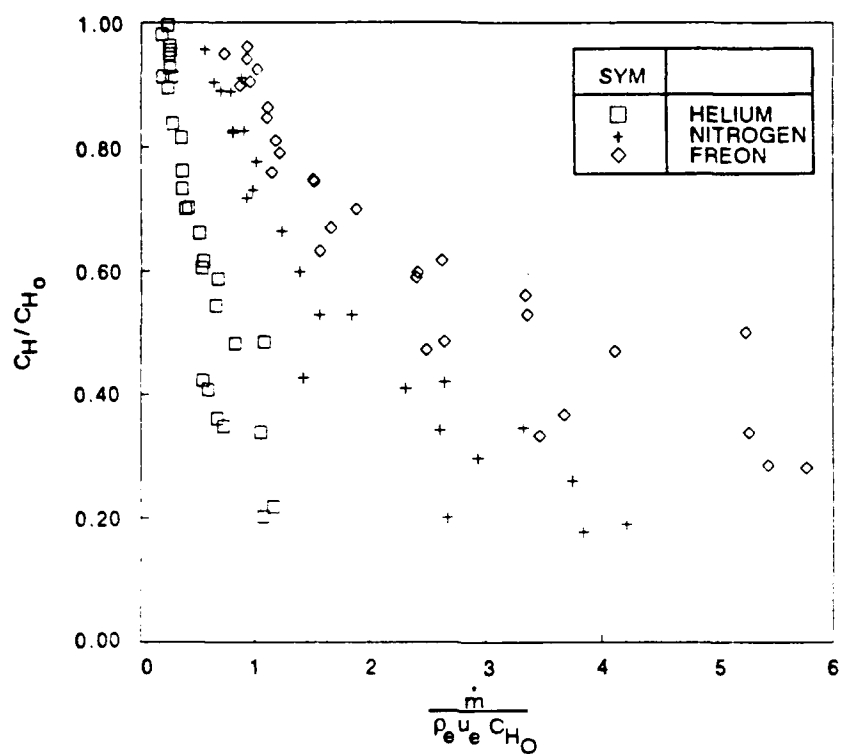


Figure 18a VARIATION OF HEAT TRANSFER WITH BLOWING PARAMETER B'_H FOR VARIOUS INJECTANTS

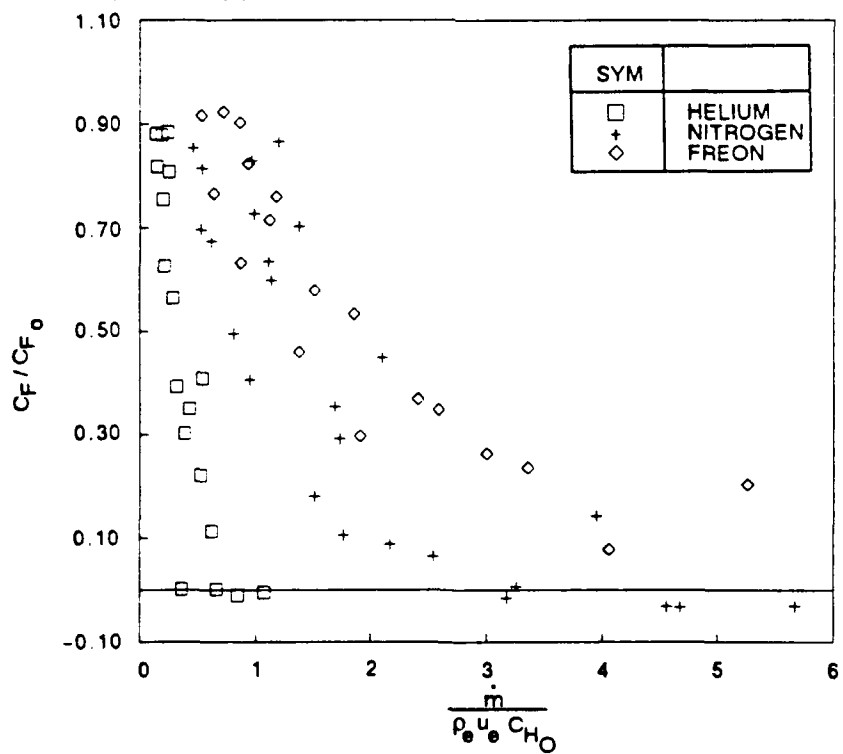


Figure 18b VARIATION OF SKIN FRICTION WITH BLOWING PARAMETER B'_F FOR VARIOUS INJECTANTS

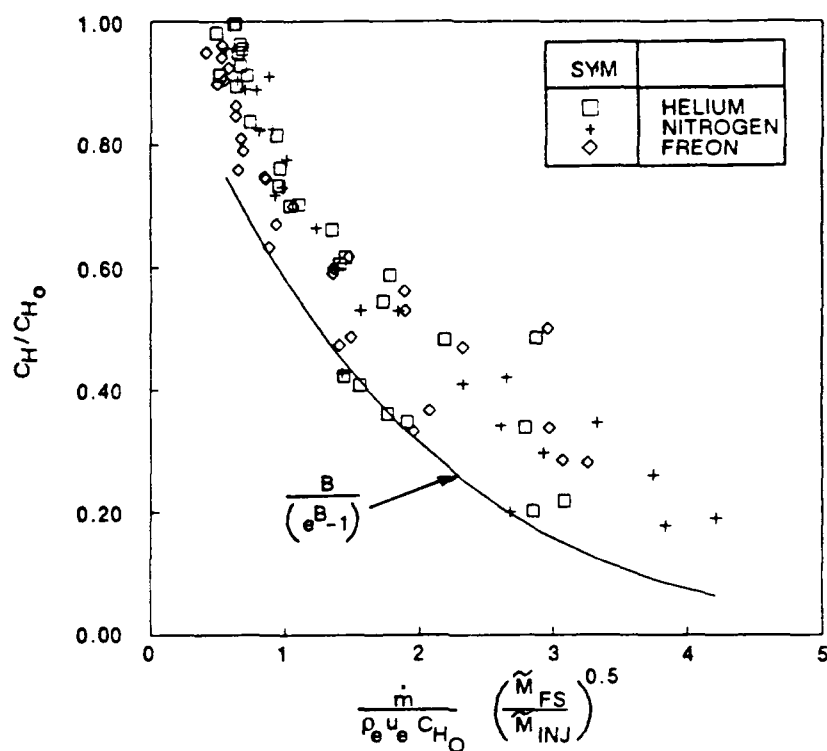


Figure 19a VARIATION OF HEAT TRANSFER WITH MODIFIED BLOWING PARAMETER B'_{MM} FOR VARIOUS INJECTANTS

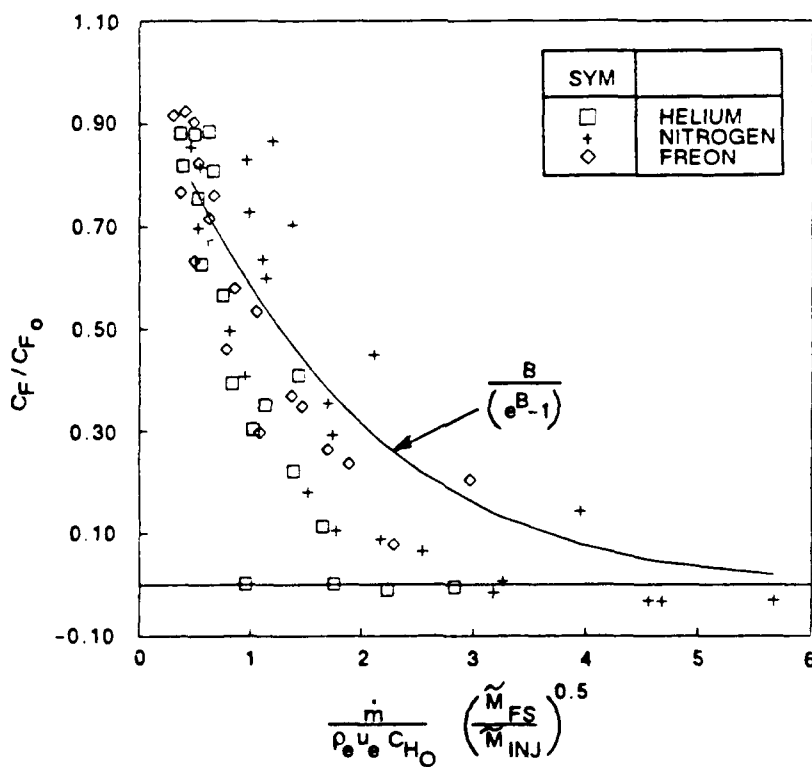


Figure 19b VARIATION OF SKIN FRICTION WITH MODIFIED BLOWING PARAMETER B'_{MM} FOR VARIOUS INJECTANTS

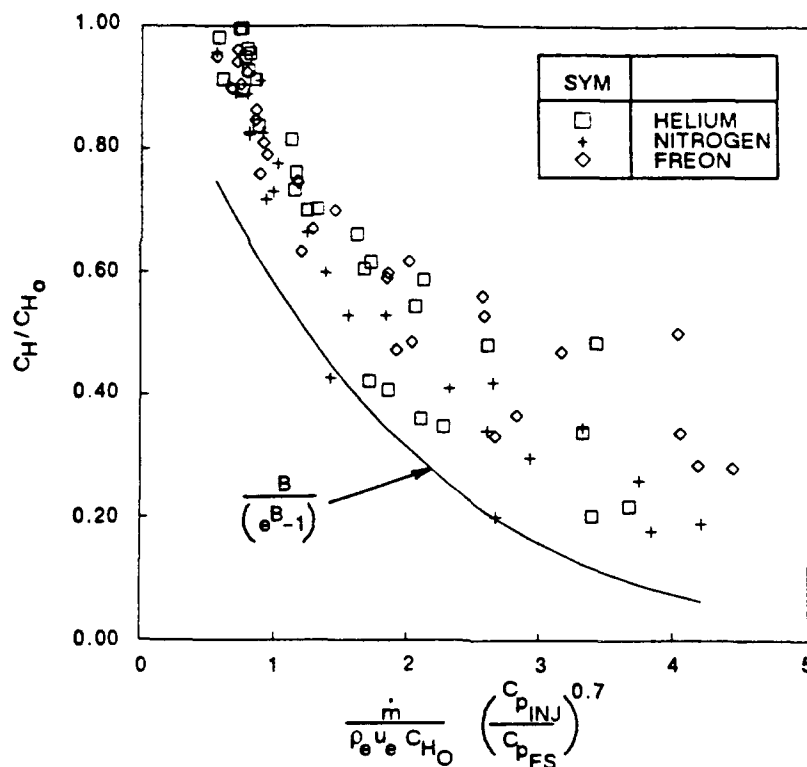


Figure 20a VARIATION OF HEAT TRANSFER WITH MODIFIED BLOWING PARAMETER B'_{MC} FOR VARIOUS INJECTANTS

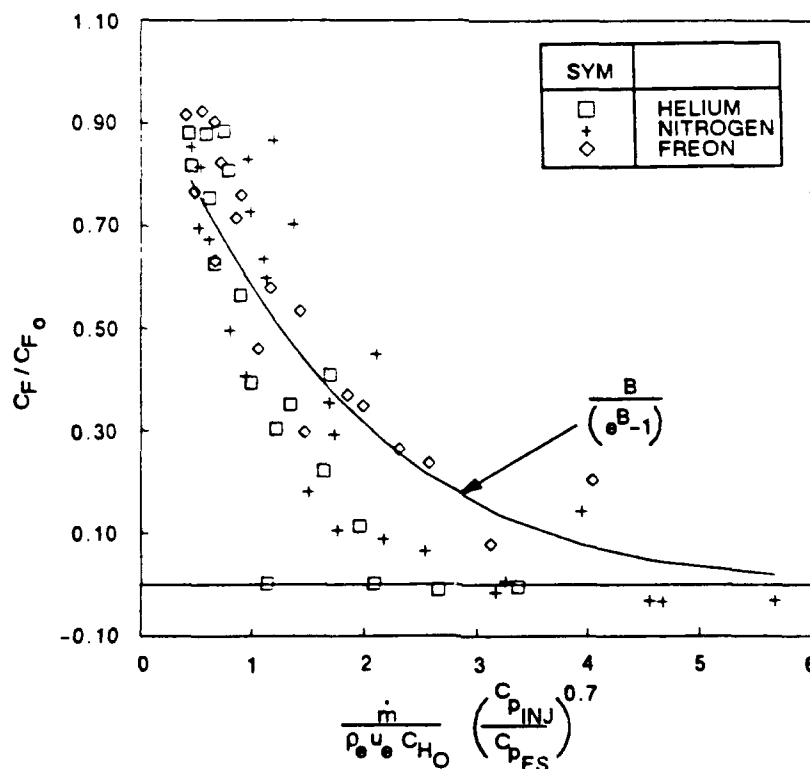


Figure 20b VARIATION OF SKIN FRICTION WITH MODIFIED BLOWING PARAMETER B'_{MC} FOR VARIOUS INJECTANTS

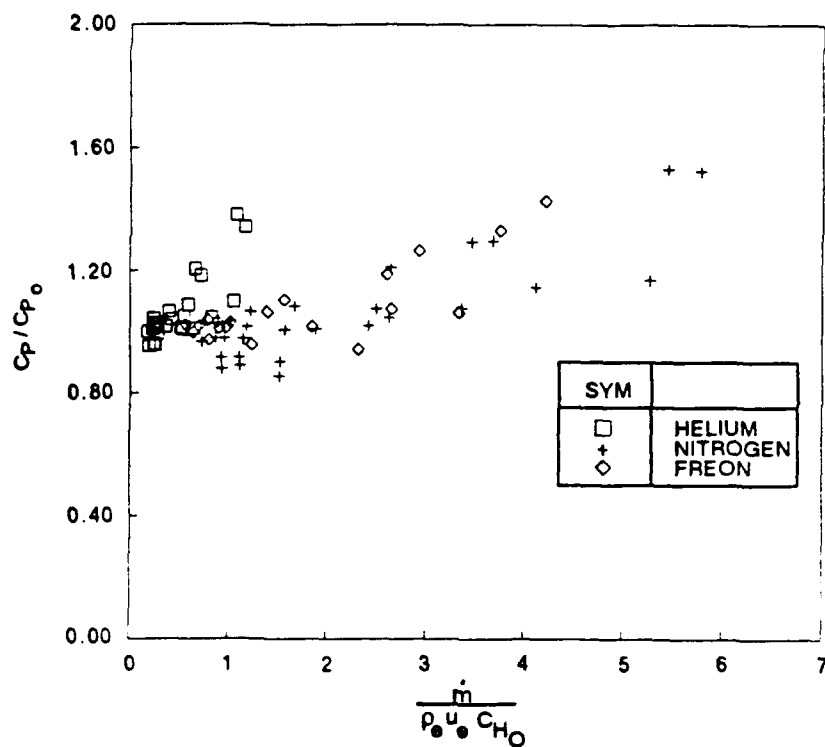


Figure 21a VARIATION OF CONE PRESSURE WITH BLOWING PARAMETER

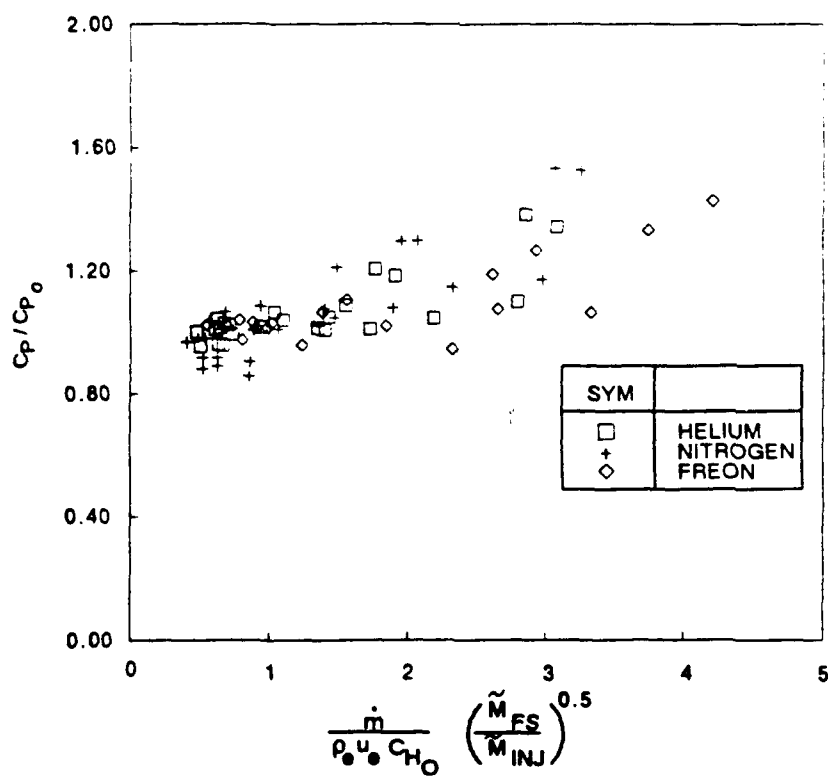


Figure 21b VARIATION OF CONE PRESSURE WITH MODIFIED BLOWING PARAMETER

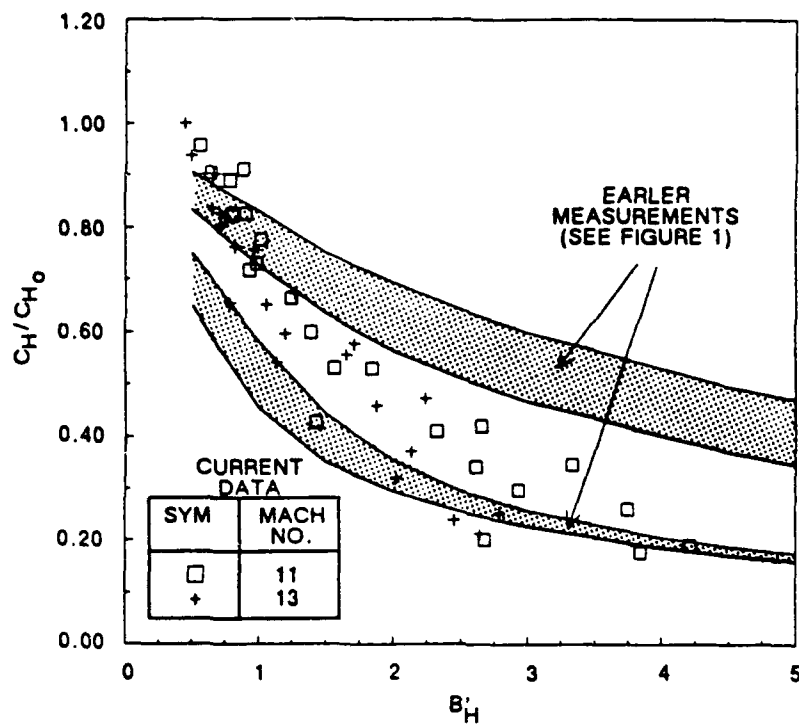


Figure 22 COMPARISON OF CURRENT MEASUREMENTS WITH EARLIER MEASUREMENTS ON CONE AND FLAT PLATES

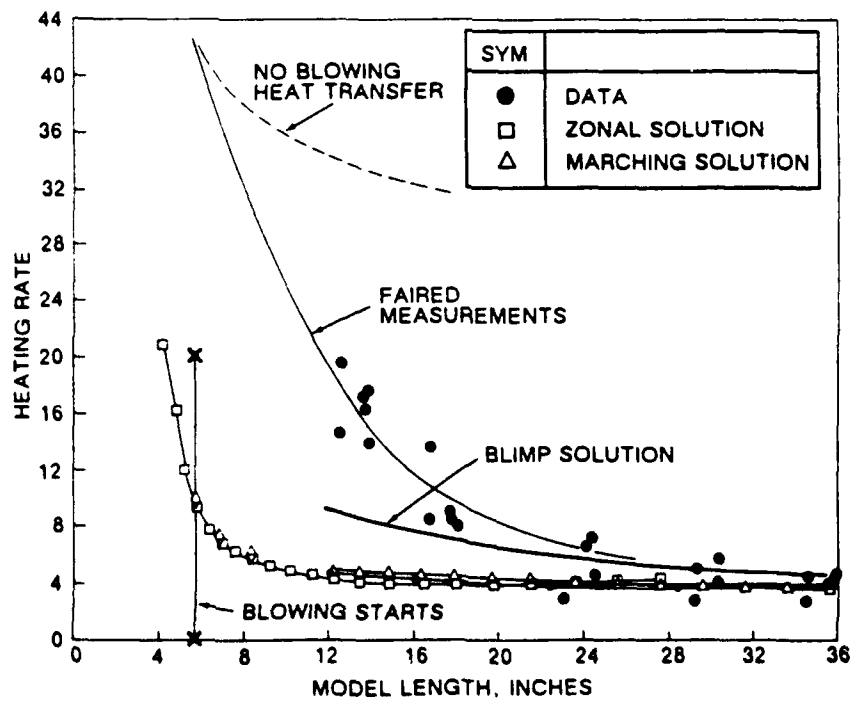


Figure 23 COMPARISON BETWEEN HEARTS CODE COMPUTATION AND MEASUREMENTS AT MACH 11

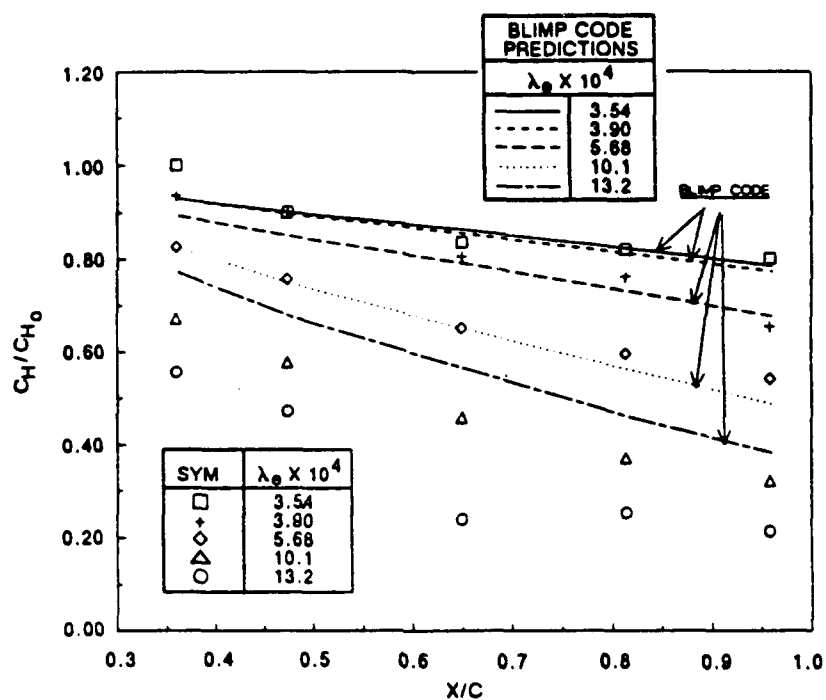


Figure 24a COMPARISON BETWEEN HEAT TRANSFER MEASUREMENTS AND BLIMP CODE CALCULATIONS (MACH 13, $RE/FT = 5 \times 10^6$)

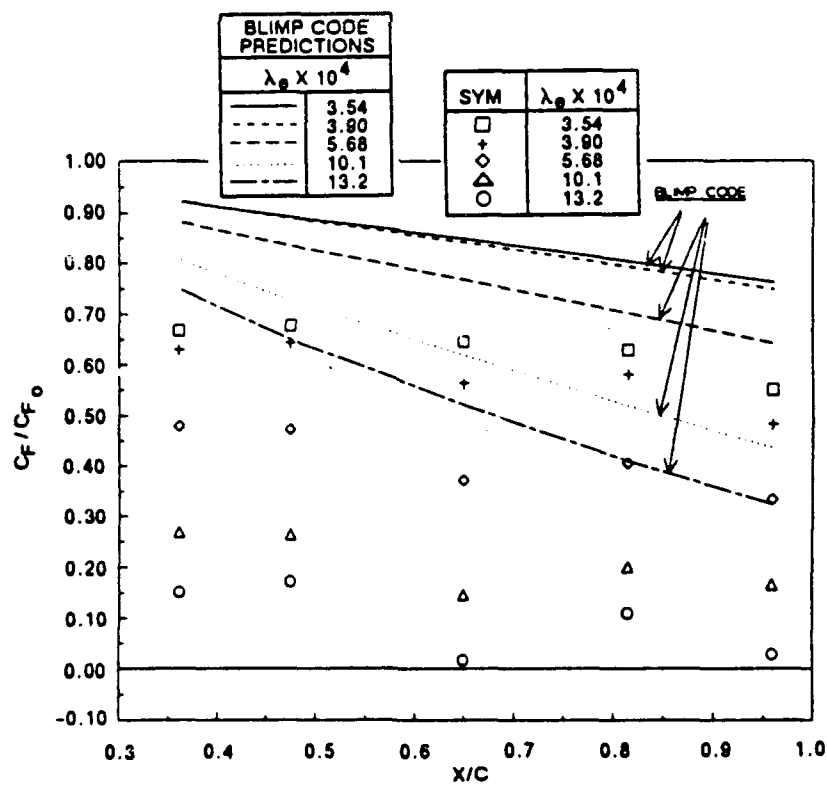


Figure 24b COMPARISON BETWEEN SKIN FRICTION MEASUREMENTS AND BLIMP CODE CALCULATIONS (MACH 13, $RE/FT = 5 \times 10^6$)

APPENDIX 4

**AN EXPERIMENTAL STUDY OF HYPERSONIC TURBULENCE
ON A SHARP CONE**



AIAA-89-1866

**An Experimental Study of Hypersonic
Turbulence on a Sharp Cone**

J. Harvey

Imperial College, London, England

and

R.C. Bergman & M.S. Holden

Calspan Corporation, Buffalo, NY

**AIAA 20th Fluid Dynamics, Plasma Dynamics
and Lasers Conference**

Buffalo, New York / June 12-14, 1989

AN EXPERIMENTAL STUDY OF HYPERSONIC TURBULENCE ON A SHARP CONE

J. Harvey
Imperial College, London, England

R.C. Bergman & M.S. Holden, Calspan Corporation
Buffalo, New York

ABSTRACT

A preliminary experimental study has been conducted in which an electron beam, and pitot and total temperature probes were used to measure the mean and fluctuating density, and mean static temperature across a Mach 7.5 turbulent boundary layer over a 4-ft long 6° sharp cone. The experimental studies were conducted in the Calspan 96" Tunnel at a free stream Mach number of 8.5 and unit Reynolds number of 5×10^6 . Our initial use of this technique has demonstrated a potential to obtain fluctuation measurements up to frequencies approaching 1 MHz. Additional improvement is expected when more advanced optics are used. The mean rotational temperature through the boundary layer can be determined from spectra obtained using an Optical Multichannel Analyzer. The electron gun has proven highly reliable and has the potential to work at equivalent densities up to over 100 torr. Further developments are anticipated employing an electron beam to stimulate a gas which is examined using a resonant laser technique.

INTRODUCTION

Powerful numerical techniques based on the Navier-Stokes equations are available for the prediction of hypersonic viscous flows. Providing these flows are laminar the accuracy of the results of the computations is impressive (Rudy et al (1989)). However if the hypersonic boundary layers or shear layers are turbulent, agreement with measured data is often unsatisfactory as a result of serious shortcomings in the time-averaged models used to represent the turbulence. The structure of turbulent boundary layers hypersonic speeds is poorly understood. This in part results from the paucity of measurements to define the fluctuatory characteristics of the turbulence which is in turn related to the severe difficulties in developing suitable instrumentation to make accurate measurements in high Mach number flows. However without a better physical understanding of the characteristics of the time dependent properties of these flows, the validity of turbulence models cannot be meaningfully evaluated.

Most models of turbulence used to describe compressible flows have been derived from concepts developed from low Mach number or other incompressible flows where fluctuations in thermodynamic quantities (density, temperature, etc.) are small enough to be neglected. As the Mach number increases these fluctuations become more important and at hypersonic speeds, they can be the most significant varying quantities. Furthermore, in many important flows there are features which pose difficulties in modeling. For example, in regions shock/boundary layer interactions, which are regions of intense heating. The way in which the turbulence responds to the rapid changes in flow conditions presently poorly understood.

To develop improved models of transition and turbulence in hypersonic flow, new experimental techniques are needed to provide basic insight into the

physics of the flows. Because of the high velocities and small physical scales of the turbulent boundary layers that can be generated in practical test facilities, measuring techniques have to be extremely fast-responding to resolve even the large scale eddies. Probes using solid sensors, such as hot wire or hot fiber anemometers, are unsuitable. Techniques in which the gas itself is excited so that its properties can be directly monitored appear to be the most viable options. Methods using electron beams or lasers to induce fluorescence (EBFT and LIF, respectively) are the two most promising techniques presently under review. Combinations of the two have also been proposed (see for example Caltolica, et al (1989)). With these techniques a beam of either electrons or photons is passed through the gas to produce fluorescence which can be observed optically (see Figure 1). Providing that the detectors can respond quickly enough, fluctuations in the density or even temperature could be resolved up to frequencies in excess of 1 MHz. The latter measurement requires a complex optical detector as the spectrum of the emitted light has to be resolved. Both EBFT and LIF have the added attraction of being non-intrusive. However, they need special equipment which in the case of LIF can be expensive, and relatively undeveloped.

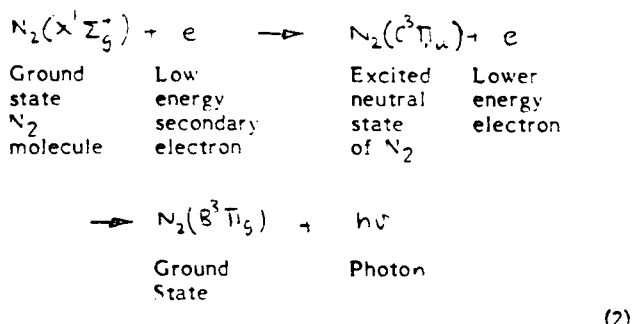
The maximum frequency of the fluctuations that can be resolved is limited by the size of the region of fluorescing gas from which light is gathered and by the speed at which the detectors can respond. In the case of the former, the dimensions are likely to be of the order of one millimeter or less and at hypersonic speeds fluctuations move through this space in less than 1 usec. The limitation is thus set by the detectors. This problem is common to both EBFT and LIF methods. Using available techniques, frequencies of the order of 100 KHz to 1 MHz can be resolved provided that the fluorescence intensities and the light gathering properties of the optics are sufficient for Shott noise difficulties to be avoided. This noise arises if the frequency of the arrival of individual photons at the detector is not considerably higher than that of the phenomenon being observed.

The Electron Beam Fluorescence Technique

EBFT is a well-established method for investigating rarefied hypersonic flowfields where the number density, n , is less than about $10^{16}/\text{cc}$ (0.5 torr room temperature equivalent pressure); see, for example, Davis & Harvey (1976). Excellent review papers by Muntz (1968) and Butterfisch and Vennemann (1974) describe and analyze the technique in detail and provide references to most, if not all, of the investigations using it up to their respective dates of writing. Earlier studies in which EBFT was applied to less rarefied and, in several cases, turbulent flows include Boyer and Muntz (1967), Dionne, Sadowski and Tradif (1967), Cama (1967), Wallace (1968) whose data was subsequently analyzed by Harvey, et al (1969), Smith and Driscoll (1975), McDonald (1975), Harvey and Hunter (1975), Bartlett (1980) and Lin and Harvey (1987). These references contain a wealth of useful information on the application of the technique to aerodynamic problems.

For nitrogen the excitation-emission mechanisms are well understood over the range of densities of interest for hypersonic aerodynamics ($n = 10^5$ to $10^{20}/\text{cc}$). Molecular nitrogen exhibits significant emissions from two band systems in the pressure range of interest. At low pressures, typically less than one torr, the N_2^+ 1st negative system (1-) is predominant but at higher pressures the N_2 2nd positive (2+) system becomes increasingly more intense. The excitation-emission mechanism for the two systems is different.

The N_2^+ (1-) system is excited chiefly by direct inelastic collisions with primary beam electrons (20-50 kV), with a small contribution from scattered electrons with sufficient energy. In contrast, the N_2 (2+) system is excited by low energy secondary electrons which result from inelastic collisions between primary electrons and gas molecules. The N_2 (2+) system becomes increasingly more important at pressures above 1 torr and dominates the total emission at higher pressures. The excitation mechanism of the N_2 (2+) system does not require ionization as the upper transition level involving the neutral molecule lies well below the N_2 ionization level. The excitation of the N_2 (2+) system can be written:



This excitation process has a small cross-section for the high energy primary electronics but has a large cross-section for the secondaries formed from the primary-ambient gas molecule collisions. The optimum accelerating voltage has been found experimentally to be approximately 50 kV for secondary production. 50 kV also provides good penetration of the beam through a relatively dense gas. The secondary electron excitation mechanism should produce a quadratic dependence of intensity on number density as the cross-section also includes a number density term. The observed pressure dependence does in fact show a quadratic relationship up to 2 to 3 torr (at room temperature), then a roughly linear dependence at higher pressures. This is due to a quenching effect wherein the upper energy levels of the higher vibrational states are partially depopulated through non-radiative transfer to the lower energy levels, whilst the lower vibrational levels such as the (0,0) and the (0,1) bands are found to experience a cascading vibrational collision mechanism which populates the excited states. This cascade process is believed to be a major factor in the continued linear growth of the (0,0) band intensity with increasing pressure whereas the higher vibrational bands exhibit significant quenching.

Using the 50 kV electron gun, shortly to be described, calibrations of intensity against density were obtained using a small test chamber filled with pure nitrogen. A result is shown in Figure 2 where the density is expressed as equivalent room temperature (20°C) pressure. The approach towards a linear behavior as the density increases can be seen. It should be noted that the level of density for which calibrations have been

achieved is about 180 torr (0.3 kg/m³). Significant attenuation of the electron beam occurs at these densities but sufficient penetration of 50 keV particles is achieved for the technique to be viable for wind tunnel studies where boundary layers are typically 1 cm or less thick. Corrections, to account for the reduction in beam current of the form

$$i(y) = i(y=0) e^{-KQ}$$

where $Q = \int_0^y \rho(y) dy$ and $K = \text{const}$

suggested by Smith and Driscott (1977) are assumed.

The Shock Tunnel Experiment

The experiment in which the feasibility of using EBFT to study dense turbulent boundary layers is being conducted in the 96" shock tunnel at Calspan. A schematic of the E-beam installation is shown in Figure 3. The model is a 6° semi-vertex angle smooth, sharp tipped cone set at zero angle of attack. A compact 50 KV gun is installed within the model and the beam is fired through a small orifice in the surface directly into the cone's boundary layer. The gun is shown in greater detail in Figure 3(b). A single electro-magnet to focus the beam has been especially designed. It is shaped to fit within the model and yet finely focus the beam at a point coincident with the surface. Here the beam passes through a very small hole in a graphite diaphragm which is shaped to be flush with the model surface. The hole allows the electrons to enter the test flow but effectively isolates the interior of the gun from the external environment. The gun is continuously pumped so as to maintain a pressure low enough for the directly-heated cathode filament to survive. The gun has been ruggedly designed to withstand the shock loading that is inevitable with intermittent wind tunnels. A Farady cup is placed on the electron gun axis outside of the test flow to safely capture the beam and record its current immediately before each test run. The beam, captured by the Faraday cup can be seen in Figure 4(b).

The optical detection system is mounted to the side of the model so as to view the beam in a direction tangential to the cone (see Figure 4(a)). The system is fitted with three slits on to which an image of the beam is focused by a lens so that three points along the beam can be viewed simultaneously. Separate photomultiplier tubes are used for each channel. A common narrowband optical interference filter ensures that only light from the $N_2(2+)$, 0-0 band, at 337.1 nm wavelength is transmitted to the photomultipliers.

A series of experiments have been conducted at Mach 8.5 in the 96" Shock Tunnel using the 'A' nozzle which has an exist diameter of 24". Time test conditions were 6 milliseconds using pure nitrogen as the test gas. The electron beam was located at 55 ins from the apex of the cone. The model was also fitted with conventional flush mounted transducers to sense the surface pressure and heat transfer. A rake of total pressure and temperature probes was mounted on the model. From their outputs, a profile of the mean velocity at the same streamwise location as the electron beam was deduced. The measured pitot and total temperature distribution is shown in Figure 5 and 6. The measurements are compared with the Crocco relationship in Figure 7. We see, as observed in our earlier studies (Holden and Havener), that a parabolic form for this relationship is a more accurate representation.

Calculations using the van Driest compressibility transformation

$$\frac{u}{u_e} = \frac{1}{A} \sin^{-1} \frac{2A^2 \left(\frac{u}{u_e} \right) - B}{(B^2 + 4A^2)^{1/2}} + \frac{1}{A} \sin^{-1} \frac{B}{(B^2 + 4A^2)^{1/2}} \quad (3)$$

where

$$A^2 = m_e \frac{T_e}{T_w}, \quad B = (1 - m_e) \frac{T_e}{T_w} - 1 \quad \text{and} \quad m_e = r \frac{\gamma - 1}{2} M_e^2$$

together with Coles modification of the Clauser incompressible relationship

$$\frac{u}{u_e} = \frac{1}{k} \log \left(\frac{u_e y}{\nu_w} \right) + C + \frac{\pi}{k} w \left(\frac{y}{\delta} \right)$$

and the generalized Crocco relationship

$$\frac{T}{T_w} = 1 + \left[(1 - c_t) (1 + m_e) \frac{T_e}{T_w} - 1 \right] \frac{u}{u_e} + \frac{T_e}{T_w} \left[c_t \left(\frac{1 + m_e}{m_e} \right) - 1 \right] m_e \left(\frac{u}{u_e} \right)^2 \quad (4)$$

where $c_t = 0$ for a linear relationship and $c_t = 0.5$ for a parabolic form are compared with the experimental measurement in Figures 8, 9 and 10.

While the velocity distribution is in reasonably good agreement with experiment these are significant difference in the measured and calculated density and Mach number distributions. The measurements of mean density with the electron beam were in good agreement with those from the probe measurements.

Preliminary data from the electron-beam reveal that the nature of the turbulent fluctuations vary considerably with distance from the wall. Examples of traces are shown in Figure 11 which were recorded digitally using a 800 KHz bandwidth system. The inherent photomultiplier noise levels were far from insignificant at these high frequencies as is evidenced by the no-flow 30 torr calibration signal shown at the bottom of the figure. Similar noise levels (see the upper trace) were detected outside the boundary layer which had a predicted thickness of 8.49 mm (0.344") at the beam location. This level of noise is superimposed on the intermediate traces also. The existence of intermittent high density spikes at the mid thickness position and the high level of density fluctuation at $y = 10.2$ mm (0.401") which is 16% outside the nominal edge are notable.

Figure 12 shows examples of the spectral band shape of the $N_2(2+)$ (0-0) transition obtained using an Optical Multichannel Analyzer (OMA). The OMA consists of a moderate resolution spectrograph fitted with an intensified silicon diode array detector. Light integration time on the detector was 4 msec. In future work we will fit theoretic spectra to these spectra to evaluate the rotational temperatures, and it can clearly be seen that the width of the envelope of the R-branch increases between the trace for the cold outer-flow and the one for the hotter room temperature example.

Conclusions

A preliminary experiment has been conducted in the 96" Shock Tunnel and the viability of using an electron beam in an intermittent facility to study the time dependent properties of turbulent boundary layers has been demonstrated. These experiments have only just begun and definitive fluctuation measurements are to be obtained but it has been shown that the technique has the potential of resolving fluctuations in density at frequencies approaching 1 MHz. Improvements in resolution of the high frequency signals is expected if more advanced optical detection is used. Spectra have also been obtained from which mean rotational temperatures can be deduced. The electron gun has

proved to be totally reliable and has the potential of operating with flow of at least three times the density tested here. This would permit its use in experiments on shock/boundary layer interaction.

Further developments of the technique, possibly in conjunction with lasers, can be envisaged. The use of an electron beam to excite the gas which is then interrogated using a resonant laser technique is attractive in comparison to the conventional LIF method which requires powerful lasers to directly induce the fluorescence. The technique also has attractive possibilities if applied to multi-constituent flows.

REFERENCES

1. Rudy, D.H., Thomas, J.L., Kumar, A., Gnoffo, P.A.: "A Validation Study of Four Navier-Stokes Codes for High Speed Flows." AIAA 89-1838.
2. Barlett, R.P. and Harvey, J.K.: "Electron Beam Measurements of the Density in a Hypersonic Turbulent Boundary Layer at $M=9$." Imperial College Aero Report No. 80-01, 1980.
3. Boyer, A.G. and Muntz, E.P.: "Experimental Studies of Turbulence Characteristics in the Hypersonic Wake of a Sharp Slender Cone," AGARD CP 19, 1967.
4. Butefisch, K.A. and Vennemann, D.: "The Electron Beam Technique in Hypersonic Rarefied Gas Dynamics," *Progress in Aerospace Sciences*, Vol. 15, ed D. Kuchemann Pergamon Press, 1974.
5. Camac, M.: "Boundary Layer Measurements with an Electron Beam," AVCO Everett Research Report 275, 1967.
6. Cattolica, R.J., Schmitt, R.L. and Palmer, R.E.: "Feasibility of Flight Experiments and Instrumentation Hardware for In-Flight Hypersonic Boundary-Layer Measurement." Sandia Report SAND89-8204-UC-13, 1989.
7. Davis, J. and Harvey, J.K.: "A Comparison between Experiment and Direct Simulation Calculations of the Hypersonic Rarefied Flow Field over a Flat Plate with and without a Forward Facing Step." Imperial College Aero Report 76-05, 1976.
8. Dionne, J.G., Sadowski, C.M., Tardif, L. and Vanoverschelde, J.: "Mean Density Measurements in Hypersonic Wakes." AGARD Conference Proceedings No. 19, 1967.
9. Harvey, W.D. and Hunter, W.W.: "Experimental Study of a Free Shear Flow at Mach 19 with Electron Beam and Conventional Probes." NASA TN D-7981, 1975.
10. Lin, Z.B. and Harvey, J.K.: "Experimental Study of the Hypersonic Turbulent Boundary Layer on a Cold Slender Cone." *J. Thermophys.* 3, 2, 105-111, 1989.
11. McRonald, A.D.: "Measurements of Density and Temperature in a Hypersonic Turbulent Boundary Layer using the Electron Beam Fluorescence Technique," University of S. California, Ph.D. Thesis, 1975.

12. Muntz, E.P.: "The Electron Beam Fluorescence Technique," AGARDOGRAPH 132, 1968.
13. Smith, J.A. and Driscoll, J.F.: "The Electron Beam Fluorescence Technique for Measurements in Hypersonic Turbulent Flows." Journal of Fluid Mechanics, Vol. 72, p. 695, 1975.
14. Wallace, J.E.: "Hypersonic Turbulent Boundary Layer Measurements using an Electron Beam." Cornell Aeronautical Laboratory, Report CAL No. AN-2112-Y-1, 1968.
15. Holden, M.S. and Havener, A.G., "Shock Wave/Turbulent Boundary Layer Interaction in High-Reynolds-Number Hypersonic Flow," USAF/USFC/AFOSR Directorate of Aerospace Sciences, Bolling AFB, DC, 20332-6448, June 1987.

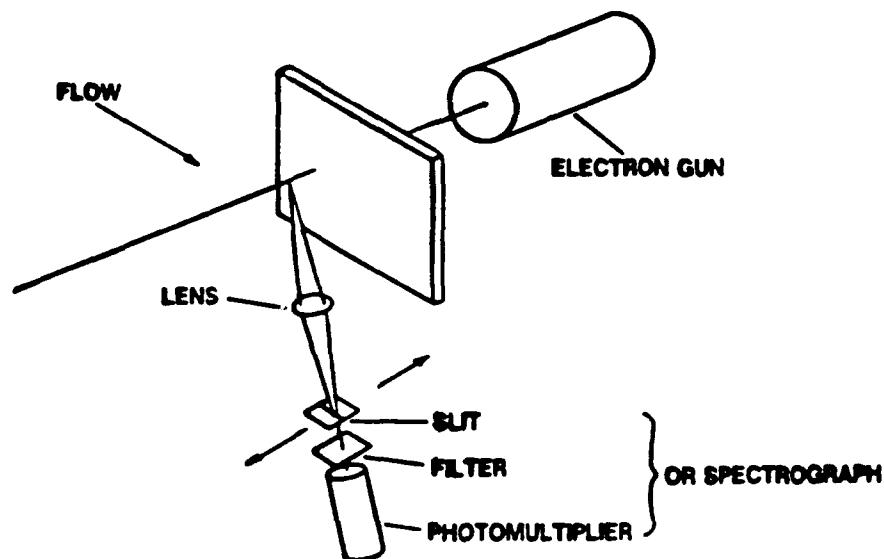


Figure 1 ELECTRON BEAM FLUORESCENCE TECHNIQUE

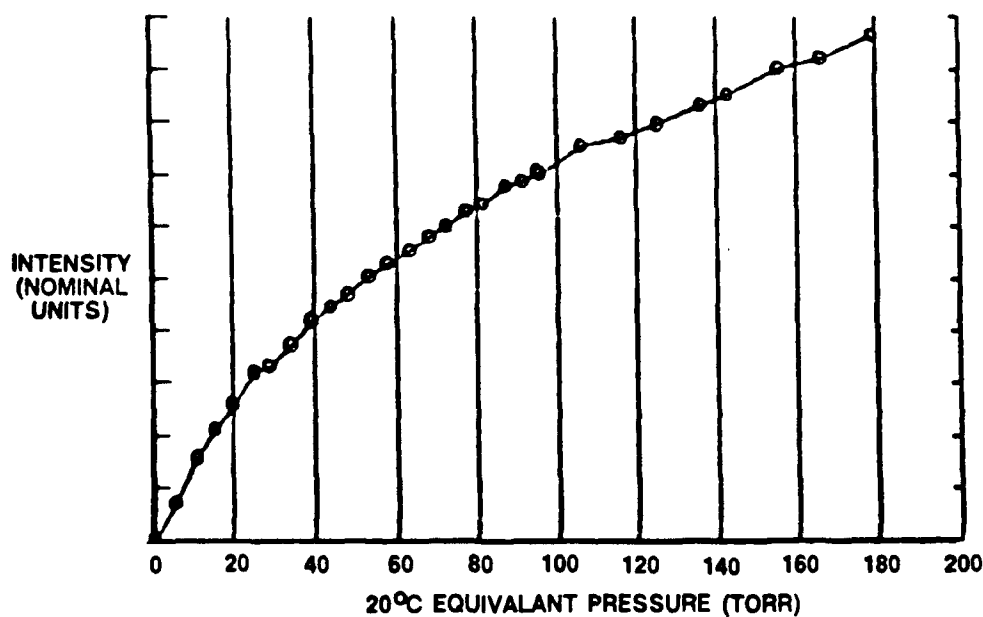
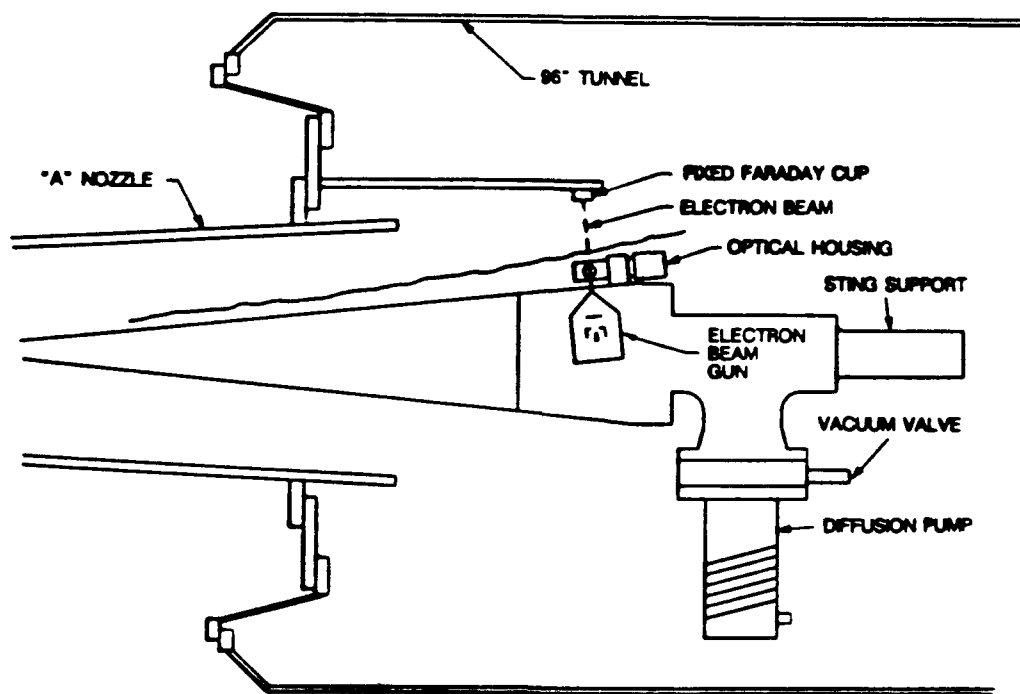
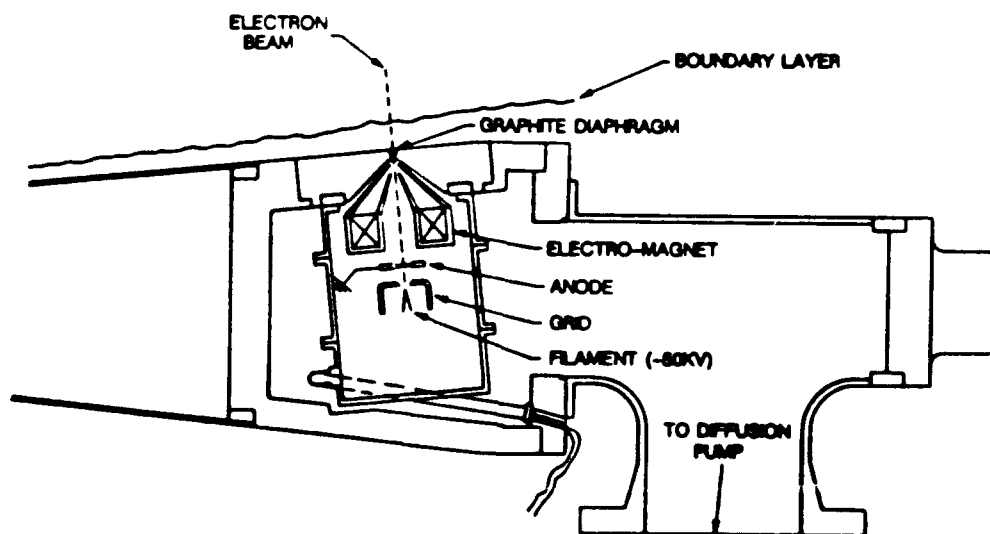


Figure 2 DENSITY-FLUORESCENCE INTENSITY CALIBRATION

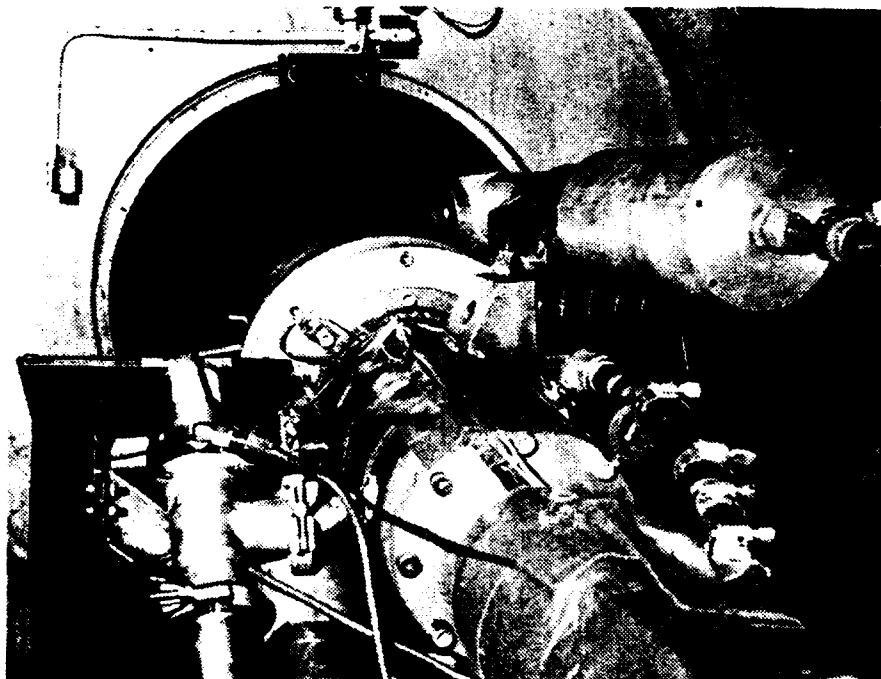


a) E-BEAM INSTALLATION IN 96 INCH SHOCK TUNNEL

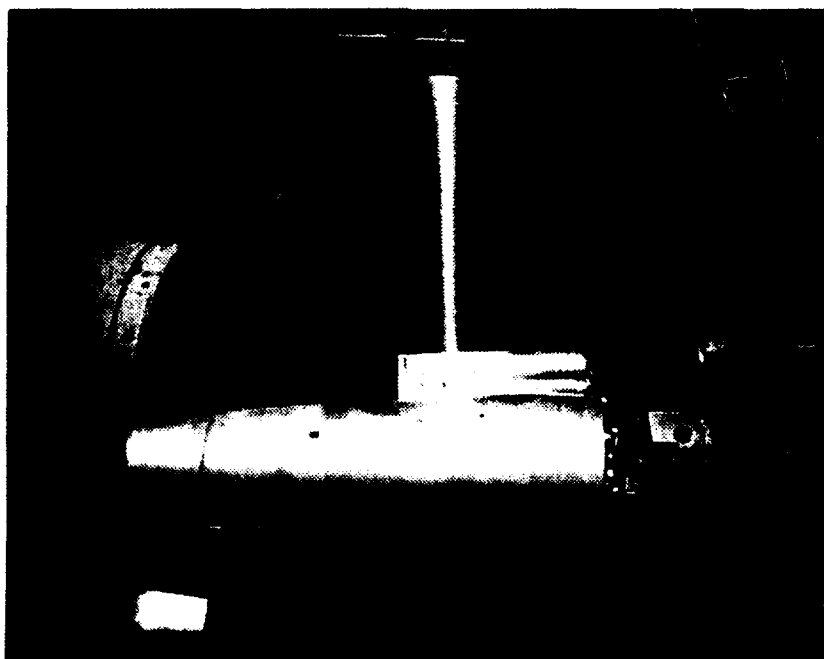


b) E-BEAM GUN INSTALLATION IN CONE MODEL

Figure 3 ELECTRON BEAM INSTALLATION



a) INSTALLATION IN 96" SHOCK TUNNEL



b) BEAMS IN OPERATION

Figure 4

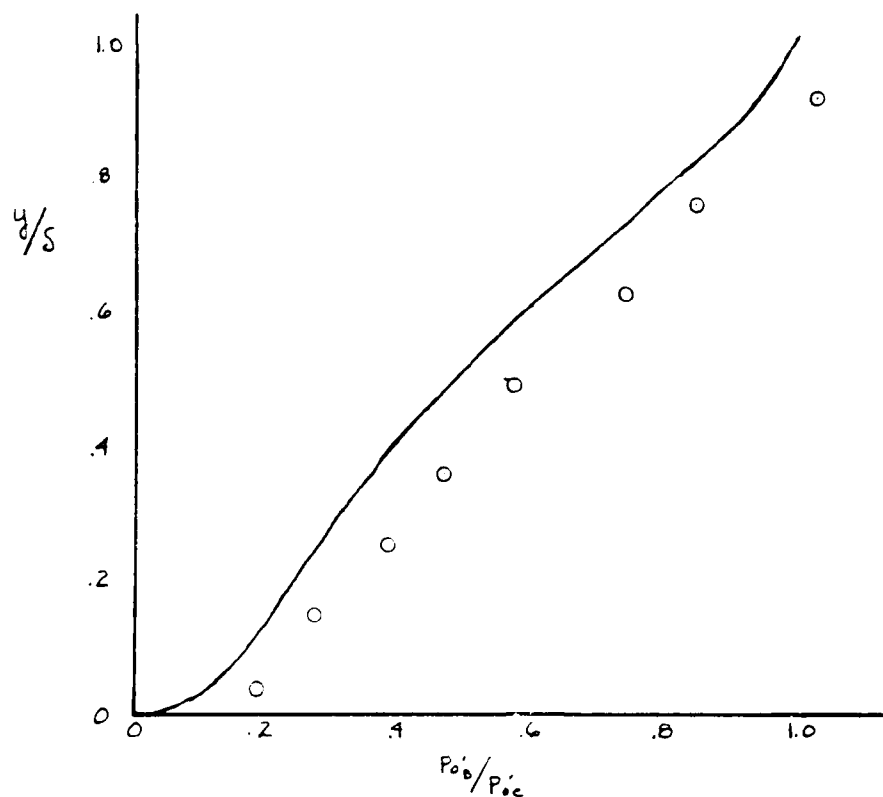


Figure 5 COMPARISON BETWEEN PITOT PRESSURE MEASUREMENTS AND PREDICTIONS BASED VAN DRIEST RELATIONSHIP

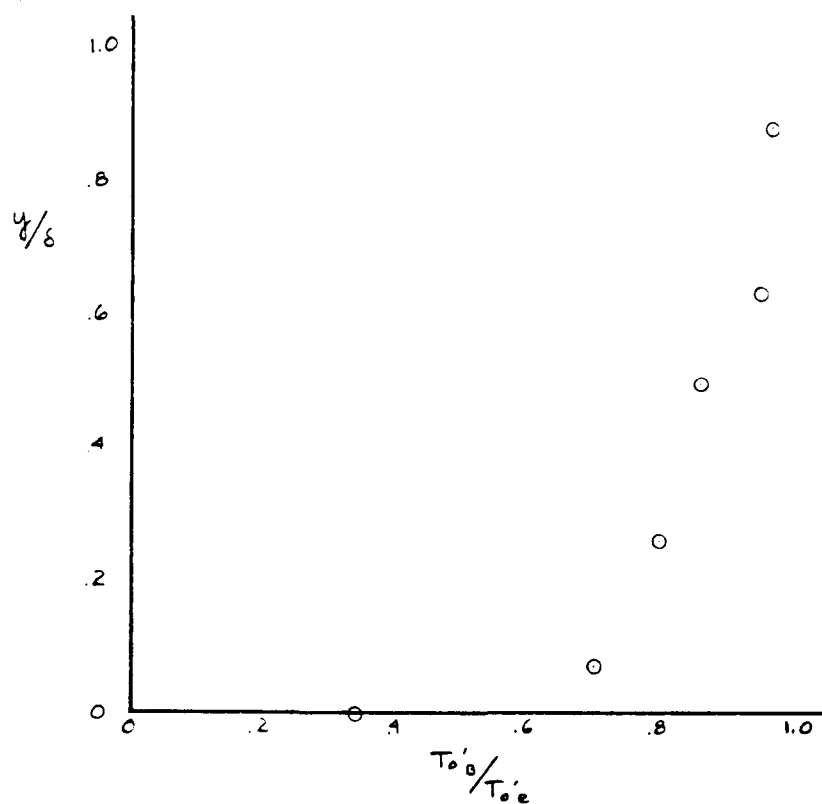


Figure 6 TOTAL TEMPERATURE MEASUREMENTS

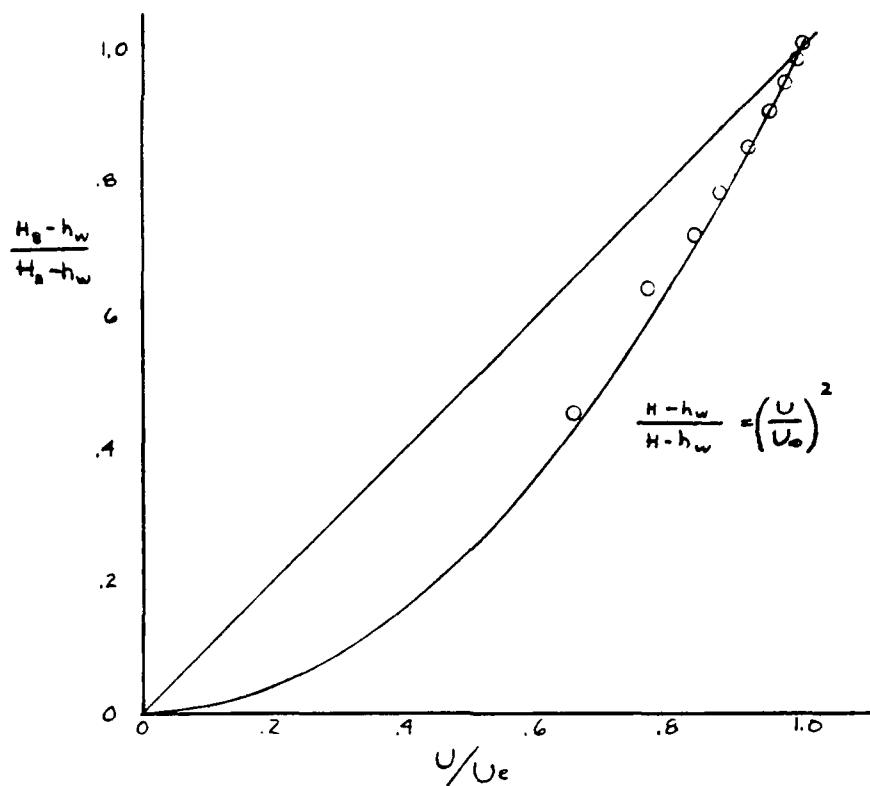


Figure 7 COMPARISON BETWEEN CROCCO RELATIONSHIP AND THE MEASUREMENT ($M_\infty = 8.5$ $Re_{LOCAL} = 40 \times 10^6$)

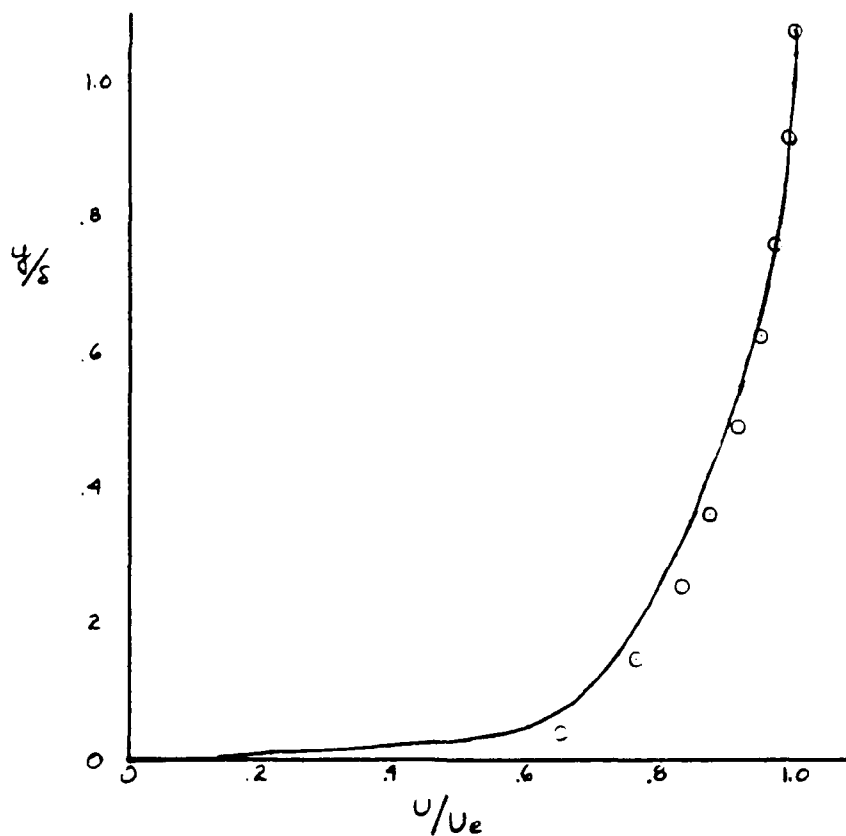


Figure 8 COMPARISON BETWEEN VELOCITY MEASUREMENTS AND THOSE PREDICTED FROM VAN DRIEST COMPRESSIBILITY RELATIONSHIP

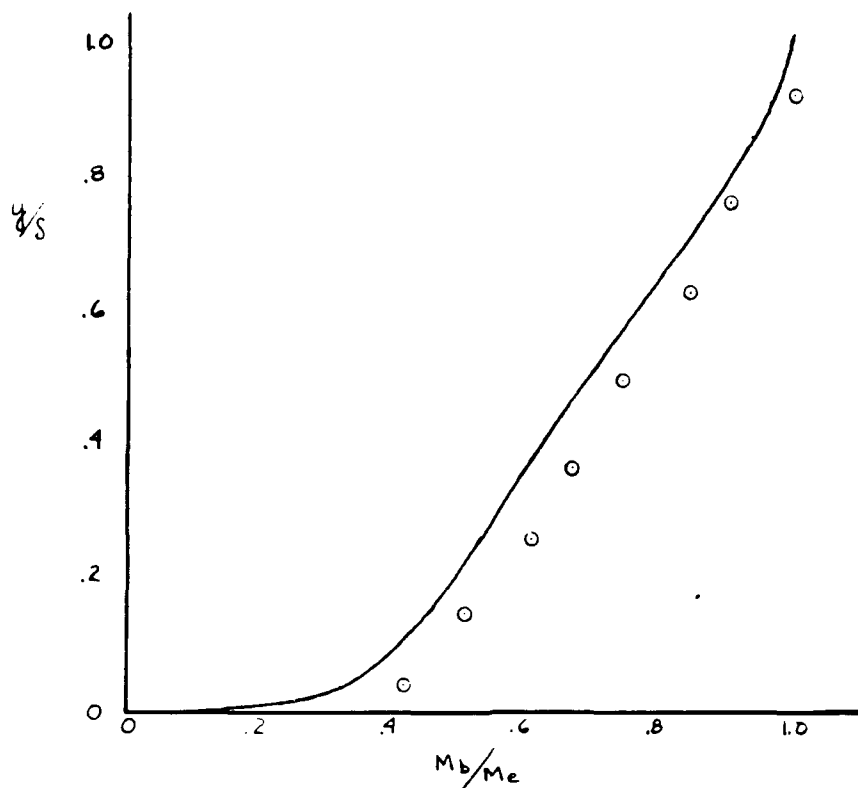


Figure 9 COMPARISON BETWEEN DENSITY MEASUREMENTS AND VAN DRIEST COMPRESSIBLE RELATIONSHIP

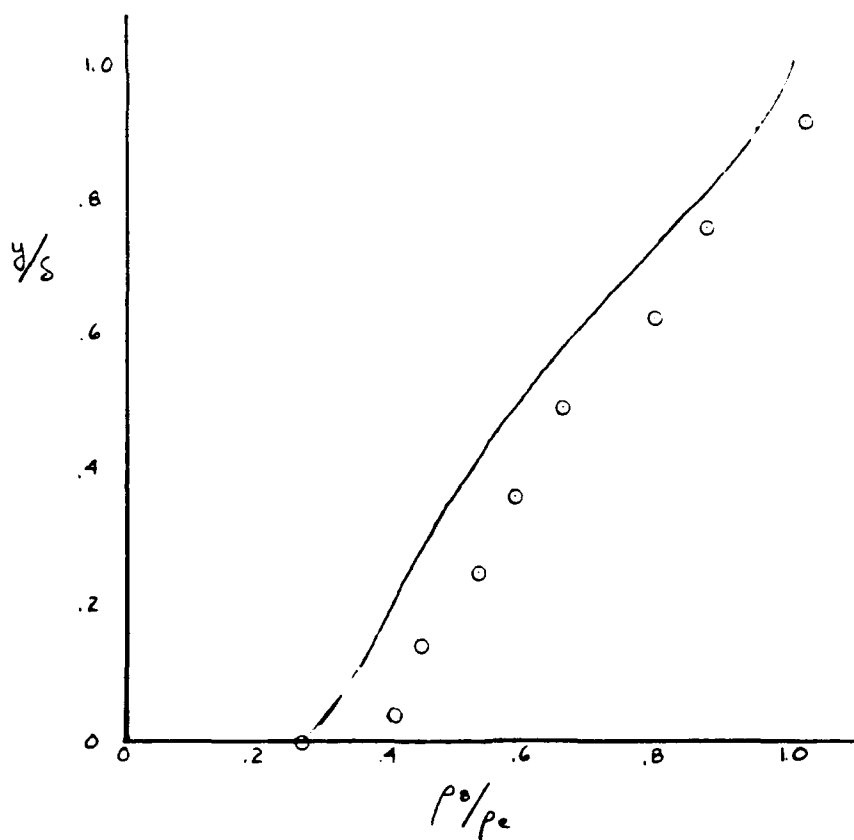


Figure 10 COMPARISON BETWEEN MACH NUMBER MEASUREMENTS AND VAN DRIEST COMPRESSIBLE RELATIONSHIP

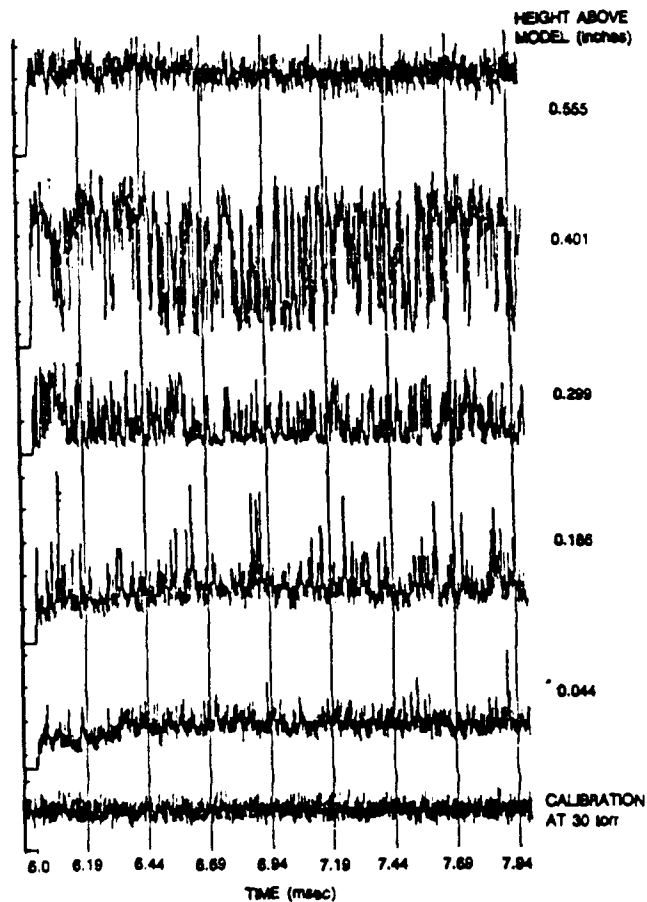


Figure 11 E-BEAM DATA ACROSS THE TURBULENT BOUNDARY LAYER

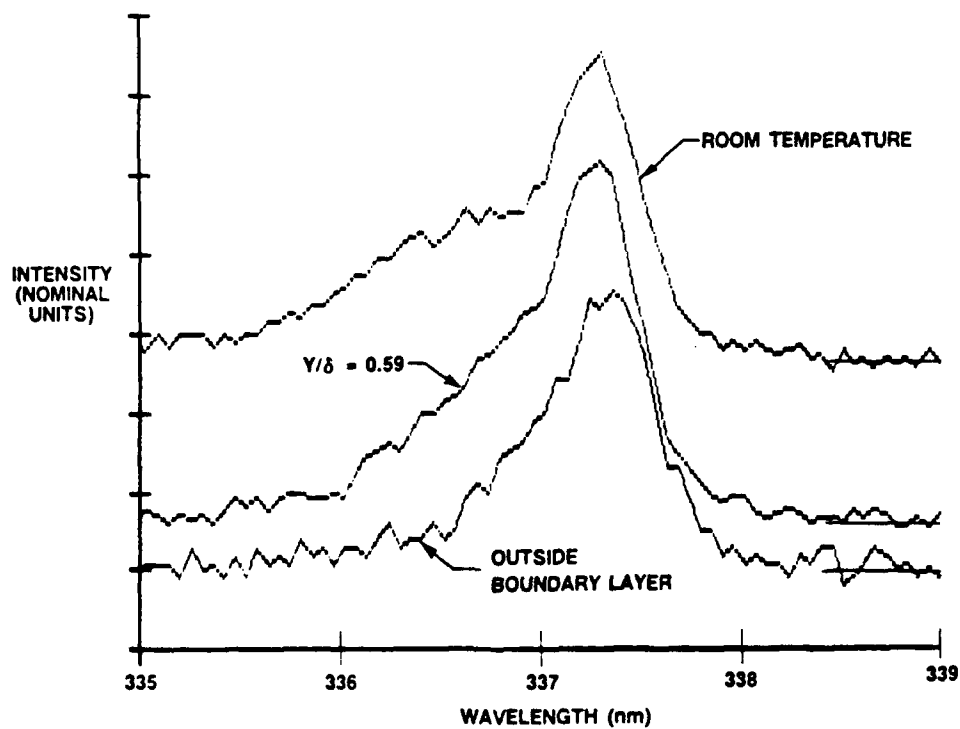


Figure 12 SPECTRA OF THE E-BEAM FLUORESCENCE

APPENDIX 5

**EXPERIMENTAL STUDIES OF THE EFFECT OF MASS ADDITION ON
THE LOW-ALTITUDE TURBULENT WAKE BEHIND
SHARP SLENDER CONES**



AIAA 91-1774

**Experimental Studies of the Effect of
Mass Addition on the Low-Altitude Turbulent
Wake Behind Sharp Slender Cones**

M.S. Holden

**Calspan-University at Buffalo Research Center
Buffalo, NY**

**AIAA 22nd Fluid Dynamics, Plasma Dynamics
& Lasers Conference**

June 24-26, 1991 / Honolulu, Hawaii

**For permission to copy or republish, contact the American Institute of Aeronautics and Astronautics
370 L'Enfant Promenade, S.W., Washington, D.C. 20024**

EXPERIMENTAL STUDIES OF THE EFFECT OF MASS ADDITION ON THE LOW-ALTITUDE TURBULENT WAKE BEHIND SHARP SLENDER CONES*

M.S. Holden**
Calspan-UB Research Center
P.O. Box 400
Buffalo, NY 14225

Abstract

An experimental program, conducted in the Calspan 96-Inch Shock Tunnel, is described in which studies were made of the effect of controlled mass addition from the conical surface of a slender cone on the structure and development of the "low-altitude" turbulent wake. The studies were conducted at Mach 11 and 13 and at Reynolds numbers based on the wetted length of the cone from 15×10^6 to 30×10^6 . Measurements of pitot and static pressure, total temperature, heat transfer, and mass concentration were made for $10 < X/\sqrt{C_D A} < 80$ for three rates of mass addition. From these studies, we have determined a quantitative relationship between the rate of mass addition and the wake velocity for conditions where the boundary layer over the cone is fully turbulent. The profile measurements demonstrated that the viscous wake did not increase significantly in size with mass addition, and that "wake narrowing" may result from fluid dynamic as well as electromagnetic phenomena.

1. Introduction

At altitudes below those where the boundary layer over a vehicle is transitional or turbulent, the turbulent diffusion in the near wake does not obey the simple, self-similar mixing model suggested by Townsend.¹ Such a model was used successfully by Lees and Hromas² to describe the structure of the near and far wakes of a body immersed in a fully laminar boundary layer. The major problem, as far as theoretical treatment of the low-altitude wake is concerned, is that an acceptable framework for modeling the development of turbulence through the base wake and into the near wake does not exist in hypersonic, high Reynolds number flows. Also, in these flows, the momentum deposited into the wake from the ablating surface of a reentry vehicle can be considerably larger than

the momentum defect resulting from the drag of the body; consequently, the structure of both the mean and fluctuating flowfields could be significantly modified by mass addition.

Describing the development of the turbulent wake from 4 to 100 body diameters behind slender reentry vehicles at low altitudes is a key problem for those interested in near-wake analysis. While a knowledge of the turbulence development over the body and in the base region is important (as it controls the initial conditions), the change in fluid mechanics of the near wake region as the boundary layer over the vehicle changes from laminar to turbulent remains to be satisfactorily explained. If large-scale disturbances can be stabilized and the initial turbulent scale size across the near wake is typically that of the cone boundary layer, then Finson³ predicts a decreased wake diffusion consistent with experimental evidence. The length of this region of decreased diffusion will depend on the turbulence modeling, while the magnitude of the axial wake velocity will depend on an accurate calculation of the width and mean properties at the beginning of the turbulent wake. On both counts, experimental measurements are required to assist in modeling those regions and to provide data against which the models can be examined.

It is clear that sharp, non-ablating models provide wakes that are less complex and, hence, make the most suitable comparison with theory. In most practical situations, however, cone roughness, nose-tip bluntness, and mass ablation significantly influence the structure and development of the near wake. It is the interrelationship between these effects and the near wake velocity that is most easily investigated in a wind tunnel program. The Mach number and Reynolds number conditions at which turbulent boundary layers are formed on vehicles traveling at reentry velocities can be duplicated in the Calspan 96-Inch

* This work was supported by the U.S. Air Force under AFOSR Contract No. AFOSR-88-0223. This paper is declared a work of the U.S. Government and is not subject to copyright protection in the United States.

** Staff Scientist; Associate Fellow, AIAA

Shock Tunnel. We can also cover the range of the mass blowing parameter $(2\dot{m})/(\rho u A)$ from the low ablators, such as graphite and carbon phenolic, to the high ablators, such as Teflon and asbestos phenolic. Here, we have the advantage of being able to vary the rate of mass addition from the surface of the cone independently of the position of transition on the cone and the velocity of the freestream.

In the experimental studies described in the following sections, measurements were made to investigate the structure and properties of the turbulent near wake of a slender cone for freestream conditions under which a turbulent boundary layer is developed over the model surface. Controlled amounts of mass were added into the flow from the conical surface of the model. The studies were conducted at Mach 11 and 13 for a range of mass injection rates that covered the range that can be anticipated under flight conditions. In the following section, we describe the test program, the model and survey rake instrumentation, and other diagnostic techniques. The results of the experimental studies are then discussed, compared with measurements made in earlier studies, and used to determine the effect of mass addition on the centerline velocity and the turbulent wake development.

2. Experimental Program

Utilizing the capabilities of the 96-Inch Shock Tunnel at high Mach number, we can generate the Reynolds numbers required to obtain a fully turbulent boundary layer over the model. The mass addition to the wake from surface ablation can be simulated by injecting gas through the porous conical surface of the model. CO_2 can be used as an injectant to simulate ablation products, as its molecular weight is typical of the average of those of the ablation products. The mass-addition rates from the conical model were selected so that they spanned the range from light to heavy reentry-vehicle ablation rates ($0 < (2\dot{m})/(\rho_\infty U_\infty A_\infty) < 0.008$). Typical free-stream conditions for the Mach 11 and 13 test conditions are shown in Table I. The sharp 8° half-angle cone used in the experimental study had a base diameter of 10 inches, so, when tested in the 48-inch contoured nozzle of the shock tunnel, the model allowed us to measure profiles up to 80 drag diameters behind the body. The test matrix employed in this program is shown in Table

II. Earlier studies at Calspan and at TRW⁴ have indicated that the wall-to-freestream stagnation temperature ratio of the model may have an important effect on wake velocity. For this reason, this ratio was held between 0.15 and 0.18, closely matching the ratios found in full-scale flight tests.

2.1 Model and Instrumentation

2.1.1 Mass-Addition Model

To simulate the flow over an ablating reentry vehicle, we designed and constructed a model from which mass can be injected through the conical surface from a self-contained reservoir within the model. A schematic diagram and photographs of the model, the model assembly, and the model suspended in the 96-Inch Shock Tunnel are shown in Figures 1 and 2. The mass is injected from the surface of the cone, beginning downstream of the point at which a fully developed turbulent boundary layer flow is established over the model under high Reynolds number conditions at both Mach 11 and Mach 13. The model is constructed in two parts: an inner reservoir and valve assembly, and an outer conical shell through which the gas is ejected. The gas contained in the reservoir is released through a pair of fast-acting "Valcor" valves, which are connected through a system of metered orifices to chambers formed in the annulus between the reservoir and the outer porous shell. The pressures in the reservoir, across the choked orifices, and in the chambers were monitored to provide information on flow establishment and mass flow rate through the model. By controlling the flow through the orifices, we can simulate the rates of ablation $(2\dot{m})/(\rho u A)$ from beryllium to Teflon-coated vehicles at high and low altitudes from Mach 8 to 15. Equilibrium flow of the injectant is established through the model in less than 5 milliseconds; so, when the Valcor valves are triggered from an acceleration switch located on the driver, steady mass flow has been established through the surface of the cone 5 milliseconds before tunnel flow establishment. For experiments performed in this sequence, the time to establish the recirculation region and wake is independent of mass addition.

2.1.2 Survey Rake Instrumentation

The survey rake shown in Figures 2 and 3 contains five types of probes: total temperature, pitot pressure, static pressure, thin-film heat transfer, and mass (gas) sampling. In the present

studies, we used the pitot and static pressure gages, total temperature and thin-film gages, and gas-sampling probes to obtain the mean properties of the wake.

2.1.3 Pitot and Static Pressure Gages

The pitot pressure gages used in the survey rake were constructed using a quartz crystal mounted to a diaphragm with a sensitive area of less than 0.01 square inch. The transducer is supported in a probe 0.125 inch in diameter. The basic calibration of the pitot probe yields typical accuracies of $\pm 2\%$, which, combined with recording errors, lead to potential errors of $\pm 6\%$ in the mean value.

Five static pressure gages were used in the present study to measure the mean variation of static pressure in the wake along and perpendicular to the axis of symmetry. Each gage, shown in Figure 3, is constructed by placing a small static pressure head over a Calspan 1/8-inch piezoelectric pressure transducer.

2.1.4 Platinum Thin-Film Gages

Each thin-film gage, shown in Figure 3, is formed by depositing a thin platinum film having dimensions of 0.03 inch by 0.002 inch in the stagnation region of a quartz hemisphere cylinder, 0.1 inch in diameter. The gages used in the present study are coated with a 0.1-micron layer of magnesium fluoride to improve their abrasion characteristics. These gages have a frequency response of up to 1 MHz, so they are ideal to measure the intermittency of the flow, thus enabling the boundaries of the turbulent wake to be identified. Outside the wake boundaries, the mean output of the thin film was related directly to the stagnation temperature of the flow, thus enabling us to check the total temperature observations made with total temperature gages.

2.1.5 Total Temperature Gages

Each total temperature gage used in the experimental program is a resistance thermometer, constructed by suspending a tungsten wire between two steel needles mounted 0.030 to 0.040 inch apart. In our earlier tests, we found that it was necessary to employ tungsten wires 0.0002 inch in thickness to ensure survival in our severe dynamic pressure environment. However, further development testing has resulted in a design with 0.0001-inch tungsten wire, spot-welded to the needles and strengthened at each junction by

electroplating copper between the tungsten wire and its supports.

2.1.6 Gas-Sampling Measurements

The gas-sampling probes used to measure the concentration of injectant across the wake were originally developed in support of air-breathing propulsion diagnostics. Each probe, shown in Figure 4, takes a direct sample of the gas flow in which it is placed, so that the composition of this sample can be determined later by mass-spectroscopic techniques. The gas sampler opens at a preselected time during the steady test flow and remains open for a period of 2 milliseconds, or less, to collect a 6cc sample. To prevent dilution of the sample, the probes and sample bottles are evacuated prior to the run. The relative concentrations of N_2 (the freestream gas) and CO_2 (the injected gas) were determined using the mass-spectrometer rig assembled for this purpose and shown in Figure 5.

3. Discussion of Experimental Measurements

3.1 Measurements on Conical Model

Measurements of heat transfer and pressure were made on the conical surface and in the base region of the sharp 8° -conical, 10-inch-base-diameter models. Pressure transducers mounted in the reservoir and across the choked orifices in the mass-addition model were used to set up and monitor the injection of mass through the orifices in the cone surface. The relationships between mass-addition rates and the reservoir and orifice pressures were determined prior to the major tunnel program. Here, the mass-addition model was placed in a reservoir of known volume, and the mass-addition rate to this volume was determined from observations of the time history of the reservoir pressure. The heat transfer measurements (using thin-film gages) on the surface of the cone demonstrated that, at both Mach 11 and Mach 13, transition was completed within 25% of the wetted cone length; thus, the momentum defect in the turbulent boundary layer at the base of the cone was within 95% of the fully turbulent value.

The measurements of base pressure made at Mach 11 and 13 in the absence of mass addition can, in Figure 6, be seen to be in good agreement with flight measurements and correlations obtained earlier by Cassanto.⁵ These measurements strongly support the contention that the shear

layer in the base wake retains fully turbulent characteristics at the wake neck. The increase in base pressure with mass-addition rate from the cone surface, found in the present experimental studies, has also been observed in flight tests, as reported by Cassanto⁶ and Batt.⁷ These observations are presented in Figure 7. The increase in base pressure with mass addition is a consequence of the modification by mass addition of the momentum distribution close to the dividing streamline in the shear layer. Here, the Chapman-Korst relationship would predict a decrease in the pressure rise at the wake stagnation point and, hence, an increase in base pressure. The studies by both Cassanto and Batt indicate that a pressure gradient exists across the base of the models, and measurements made at Calspan⁸ support these observations.

3.2 Measurements in the Near Wake

Measurements of pitot and static pressure, total temperature, species concentration, and total heat transfer were made across the wake behind the cone model at a series of downstream stations between 10 and 80 drag diameters behind the base. Table II shows a diagram of the test matrix. The measurements of pitot pressure, static pressure, temperature, and relative CO_2/N_2 concentrations at each point in the wake were combined to yield the velocity defect along and normal to the wake axis. The fluctuating outputs from the thin-film (total heat transfer) gages were examined to provide a measure of the turbulent wake width.

3.3 Measurements Without Mass Addition

The measurements of the velocity defect made at Mach 11 and 13 for flows without mass addition are compared, in Figure 8, with the corresponding measurements made in an earlier study behind a sharp 8° cone with a base diameter of 6.7 inches. The good agreement between these measurements reaffirmed the choice of $X/\sqrt{C_D A}$ as a parameter of key importance in correlating velocity measurements behind vehicles of different sizes. The agreement between the levels of velocity defect in the wakes at Mach 11 and 13 is to some extent fortuitous. In developing the maximum Reynolds number at each test condition, we operated the tunnel such that $(T_{\text{CONE}}/T_{\text{STAGNATION}})$ was slightly larger at Mach 11 than at Mach 13. Our current understanding of the problem suggests that this would tend to bring the velocity measurements at Mach 11 and 13 closer together than would be the case

if $(T_{\text{CONE}}/T_{\text{STAGNATION}})$ were held constant. It is clear that the velocity decay in the wake under conditions where the boundary layer over the cone is turbulent is significantly less than the $2/3$ law predicted by the Lees-Hromas theory for laminar boundary layer conditions over the cone, and shown by earlier wind tunnel measurements at lower Mach number and Reynolds number conditions.

3.4 Measurements With Mass Addition

The structure and development of the wake was examined for values of the mass-addition parameter $(2\dot{m})/(\rho u A)$ of 0, 0.04, and 0.08, which correspond to the nominal ablation rates from vehicles coated with graphite, silica phenolic, and Teflon, respectively, and traveling at reentry velocities. However, the main intent was to examine how mass addition affects the centerline velocity and the structure of the near wake. In fact, the experiments were performed at conditions close to those encountered in reentry.

The measurements of axial variations of pitot pressure and total temperature are shown in Figures 9 and 10 for the three levels of mass addition. We see that increasing the mass-addition rate decreases both the total temperature and the pitot pressure on the wake axis. These measurements also exhibit a decrease in the axial gradients of properties with increased mass addition. Both of these observations, we will see later, are reflected in marked changes in the magnitude of the axis velocity.

A typical development of the pitot pressure profile with downstream distance is shown in Figure 11. Here, the position of the wake shock is well defined close to the body but becomes more diffuse with downstream distance. While the wake shock is moved out by mass addition, the increase in wake width is insufficient to account for the increase in momentum defect resulting from mass addition. Consequently, an increase in the velocity defect must occur.

The development of the velocity profile with downstream distance is shown in Figure 12 for a condition without mass addition. Here, we have determined the edge of the viscous wake with the aid of the fluctuation measurements made with the thin-film gages. We see that the non-dimensionalized profiles become measurably "fuller" with downstream distance. This non-similar development is at variance with the current wake models, and our measurements suggest that this

non-similar development is an inherent feature of turbulent wakes at high Reynolds numbers.

A unique series of wake measurements made in the present program were those obtained with the concentration (gas-sampling) probes. A typical set of concentration measurements depicting the development of the distribution across the wake is shown in Figure 13. These measurements, made at Mach 11.3 for $(2\dot{m})/(\rho u A) = 0.085$, demonstrate that the diffusion of the injectant does not occur in a self-similar fashion. The rapid mixing that occurs at the outer edge of the wake causes a rapid dilution of the CO_2 . While the mass flux at the edge of the wake is significantly larger than the axis value, this effect alone is insufficient to produce the rapid dilution observed. If the ablation material covering a reentry vehicle influences the electron concentration in the wake, the fluid dynamic effect described above may itself affect the wake velocity to produce an effective wake narrowing. The effective fluid dynamic wake narrowing described above and the non-similar development of the velocity profiles may combine to yield an axial distribution of wake velocity very different from the equivalent distribution for laminar flow over the cone.

The measurements of the variation of centerline velocity with downstream distance and mass-addition level made at Mach 11 and Mach 13 are shown in Figure 14a and Figure 14b, respectively. We see that mass addition from the cone surface causes a significant increase in the axial wake velocity defect. Mass addition also decreases the rate at which the velocity defect decays with downstream distance. The measurements at Mach 11 and 13 are compared in Figure 15, and we see that both the absolute velocity and the rate of velocity decay do not appear to be strongly influenced by Mach number.

The variation of centerline velocity defect with the momentum defect in the wake $(C_f + (2\dot{m})/(\rho u A))$ is shown for Mach 11 and for Mach 13 in Figure 16 and Figure 17, respectively. We see that, at a given distance behind the body, the velocity defect increases uniformly with mass addition. While the velocity defect is largest close to the body, the observed trend appears relatively independent of downstream position or Mach number.

A major objective of the present program was to determine the magnitude of and mechanisms associated with the increase in fluid dynamic wake velocity with mass addition. We are

interested in the increase in velocity that occurs with the addition of mass through an initially turbulent boundary layer. Even of greater interest is the velocity jump that occurs in the wake as the boundary layer over the vehicle goes from laminar to turbulent with mass addition, for this is the velocity jump of greatest relevance to those interested in reentry. The velocity defect jump ratio $(V_{\text{MASS ADDITION}}/V_{\text{TURB}})$ determined from the measurements with and without mass addition for a condition that induces turbulent boundary layers over the model is shown in Figure 18. We see that this ratio is strongly dependent on mass-addition rate and relatively independent of downstream distance and Mach number. The centerline velocity defect jump ratio from laminar to turbulent with mass addition, calculated with the aid of measurements made in our earlier test program, is presented in Figure 19. Also shown are calculations from the semi-empirical method presented by Holden in an earlier test program. We see that a velocity jump by as much as a factor of 5 can occur for high levels of mass ablation. While the prediction method overpredicted the turbulent-to-turbulent-with-mass-addition jump, it is in good agreement with the velocity jump shown in Figure 19. We believe that these results re-emphasize the importance of the fluid dynamics in the phenomenology of low-altitude wakes.

4. Conclusions

Experimental studies have been successfully conducted to determine the effect of mass addition on the properties of the turbulent wake. Measurements in the wake at stations $15 < X/\sqrt{C_D A} < 80$ have been made for values of the mass-addition parameter $(2\dot{m})/(\rho u A)$ from 0 to 0.08. The measurements have suggested a strong relationship between wake velocity and mass addition. Our studies suggest that the increase in the wake velocity may result both from the direct increase in this velocity with mass addition and from fluid dynamic effects that tend to "weight" the velocities at the wake center.

Nomenclature

A	Base Area
C_D	Drag Coefficient
C_f	Skin Friction on Cone
H	Total Enthalpy

M	Mach Number
M_i	Incident Mach Number
\dot{m}	Mass-Addition Rate/Unit Area
P	Pressure
P_B	Base Pressure
P'	Static Pressure Fluctuation
P_o'	Pitot Pressure
Q, q	Dynamic Pressure
R	Base Radius
Re/ft	Unit Reynolds Number
Re_D	Reynolds Number at Diameter
r	Radial Dimension
T	Temperature
U, u	Velocity
U_B	Base Velocity
U_e	Local Velocity on Cone
U_x	Velocity Outside Wake
V	Velocity
$V_{MASS\ ADDITION}$	Mass-Addition Velocity
V_{TURB}	Turbulent Velocity Conditions
X	Wake Length
Y_w	Wake Width
GREEK SYMBOLS	
ΔU	$= U_x - U'$
μ	Viscosity
ρ	Density
SUBSCRIPTS	
0	Under Stagnation Conditions
$CONE$	Conditions Over Cone
L	Under Laminar Conditions
$MASS$	Under Mass-Addition Conditions
$NO\ MASS$	Without Mass Addition
$STAGNATION$	Under Stagnation Conditions

T	Under Turbulent Conditions
w	At-Wall Conditions
$\bar{\epsilon}$	Centerline Value
∞	Freestream Value

References

- 1) Townsend, A.A., *The Structure of Turbulent Shear Flow*, Cambridge University Press, Cambridge, England, 1956.
- 2) Lees, L. and Hromas, L., "Turbulent Diffusion in the Wake of a Blunt-Nosed Body at Hypersonic Speeds," *J. Aerospace Sci.* **29**, 976 (1962).
- 3) Finson, M.L., "Hypersonic Wake Aerodynamics at High Reynolds Numbers," AIAA Paper No. 72-701, Presented at AIAA 5th Fluid and Plasma Dynamics Conference, Boston, Massachusetts, June 26-28, 1972.
- 4) Fox, J., "Fine-Scaled Hypersonic Wakes at High Reynolds Number," AIAA Paper No. 74-577, Presented at Fluid and Plasma Dynamics Conference, Palo Alto, California, June 17-19, 1974.
- 5) Cassanto, J.M., "Flight Test Base Pressure Results at Hypersonic Mach Numbers in Turbulent Flow," *AIAA Journal*, Vol. 10, No. 3, March 1972, pp. 329-331.
- 6) Cassanto, J.M. and Hoyt, T.L., "Flight Results Showing the Effect of Mass Addition on Base Pressure," *AIAA Journal*, Vol. 8, No. 9, September 1970, pp. 1705-1707.
- 7) Batt, R.G., "Flight Test Base Pressure Results for Sharp 8° Cones," *AIAA Journal*, Vol. 12, No. 4, April 1974, pp. 555-557.
- 8) Holden, M.S., "A Preliminary Experimental Study of the Turbulent Near Wake in High Reynolds Number Hypersonic Flow," Calspan Report AB-5211-A1, January 1973.

Table I
Test conditions

M	—	3.37	3.37
P_o	psia	18,360	18,590
H_o	ft-lb/slug	17.20×10^6	21.25×10^6
T_o	$^{\circ}\text{R}$	2,710	3,237
M_s	—	11.31	12.99
U_s	ft/sec	5,756	6,428
T_s	$^{\circ}\text{R}$	107.7	101.9
P_s	psia	0.2105	0.07992
Q_s	psia	18.87	9.444
σ_s	slug/ft ³	1.640×10^{-4}	6.583×10^{-5}
u_s	slug ft/sec	9.062×10^{-7}	8.571×10^{-7}
R_s/μ	—	10.42×10^7	4.937×10^8
ρ_s/μ	psia	24.94	17.55
H_{ss}	ft-lb/slug	1.166×10^7	3.177×10^7
τ	sec	8.77	8.20

Table II
Test program (19 runs)

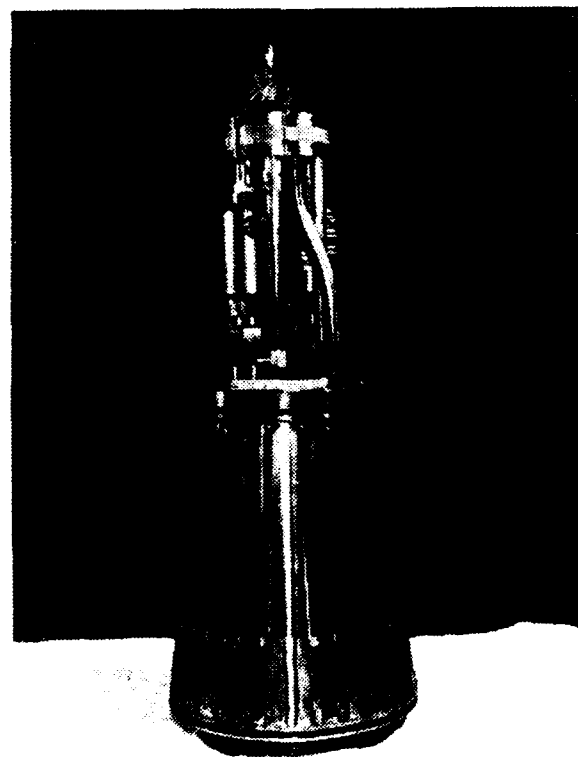
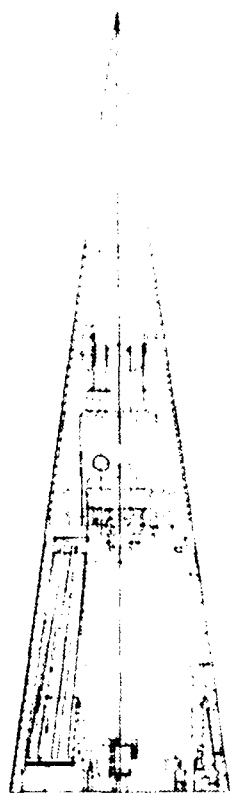
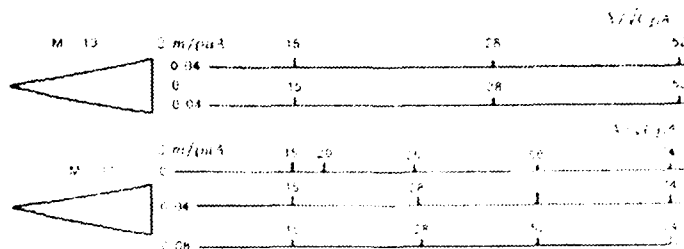


Figure 1. Mass-addition model

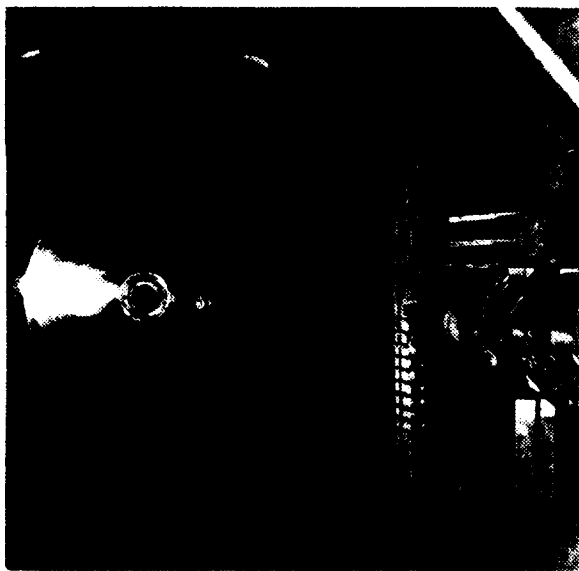
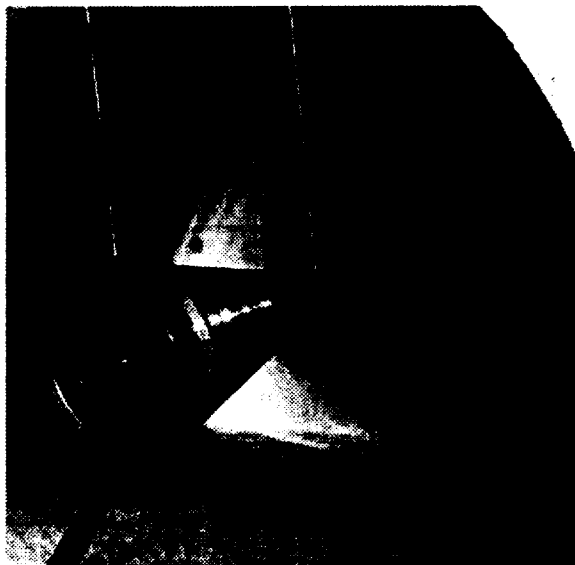


Figure 2 Mass addition model mounted in tunnel

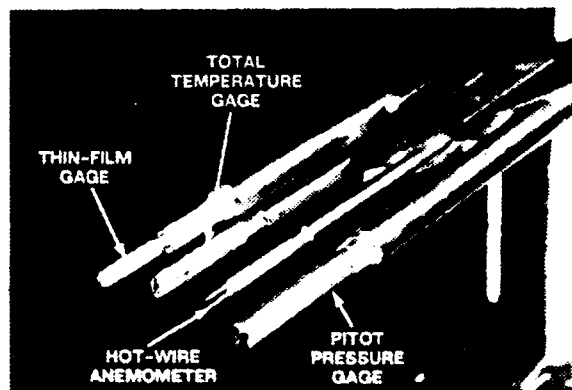
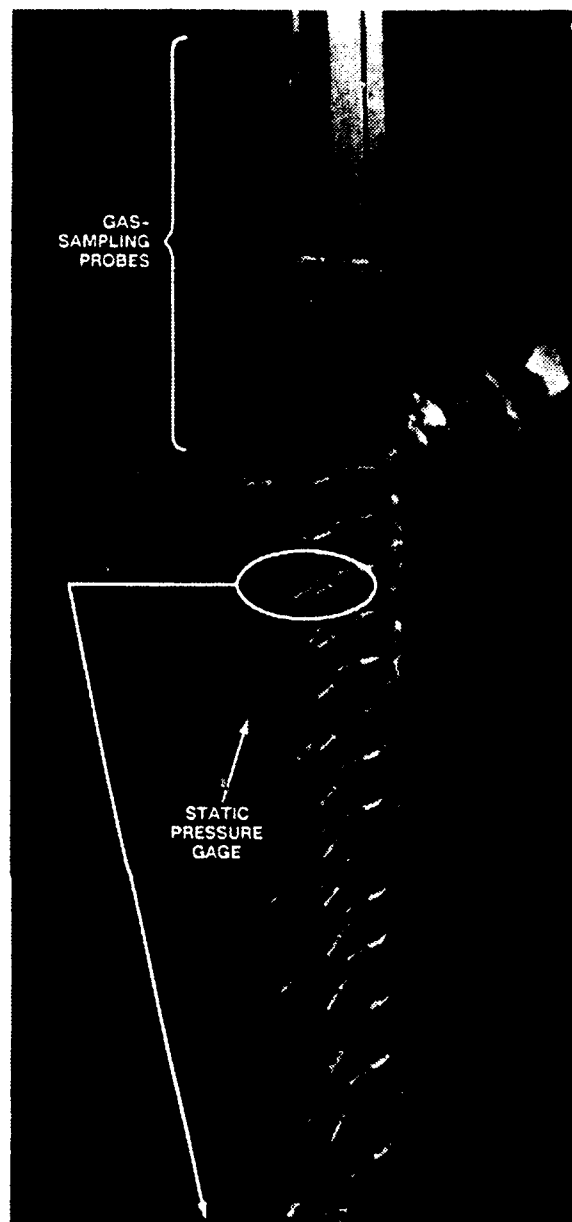


Figure 3 Probes mounted on survey rake

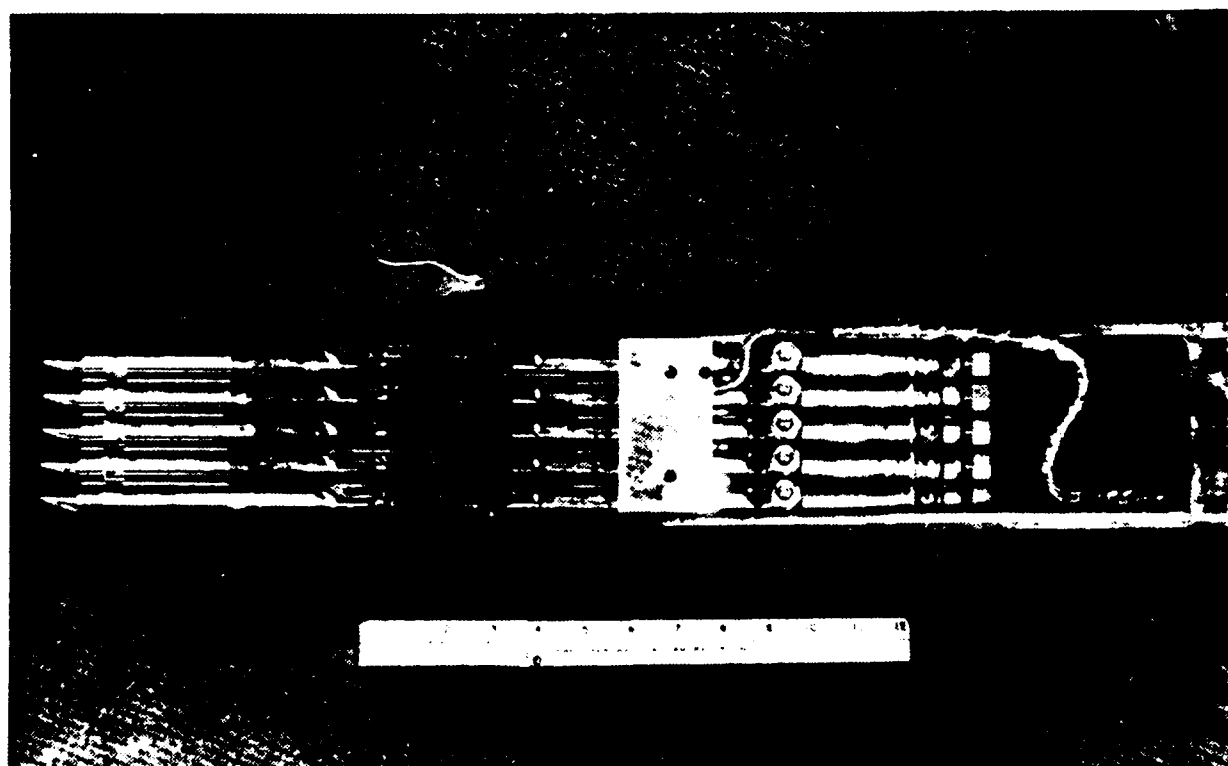
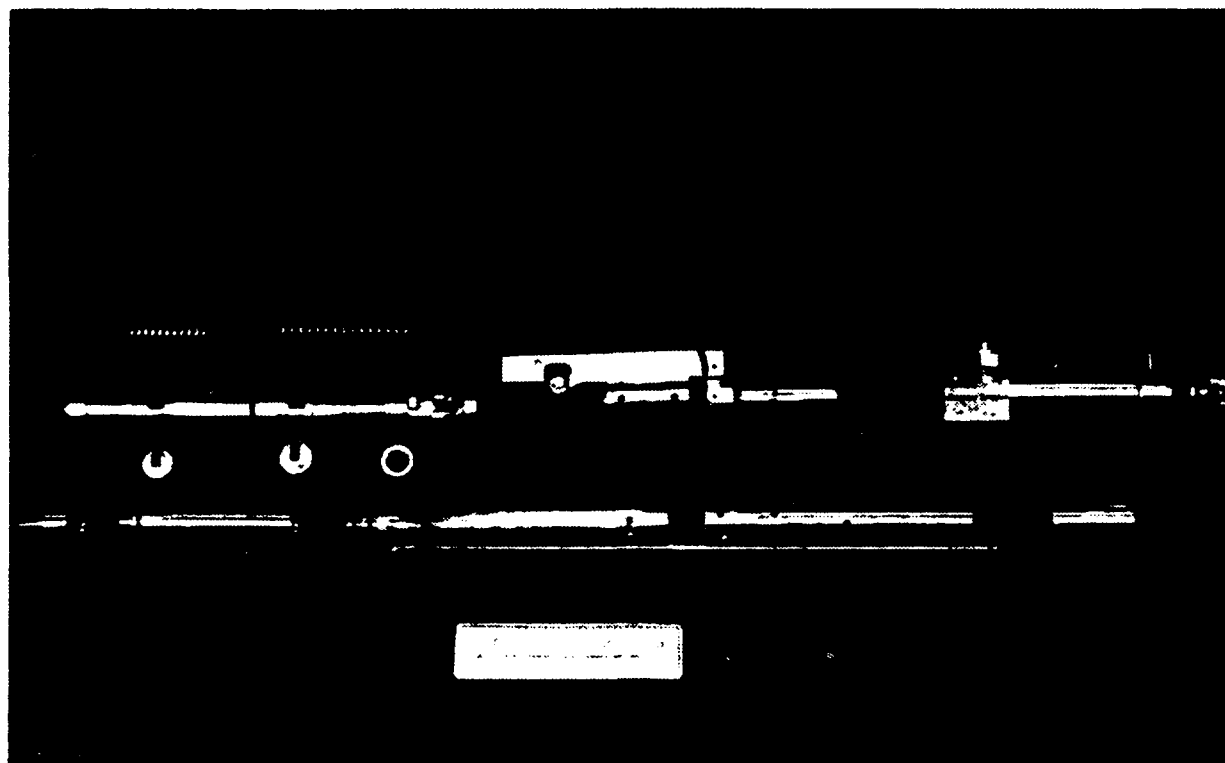


Figure 1. Gas sampling probes.

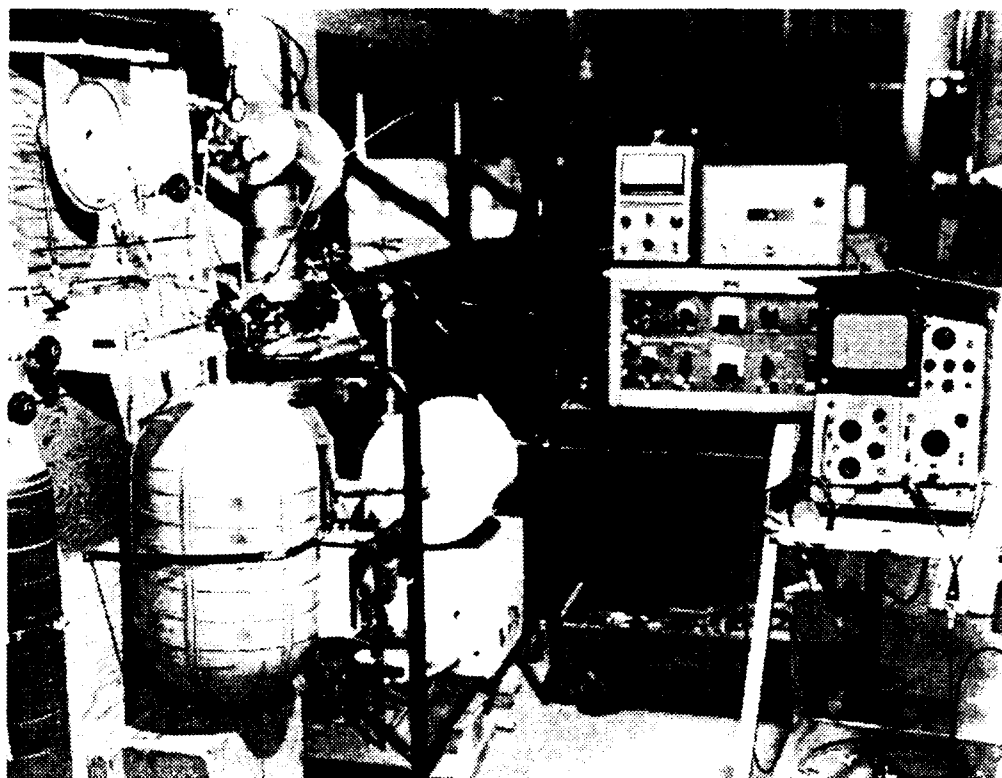


Figure 5. Mass-spectrometer apparatus

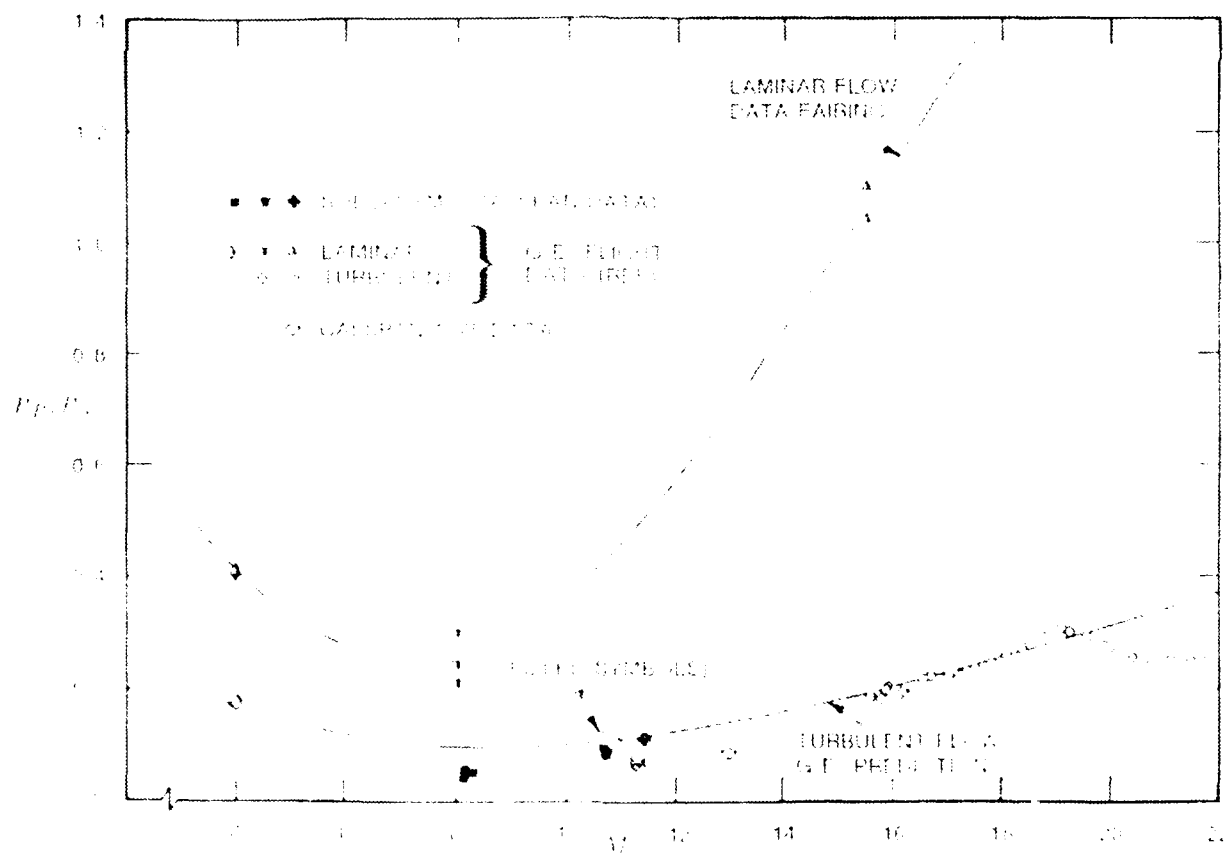


Figure 6. Correlation of base pressure measurements

○ CALSPAN $M_\infty = 11.3$

□ CALSPAN $M_\infty = 13.0$

○ CASSANTO & HOYT

△ $r/R = .33$ CASSANTO & HOYT

◇ ζ BATT

◇ $r/R = .36$ BATT

◇ $r/R = .46$ BATT

FROM
FLIGHT
DATA

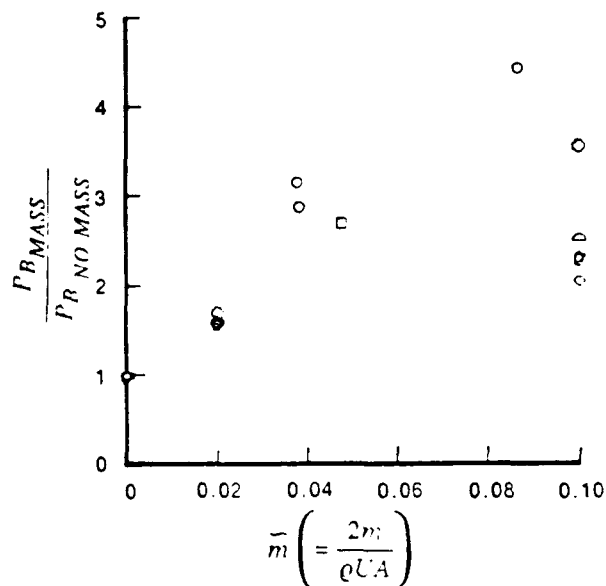


Figure 7. Base pressure variation with \tilde{m} .

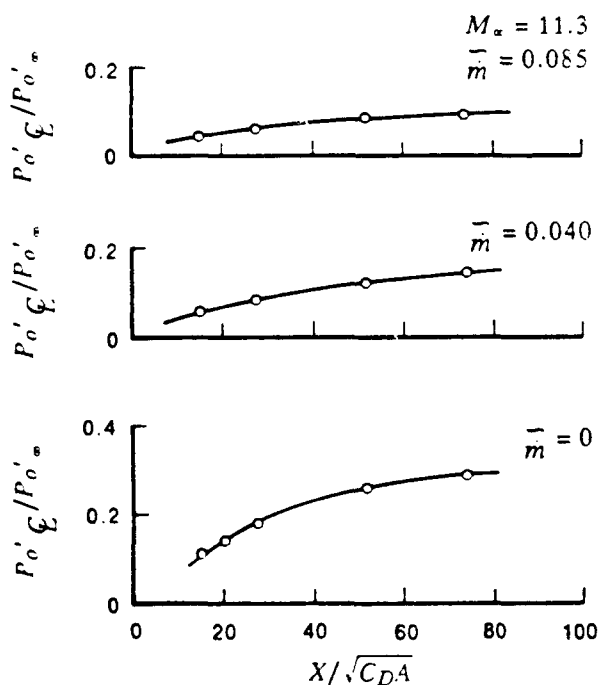


Figure 9a. Variation of pitot pressure on axis with $X/\sqrt{C_D A}$ and \tilde{m} at mach 11.3

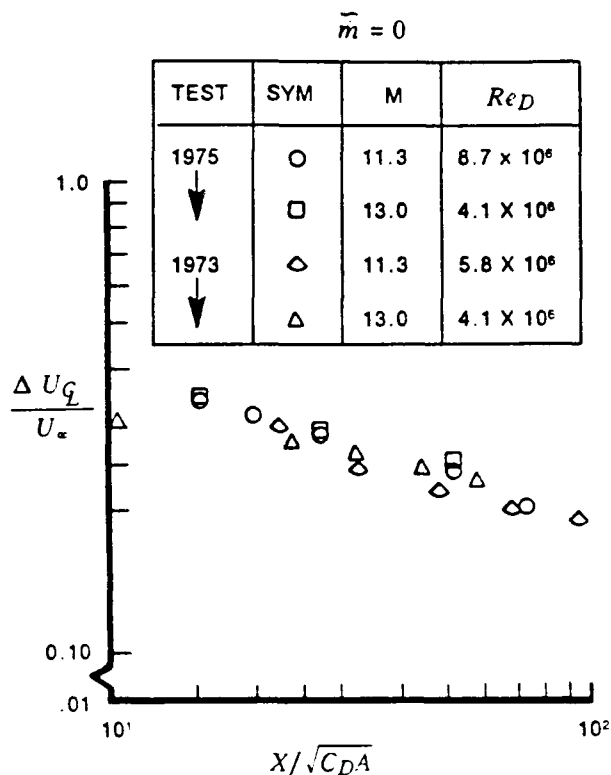


Figure 8. Comparison between velocity measurements made behind 6.7-inch-diameter and 10-inch-diameter cones

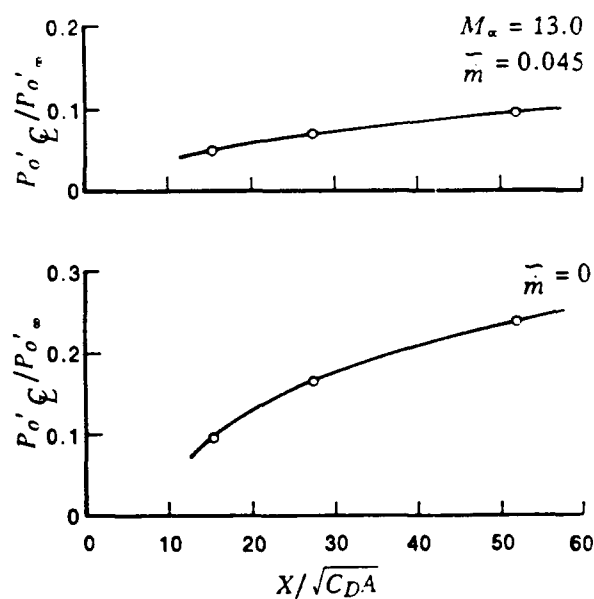


Figure 9b. Variation of pitot pressure on axis with $X/\sqrt{C_D A}$ and \tilde{m} at mach 13

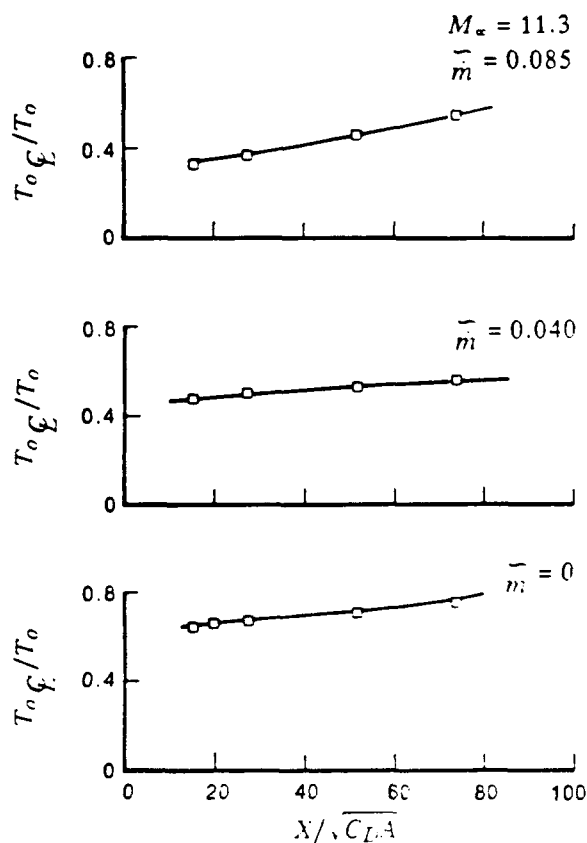


Figure 10a. Variation of total temperature on axis with $X/\sqrt{C_D A}$ and \bar{m} at mach 11.3

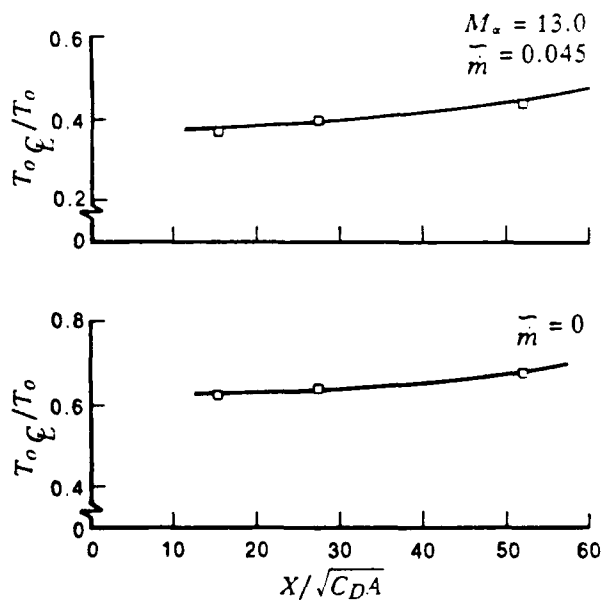


Figure 10b. Variation of total temperature on axis with $X/\sqrt{C_D A}$ and \bar{m} at mach 13

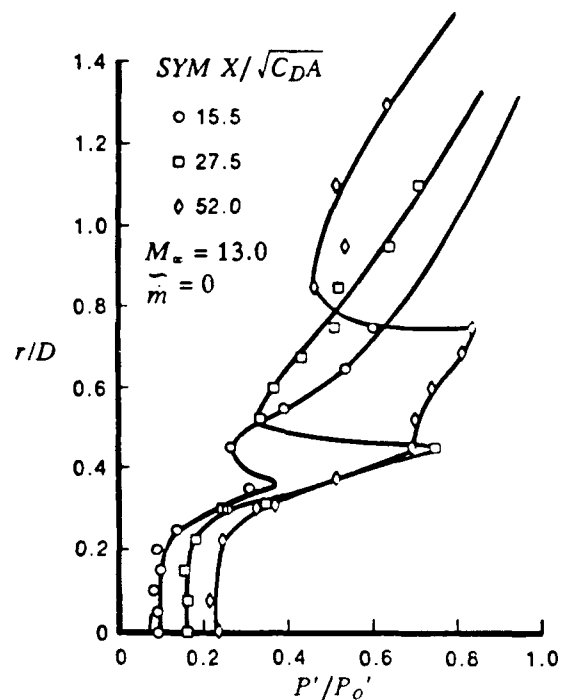


Figure 11a. Variation of pitot pressure distribution with downstream distance, $\bar{m} = 0$

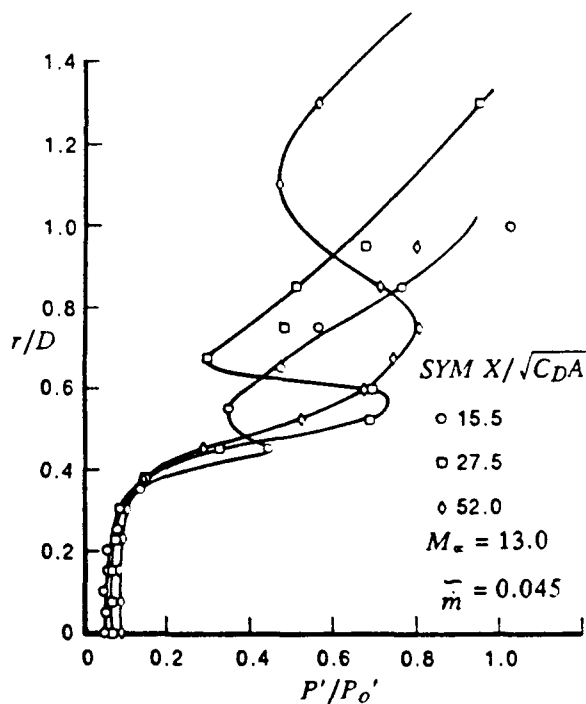


Figure 11b. Variation of pitot pressure distribution with downstream distance, $\bar{m} = 0.045$

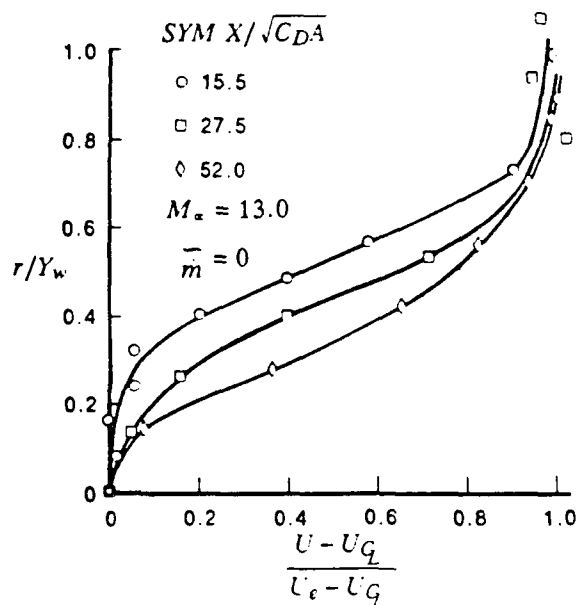


Figure 12. Development of velocity profile with downstream distance

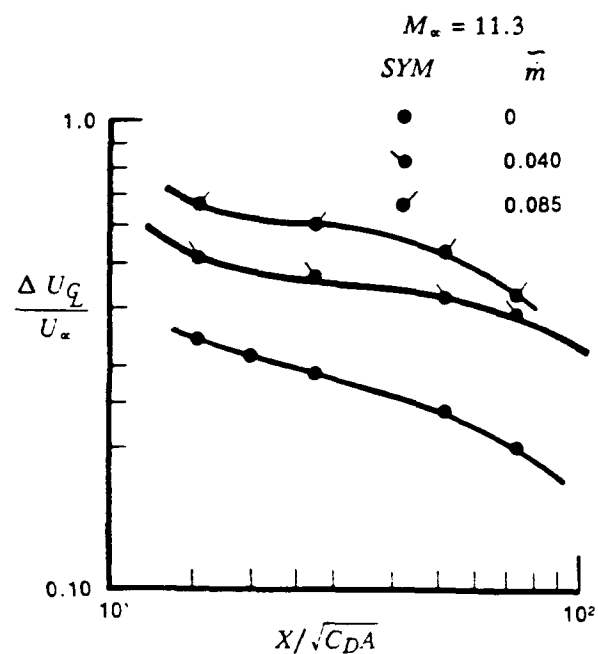


Figure 14a. Variation in centerline velocity defect with \bar{m} at mach 11.3

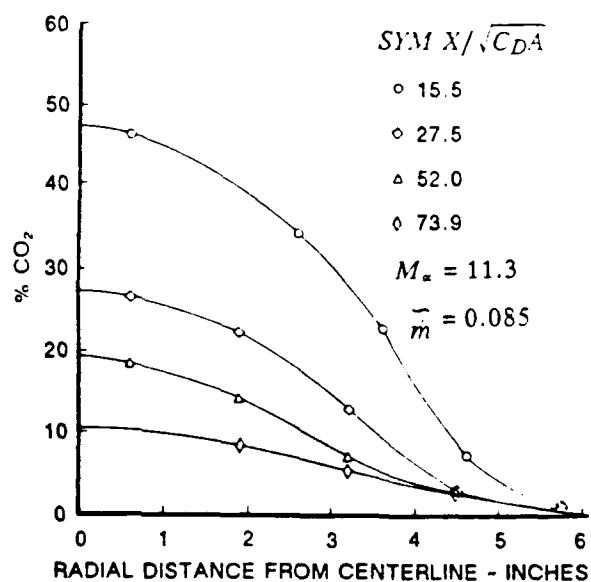


Figure 13. Radial distribution of CO_2 concentration

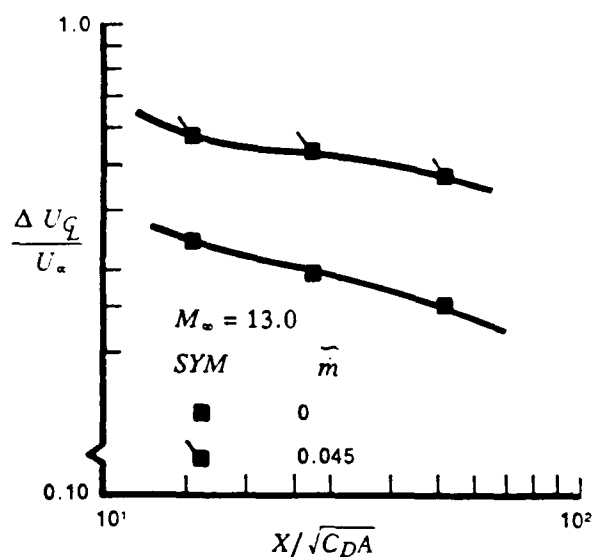


Figure 14b. Variation in centerline velocity defect with \bar{m} at mach 13

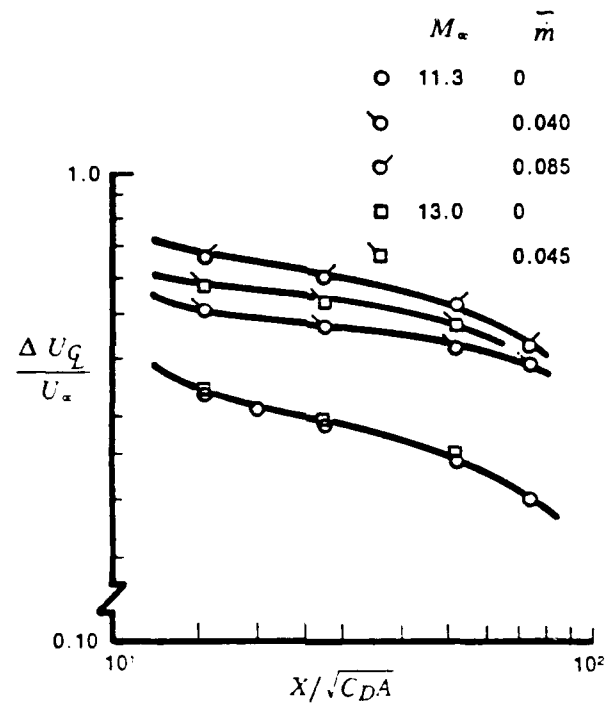


Figure 15. Comparison between axis velocity measurements at mach 11.3 and mach 13

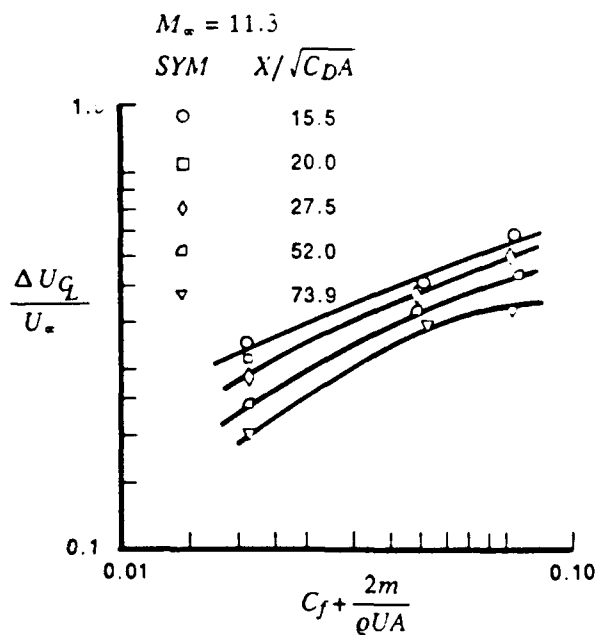


Figure 16. Variation of centerline velocity defect with $C_f + \bar{m}$ at mach 11.3

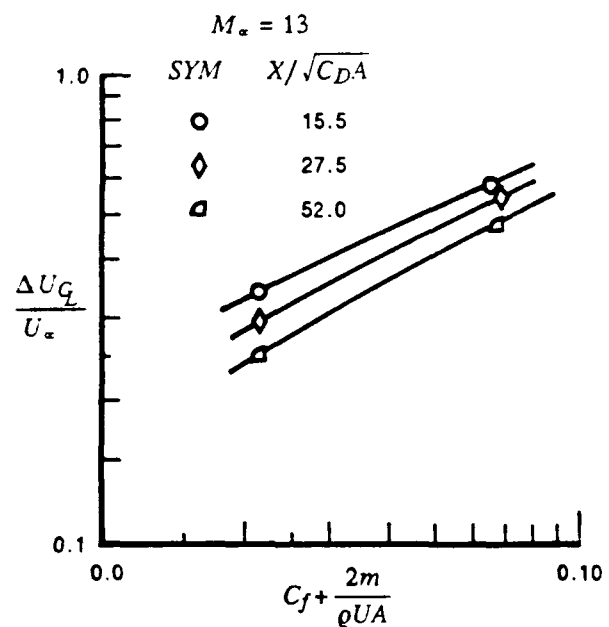


Figure 17. Variation of centerline velocity defect with $C_f + \bar{m}$ at mach 13

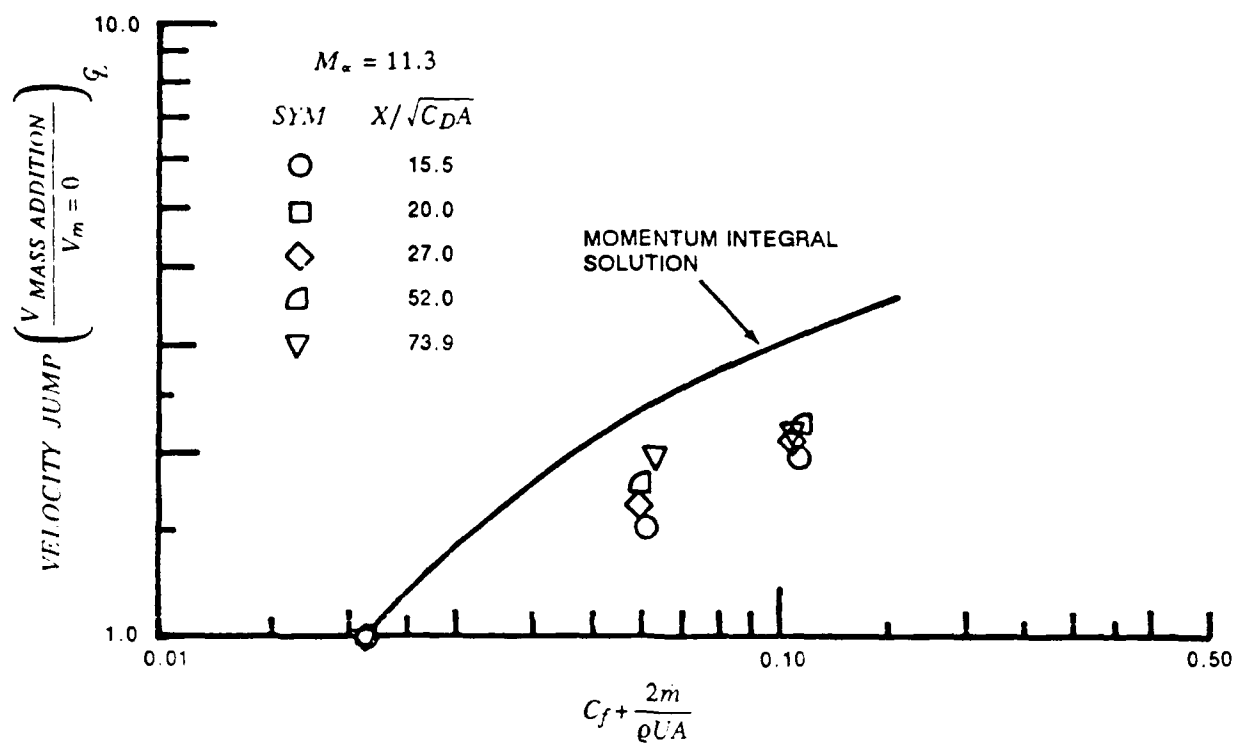


Figure 18. Velocity jump from turbulent to turbulent with mass addition

SYM	$X / \sqrt{C_D A}$	SOURCE
□	52.0	CALSPAN
▽	73.9	CALSPAN

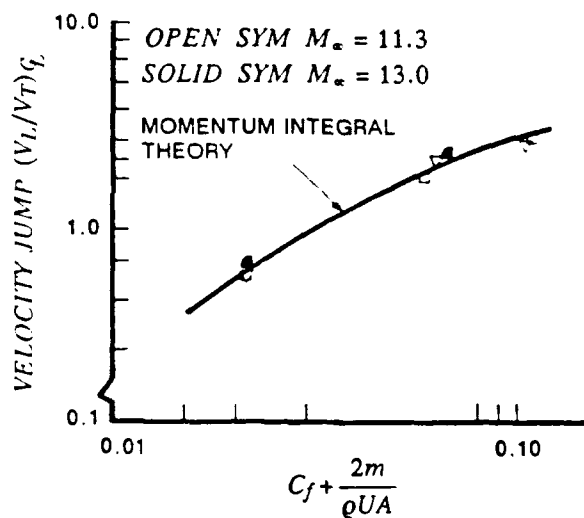


Figure 19. Velocity jump from laminar to turbulent boundary layers with mass addition

APPENDIX 6

**STUDIES OF THE MEAN AND UNSTEADY STRUCTURE OF
TURBULENT BOUNDARY LAYER SEPARATION
IN HYPERSONIC FLOW**



AIAA 91-1778

**Studies of the Mean and Unsteady
Structure of Turbulent Boundary Layer
Separation in Hypersonic Flow**

M.S. Holden

Calspan-University at Buffalo Research Center
Buffalo, NY

**AIAA 22nd Fluid Dynamics, Plasma Dynamics
& Lasers Conference**

June 24-26, 1991 / Honolulu, Hawaii

STUDIES OF THE MEAN AND UNSTEADY STRUCTURE OF TURBULENT BOUNDARY LAYER SEPARATION IN HYPERSONIC FLOW*

M.S. Holden**
Calspan-UB Research Center
P.O. Box 400
Buffalo, NY 14225

Abstract

An experimental study in which surface and flowfield measurements were made has been conducted to examine the structure of turbulent flow separation over large cone/flare configurations. This study was conducted in Calspan's 96-Inch Shock Tunnel, at Mach numbers of 11, 13 and 16, and at Reynolds numbers up to 100×10^6 . Surface heat transfer and pressure measurements were made in attached and separated flows at the cone/flare junction for 30° and 36° flare angles. Flowfield surveys were made in the separated region with pitot pressure and total temperature rakes. Holographic interferometry and Schlieren photography were used to obtain details of the flowfield structure. This study suggests that, in hypersonic flow, the separation region extends only a very small fraction of the boundary layer thickness and is a highly unsteady process. Only by employing instrumentation with frequency response high enough to follow the unsteady movement of the separation shock is it possible to determine the fundamental structure of flow separation in turbulent hypersonic flows.

1. Introduction

The emergence of advanced high-speed computing capabilities and numerical techniques, coupled with major increases in the need for numerical solutions to the full and reduced Navier-Stokes equations, has resulted in a refocusing of both pure and applied experimental research. Direct experimental simulation of complete aerodynamic configurations has in the past been the backbone of design efforts for new aerospace vehicles. However, recent applied experimental research has been increasingly directed toward acquiring more detailed measurements on segments of such configurations for code "validation" purposes. This is particularly true for hypersonic

vehicle design, where complete experimental simulation is difficult above Mach 13. Likewise, in pure research, the role of recent experiments has been increasingly one of providing insight into the macroscopic modeling of the flow (e.g., turbulence modeling) rather than as a means of constructing and validating gross flowfield models. In both cases, there is an increasing emphasis on the determination of flowfield properties, which, in many cases, provides the more direct and definitive evaluation of the modeling employed in the codes. Also, the increased emphasis on turbulent interacting and separated flows has resulted in a key need for time-resolved measurements over a broad frequency range. These requirements place a premium on flow quality and duration of tests, as well as on sophisticated high-frequency surface and flowfield instrumentation.

Recently, intense use of numerical solutions of full or reduced time-averaged Navier-Stokes equations has resulted in significant progress in the development of efficient and stable numerical algorithms and in greater understanding of gridding techniques. However, little real progress has been made in developing the fluid mechanical models required for these codes. In many instances, the phenomena of greatest importance in the aerothermal design of advanced vehicles are also the most difficult to model in the codes. The aerothermal loading and flowfield distortion that often accompany regions of viscous/inviscid interaction in hypersonic flow present some of the most important and difficult problems for both the designer and the predictor. Compressibility effects, shock/turbulence interaction, and the gross instabilities associated with separated flows must also be studied. In hypersonic flows, modeling of turbulence in regions of strong pressure gradients, embedded shocks, and separated flow is a key problem.

* This work was supported by the U.S. Air Force under AFOSR Contract No. AFOSR-88-0223. This paper is declared a work of the U.S. Government and is not subject to copyright protection in the United States.

** Staff Scientist; Associate Fellow, AIAA

To provide the information required to construct and verify the turbulence models used in the codes, flowfield measurements and direct measurements of skin friction and heat transfer must be obtained. Surface pressure data provide little information to validate codes and do not provide insight for turbulence modeling. To understand the structure of hypersonic turbulent boundary layers and shear layers as well as boundary layer separation in regions of shock wave/boundary layer interaction, we must understand the structure of the flow at the base of the boundary layer (at the wall and sublayer of the turbulent flow). For separated flows, such measurements can be made only with nonintrusive techniques with high spatial resolution on large models. As difficult as it is to make such measurements in high-enthalpy hypersonic flows, only by obtaining both the mean and fluctuating components of these flows can sufficient evidence be obtained to construct meaningful models of these flows.

For the last four years, we have embarked upon a program to design, develop, and construct the experimental tools required to: (i) make mean and fluctuating surface and flowfield measurements, and (ii) provide the insight and model validation required to develop detailed numerical solutions that would form the basis for future predictive capabilities. We have also pursued design studies and a shock tunnel modification program to provide a test capability tailored to generate flows of the highest quality and duration for fundamental studies of turbulent hypersonic flows. Instrumentation already developed includes miniature pitot pressure and total temperature probes for high-enthalpy, high Reynolds number flows, and a range of unique surface instrumentation. Two flowfield measurement techniques have also been developed specifically for shock tunnel studies of high Reynolds number hypersonic flows. Electron-beam fluorescence instrumentation was developed specifically to make mean and fluctuating density measurements in turbulent boundary layers at pressures up to 100 torr. Holographic interferometry techniques are being developed to measure flowfields in complex shock interaction regions. Presently, we are constructing and testing a series of unique models that will enable us to develop and explore the flow phenomena that we believe are central to developing prediction techniques that accurately describe complex interacting turbulent flows, with embedded separated regions.

This paper describes a program of experimental research to examine the mean and fluctuating boundary and shear layer structures in regions of strong pressure gradient and flow separation over models in hypersonic flows. Section 2 describes the objective and design of the experimental program, and the facilities, test conditions, models, and instrumentation used in the study. The results of the preliminary study are described in Section 3. In Section 4, we discuss the design of our current program. The conclusions of the preliminary study are summarized in Section 5.

2. Experimental Program

2.1 Program Objectives and Design of the Experimental Study

The major objective of this study was to develop and use models and instrumentation to obtain detailed measurements of the profile characteristics of a turbulent boundary layer ahead of and through regions of flow separation induced by shock wave/boundary layer interaction over a large cone/flare configuration. Such measurements are of key importance in evaluating the theoretical modeling of the turbulent separation process in hypersonic flows. As discussed in the introduction, current turbulence models are incapable of describing the complex development of turbulence in regions of strong pressure gradients and boundary layer separation in hypersonic flow. For these flows, we believe that compressibility, shock/turbulence interaction, and gross flow unsteadiness are important under hypersonic highly cooled wall conditions. In hypersonic high Reynolds number flows over highly cooled walls, the "wall layer," in which our earlier studies¹ have suggested separation first takes place, and which contains the principal information on the character of the boundary layer, is very thin. Boundary layer thicknesses of over 1 inch are required to enable this layer to be probed with the required resolution. While turbulent boundary layers originating on the walls of hypersonic nozzles have been used as sources of thick turbulent boundary layers in experimental studies, it has been shown that significant turbulent non-equilibrium effects can exist in these nozzle flows². The distortion of the structure and turbulent characteristics of the boundary layer generated through the strong expansion in the nozzle can persist well downstream of the nozzle exit plane and can significantly influ-

ence the characteristics of a separating turbulent boundary layer.¹ For this reason, we elected to perform a study to examine the characteristics of the constant-pressure turbulent boundary layer ahead of and in regions of shock wave/boundary layer interaction on a large slender cone/flare configuration in the large contoured "D" nozzle in the Calspan 96-Inch Shock Tunnel. The technique employed in the design of the "D" nozzle, and indeed most contoured nozzles, is such that the test core is a cone-shaped region of uniform flow that originates well upstream of the exit plane. Thus, by designing a conical model so that it can be fit within this uniform conical region, it is possible to develop a constant-pressure boundary layer over a large conical model that extends well into the contoured nozzle. The ultimate objective of the overall program is to obtain both mean and fluctuation measurements on the surface and across the turbulent layer. However, during this preliminary study, we concentrated on obtaining measurements of the mean properties across the viscous layer—more specifically, measurements of the pitot pressure, total temperature, total heat transfer rate, and (using holographic interferometry) the mean density distribution.

2.2 Experimental Facilities and Test Conditions

The experimental study was conducted in the Calspan 96-Inch Shock Tunnel at Mach 11, 13, and 16 for Reynolds numbers from 30×10^6 to 80×10^6 . Under these conditions, the boundary layer is fully turbulent well upstream of the cone/flare junction, and, as discussed in the following section, the measurements of heat transfer were in good agreement with prediction techniques based on a large number of measurements on highly cooled walls in high Reynolds number hypersonic flows. The test conditions at which the studies were conducted are listed in Table 1.

The facility and its performance characteristics are described in Reference 3. The shock tunnel is basically a "blowdown tunnel" with a shock compression heater. The 96-inch shock tunnel used in this study is shown in Figure 1a. The operation of the shock tunnel in the reflected-shock mode is shown with the aid of the wave diagram in Figure 1b. The tunnel is started by rupturing a double diaphragm, permitting high-pressure helium in the driver section to expand

Table 1
TEST CONDITIONS, LARGE 6° CONE

	AIR			N ₂
	3,4,8	6,7	9	5,10-15
M_i	3.345E+00	3.633E+00	4.200E+00	2.635E+00
p_o (psia)	7.216E+03	1.760E+04	1.705E+04	5.430E+03
H_o (ft ² /sec ²)	1.825E+07	2.147E+07	2.795E+07	1.287E+07
T_o (°R)	2.717E+03	3.104E+03	3.875E+03	1.939E+03
M	1.096E+01	1.301E+01	1.543E+01	1.111E+01
U (ft/sec)	5.922E+03	6.458E+03	7.404E+03	4.981E+03
T (°R)	1.214E+02	1.026E+02	9.574E+01	8.065E+01
p_∞ (psia)	9.172E-02	7.345E-02	1.860E-02	6.698E-02
q_∞ (psia)	7.721E+00	8.712E+00	3.104E+00	5.800E+00
q_∞ (slug/ft ³)	6.340E-05	6.038E-05	1.631E-05	6.734E-05
μ_∞ (slug/ft/sec)	1.021E-07	8.634E-08	8.054E-08	6.783E-08
Re/ft	3.680E+06	4.544E+06	1.499E+06	4.945E+06
p_o' (pitot)(psia)	1.431E+01	1.619E+01	5.798E+00	1.070E+01

into the driven section. This generates a normal shock, which propagates through the low-pressure air. A region of high-temperature, high-pressure air is produced between this normal-shock front and the gas interface (often referred to as the contact surface) between the driver and driven gases. When the primary or incident shock strikes the end of the driven section, it is reflected, leaving a region of almost stationary, high-pressure, heated air. This air is then expanded through a nozzle to the desired freestream conditions in the test section.

The stagnation and freestream test conditions were determined based on measurements of the incident shock wave speed, U_i , the initial temperature of the test gas (in the driven tube), T_1 , the initial pressure of the test gas, p_1 , and the pressure behind the reflected shock wave, p_o . We calculated the incident shock wave Mach number, $M_i = U_i/a_1$, where the speed of sound, a_1 , is a function of p_1 and T_1 . The freestream Mach number, M_∞ , was determined from correlations of M_∞ with M_i and p_o . These correlations were based on previous airflow calibrations of the "D" nozzle used.

Freestream test conditions of pressure, temperature, Reynolds number, etc., were computed based on isentropic expansion of the test gas from the conditions behind the reflected shock wave to the freestream Mach number. Real gas effects were taken into account for this expansion under the justified assumption that the gas was in thermochemical equilibrium. In the freestream, the static temperature, T_∞ , was sufficiently low that the ideal gas equation of state, $p_\infty = \rho \bar{R} T_\infty$, was applicable, where \bar{R} is the gas constant for the test gas.

The stagnation enthalpy, H_o , and temperature, T_o , of the gas behind the reflected shock wave (shown as region 4 in Figure 1b) were calculated from:

$$H_o = (H_4/H_1)H_1 \text{ and } T_o = (T_4/T_1) T_1 \quad (1)$$

where (H_4/H_1) and (T_4/T_1) are functions of U_i (or M_i) and p_1 and are given in Reference 4 for air. H_1 was obtained from Reference 5 for air, knowing p_1 and T_1 .

The freestream static temperature was found from the energy equation, knowing H_o and M_∞ .

$$T_\infty = \frac{H_o}{c_p} \left(\frac{1}{1 + \frac{(\gamma-1)}{2} M_\infty^2} \right) \quad (2)$$

where $c_p = 6006 \text{ ft-lb/slug/R}^\circ$ and $\gamma = 1.40$.

The freestream static pressure was calculated from

$$p_\infty = \frac{P}{P_p} p_o \left(1 + \frac{(\gamma-1)}{2} M_\infty^2 \right) \left(\frac{-\gamma}{\gamma-1} \right) \quad (3)$$

$$\text{where } \frac{P}{P_p} = \frac{(p_\infty/p_o)_{\text{REAL}}}{(p_\infty/p_o)_{\text{IDEAL}}} \quad (4)$$

is the real gas correction to the ideal gas static-to-total pressure ratio as described in Reference 6. The sources for the real gas data used in this technique are References 7 and 8.

The freestream velocity was determined from

$$U_\infty = M_\infty a_\infty \quad (5)$$

$$\text{where } a_\infty = \sqrt{\gamma \bar{R} T_\infty} \quad (6)$$

the speed of sound.

The freestream dynamic pressure was found from

$$q_\infty = 1/2 \rho_\infty M_\infty^2 \quad (7)$$

and the freestream density then was calculated from the ideal gas equation of state

$$\rho_\infty = p_\infty / \bar{R} T_\infty \quad (8)$$

where $\bar{R} = 1717.91 \text{ ft-lb/slug/R}^\circ$ for air. Values of the absolute viscosity, μ , used to compute the freestream Reynolds number per foot were obtained using the technique described in Reference 4.

The test section pitot pressure, p_o' , was determined from q_∞ and the ratio (p_o'/q_∞) . This

ratio has been correlated as a function of M_∞ and H_o for normal-shock waves in air in thermodynamic equilibrium.

For the test conditions at which our study was conducted, the uncertainty in pitot pressure measurements from errors in calibration and recording is $\pm 2.5\%$. The reservoir pressure can be measured with an uncertainty of $\pm 2.0\%$, and the total enthalpy (H_o) can be determined from the driven tube pressure and the incident-shock Mach number with an uncertainty of $\pm 1.5\%$. These measurements combine to yield an uncertainty in the Mach number and dynamic pressure measurements of $\pm 0.8\%$ and $\pm 3.5\%$, respectively.

2.3 Models and Instrumentation

2.3.1 Cone/Flare Model

As discussed in the previous subsection, the large conical region of uniform flow that extends well into the contoured "D" nozzle allows us to generate a constant-pressure boundary layer on a conical model that extends into the nozzle.

For this study, we selected a large 6° cone with flares of 30° and 36° attached at its base. The cone/flare configuration is shown in Figure 2. The cone angle and length were selected, on the basis of calculations, to achieve the maximum length over which uniform constant-pressure flow could be established within the further constraints of tunnel blockage and sting loading. A diagram of the cone/flare model and its positioning within the "D" nozzle is shown in Figure 3. In an initial experiment to demonstrate that this large model could be used to produce the required flow, we obtained pressure and heat transfer for this model equipped with both sharp and blunt nosetips. The good agreement between the measured pressure and heat transfer distributions and theory for these configurations, shown in Figures 4 through 8, is described in Section 3 and demonstrates that the design and positioning of the model have produced the required testing environment.

2.3.2 Heat Transfer Instrumentation

Platinum thin-film instrumentation was used to obtain heat transfer measurements on the surface of the cone/flare model and as the sensing element of the 0.05-inch-diameter stagnation heating probes. Because each of these gages has a 1-MHz frequency response, it can be used to examine the unsteady characteristics of the turbulent boundary layer and separated region. The large

gradients that are generated along the walls and in the flow in the separation and reattachment region of shock wave/boundary layer interactions make it essential that distortion of the heat transfer distribution resulting from lateral heat conduction be minimized by employing models constructed with low-conductivity materials. The Pyrex-backed thin-film gages, with their high resolution, sensitivity, and frequency response, are almost ideal for this type of study. The platinum thin-film probes shown in Figure 9 were used, in conjunction with the total temperature instrumentation, to examine the structure of the turbulent boundary layer and shear layer.

The thin-film heat transfer gage is a resistance thermometer that reacts to the local surface temperature of the model. The first step of the data reduction was to convert the measured voltage time history for each gage to a temperature time history, taking into account the gage resistance, the current through the gage, the gage calibration factor, and the amplifier gain. The theory of heat conduction was used to relate the surface temperature to the rate of heat transfer. The platinum resistance element has negligible heat capacity and, hence, negligible effect on the Pyrex-substrate surface temperature. The substrate can be characterized as being homogeneous and isotropic. Furthermore, because of the short duration of a shock tunnel test, the substrate can be treated as a semi-infinite body. The final data reduction was done using the Cook-Felderman⁹ algorithm.

The Stanton number, C_H , based on the freestream conditions, was calculated from the following

$$C_H = \frac{\dot{q}}{\rho_\infty U_\infty (H_o - H_w)} \quad (9)$$

where H_w is the enthalpy at the measured wall temperature.

For the thin-film heat transfer instrumentation, the uncertainties associated with the gage calibration and the recording equipment are estimated to be $\pm 5\%$ for the levels of heating obtained in the preliminary study.

2.3.3 Pitot and Static Pressure

Instrumentation

Calspan-designed and constructed piezo-electric pressure transducers mounted in pitot pressure rakes, and beneath orifices in the model surface, were used to obtain the mean pitot pressure through the boundary layer and the static pressure along the surface, respectively. The pitot pressure gages had 0.030-inch orifices and were staggered as shown in Figure 9 to achieve a transverse spacing of 0.010 inch at the base of the boundary layer.

The pressures were converted to absolute pressures (psia) by adding the measured initial vacuum pressure in the test section. The latter was the reference pressure for the transducers. The pressures were then averaged over the time interval of steady flow to obtain an average value for each case. The values of the pressure coefficients, C_p , were calculated from

$$C_p = p / (1/2 \rho_\infty U_\infty^2) \quad (10)$$

where p was the measured model pressure (psia).

The uncertainties in the pressure measurements associated with the calibration and recording apparatus are $\pm 3\%$. Again, the variations associated with the unsteady nature of the fluid dynamics can be as large as $\pm 15\%$.

2.3.4 Total Temperature Instrumentation

A significant effort was devoted to the design and development of a total temperature gage that responded within 2 milliseconds, withstood the large static and dynamic pressures generated in regions of shock/boundary layer interaction in the shock tunnel flows, and was small enough to resolve the total temperature in the wall layer. The result of this development was a gage 0.030 inch in diameter that uses a 0.0005-inch butt-welded iron/constantan thermocouple in the arrangement shown schematically in Figure 10. The typical response of one of these gages (Figure 11) clearly shows that we have adequate time to obtain accurate measurement. A small amount of radiation (2% of full scale) is applied, and this factor is checked for measurements in the freestream, where the total temperature is known accurately. The gages were deployed in a staggered array (Figure 9) similar to that employed for the pitot pressure gages.

2.3.5 Flow Visualization

We used a single-pass Schlieren system with a focal length of 10 feet for flow visualization in these studies. The horizontal knife edge used in these studies was adjusted to give between 15% and 50% cutoff. A single microsecond spark was triggered close to the end of the steady run time. The tunnel windows have 16-inch diameters.

3. Results and Discussion

The experimental study had two objectives. First, we sought to generate a model and environment in which we could establish a thick, well-developed and defined turbulent boundary layer under constant-pressure conditions. We then sought to design, develop, and use instrumentation to obtain mean and fluctuating profile measurements: first, in the constant-pressure boundary layer; then, in regions of strong adverse pressure gradient in regions of shock wave/boundary layer interaction generated at a cone/flare junction. In the preliminary study, we employed two cone/flare configurations, one (a 30° flare) that promoted a flow close to incipient separation, and a second (a 36° flare) that promoted a well-separated flow.

The measurements of the heat transfer and pressure distributions over the two cone/flare configurations are shown in Figures 4 through 8. The measurements of the pressure along the entire length of the cone were in good agreement with predictions based on Sim's solutions for a sharp cone, and the pressures at the back of the flare were in good agreement with calculations based on an inviscid shock compression from the cone to the flare, as shown in Figures 5 and 6. Based on comparisons and correlations with a large number of heat transfer and skin friction measurements made on flat plates and cones in the shock tunnels and in other high Reynolds number hypersonic facilities, we have found that predictions based on the Van Driest(II) technique¹⁰ are in best agreement for hypersonic flows over highly cooled walls. The Van Driest method is based on a transformation to relate measurements in compressible flow to those in incompressible flow. Here, the measured coefficient of local skin friction and heat transfer rate (C_f and C_H) are related to an equivalent quantity in an incompressible flow (C_{f_i} and C_{H_i}) through the relationships

$$C_{f_i} = F_c \left(M_e, \frac{T_w}{T_o} \right) C_f \quad \text{and} \quad C_{H_i} = F_c \left(M_e, \frac{T_w}{T_o} \right) C_H$$

The local Reynolds numbers, Re_θ and Re_x , based on the momentum thickness, θ , and on the distance from the virtual origin, X_v , respectively, are related to similar quantities in the incompressible plane through the relationships

$$\begin{aligned} F_c C_f &= F_\theta Re_\theta \\ F_c C_H &= F_x Re_x \end{aligned}$$

We have assumed the Karman-Schoenherr¹¹ relationship

$$\log_{10}(Re_x C_{f_i}) = \log_{10}(2Re_\theta) = 0.242(C_{f_i})^{-1/2}$$

where the average skin friction, C_{f_i} , is related to the local skin friction, C_{f_l} , by

$$C_{f_i} = 0.242 C_{f_l} [0.242 + 0.8686(C_{f_l})^{1/2}]^{-1}$$

Van Driest's analysis is based on the Prandtl-Karman¹² mixing length model, together with a compressibility transformation, to describe the compressible turbulent boundary layer over a flat plate. From this analysis, the transformation or compressibility factors are

$$(F_c)_{VD} = rm_e (\sin^{-1} \alpha + \sin^{-1} \beta)^{-2}$$

$$(F_\theta)_{VD} = \mu_e / \mu_w$$

and

$$F_x = F_\theta F_c^{-1}$$

where

$$\alpha = (2A^2 - B)/(4A^2 + B^2)^{1/2} \quad \text{and} \quad \beta = B/(4A^2 + B^2)^{1/2}$$

and

$$A = \left[rm_e \left(\frac{T_w}{T_e} \right)^{-1} \right]^{1/2} \quad \text{and} \quad B = \left(1 + rm_e - \frac{T_w}{T_e} \right) \left(\frac{T_w}{T_e} \right)^{-1}$$

where a recovery factor, r , of 0.89 was used, and $m_e = \frac{\gamma-1}{2} M_e^2$.

To compare the prediction methods with the experimental measurements in the $C_f F_c - F_\theta Re_\theta$ plane, the momentum thickness, θ , must be calculated. We have used the relation-

ship from the momentum equation $\theta = \int_0^x C_f / 2 dx$ to calculate this quantity. For our measurements in transitional and turbulent flows, we found that the Reynolds analogy factor was close to unity, as shown in Figures 12 and 13. Thus, when only heat transfer measurements were available, we calculated the momentum thickness from the expression $\theta = \int_0^x C_H dx$.

In correlating the measurements made on the conical models in the expression $F_c C_H - F_{R_x} Re_x$, we employed the Mangler¹³ transformation in the form suggested by Bertran and Neal¹⁴ to relate the measurements on the cones to an equivalent two-dimensional flow. For an equal distance from the virtual origin of the turbulent boundary layer on flat plates and cones, the local Stanton number on the cone would be larger than that on a flat plate by the ratio

$$\begin{aligned} \frac{(C_H)_{conc}}{(C_H)_{fp}} &= \left(\frac{2n-1}{n-1} \right)^{1/n} \left[\left(1 + \frac{R_{xv}}{R_x} \right) \right. \\ &\quad \left. - \frac{R_{xv}}{R_x} \left(\frac{R_{xv}/R_x}{1 + (R_{xv}/R_x)} \right)^{n/(n-1)} \right]^{1/n} \end{aligned}$$

where $n = 0.429 + 0.404 \ln(F_x \cdot Re_x)$.

By employing the above equation, the measurements on the conical bodies were transformed into the equivalent two-dimensional compressible plane, and, subsequently, to the incompressible plane.

A typical comparison between a large body of heat transfer measurements obtained earlier and the Van Driest approach is shown in Figure 14. The good agreement between the heat transfer measurements on the large cone and the Van Driest prediction technique suggests that, at both Mach 11 and 13 (shown in Figures 12 and 13), the boundary layers are well developed.

Flowfield surveys were made to determine the distributions of pitot pressure, total temperature, and total heat transfer at a number of stations through the interaction region at each of the flow conditions described above. Figures 15 and 16 show the pitot and total temperature measurements for the Mach 11 condition with a 30° flare. The profiles, which were obtained at 2, 1.2, 0.8, and 0 inches ahead of the cone/flare junction, indicate that there is very little upstream influence

at this condition. (A similar set of measurements for the 36° flare is shown in Figures 17 and 18.)

$$\frac{T}{T_w} = 1 + \left[(1 - C_t)(1 + m_e) \frac{T_e}{T_w} - 1 \right] \frac{u}{u_e} + \frac{T_e}{T_w} \left[C_t \left(\frac{1 + m_e}{m_e} \right) - 1 \right] m_e \left(\frac{u}{u_e} \right)^2$$

$0 < C_t < 0.5$; $C_t = 0$ for Crocco, $C_t = 0.5$ for quadratic.

These measurements are compared with the Crocco relationship between enthalpy and velocity in Figure 19. It is clear that our measurements follow a parabolic relationship

$$\frac{\bar{p}_{wake}}{\bar{p}_{cone}} = \left[\frac{(\gamma + 1) M_b^2}{2} \right]^{\frac{\gamma}{\gamma - 1}} \cdot \left[\frac{\gamma + 1}{2\gamma M_b^2 - (\gamma - 1)} \right]^{\frac{1}{\gamma - 1}} \frac{u_b}{u_e} = \left(\frac{M_b}{M_e} \right) \left(\frac{T_{ob}}{T_{oe}} \right)^{1/2} \left(\frac{1 + m_b}{1 + m_e} \right)^{1/2}$$

rather than Crocco's linear relationship

$$\frac{T_e}{T_w} = 1 + B \left(\frac{u}{u_e} \right) - A^2 \left(\frac{u}{u_e} \right)^2$$

In the past, it has been assumed that the "fuller than Crocco" velocity profile obtained in studies over tunnel walls was associated with turbulent nonequilibrium effects related to the strong favorable pressure gradient upstream on the nozzle wall; however, no such explanation can be advanced to explain our results.

Of the transformation techniques that have been postulated to cast the compressible flow measurements into an equivalent incompressible form, the relationships derived by Van Driest have received the greatest support. Van Driest starts with the assumption that the Crocco relationship is valid and uses the mixing length theory to calculate the Reynolds stresses in the flow. By inspection, the transformation is

$$\frac{u^*}{u_e} = \frac{1}{A} \sin^{-1} \left(\frac{2A^2 \frac{u}{u_e} - B}{(B^2 + 4A^2)^{1/2}} \right) + \frac{1}{A} \sin^{-1} \left(\frac{B}{(B^2 + 4A^2)^{1/2}} \right)$$

The original form of the incompressible law of the wall relationship is

$$\frac{u^*}{u_\tau} = \frac{1}{K} \ln y^* + C$$

However, because the wake region of the flow is so extensive, Maisie and McDonald¹⁵ have suggested that the Coles¹⁶ wake function be included:

$$\frac{u^*}{u_\tau} = \frac{1}{K} \ln y^* + C + \frac{\pi}{K} W \left(\frac{y}{\delta} \right)$$

They, in fact, suggest a defect form of this relationship:

$$\frac{u_e^* - u^*}{u_\tau} = f \left(\frac{y}{\delta} \right) = \frac{1}{K} \ln \left(\frac{y}{\delta} \right) + C(2 - W)$$

Comparisons between our measurements in each of the incompressible formats are shown in Figures 20 and 21. It is clear that the transform is not as successful at these high Mach numbers as it has been below Mach 5. Comparisons between the measurements and these prediction techniques in the compressible plane are shown in Figure 22. It can be seen that this is a relatively insensitive way of examining the measurements.

4. Ongoing Studies

We are now studying the mean and fluctuating turbulent flow structure over two basic flow axisymmetric configurations: (i) a large cone/flare model (Figure 23) and (ii) an axisymmetric curved compression ramp (Figure 24). The measurements made in each of these flows are designed principally to examine the response of the turbulent flow structure in a flow strained by an adverse pressure gradient—in one case, with a strong embedded shock system. Flowfield measurements with both non-intrusive and intrusive instrumentation are focused on obtaining the streamwise variation of turbulent scale size through the interaction regions. We are examining the surface and flowfield fluctuation measurements to determine shock/turbulence interaction and the magnitude and mechanisms of large-scale flow instabilities in separated interaction regions. Direct measurements of density and density fluctuation with the electron-beam fluorescence equipment enable us to determine directly the magnitude of turbulent compressibility effects in these flows. The experimental studies are being conducted at freestream Mach numbers of 11, 13, and 15, which give conditions on the cone from

Mach 9 to 12 where we believe compressibility effects are of importance. The large model scale enables us to obtain boundary layer thicknesses up to 2 inches, which give good resolution at the base of the viscous layer as well as generate high Reynolds number, fully turbulent flows.

The models are equipped with high-frequency heat transfer, skin friction, and pressure instrumentation. The major flowfield instrumentation is electron-beam fluorescence equipment, installed as shown schematically in Figure 25. The traverse mechanism shown in Figure 26 enables flowfield measurements to be made at streamwise stations encompassing the complete interaction region. High-frequency thin-film, pitot pressure, and total temperature measurements can be made at each streamwise station of interest. The large aperture optical system being used is designed to enable us to record and analyze turbulent fluctuation measurements up to 1 MHz. These optics give us the ability to obtain a 0.010-inch resolution across the 1.5-inch boundary layer, as shown in Figure 27.

Detailed flowfield fluctuation measurements are being made for three cone/flare configurations to obtain attached, incipient separated, and well-separated flow, respectively. Figure 26 shows the basic cone/flare model configuration with the electron-beam optics installed and the separated flow generated by a 36° ramp (flare). Two additional ramp angles, of 30° and 28° are being employed in these studies. Additional studies of the response of turbulence to adverse pressure gradients are being conducted for the axisymmetric curved compression ramp model shown in Figure 28. Here, the turbulence is not subjected to as great an adverse pressure gradient, and we do not expect the shock/turbulence interaction associated with the shock system embedded within the boundary layer to be as significant.

Double-pulsed holographic interferometry is being used to determine both the mean flowfield density distribution and, with pulse separations of the order of 1 microsecond, the variation of turbulent scale size through the interaction region. The mean distributions of flow properties across the boundary layers and shear layers are being determined from the probes and from the electron-beam and interferometry measurements, so we have a number of independent ways of calculating the same property. For example, the mean density can be deduced independently from measurements using the electron beam, using in-

terferometry, and using a combination of total temperature and total pressure measurements. Static temperatures can be determined directly from the electron-beam measurements and from a combination of probe measurements. The major efforts in analysis of the measurements are being directed to definition of the turbulent and unsteady structure of these flows. Knowledge of the streamwise and transverse variations of turbulent scale size through the interaction regions is of key importance to the evaluation of the models of turbulence. Scale size measurements are to be determined independently from cross-correlations of transverse-fluctuation measurements with those obtained using electron-beam, pitot pressure, and thin-film instrumentation. Turbulent spectra will also be obtained from the various measurement techniques to provide the correlations required for evaluating the turbulence models and for providing insight into the fluid mechanics associated with compressibility effects, shock/turbulence interaction, and large-scale flow unsteadiness.

5. Summary and Conclusions

An experimental study has been conducted to examine the detailed flowfield structure of a separated boundary layer flow over a large cone/flare model. In this study, the structure of the separating boundary layer was examined with pitot, total temperature, and laser holography measurements. These measurements suggest that the total temperature/velocity relationship in the cone boundary layer is quadratic rather than the usually assumed linear form suggested by Crocco. The Van Driest transformation, which has been used successfully in supersonic flows over adiabatic walls to relate the measured velocity to similar measurements in subsonic flow, is apparently not as effective in hypersonic flows over highly cooled walls. The measurements portray the rapid change in the structure of the sublayer as separation takes place, as well as the formation of strong shock waves in the turbulent shear layer.

Studies are now being made to examine the mean and fluctuating characteristics of boundary layers and separated shear layers in regions of adverse pressure gradient and shock wave/turbulent boundary layer interaction. In these studies, conducted at Mach numbers between 8 and 16, high-frequency heat transfer, skin friction, and pressure measurements are being made on a large cone/flare model and an axisymmetric curved

compression ramp model. Flowfield measurements are also being made with high-frequency pitot pressure, hot-film, and total temperature instrumentation, and advanced electron-beam fluorescence and holographic interferometry techniques will be used to make non-intrusive measurements of the mean and fluctuating density and the static temperature distributions throughout the flowfields.

Nomenclature

A	As Defined in Section 3
a	Speed of Sound
B	As Defined in Section 3
C	Constant
C_F	Average Skin Friction Coefficient
C_f	Local Skin Friction Coefficient
C_H, CH	Stanton Number
C_p, CP	Pressure Coefficient
c_F	Specific Heat at Constant Pressure
C_t	As Defined in Section 3
F_c	As Defined in Section 3
F_R	As Defined in Section 3
F_θ	As Defined in Section 3
H	Total Enthalpy
K	Mixing Length Constant
M	Mach Number
m	$= \frac{\gamma - 1}{2} M^2$
p	Pressure
p_0'	Pitot Pressure
q	As Defined in Section 3
\dot{q}	Heat Transfer Rate
q_∞	Dynamic Pressure
\bar{R}	Gas Constant
Re	Reynolds Number
Re_θ	As Defined in Section 3
T	Temperature
U	Velocity
u_τ	$= (\tau_w / \rho_w)^{1/2} = u_e \left(\frac{C_f T_w}{2 T_e} \right)^{1/2}$
W	Wake Function
X_y	Distance from Normal Origin

y	Normal Distance from Surface
y^*	As Defined in Section 3

GREEK SYMBOLS

γ	Ratio of Specific Heat
δ	Boundary Layer Thickness
δ_F, δ_{FLARE}	Flare Angle
θ	Momentum Thickness
μ	Viscosity
π	As Defined in Section 3
ρ	Density

SUBSCRIPTS

b	Boundary Layer
BE	Beginning-to-End
C	As Defined in Section 3
c	As Defined in Section 3
$conc$	Cone Value
e	Edge
f_F	Flat-Plate Value
i	Incident
i	Incompressible
$IDEAL$	Ideal Gas
P	Perfect Gas
$REAL$	Real Gas
VD	Van Driest
w	Wall
x	Distance from Virtual Origin
ξ	As Defined in Section 3
0	Stagnation Value
1	Initial Value
$1, 4$	Regions 1 and 4 As Defined in Figure 1(b)
∞	Freestream Value

SUPERSCRIPIT

\cdot	Incompressible Conditions
---------	---------------------------

References

1. Holden, M.S., "Shock-Wave Turbulent Boundary Layer Interaction in Hypersonic Flow," AIAA Paper No. 72-74, Presented at AIAA 10th Aerospace Sciences Meeting, San Diego, CA, 17-19 January 1972.

2. Knight, D., "Improved Calculation of High-Speed Inlet Flows: Part I. Numerical Algorithm and Part III. Results," *AIAA Journal*, Vol. 19, pp. 34-41, 1972-1979, 1980.
3. "Calspan Hypersonic Shock Tunnel, Description and Capabilities Brochure," 1975.
4. Lewis, C.H. and Burgess, E.G., III, "Charts of Normal Shock Wave Properties in Imperfect Air (Supplement M = 1 to 10)," AEDC-TR-196, September 1965.
5. Hilsenrath, J., et al., "Tables of Thermal Properties of Gases," NBS Circular 565, 1955.
6. Reece, J.W., "Test Section Conditions Generated in the Supersonic Expansion of Real Air," *Journal of Aeronautical Sciences*, Vol. 29, No. 5, May 1962, p. 617, 618.
7. Hilsenrath, J., et al., "Tables of Thermodynamic Properties of Air Including Dissociation and Ionization from 1500°K to 15,000°K," AEDC-TR-59-20, December 1959.
8. Neil, C.A. and Lewis, C.H., "Interpolations of Imperfect Air Thermodynamic Data, II — at Constant Pressure," AEDC-TDR-64-184, September 1964.
9. Cook, W.J., "Determination of Heat Transfer Rates from Transient Surface Temperature Measurements," *AIAA Journal*, Vol. 8, No. 7, July 1970, pp. 1366-1368.
10. Van Driest, E.R., "Problem of Aerodynamic Heating," *Aeronautical Engineering Review*, Vol. 15, No. 10, October 1956.
11. Schoenherr, K.E., "Resistance of Flat Surfaces Moving Through a Fluid," *Soc. of Naval Arch. and Marine Engrs. Trans.*, Vol. 40, pp. 279-313, 1932.
12. von Karman, T., *The Problems of Resistance in Compressible Fluids*, GALCIT Pub. No. 75, 1936.
13. Howarth, L., *Modern Developments in Fluid Dynamics*, Oxford University Press, NY, 1953, pp. 382-386.
14. Bertram, M.H. and Neal, L., Jr., "Recent Experiments in Hypersonic Turbulent Boundary Layers," NASA Report No. TMX-56335, May 1965.
15. Maise, G. and McDonald, H., "Mixing Length and Kinematic Eddy Viscosity in a Compressible Boundary Layer," AIAA Paper No. 67-199, January 1967.
16. Coles, D., "Measurements in the Boundary Layer on a Smooth Flat Plate in Supersonic Flow," Ph.D. Thesis, California Institute of Technology, 1953.

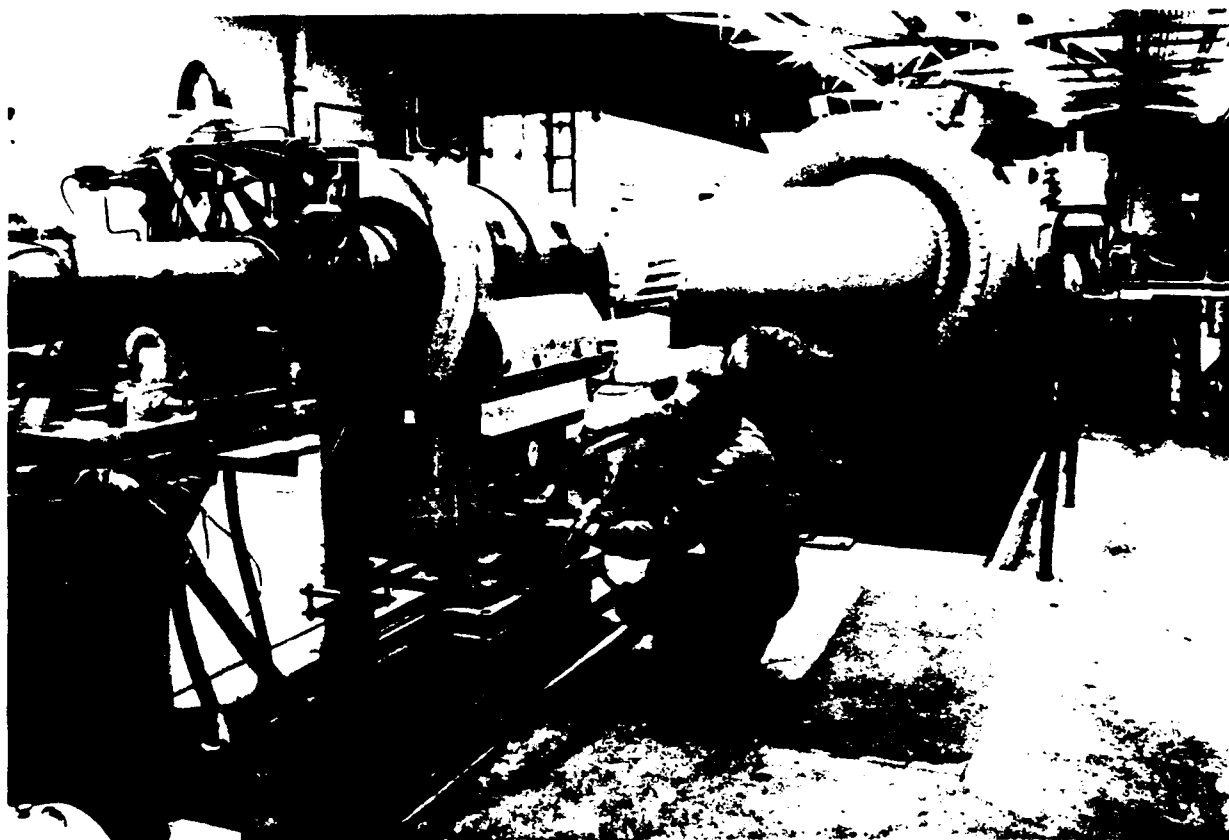


Figure 1 (a) CALSPAN'S 96-INCH SHOCK TUNNEL

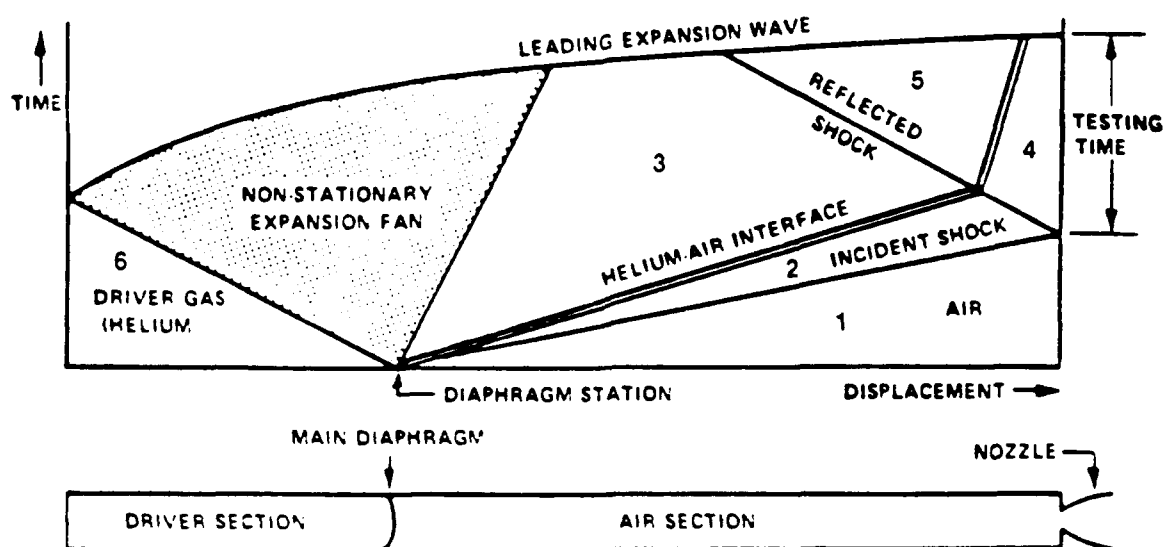


Figure 1 (b) WAVE DIAGRAM FOR TAILORED-INTERFACE SHOCK TUBE



Figure 2

**NINE-FOOT-LONG, SHARP 6° CONE/30° FLARE MODEL INSTALLED IN
CALSPAN'S 96-INCH SHOCK TUNNEL**

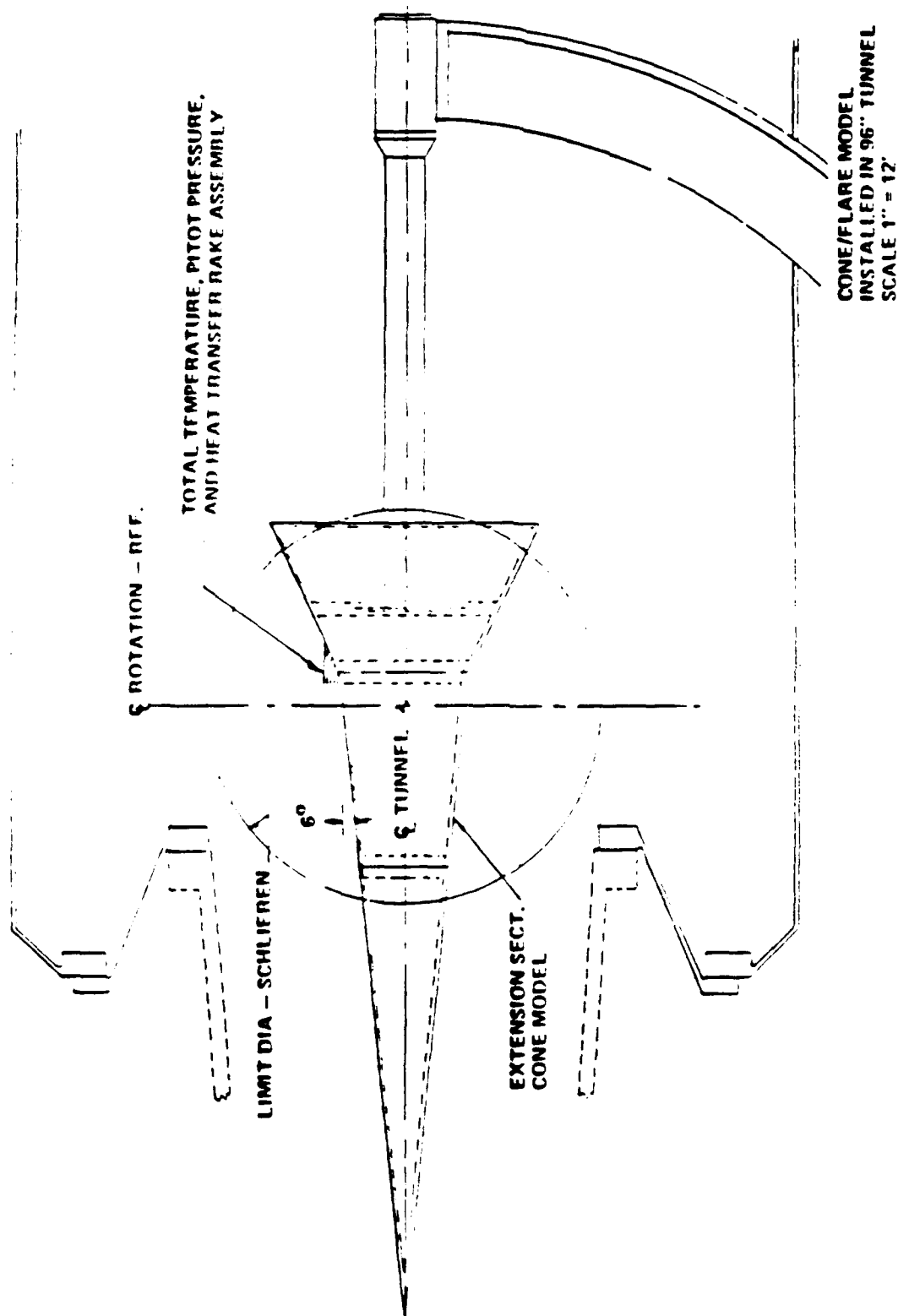


Figure 3 INSTALLATION DRAWING OF CONE/FLARE MODEL

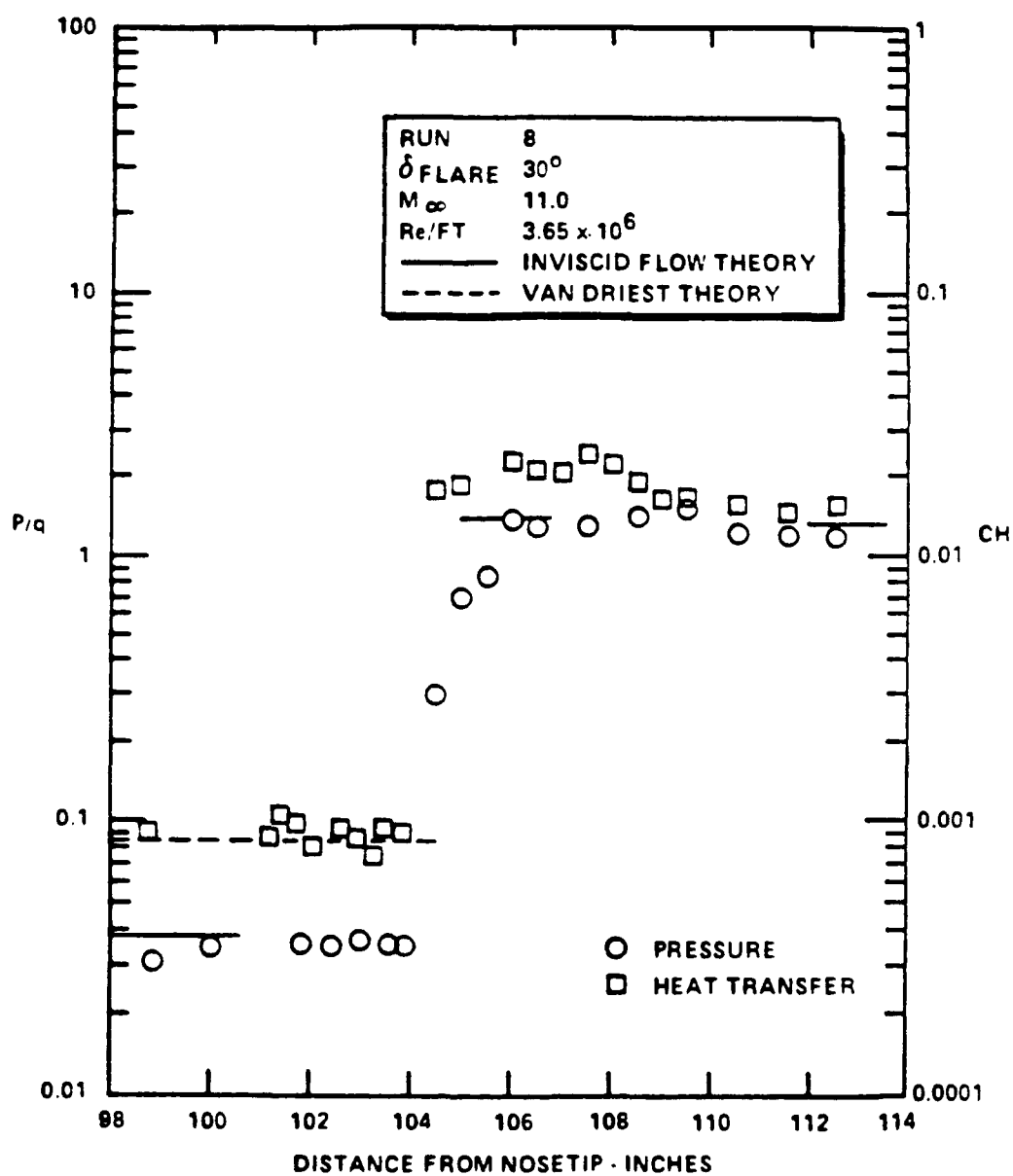
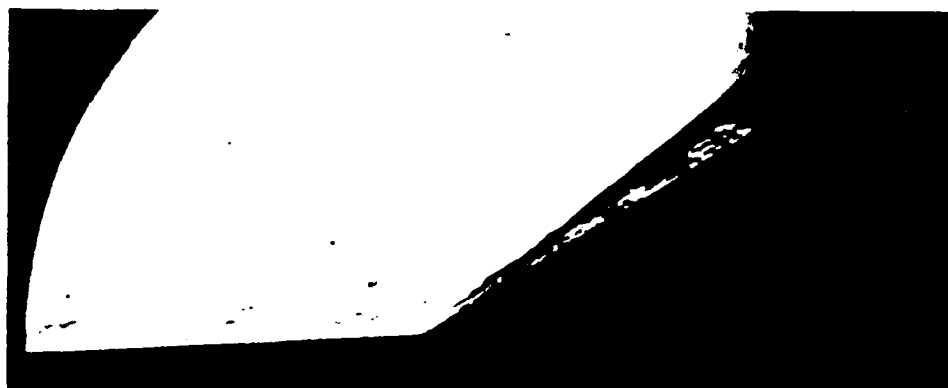


Figure 4 DISTRIBUTION OF PRESSURE AND HEAT TRANSFER IN ATTACHED FLOW OVER THE LARGE 6° CONE/ 30° FLARE CONFIGURATION

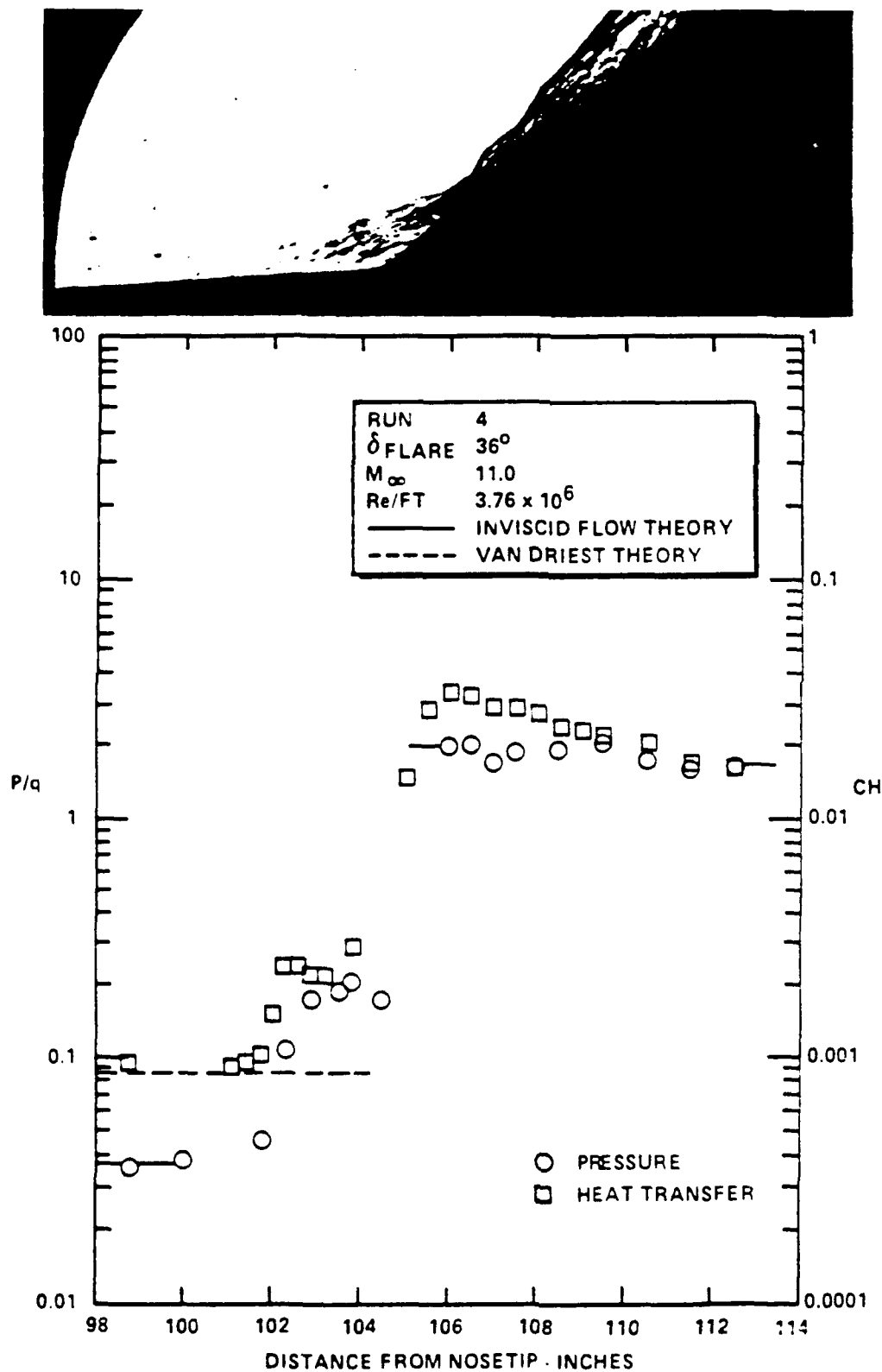


Figure 5 DISTRIBUTION OF PRESSURE AND HEAT TRANSFER IN SEPARATED FLOW OVER THE LARGE 6° CONE/ 36° FLARE CONFIGURATION

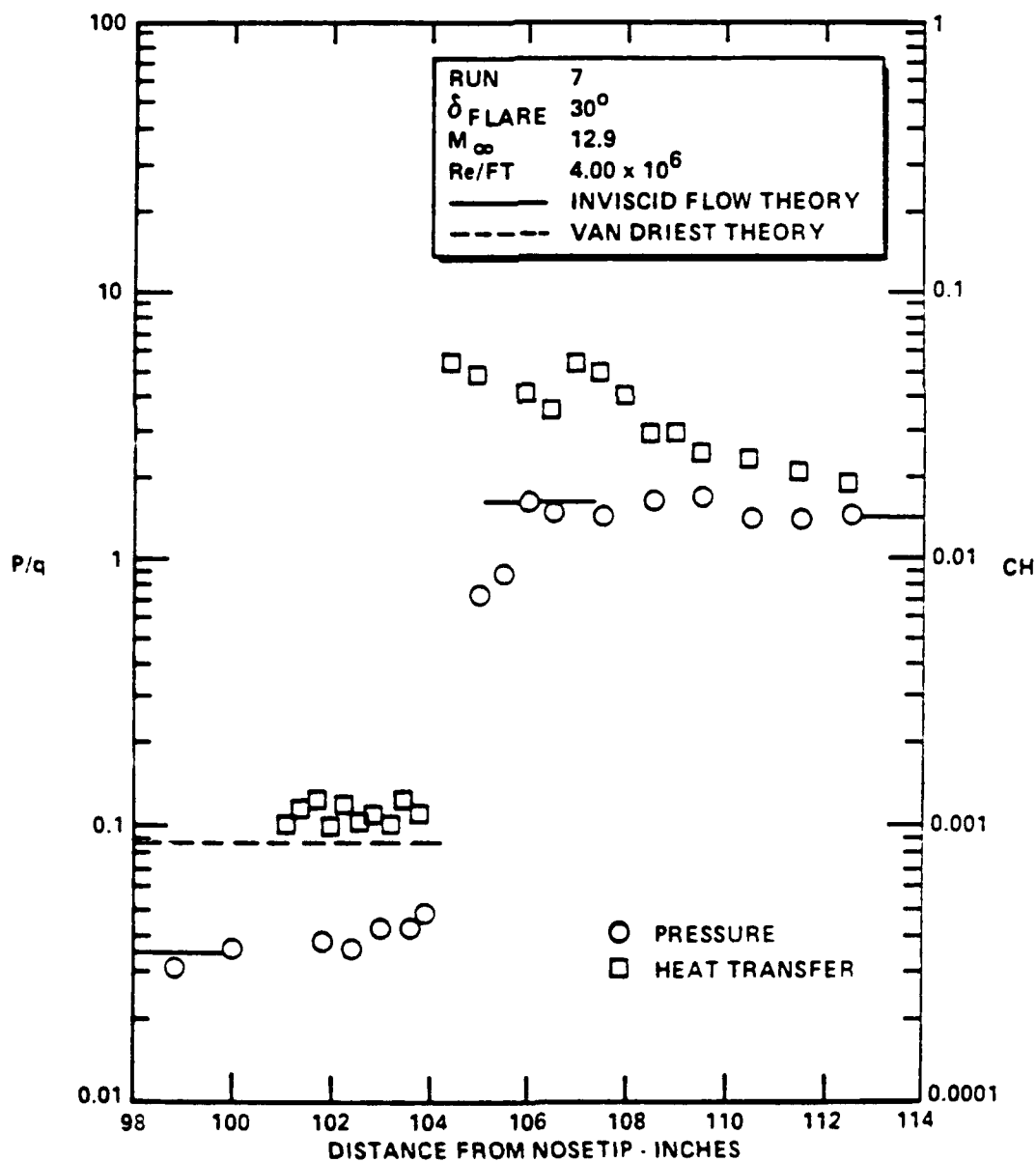
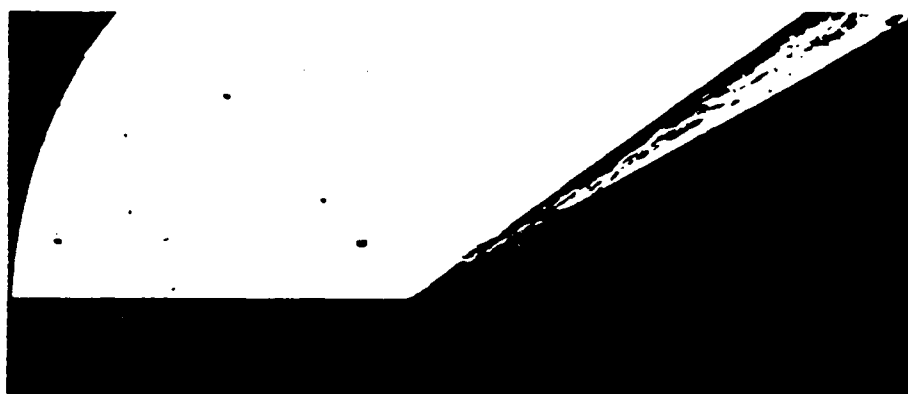


Figure 6 DISTRIBUTION OF PRESSURE AND HEAT TRANSFER IN ATTACHED FLOW OVER THE LARGE 6° CONE/30° FLARE CONFIGURATION

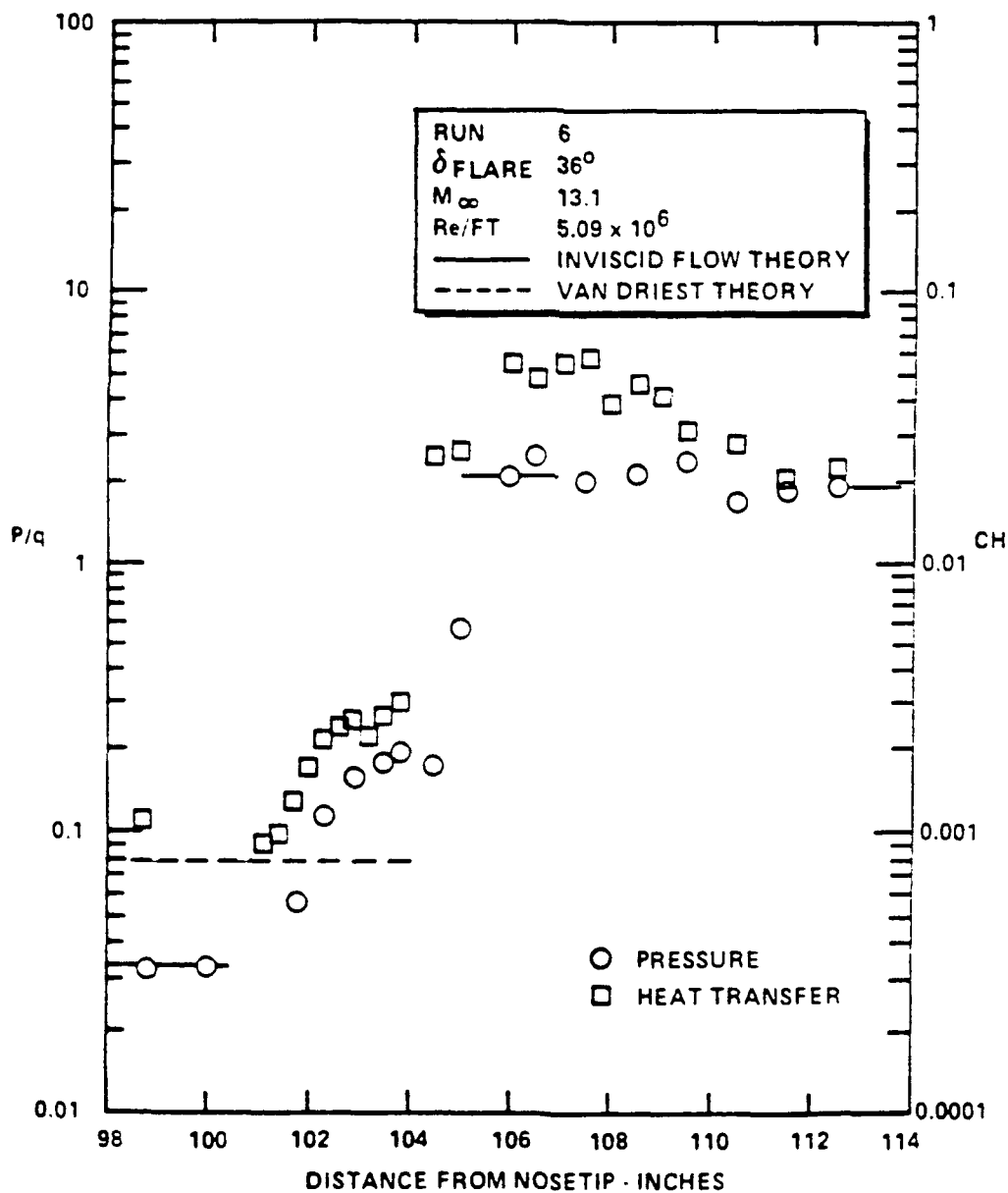
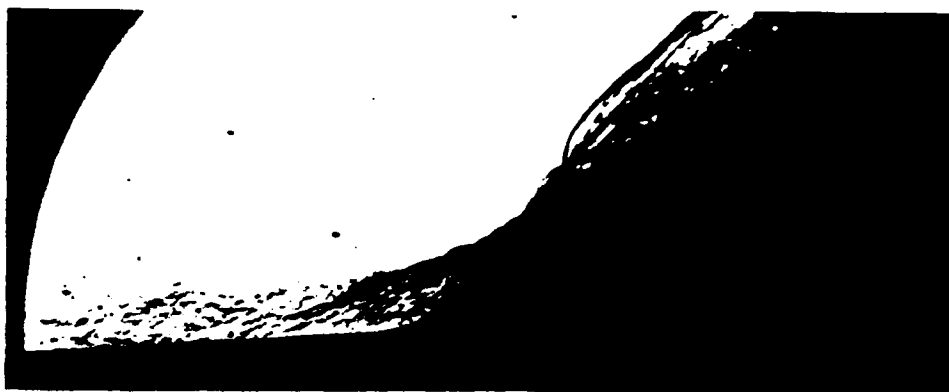


Figure 7 DISTRIBUTION OF PRESSURE AND HEAT TRANSFER IN SEPARATED FLOW OVER THE LARGE 6° CONE/ 36° FLARE CONFIGURATION

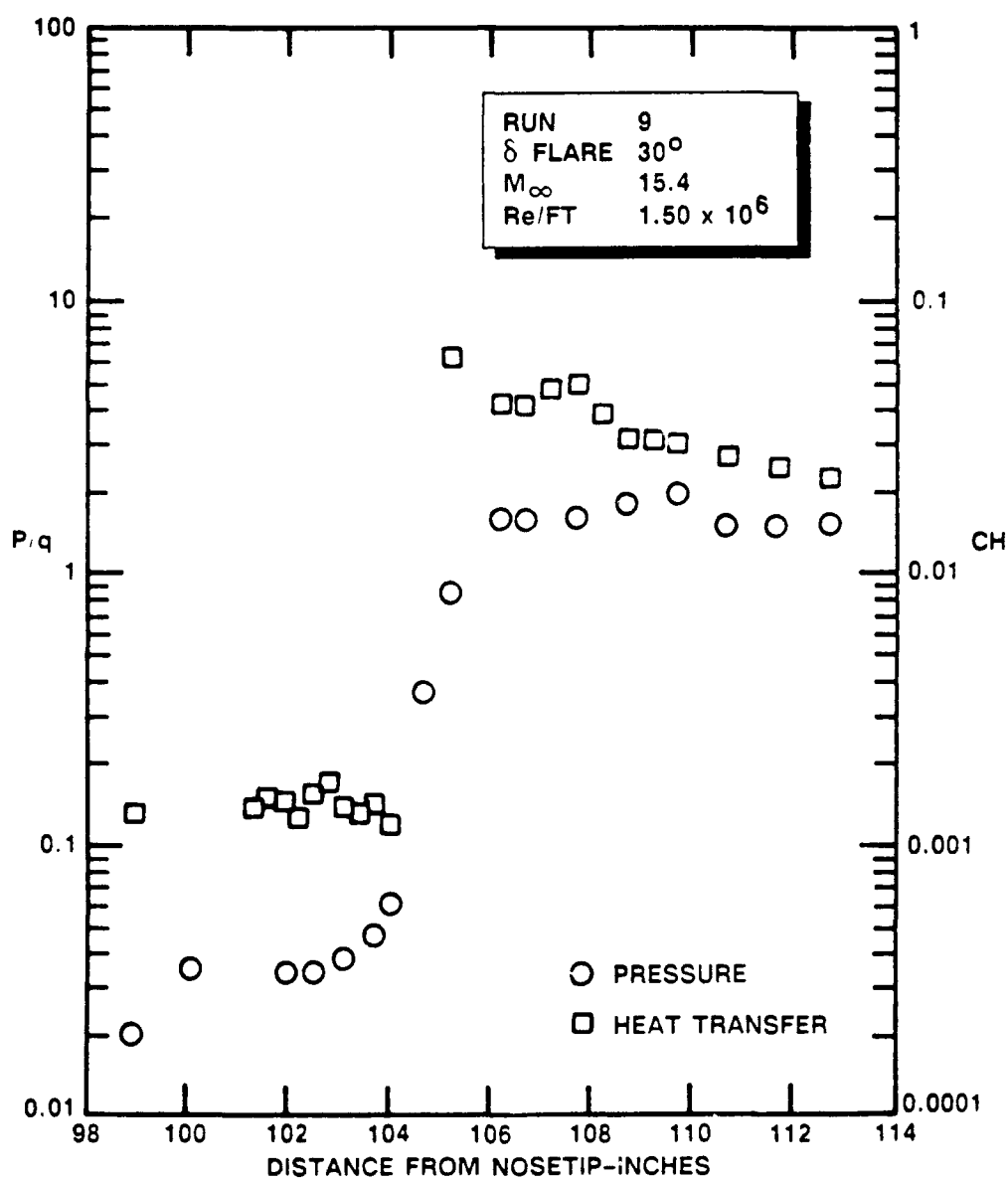
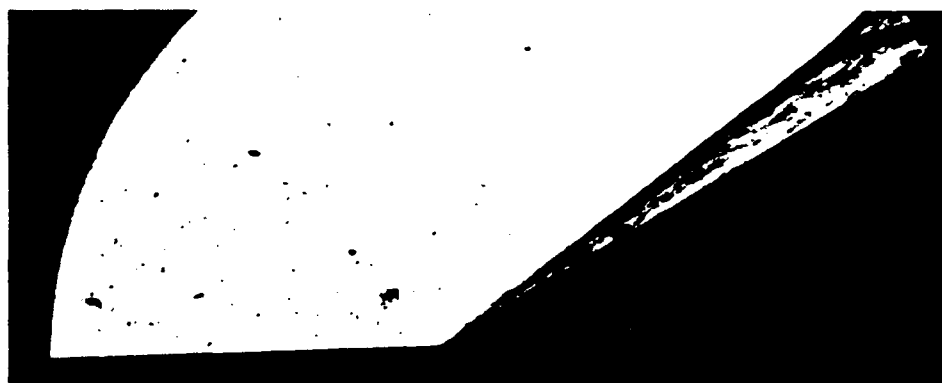


Figure 8 DISTRIBUTION OF PRESSURE AND HEAT TRANSFER IN ATTACHED FLOW OVER THE LARGE 6° CONE/ 30° FLARE CONFIGURATION

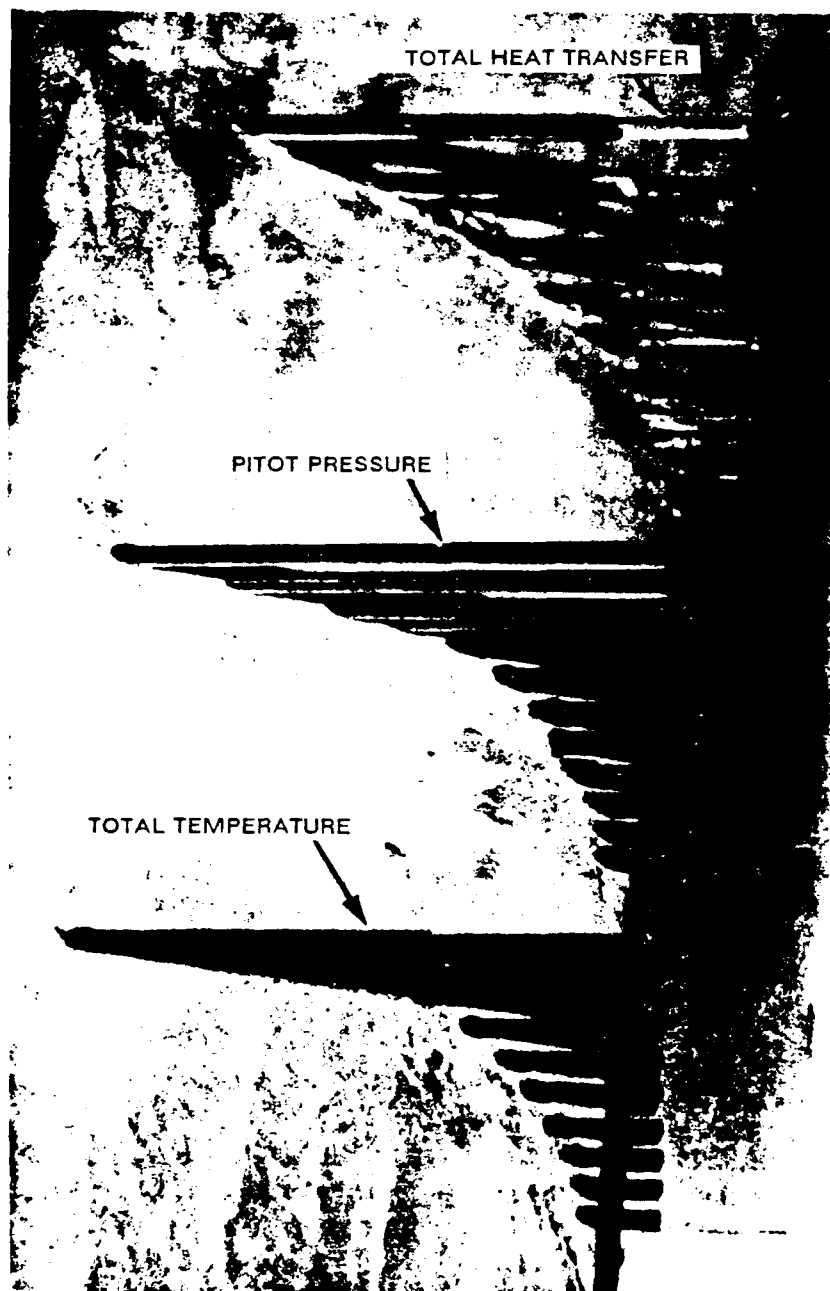


Figure 9 RAKE ASSEMBLY

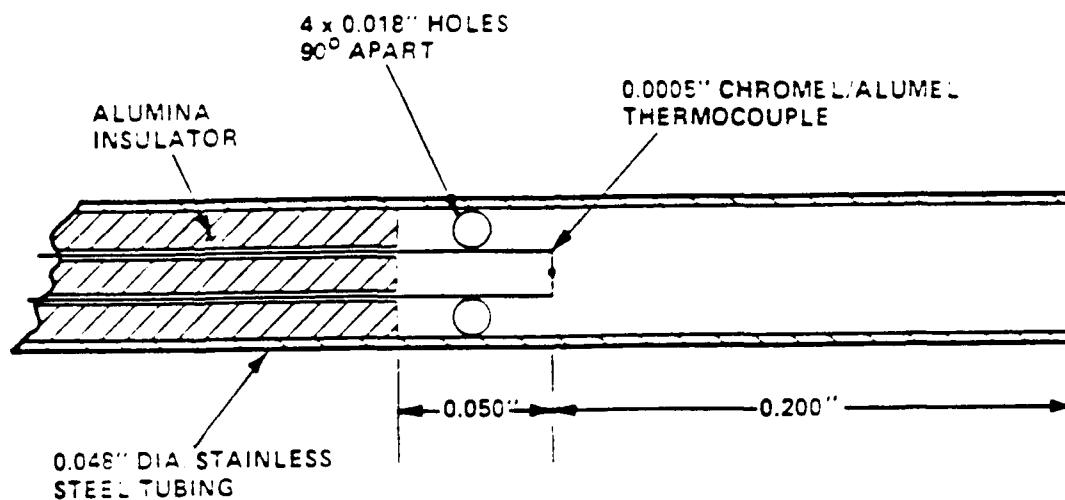


Figure 10 SCHEMATIC DIAGRAM OF TOTAL TEMPERATURE GAGE

Mean = 5.789E+00 (+/- .5%)

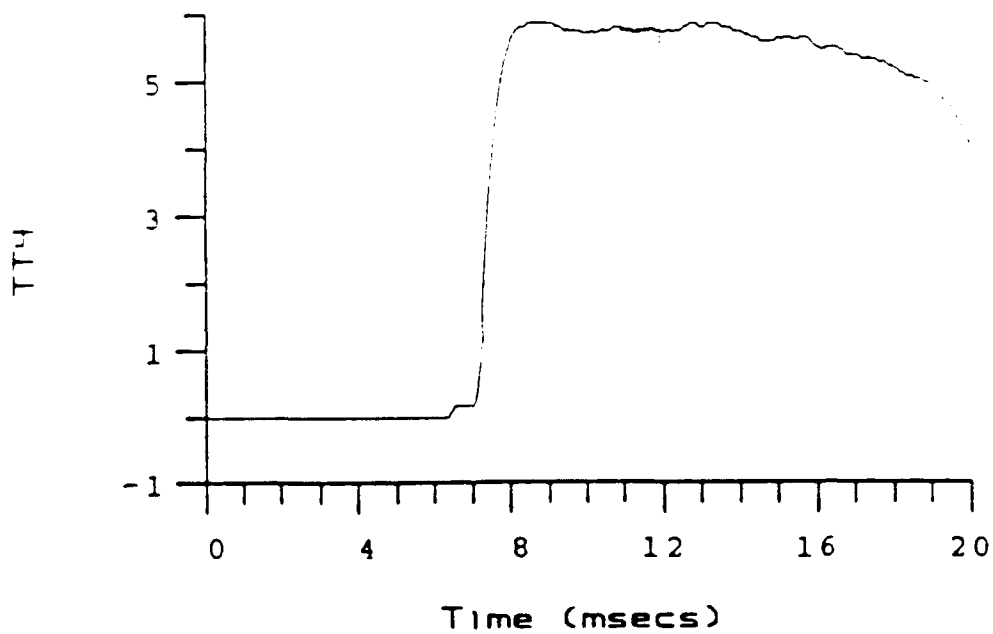


Figure 11 TYPICAL RESPONSE OF TOTAL TEMPERATURE GAGE

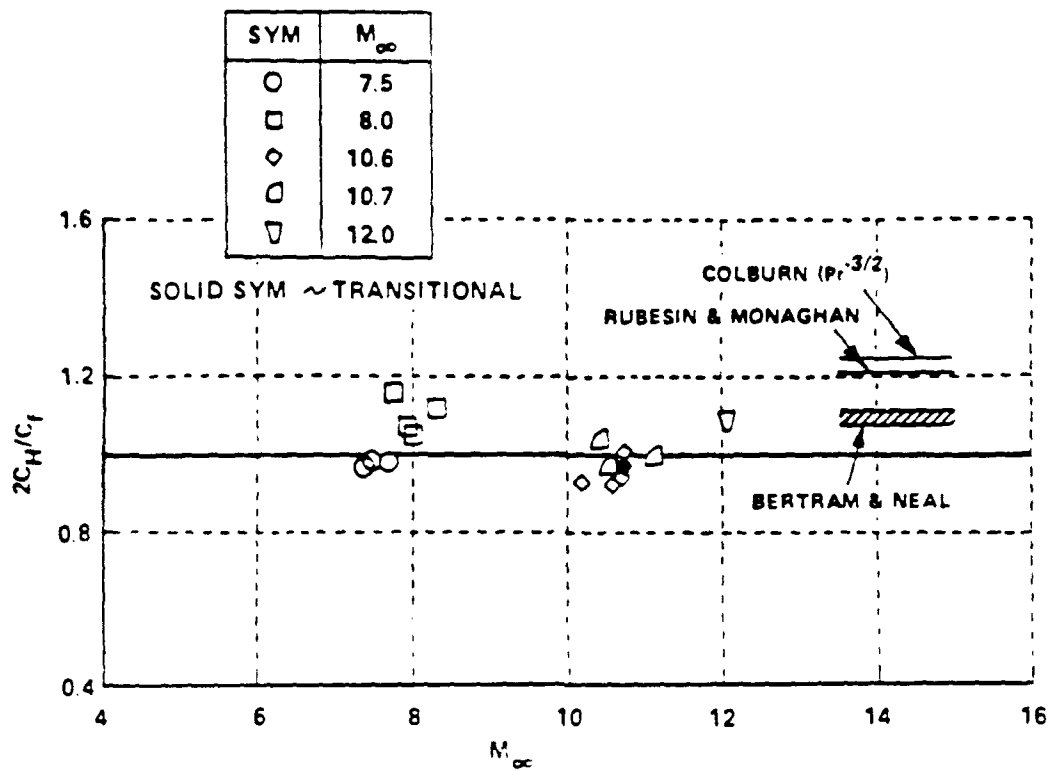


Figure 12 REYNOLDS ANALOGY FACTORS FOR TURBULENT
HYPERSONIC BOUNDARY LAYERS

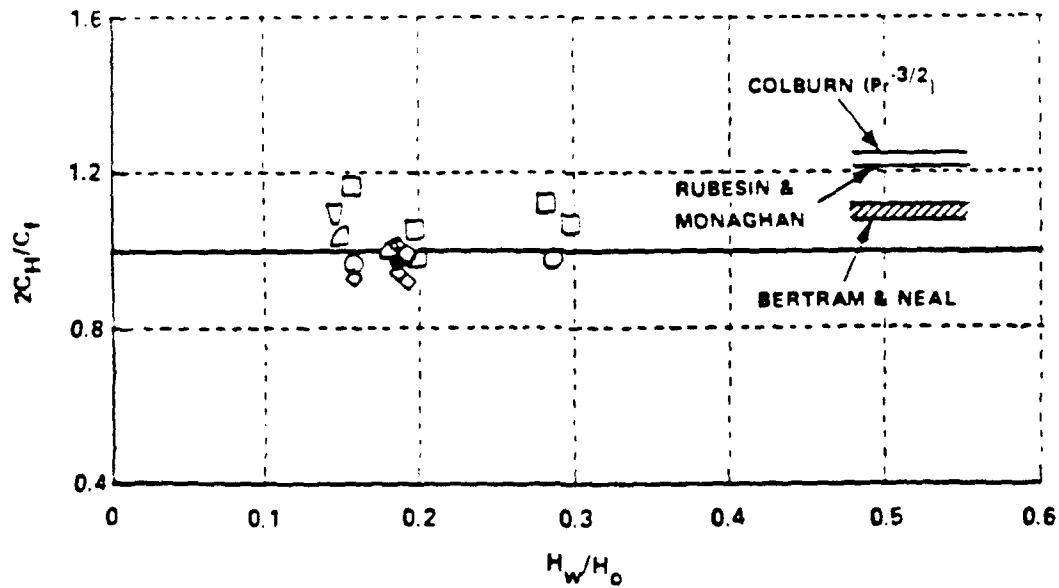


Figure 13 REYNOLDS ANALOGY FACTORS FOR TURBULENT
HYPERSONIC BOUNDARY LAYERS

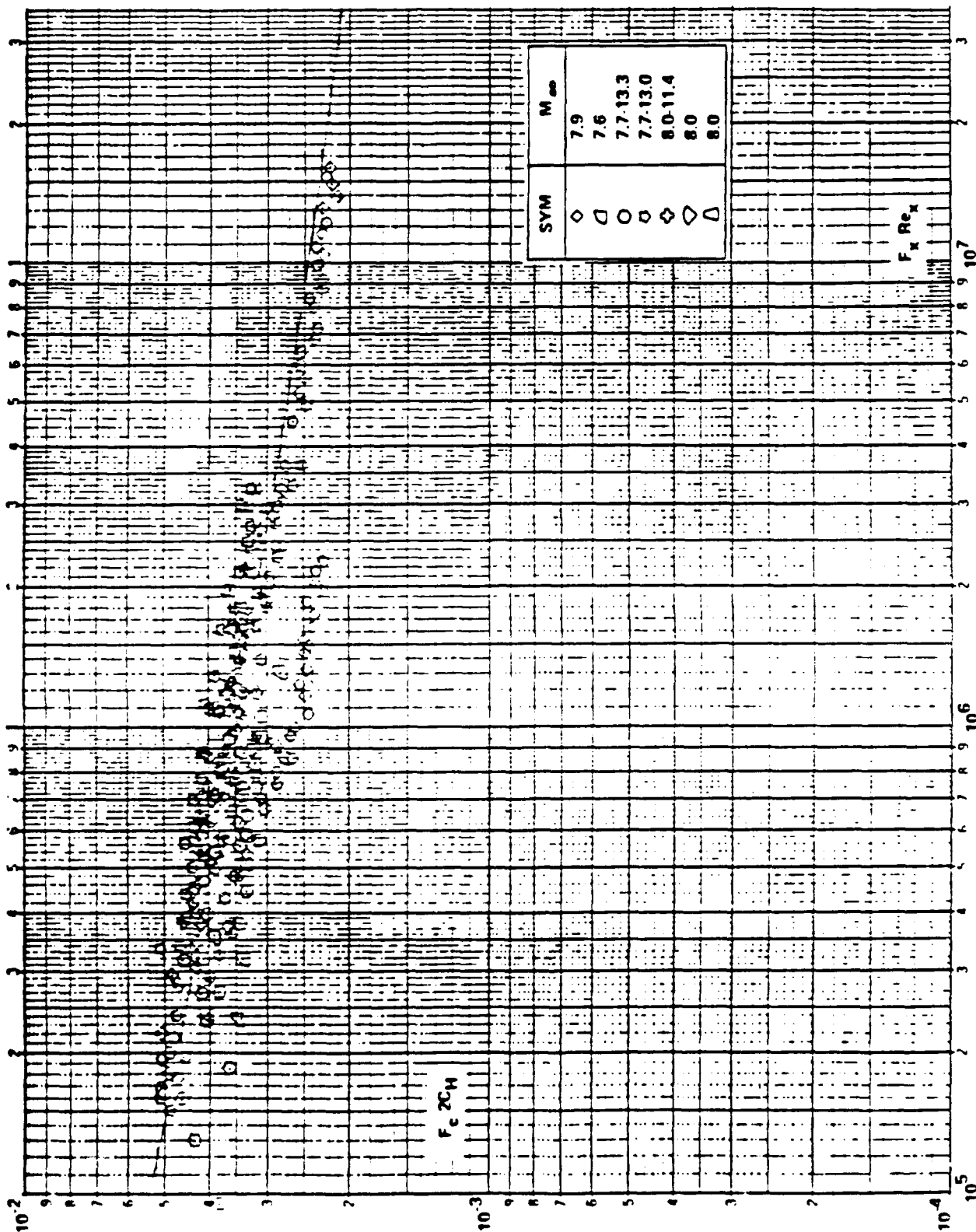


Figure 14 COMPARISON BETWEEN THE MEASURED HEAT TRANSFER AND
THE THEORY OF VAN DRIEST ON SHARP CONES ($Q_V = Q_R + Q_{RF}/2$)

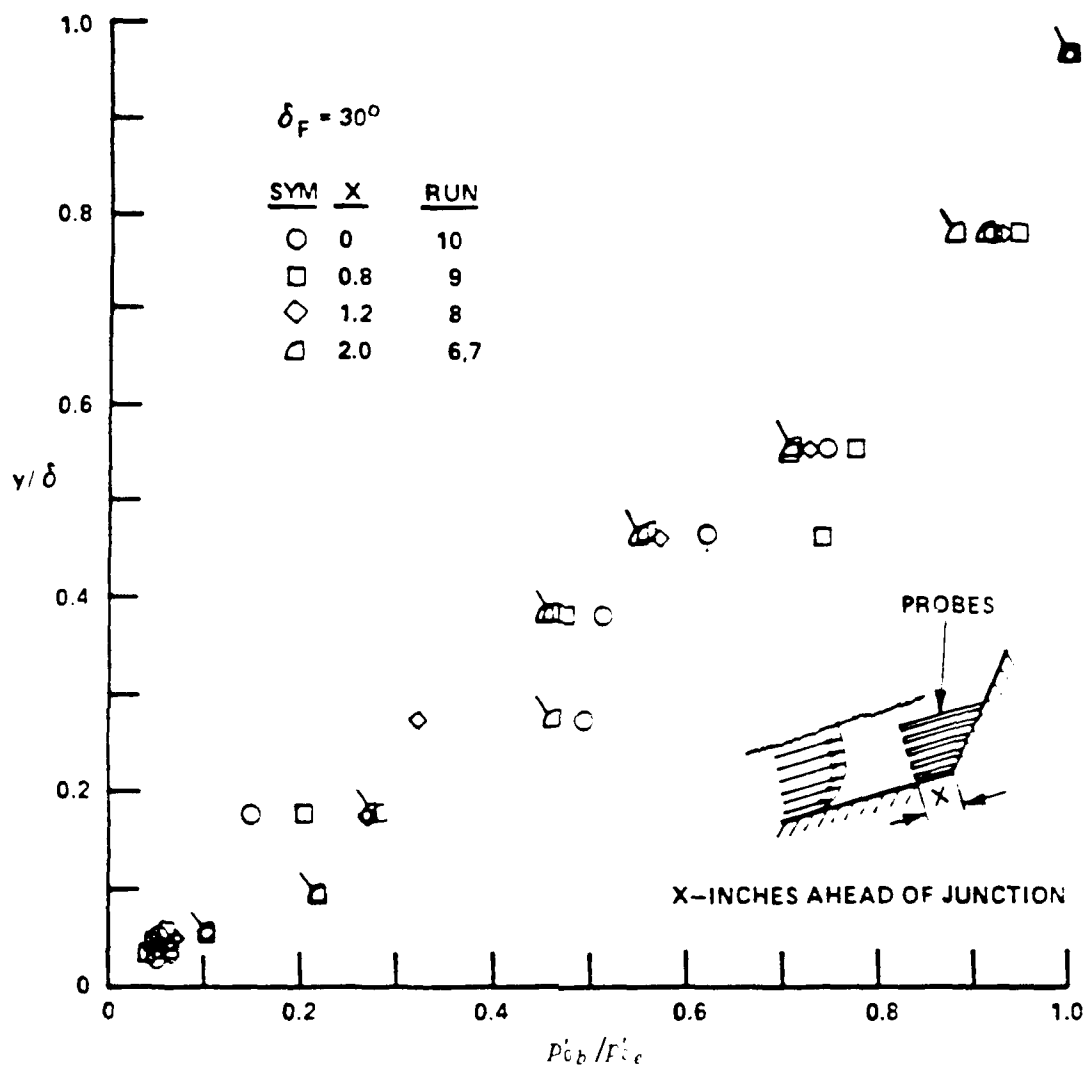


Figure 15 DISTRIBUTION OF PITOT PRESSURE ACROSS BOUNDARY LAYER UPSTREAM OF CONE/FLARE JUNCTION, 30° FLARE

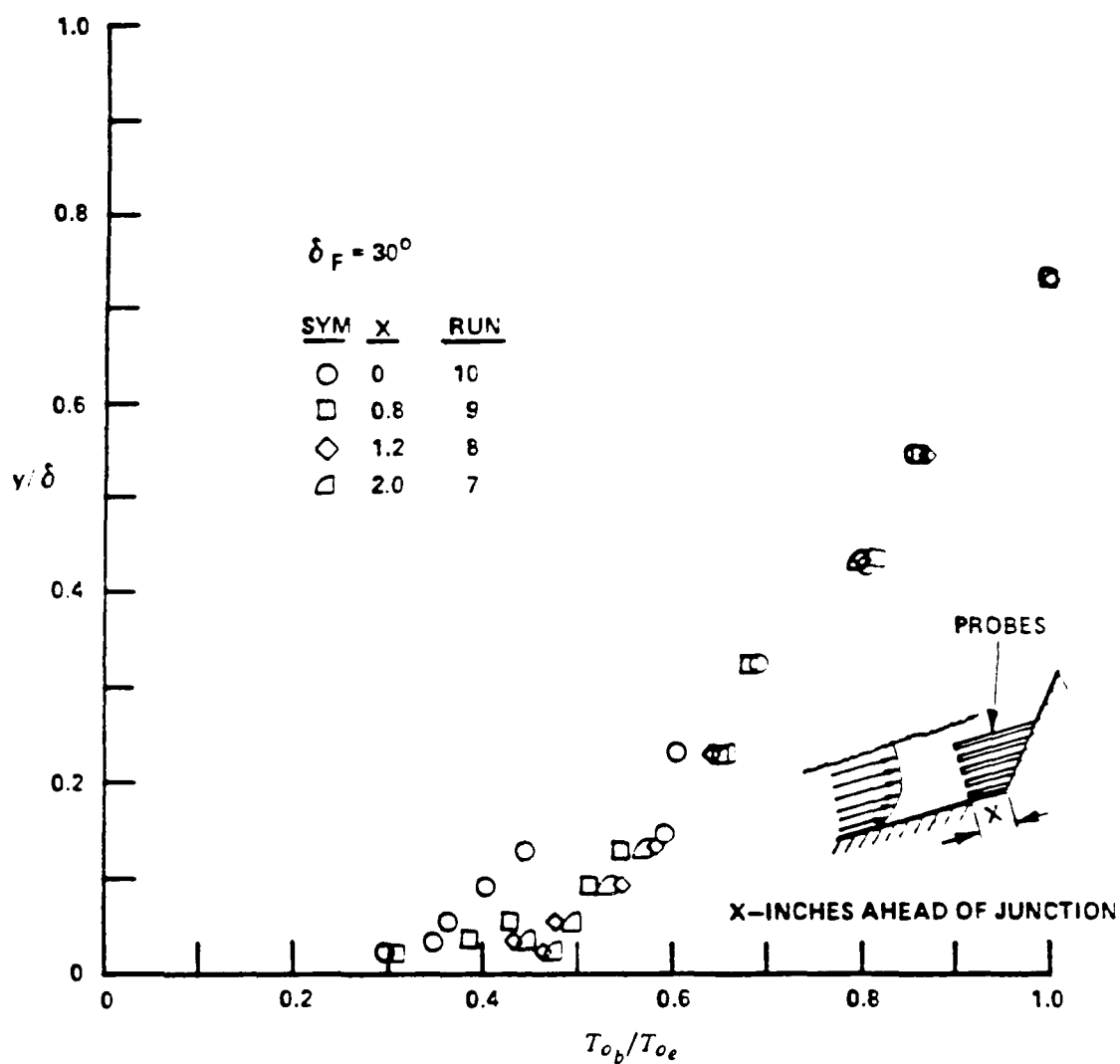


Figure 16 DISTRIBUTION OF TOTAL TEMPERATURE ACROSS BOUNDARY LAYER
UPSTREAM OF CONE/FLARE JUNCTION, 30° FLARE

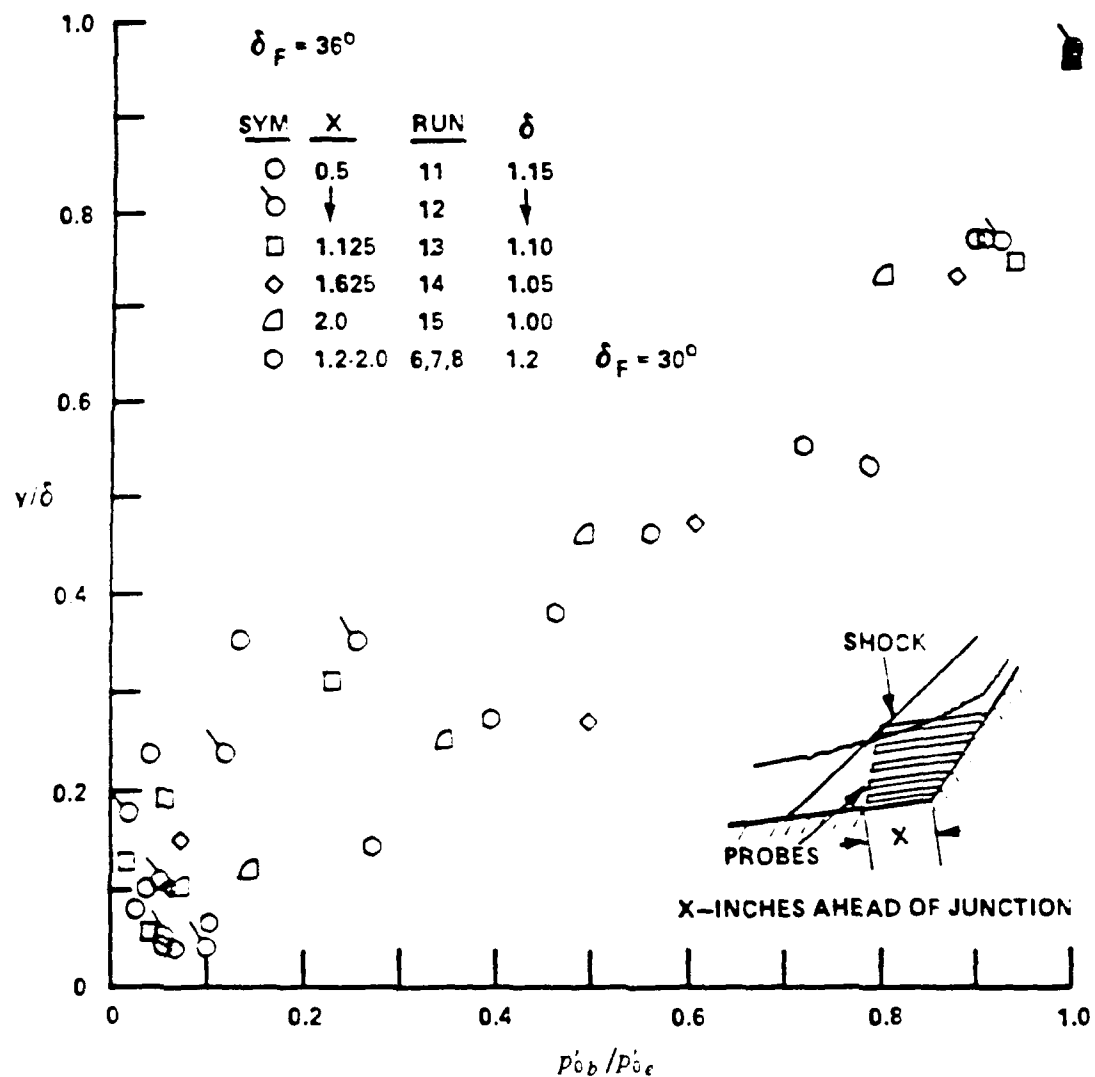


Figure 17 DISTRIBUTION OF PITOT PRESSURE ACROSS BOUNDARY LAYER
UPSTREAM OF CONE/FLARE INTERACTION, 36° FLARE

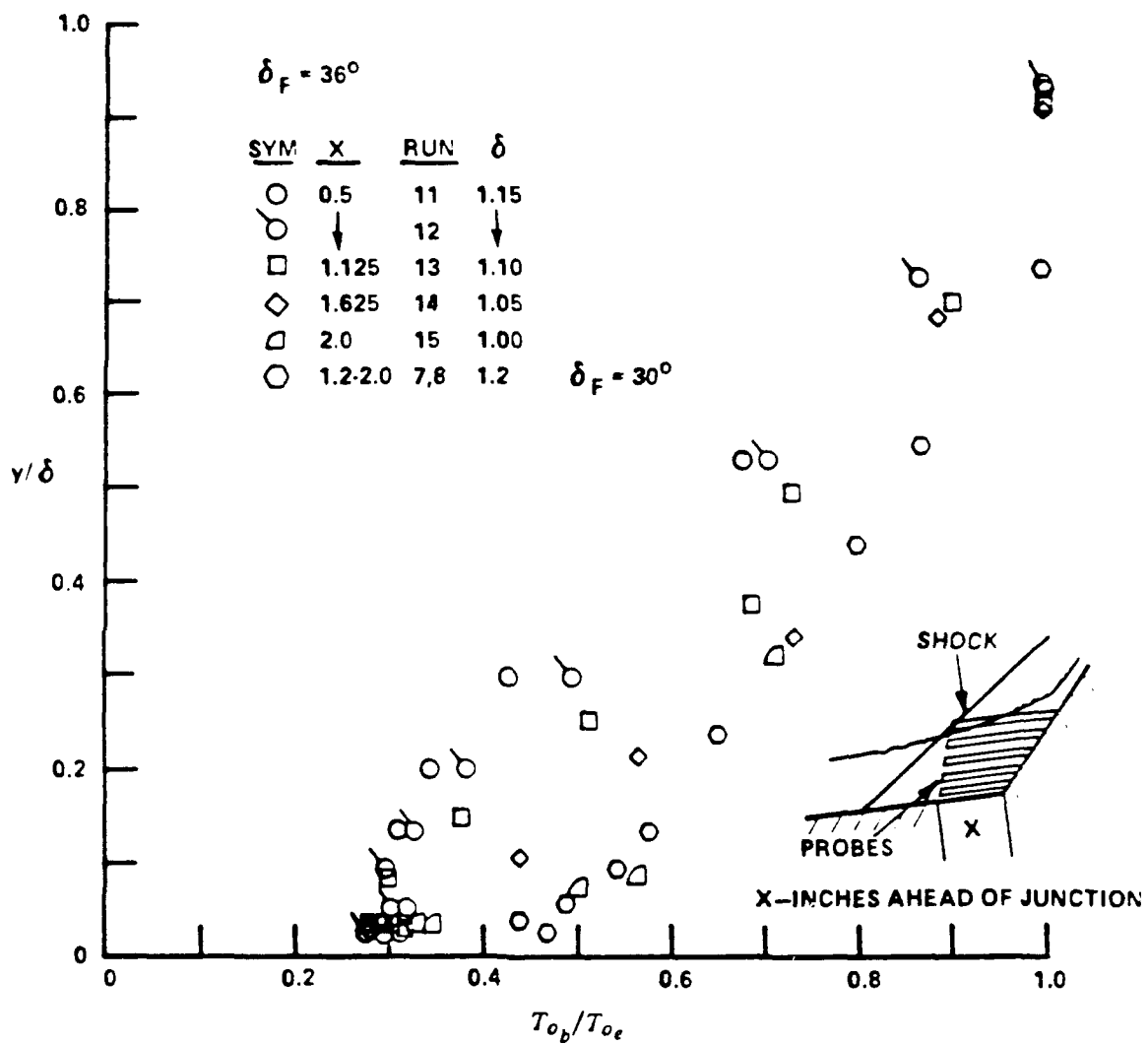


Figure 18 DISTRIBUTION OF TOTAL TEMPERATURE ACROSS BOUNDARY LAYER
UPSTREAM OF CONE/FLARE JUNCTION, 36° FLARE

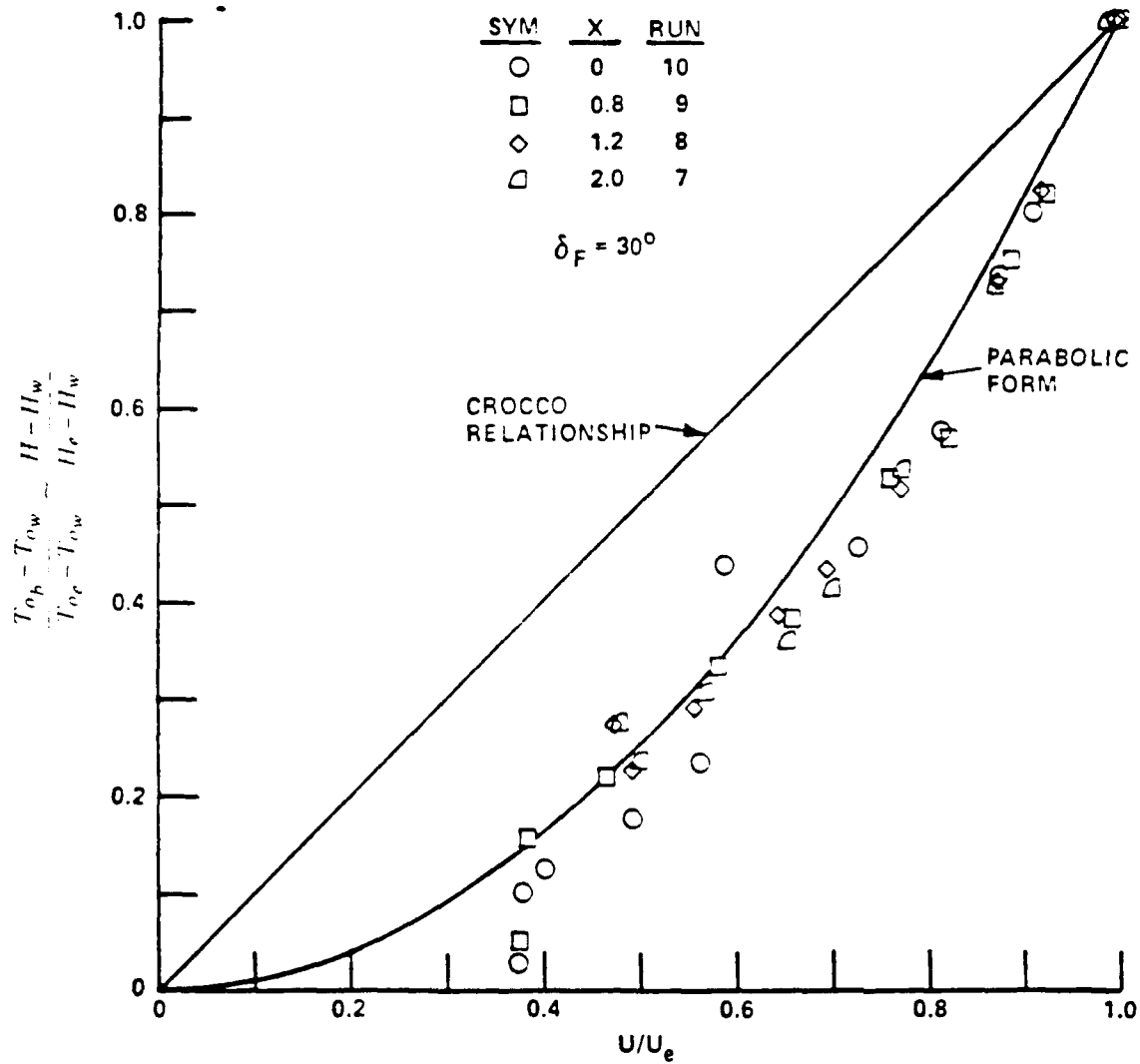


Figure 19 TOTAL TEMPERATURE AND VELOCITY MEASUREMENTS PRESENTED IN CROCCO FRAMEWORK

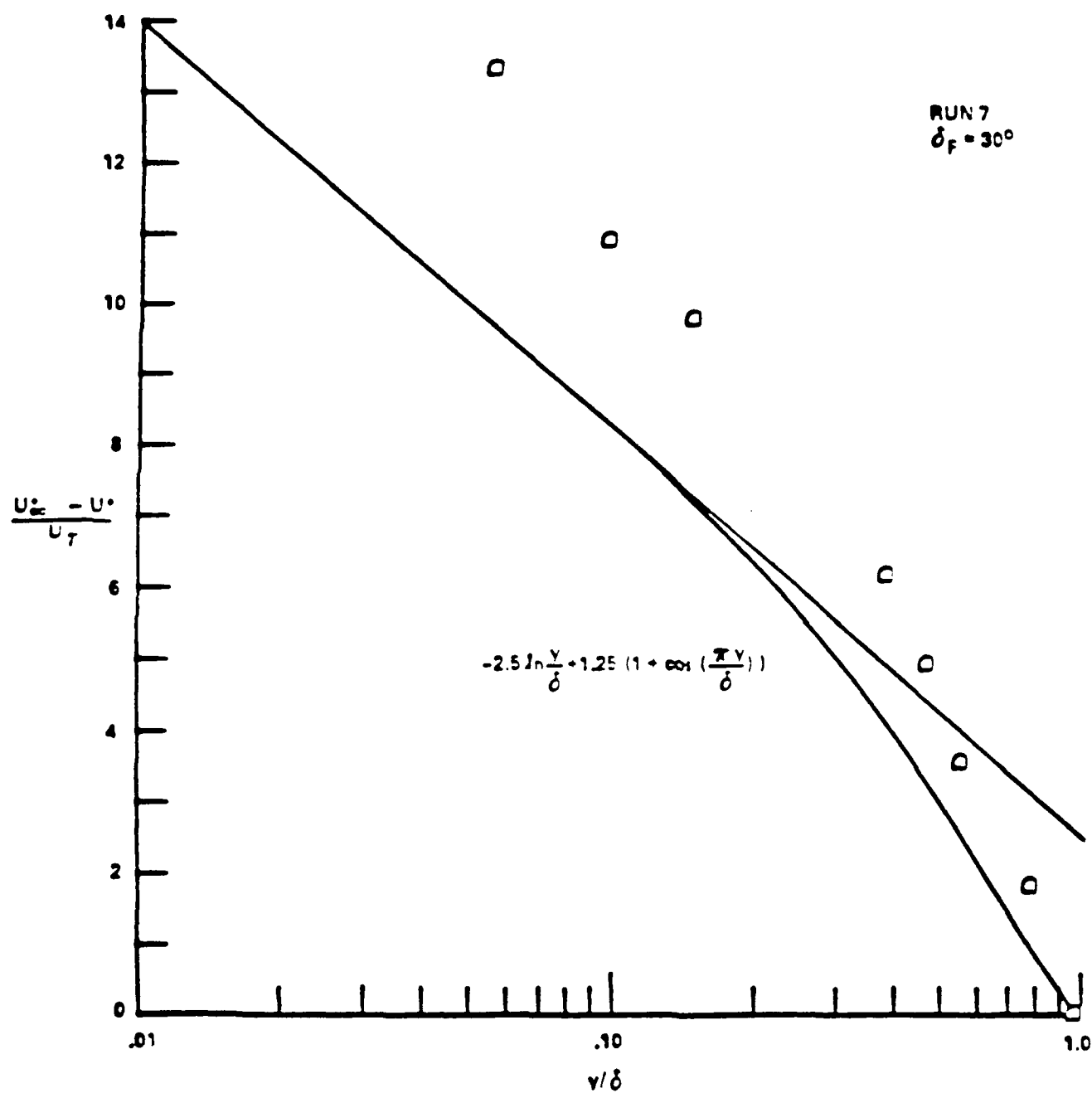


Figure 20 INCOMPRESSIBLE VELOCITY PROFILE MEASUREMENTS IN DEFECT FORM

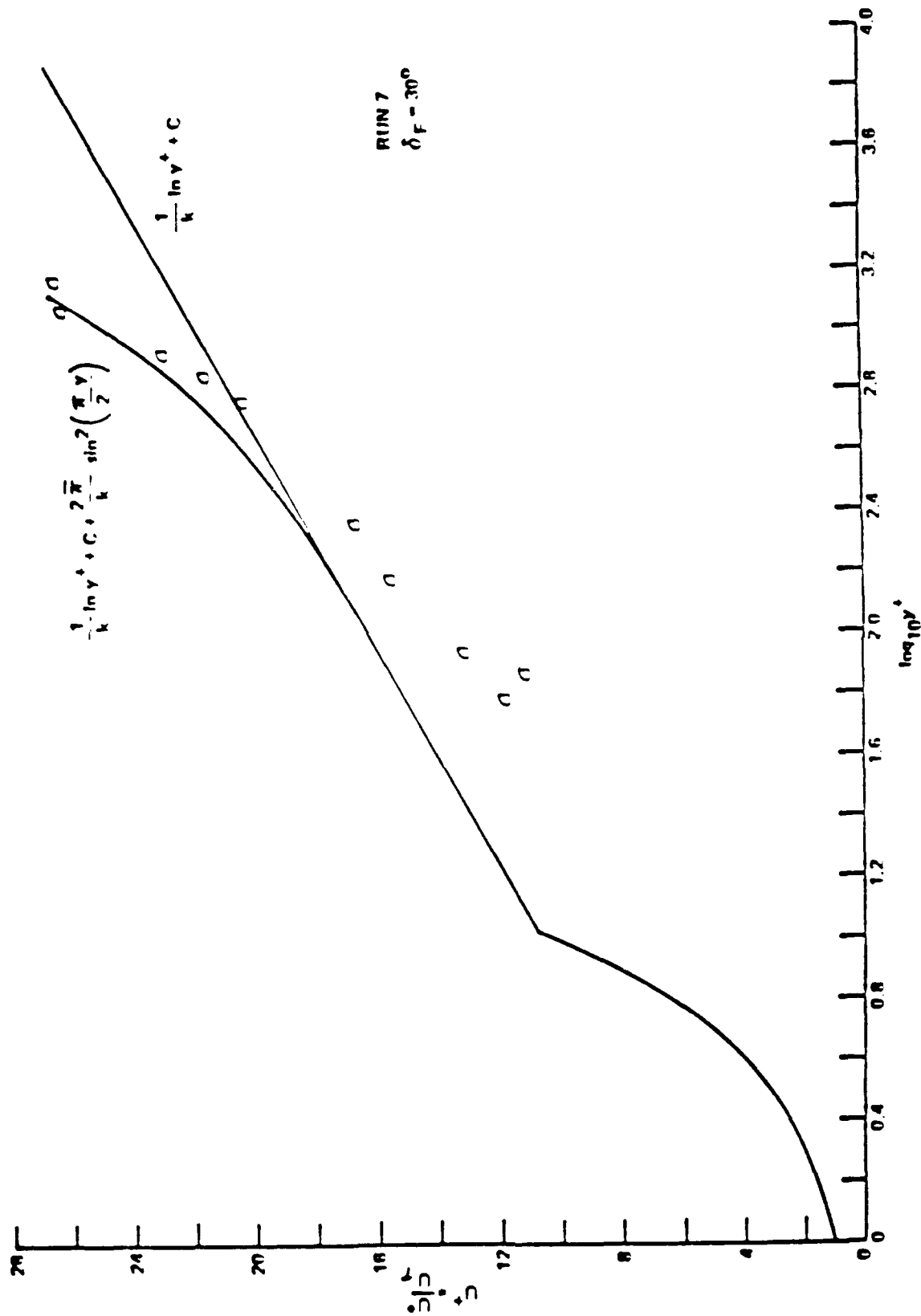


Figure 21 VELOCITY PROFILE MEASUREMENTS IN INCOMPRESSIBLE WALL COORDINATES

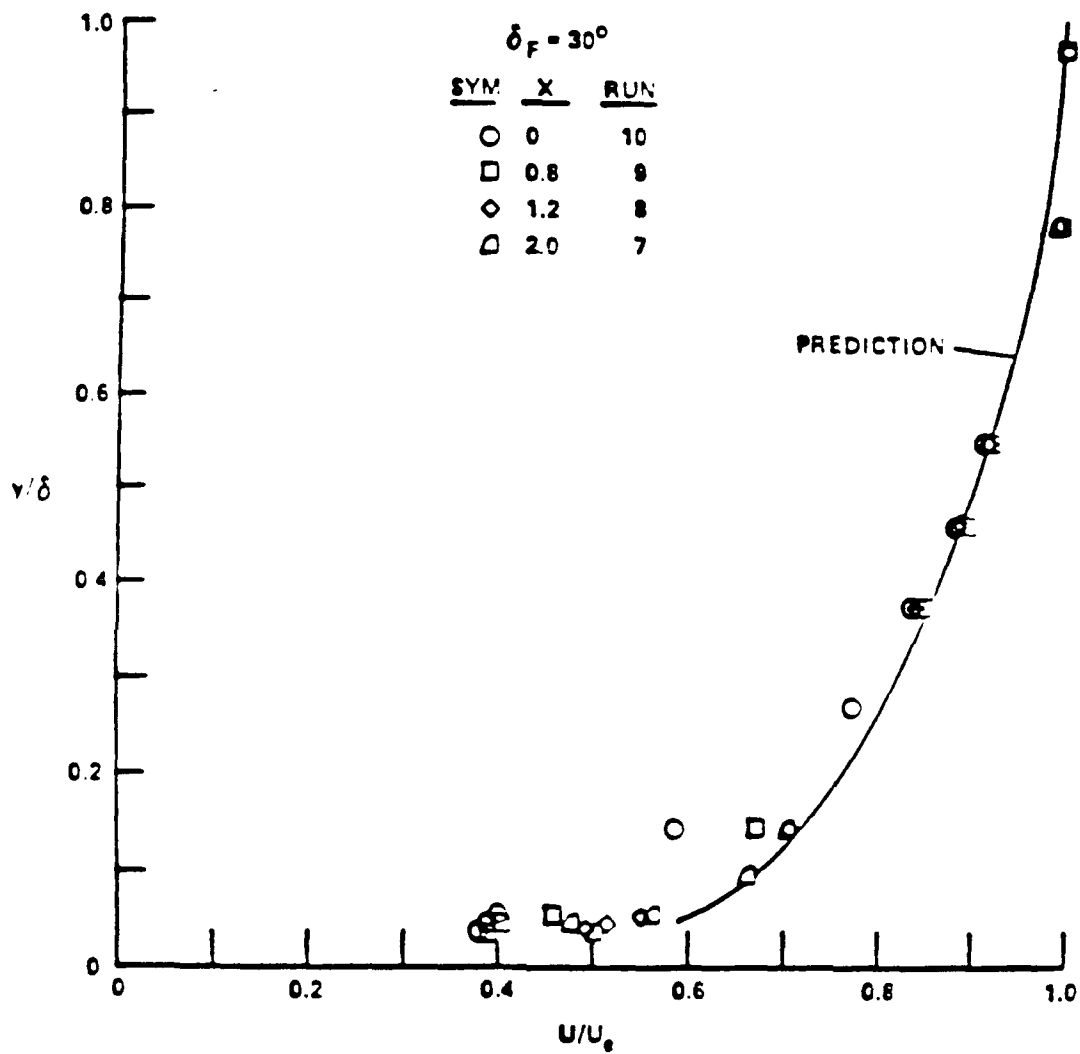


Figure 22 COMPARISON BETWEEN MEASURED AND PREDICTED VELOCITY DISTRIBUTION

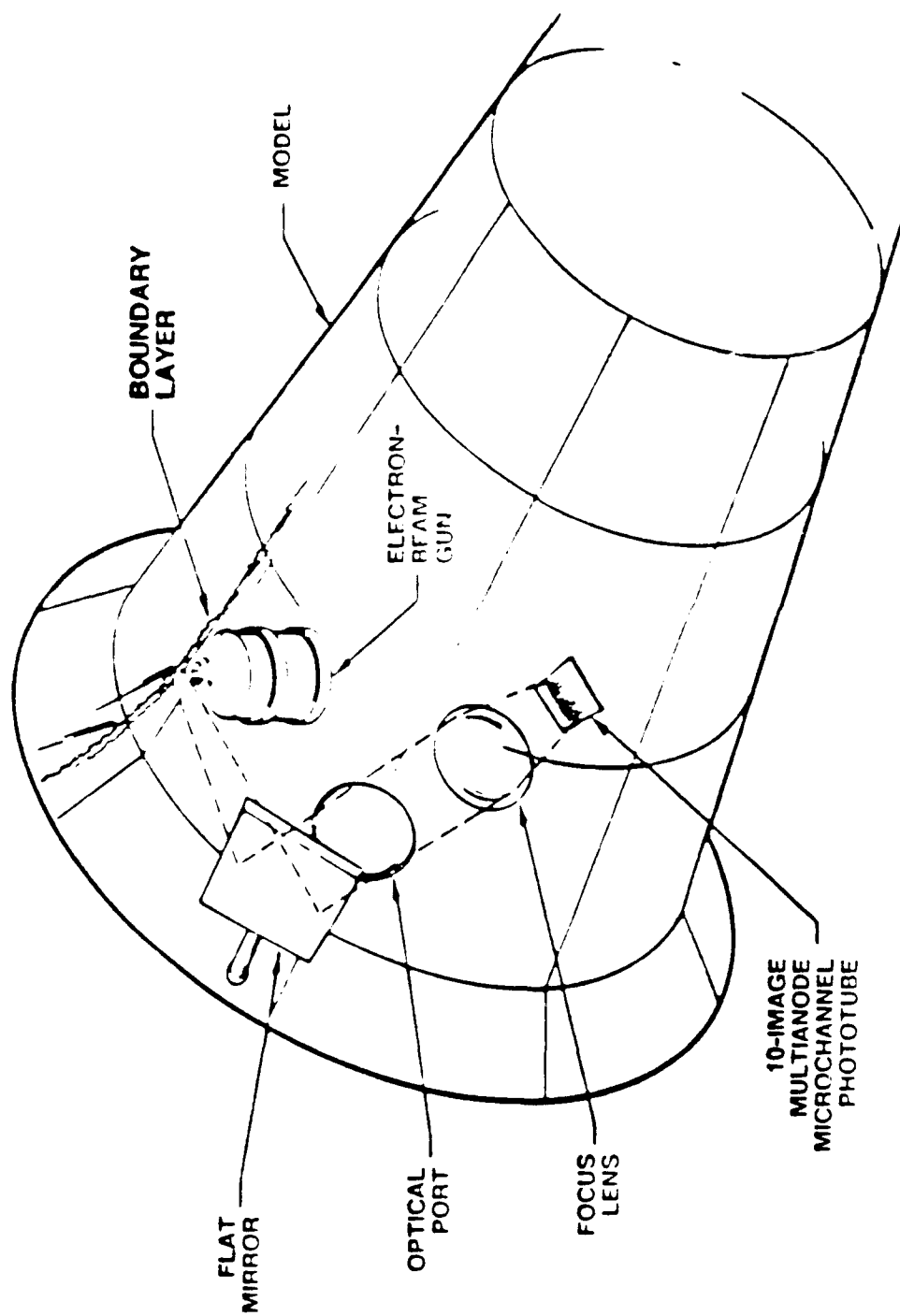


Figure 23 GENERAL LAYOUT OF ELECTRON-BEAM APPARATUS IN CONE/FLARE MODEL

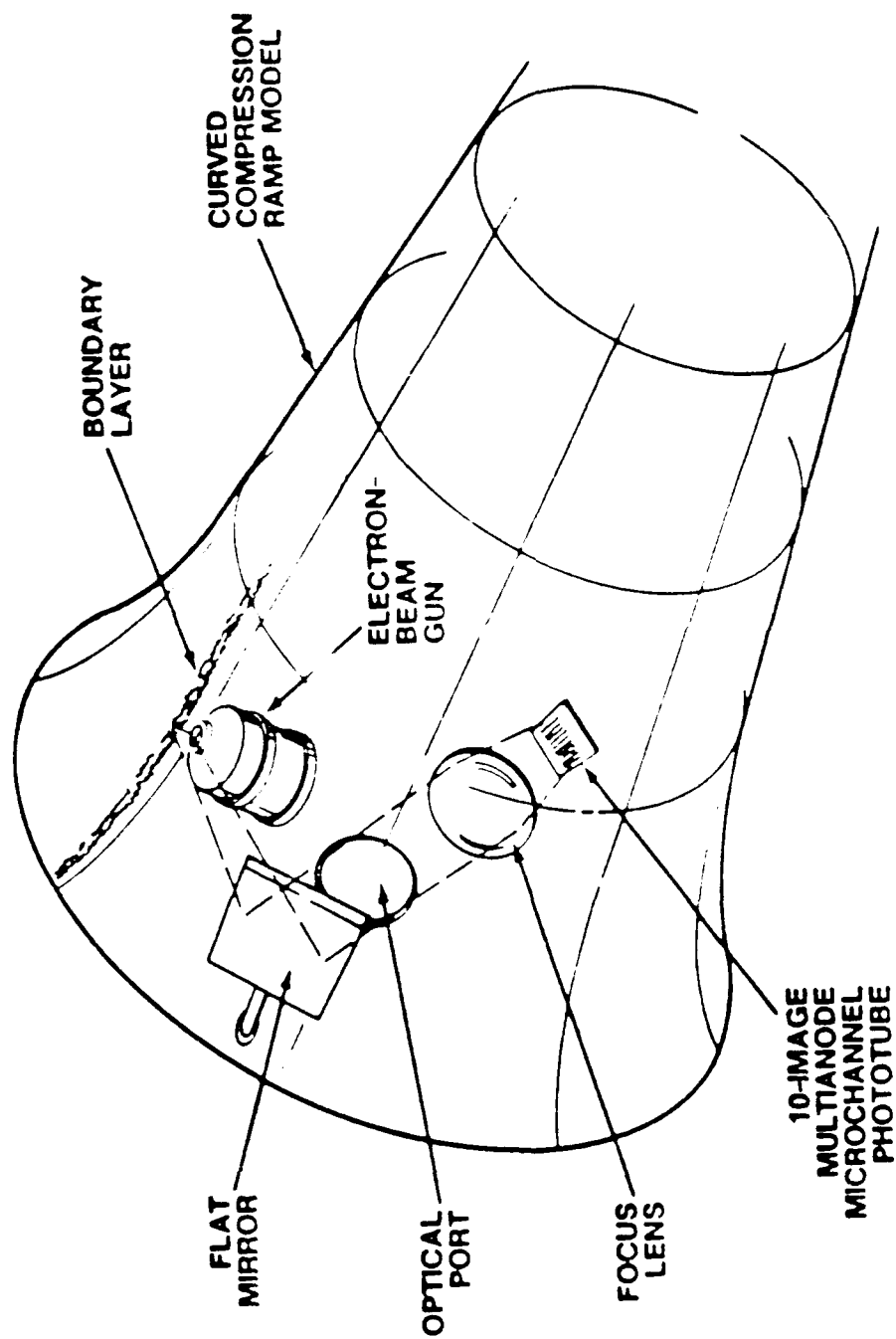


Figure 24 E-BEAM GUN INSTALLATION IN AXISYMMETRIC CURVED COMPRESSION-RAMP MODEL

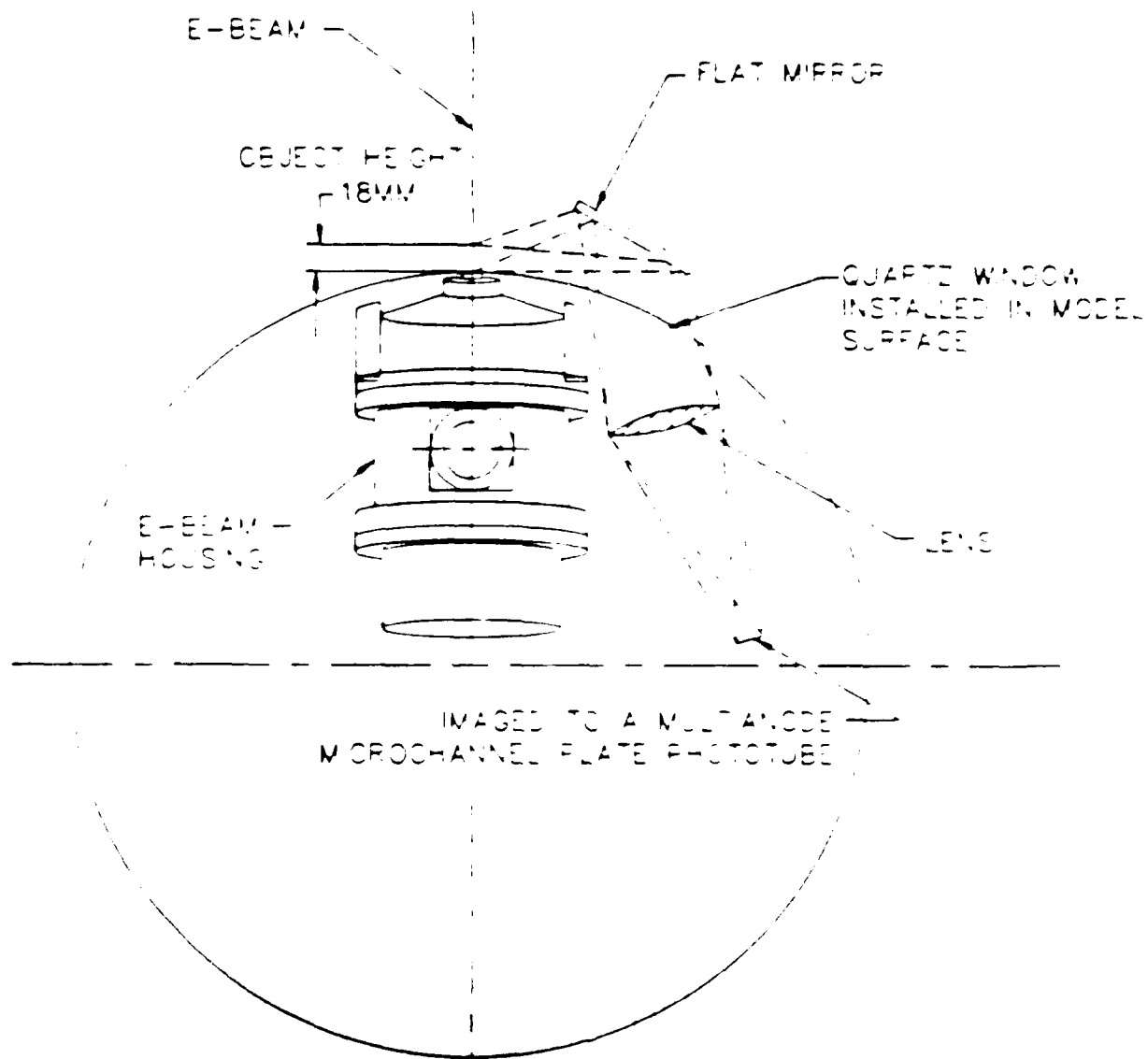


Figure 25 GENERAL LAYOUT OF OPTICAL SYSTEM FOR ELECTRON-BEAM DETECTORS

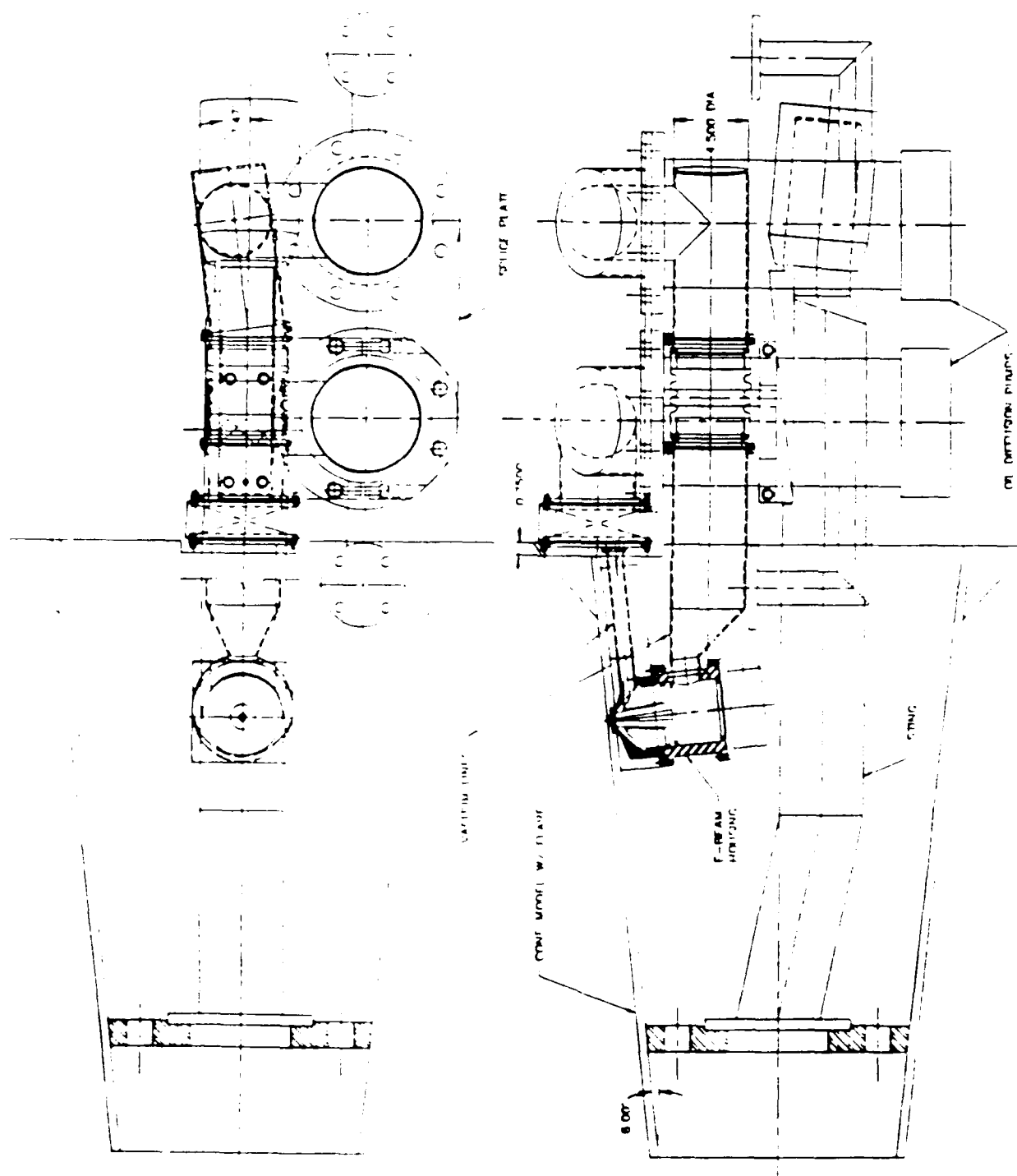


Figure 26 DETAIL 2D DRAWING OF CONE/FLARE MODEL AND PUMPING SYSTEM

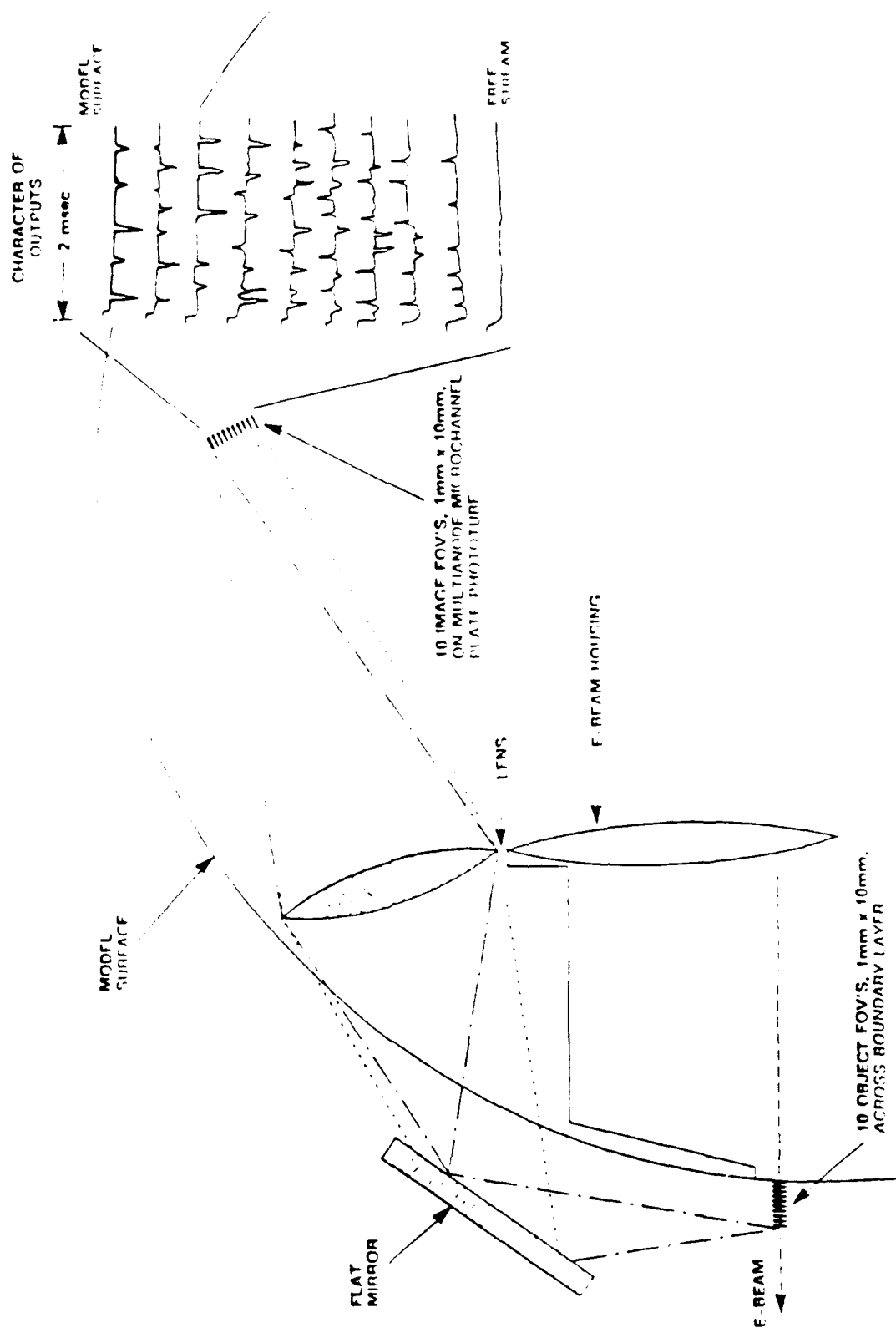


Figure 27 OPTICAL RESOLUTION OF DETECTOR SYSTEM

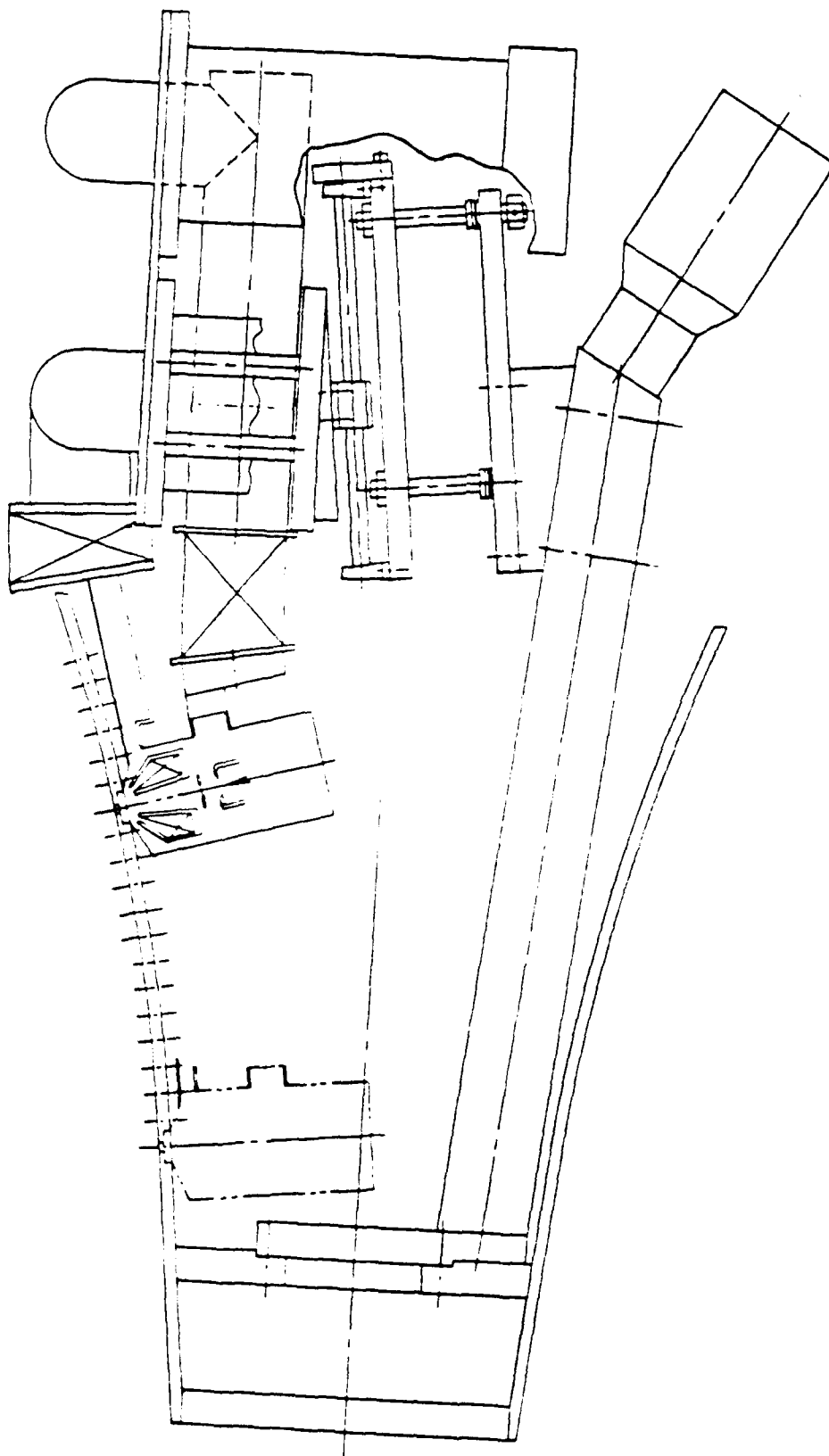


Figure 28 DETAILED DRAWING OF CONE/FLARE MODEL AND PUMPING SYSTEM SHOWING
AXIAL LOCATIONS OF ELECTRON-BEAM SURVEYS

APPENDIX 7

**A VALIDATION STUDY OF FOUR NAVIER-STOKES CODES
FOR HIGH-SPEED FLOWS**



AIAA-89-1838

**A Validation Study of Four Navier-Stokes Codes
for High-Speed Flows**

David H. Rudy

James L. Thomas

Ajay Kumar

Peter A. Gnoffo

NASA Langley Research Center

Hampton, VA

and

Sukumar R. Chakravarthy

Rockwell International Science Center

Thousand Oaks, CA

**AIAA 20th Fluid Dynamics, Plasma Dynamics
and Lasers Conference**

Buffalo, New York / June 12-14, 1989

For permission to copy or republish, contact the American Institute of Aeronautics and Astronautics
370 L'Enfant Promenade, S.W., Washington, D.C. 20024

A VALIDATION STUDY OF FOUR NAVIER-STOKES CODES FOR HIGH-SPEED FLOWS

David H. Rudy*
James L. Thomas †
Ajay Kumar ‡
Peter A. Gnoffo §

NASA Langley Research Center
Hampton, VA 23665

and

Sukumar R. Chakravarthy¶
Rockwell International Science Center
Thousand Oaks, CA 91360

Abstract

A code validation study has been conducted for four different codes for solving the compressible Navier-Stokes equations. Computations for a series of nominally two-dimensional high-speed laminar separated flows were compared with detailed experimental shock-tunnel results. The shock wave-boundary layer interactions considered were induced by a compression ramp in one case and by an externally-generated incident shock in the second case. In general, good agreement was reached between the grid-refined calculations and experiment for the incipient- and small-separation conditions. For the most highly separated flow, three-dimensional calculations which included the finite-span effects of the experiment were required in order to obtain agreement with the data. The finite-span effects were important in determining the extent of separation as well as the time required to establish the steady-flow interaction. The results presented provide a resolution of discrepancies with the experimental data encountered in several recent computational studies.

*Computational Methods Branch. Member AIAA.

†Analytical Methods Branch. Associate Fellow AIAA.

‡Computational Methods Branch. Associate Fellow AIAA.

§Aerothermodynamics Branch. Senior Member AIAA.

¶CFD Department. Member AIAA.

Nomenclature

C_f	skin-friction coefficient, $2\tau_w/\rho_\infty u_\infty^2$
C_h	heat-transfer coefficient, $\dot{q}/\rho_\infty u_\infty (H_\infty - H_w)$
C_p	pressure coefficient, $2p/\rho_\infty u_\infty^2$
H	total enthalpy
L	reference length
M	Mach number
p	pressure
\dot{q}	heat-transfer rate
Re	unit Reynolds number, $\rho_\infty u_\infty/\mu_\infty$
T	temperature
u	streamwise velocity
x	streamwise coordinate
α	angle of attack
β	shock angle
γ	ratio of specific heats
θ	compression-ramp or wedge angle
μ	molecular viscosity
ρ	density
τ	shear stress

subscripts

a	reattachment point
s	separation point
w	wall
∞	free stream

Introduction

The need for development and validation of computational methods for solving the Navier-Stokes equations for high-speed flows has increased because of the National

This paper is declared a work of the U.S. Government and is not subject to copyright protection in the United States.

Aero-Space Plane project. The propulsion system of advanced hypersonic vehicles will likely use the external vehicle contours as compression and expansion surfaces for the inlet and nozzle, respectively. Thus, the integration of the engine and airframe is an important design consideration. This design process relies heavily upon the development of computer codes with appropriate geometric flexibility and physical models since many of the high Mach-number, high enthalpy flow conditions the vehicle may encounter in flight cannot presently be simulated in ground-based facilities.

Before such a code can be used with confidence as an analysis or design tool, the range of validity of the solution procedure and physical modeling must be known. The verification process typically involves three distinct types of testing: (1.) internal consistency checks; (2.) comparisons with other codes; and (3.) comparisons with experimental data. The first of these tests consists of checking the code for proper conservation of mass, momentum, and energy. The simplest such test would be verifying that the code can preserve free-stream flow. Other tests would include the computation of flows for which analytic solutions are available. In these tests, studies can be made of the effects of grid refinement and parameter variations in the numerical scheme. The second level of testing is the comparison of computed results with those obtained using other similar but well-established codes that also solve the Navier-Stokes equations. Comparisons could also be made with results from boundary-layer codes or space-marching parabolized Navier-Stokes codes for appropriate test problems. The third level of testing is the comparison of computed results with highly-accurate benchmark experimental data sets.

The present paper describes a comparison of computed results from four different computer codes for solving the compressible Navier-Stokes equations with experimental data for two different test problems. Both of these test problems have features typical of high-speed internal flow problems of practical importance in the design and analysis of the inlet portion of a scramjet engine on an advanced hypersonic vehicle. Previous related code-validation studies are given by Rudy et al.¹ and Thomas et al.²

Description of Codes

CFL3D

Three of the four computer codes use similar recently-developed upwind technology. The first of these, CFL3D (Computational Fluids Laboratory 3-D code), was developed by Thomas for the thin-layer Navier-Stokes equations and is described in Ref. 3. This code uses a finite-volume method in which the convective and pressure terms are discretized with the upwind-biased flux-

difference splitting technique of Roe. The reconstruction of the cell-centered variables to the cell-interface locations is done using a monotone interpolation of the primitive variables such that third-order accuracy in one-dimensional inviscid flow is obtained. The differencing for the diffusion terms representing shear stress and heat transfer effects corresponds to second-order-accurate central differencing so that the global spatial accuracy of the method is second order. The time-differencing algorithm is a spatially-split approximate-factorization scheme.

USA-PG2

The second of the upwind codes, USA-PG2 (Unified Solution Algorithm-Perfect Gas, 2-D), was developed by Chakravarthy⁴ and solves the full Navier-Stokes equations. The corresponding three-dimensional version is designated USA-PG3. In these codes, the convective terms are modeled using a family of high-accuracy Total-Variation-Diminishing (TVD) upwind-biased finite-volume schemes based on Roe's approximate Riemann solver. Second-derivative viscous terms, except cross-derivative terms, are modeled with conventional central-difference approximations. The cross-derivative terms are treated so that their discretization also contributes to the diagonal dominance of the implicit time discretization. For the present calculations, the implicit formulation was solved using approximate-factorization methods.

LAURA

The third upwind code, LAURA (Langley Aerothermodynamic Upwind Relaxation Algorithm), is a finite-volume, single-level storage implicit upwind-differencing algorithm developed by Gnoffo^{5,6} to solve both the full and thin-layer Navier-Stokes equations with particular emphasis on external, reacting, hypersonic flows over blunt bodies with detached shock waves. The perfect-gas version was implemented in the present study. The inviscid components of flux across cell walls are described with Roe's averaging and Harten's entropy fix with second-order corrections based on Yee's Symmetric TVD scheme. The viscous terms are discretized using central differences. A point-implicit relaxation strategy is used.

NASCRIIN

The fourth computer code, NASCRIN (Numerical Analysis of SCRamjet INlets), was developed by Kumar^{7,8} and uses the original unsplit explicit technique of MacCormack⁹ to solve the full Navier-Stokes equations. This technique is a two-step, predictor-corrector scheme which is second-order accurate in both space and time. Fourth-order artificial viscosity based on the gradients of pressure and temperature is used near shock waves to suppress numerical oscillations.

Test Cases

The two test cases considered in the present study are shown schematically in Fig. 1. Both cases are hypersonic flows with viscous/inviscid interactions typical of those found in the flow field within the propulsion system of a hypersonic vehicle. The first of these test cases was the two-dimensional flow over a compression corner formed by the intersection of a flat plate and a wedge tested by Holden and Moselle¹⁰ in the Calspan 48-inch Shock Tunnel. The flow field shown in Fig. 1(a) shows the separated flow which forms in the corner region for a sufficiently large wedge angle. Downstream of the reattachment point, the boundary layer thins rapidly due to the compression, resulting in large increases in skin friction and heat transfer on the wedge surface. Furthermore, the compression waves produced by the corner coalesce into a shock wave which intersects with the leading-edge shock, producing an expansion fan and a shear layer, both of which affect the flow on the ramp. Three wedge angles tested by Holden and Moselle are considered here. The flow remained attached on the 15-degree wedge, a small separated-flow region occurred with the 18-degree wedge, and a large separated-flow region was produced by the 24-degree wedge.

The nominal flow conditions for this case were $M_\infty = 14.1$, $T_\infty = 160^\circ R$, and $Re = 7.2 \times 10^4$ per foot. The wall temperature, T_w , was $535^\circ R$. The Reynolds number was low enough that the flow remained completely laminar, thereby eliminating the issue of turbulence modeling from the present study. Furthermore, even though the free-stream Mach number was high, the free-stream temperature was low enough that there were no significant real-gas effects. In the experiment, values of surface pressure, skin friction, and heat transfer were measured in the centerplane of the model which had a spanwise length that was thought to be sufficient to produce two-dimensional flow in the measurement region.

This test case has been used in previous computational studies by other investigators. The first computation using the full Navier-Stokes equations for this case was made by Hung and MacCormack.¹¹ They obtained good agreement with the experimental data for the 15- and 18-degree wedges, but their solution significantly underpredicted the size of the separated-flow region for the 24-degree wedge. Recent studies have been presented by Power and Barber,¹² Ng et al.,¹³ and Risetta and Mach.¹⁴ In addition, the fully-attached flow with the 15-degree wedge has been used for comparisons with computations using the parabolized Navier-Stokes equations in various studies such as in Refs. 15 to 17.

The second test case, shown in Fig. 1(b), was the interaction of an incident shock produced by a shock-generator

wedge with a flat-plate boundary layer in hypersonic flow. The features of this flow field are very similar to those produced by the compression corner. In this case, the incident shock produces a separated-flow region. Downstream of this region, the boundary layers thin rapidly due to the compression. As in the first case, measurements were made in the centerplane of the model which had a spanwise length judged sufficient to produce two-dimensional flow in the measurement region. The experimental data were obtained by Holden¹⁸ in the Calspan 48-inch Shock Tunnel. The nominal flow conditions for this case were $M_\infty = 15.6$, $T_\infty = 77^\circ R$, and $Re = 1.36 \times 10^5$ per foot. The wall temperature, T_w , was $535^\circ R$. Solutions were computed for two different shock-generator wedge angles, 4.017° and 6.45° . As in the compression-corner experiments, the flow was completely laminar and real gas effects were not significant.

Results and Discussion

Compression-corner case

Comparisons were made between the computed solutions from all four codes and experimental data for the 15- and 24-degree wedges using two different grids. The first grid had 51 points in the streamwise direction and 51 points in the vertical direction. In the streamwise direction, the grid was clustered near the leading edge of the flat plate and in the corner region. In the normal direction, the grid was clustered near the model surface. Above the wedge, a simple sheared grid was used, producing a non-orthogonal grid in this region. A second grid with twice the resolution was constructed from the first grid using 101 points in each direction while maintaining the same grid stretching.

15° wedge. Fig. 2(a) shows a comparison of the computed surface-pressure coefficient with experimental values for all four codes on two different grids. The pressure coefficient is plotted as a function of x/L , where x is measured from the leading edge of the flat plate and L is the length of the flat-plate portion of the model. As shown, there are only very slight differences in the predictions from the four codes for the 51 x 51 grid; however, the four solutions are virtually identical for the 101 x 101 grid. The computed pressures are generally higher than the experimental values even on the flat-plate portion of the model. However, the computed pressures were in excellent agreement with those given by hypersonic strong-interaction theory (not shown). The corresponding comparison of the computed surface heat-transfer coefficient with experimental values for all four codes on the two grids is shown in Fig. 2(b). As with the pressure coefficient, the calculations on the 101 x 101 grid produce the best agreement among the codes. The largest differences occur along the ramp. The trends in the experimental

data are again predicted well, but the computed values are generally slightly higher than those found in the experiment.

24° wedge. Fig. 3 shows the streamlines in the flow field of the 24-degree wedge computed using the USA-PG2 code. The large size of the separated-flow region and the thinning of the boundary layer on the ramp downstream of the reattachment point can be clearly seen. Fig. 4 shows the comparison of the computed surface-pressure coefficient with experimental values for this case. The four codes predict different extents of separation even with the 101 x 101 grid. A solution using a 201 x 201 grid was also made with CFL3D. The predictions for surface pressure, skin friction, and surface heat transfer for this grid were almost identical to those found with the 101 x 101 grid with only a slight increase in the predicted extent of separation. Therefore, the 101 x 101 grid calculation with CFL3D can be considered to be sufficiently grid-refined for this flow. All four of the codes demonstrated a trend with grid convergence towards a similar longitudinal extent of separation which is much larger than that found in the experiment. As a result of the larger separation extent, the shock interaction is altered, moving the peak value of pressure on the ramp downstream in comparison to the experiment.

Time-accurate computations. In order to help resolve these differences between the computation and experiment, time-accurate calculations were made with three of the codes to study the question of whether the experimental data might have been obtained before steady flow had been fully established during the short run time available in the shock tunnel. The flow in the experiment reached a steady state in approximately 4 ms., and the total run time was approximately 10 ms. Fig. 5 shows the solutions obtained with CFL3D at five intermediate times one millisecond apart between 1 and 5 ms. These results are representative of the time variation computed with all three of the codes used, CFL3D, USA-PG2, and NASCRIN. It can be seen that the separated-flow region is predicted reasonably well at a point in time between 2 and 3 ms., but the size of the region continues to increase as the solution is further advanced in time. It took more than 12 ms to establish steady flow in the computations, which is more than the testing time available in the experiment.

Calculations were also made with CFL3D for wedge angles of 18, 19.5, 21, and 22.5 degrees. (Calculations made with USA-PG2 for 18- and 21-degree wedges verified the CFL3D results.) The results of these computations are summarized in Fig. 6, which shows the effect of wedge angle on the size of the separated-flow region. For the smallest separated-flow region, which occurred with the 18-degree wedge, the extent of separation using a 101 x

101 grid differed from the experimental value by approximately 23 percent. For the 24-degree wedge, the computed extent of separation differed from the experimental value by approximately 48 percent for the 101 x 101 grid. The 21-degree wedge case produced a computed separated-flow region comparable in size to that found experimentally with the 24-degree wedge. Fig. 7 shows the positions of the upstream and downstream boundaries of the separated-flow region for this case as functions of time. As shown, it required significantly more time than 4 ms. for the computed flow field to reach its steady-state even for a separated-flow region with a size comparable to that found in the experiments.

Three-dimensional calculations. Since the results from the two-dimensional computations did not match the experimental data, three-dimensional calculations were made with CFL3D to investigate the possibility of flow in the spanwise direction affecting the flow in the center of the plate. For the experimental data for which comparisons are shown below, no side plates were used. The spanwise length of the plate was 2 ft. Calculations were made with two different grids, 51 x 51 x 25 and 101 x 101 x 25. Because the flow is symmetric about the centerplane, the computational domain included only half of the plate. The spanwise grid contained 19 points on the plate and 6 points in the free stream. Approximate supersonic outflow boundary conditions were used at the sides of the computational domain outside of the ramp surface. Fig. 8 shows results from the calculation with a 101 x 101 grid in each streamwise plane. The streamlines in the flow very near the model surface are visualized using particle traces. The separation and reattachment lines show that the size of the separated-flow region decreases across the plate from the centerplane to the edge. The pressure contours in the downstream plane on the ramp at the end of the computational domain show an expansion of the flow in the spanwise direction near the edge of the plate to reduce the pressure to the free-stream value. A comparison of the computed 2-D and 3-D centerplane surface-pressure distributions with the experimental data are shown in Fig. 9 using solutions from CFL3D for all of the grids used in the present study. As shown, the three-dimensional effects produce a smaller separated-flow region in the centerplane than that predicted in the two-dimensional calculations. Furthermore, the size of the separated-flow region and the pressure level in that region are in excellent agreement with the data for the finest mesh in the 3-D calculation. However, the computed pressure rise on the surface of the wedge differs from the experiment even though the peak value is well-predicted.

Fig. 10 shows the normalized locations of the upstream and downstream boundaries of the separated-flow region

as functions of time for both the 2-D and 3-D computations with CFL3D for the 24-degree wedge. Quite surprisingly, the time to establish the steady state for the 3-D flow is dramatically less than that required for the 2-D flow. For the 3-D computation, a steady-state has been established in approximately 4 ms, which is in agreement with the experiment.

Angle-of-attack correction. It was found that incorporating a one-degree angle of attack significantly improved the agreement with the experimental data in all cases for all quantities. The one-degree angle-of-attack correction was used previously by Lawrence et al.¹⁷ Fig. 11 shows the computed surface-pressure coefficient for both the 15- and 24-degree wedges with and without the angle-of-attack correction. The correction brought the computed values into agreement with the data on both the flat-plate and wedge portions of the model. Similar improvements were found for the skin friction and surface heat transfer.

Summary comparisons. Fig. 12 shows a summary comparison of the CFL3D solutions with with experimental data for each of the three wedges. The 3-D solution in the centerplane is shown for the 24-degree wedge, and 2-D solutions are shown for both the 15- and 18-degree cases. In each case, the one-degree angle-of-attack correction is used as well as the exact free-stream conditions measured in the experiment. These flow conditions were slightly different from the nominal values listed above. Excellent agreement of the calculations with experimental data was found for pressure, heat transfer, and skin friction for all three wedge angles.

The present results reconcile several discrepancies between numerical computations and experiment for the 24-degree compression ramp presented in the literature. The original work of Hung and MacCormack¹¹ in 1976 compared well with the 15- and 18-degree ramp deflections but underpredicted the extent of separation for the 24-degree deflection. This can be attributed to the coarseness of the computational grid in that study since the present investigation indicates that the 24-degree compression ramp requires a much finer grid than that required with the lower angles to attain grid convergence. The more recent work of Ng et al.¹³ and Risetta and Mach¹⁴ with much finer grids indicate a separation extent that is much larger than experiment for the 24-degree case. These results are consistent with those of the present study in that incorporation of the three-dimensional effect due to spanwise extent is required in order to agree with experiment. Finally, the recent work of Power and Barber¹² indicates less separation than experiment, in contrast to the present results. This smaller predicted extent of separation is believed to be due to a termination of the calculations after the free stream had swept the computational domain four times, which is sig-

nificantly less than the present calculations indicate are required for the flow to establish a steady state.

Shock-boundary layer interaction case

Computations were made for two of the five shock-generator-wedge angles tested by Holden at $M_\infty = 15.6$. These angles were 4.017° and 6.45° , which represent the smallest and the next-to-the-largest angles tested. The first set of calculations was made in two parts. The flow over the shock-generator wedge was computed separately using CFL3D. The shock angle obtained from this calculation was then used to specify the flow at the upper boundary of the computational domain used to compute flow over the flat plate. For $\theta = 4.017^\circ$, computations were made for three of the codes, CFL3D, USA-PG2, and NASCRIN. For $\theta = 6.45^\circ$, computations were made using only CFL3D and USA-PG2. The grid for the flat plate had 151 points in the streamwise direction which were clustered near the leading edge of the plate and in the shock-boundary layer interaction region. The grid in the normal direction extended 3 inches above the surface of the plate and had 81 points which were clustered near the wall. For $\theta = 4.017^\circ$, the shock angle, β , was 8° , and the shock crossed the upper boundary at the grid point at $x=0.912$ inches. In this case, the shock position required to properly match the shock-impingement location was actually upstream of that estimated from the analysis of the computed shock-generator-wedge flow field. For $\theta = 6.45^\circ$, the shock angle was 10.5° and the shock crossed the upper boundary at the grid point at $x=6.429$ inches.

A comparison of the computed surface-pressure coefficient with experimental data for both wedge angles is shown in Fig. 13. The results for the two upwind codes are virtually identical. The pressure rise in the interaction region computed by NASCRIN occurs slightly downstream of the upwind predictions. This difference is a consequence of the shock wave being introduced along the upper boundary one-half grid cell further downstream in the finite-difference method than in the two upwind methods. The expansion downstream of the interaction region is not predicted for either wedge angle by any of the methods.

Comparisons of the computed skin-friction coefficient and surface heat-transfer coefficient are shown in Figs. 14 and 15, respectively. The differences between the solutions from the two upwind methods are very small, and the overall levels and trends of the heat-transfer and skin-friction data upstream of and through the interaction region are well-predicted.

Computations were also made using CFL3D which included the flow over the shock generator wedge as well as the flow over the plate as part of a single simulation.

The grid for this case is shown in Fig. 16(a). The grid over the flat plate remained the same as in the previous calculations, and the grid near the wedge contained the same amount of clustering in the normal direction as the grid near the plate. The grid contained 191 points in the streamwise direction and 151 points in the normal direction. The upper boundary downstream of the trailing edge of the shock generator wedge was simulated as a flat plate parallel to the free-stream flow. Contours of pressure and Mach number for the $\theta = 6.45^\circ$ simulation are shown in Figs. 16(b) and (c), respectively. The pressure contours illustrate the intersection of the wedge and flat-plate leading-edge shocks as well as the interaction of the wedge shock with the flat-plate boundary layer. The Mach-number contours highlight the boundary-layer development and the shock waves and also indicate a separation zone in the interaction region on the lower flat plate. The corresponding calculation for the case with $\theta = 4.017^\circ$ produced a wedge shock which impinged on the flat-plate boundary layer downstream of the measured impingement, consistent with the observation noted above for the specified-shock calculations. To match the experimental impingement location, the height of the trailing edge of the shock-generator wedge above the flat plate was changed from the value of 3.625 inches reported for the experimental configuration to 3.242 inches.

Fig. 17 shows a comparison of the surface-pressure coefficient for the specified-shock calculation and the complete flow-field simulation for CFL3D for both wedge angles. The only difference between the two results occurs downstream of the interaction where the complete simulation captures the expansion produced by the flow from the trailing edge of the generator wedge.

Concluding Remarks

A code-validation study has been conducted for four different codes for solving the compressible Navier-Stokes equations. Two test cases involving high-speed separated flows have been used to compare the results from the codes. Computations for a series of nominally two-dimensional high-speed laminar separated flows were compared with detailed experimental shock-tunnel results. The shock wave-boundary layer interactions considered were induced by a compression ramp in one case and by an externally-generated incident shock in the second case. In general, good agreement was reached between the grid-refined calculations and experiment for the incipient- and small-separation conditions. For the most highly separated flow, three-dimensional calculations which included the finite-span effects of the experiment were required in order to obtain agreement with the data. The finite-span effects were important in determining the extent of separation as well as the time

required to establish the steady-flow interaction. The results presented provide a resolution of discrepancies with the experimental data encountered in several recent computational studies.

The present study demonstrated that the four codes are capable of accurately representing both qualitatively and quantitatively the types of complex hypersonic flows with strong viscous-inviscid interactions considered. For sufficiently-refined grid, the predictions from the codes were in good agreement with each other and with experimental data considered to be benchmark data for these types of flows. The emphasis of the present study was the grid-refined accuracy of the codes and, therefore, the study did not address either the issue of the relative efficiency of the codes or the minimum computational requirements to simulate the flows considered.

Acknowledgments

The authors thank M. S. Holden of the Calspan-UB Research Center for fruitful discussions related to the experimental tests and D. P. Rizzetta of the U. S. Air Force Wright Research and Development Center for the interchange of computational results for the compression-ramp study.

References

- ¹Rudy, David H.; Kumar, Ajay; Thomas, James L.; Gnoffo, Peter A.; and Chakravarthy, Sukumar R.: A Comparative Study and Validation of Upwind and Central-Difference Navier-Stokes Codes for High-Speed Flows. Validation of Computational Fluid Dynamics. AGARD-CP-437, Vol. 1, Dec. 1988, pp. 37-1 to 37-15.
- ²Thomas, James L.; Rudy, David H.; Chakravarthy, Sukumar R.; and Walters, R. W.: Patched-Grid Computations of High-Speed Inlet Flows. Advances and Applications in Computational Fluid Dynamics. A.S.M.E., FED-Vol. 66, Nov.-Dec. 1988, pp. 11-22.
- ³Vatsa, V. N.; Thomas, J. L.; and Wedan, B. W.: Navier-Stokes Computations of Prolate Spheroids at Angle of Attack. AIAA Paper 87-2627CP, 1987.
- ⁴Chakravarthy, S. R.; Szema, K.-Y.; Goldberg, U.; Gorski, J. J.; and Osher, S.: Application of a New Class of High Accuracy TVD Schemes to the Navier-Stokes Equations. AIAA Paper 85-0165, 1985.
- ⁵Gnoffo, Peter. A.: Application of Program LAURA to Three-Dimensional AOTV Flow Fields. AIAA Paper 86-0565, 1986.
- ⁶Gnoffo, Peter. A.: Upwind-Biased, Point-Implicit Relaxation Strategies for Viscous Hypersonic Flow. AIAA Paper 89-1972CP, 1989.

⁷Kumar, Ajay: Numerical Simulation of Scramjet Inlet Flow Fields. NASA TP-2517, May 1986.

⁸Kumar, Ajay: User's Guide for NASCRIN - A Vectorised Code for Calculating Two-Dimensional Supersonic Internal Flow Fields. NASA TM-85708, 1984.

⁹MacCormack, R. W.: The Effect of Viscosity in Hypervelocity Impact Cratering. AIAA Paper 69-354, 1969.

¹⁰Holden, M. S.; and Moselle, J. R.: Theoretical and Experimental Studies of the Shock Wave-Boundary Layer Interaction on Compression Surfaces in Hypersonic Flow. ARL 70-0002, January 1970.

¹¹Hung, C. M.; and MacCormack, R. W.: Numerical Solutions of Supersonic and Hypersonic Laminar Compression Corner Flows. AIAA J., Vol. 14, No. 4, April 1976, pp. 475-481.

¹²Power, G. D.; and Barber, T. J.: Analysis of Complex Hypersonic Flows with Strong Viscous/Inviscid Interaction. AIAA J., Vol. 26, No. 7, July 1988, pp. 832-840.

¹³Ng, W. F.; Mitchell, C. R.; Ajmani, K.; Taylor, A. C., III; and Brock, J. S.: Viscous Analysis of High Speed Flows Using An Upwind Finite Volume Technique. AIAA Paper 89-0001, January 1989.

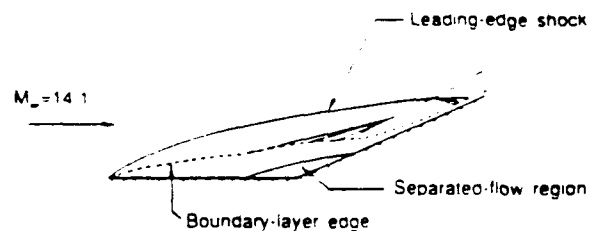
¹⁴Rizsetta, Donald P.; and Mach, Kervyn D.: Comparative Numerical Study of Hypersonic Compression Ramp Flows. AIAA Paper 89-1877, June 1989.

¹⁵Ota, D. K.; Chakravarthy, S. R.; and Darling, J. C.: An Equilibrium Air Navier-Stokes Code for Hypersonic Flows. AIAA Paper 88-0419, January 1988.

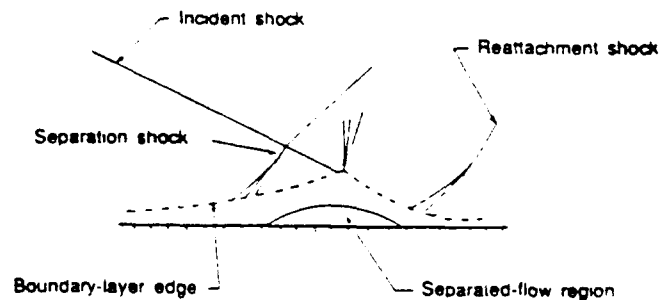
¹⁶Korte, J. J.; and McRae, D. S.: Explicit Upwind Algorithm for the Parabolised Navier-Stokes Equations. AIAA Paper 88-0716, January 1988.

¹⁷Lawrence, S. L.; Tannehill, J. C.; and Chaussee, D. S.: An Upwind Algorithm for the Parabolised Navier-Stokes Equations. AIAA Paper 86-1117, May 1987.

¹⁸Holden, M. S.: A Study of Flow Separation in Regions of Shock Wave-Boundary Layer Interaction in Hypersonic Flow. AIAA Paper 78-1169, 1978.

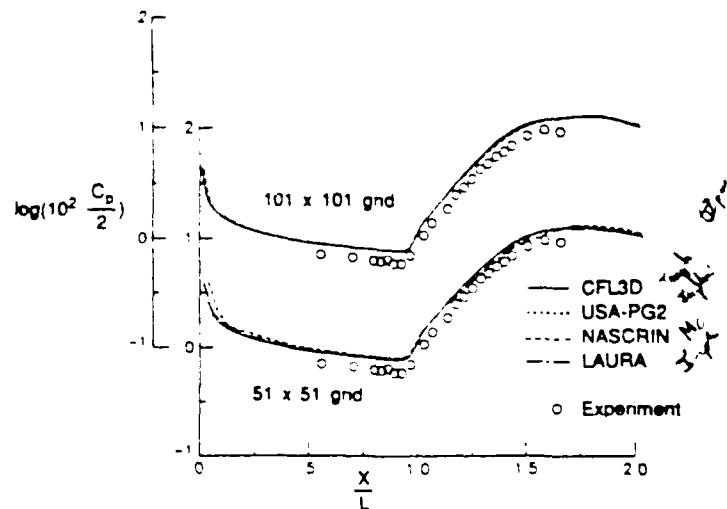


(a.) Compression corner



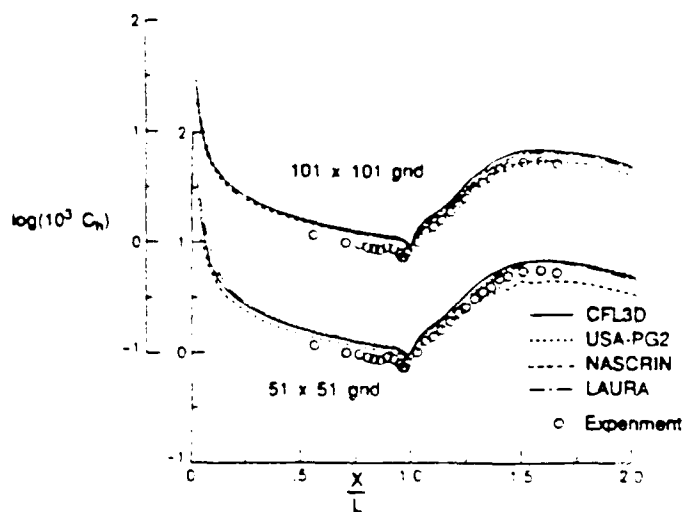
(b.) Shock-boundary layer interaction

Fig. 1 Test cases.



(a.) Surface pressure

Fig. 2 Comparison of computation and experiment for 15° wedge.



(b.) Surface heat transfer

Fig. 2 Concluded.



Fig. 3 Streamlines for flow past 24° compression corner. USA-PG2 solution.

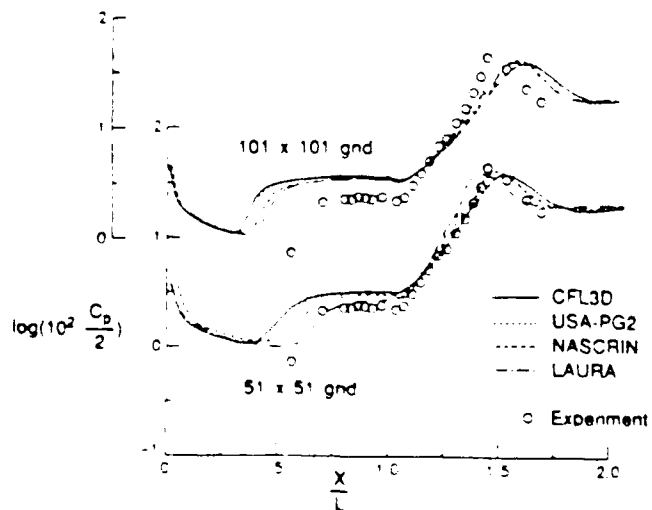


Fig. 4 Comparison of computation and experiment for 24° wedge.

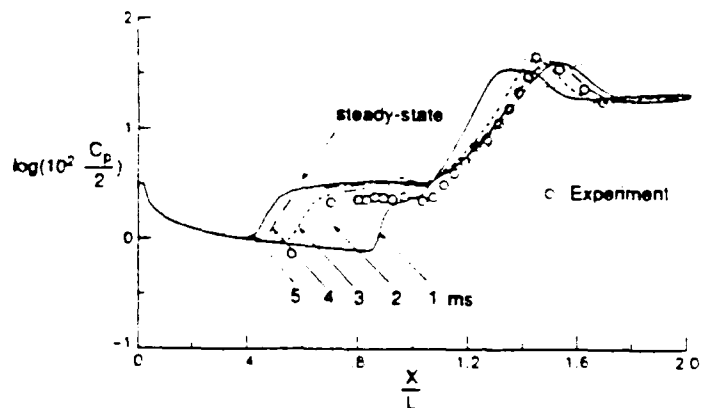


Fig. 5 Time history of surface pressure. CFL3D solution. 24° wedge.

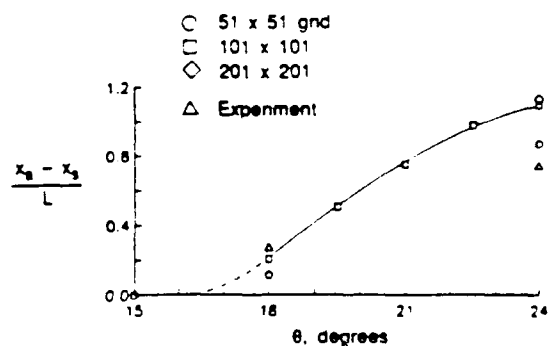


Fig. 6 Effect of wedge angle on extent of separation. CFL3D solutions.

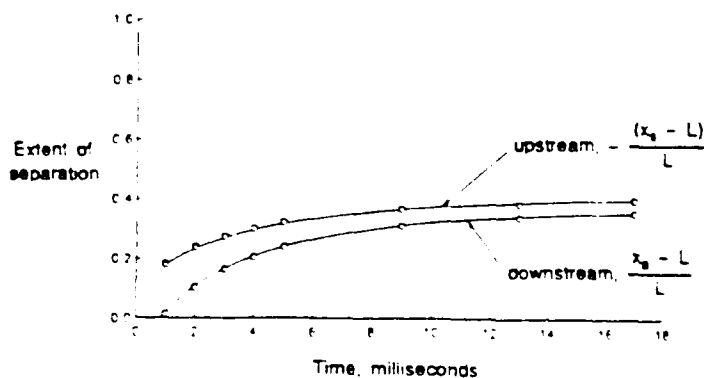


Fig. 7 Time history of separation extent for 21° wedge. CFL3D solution.

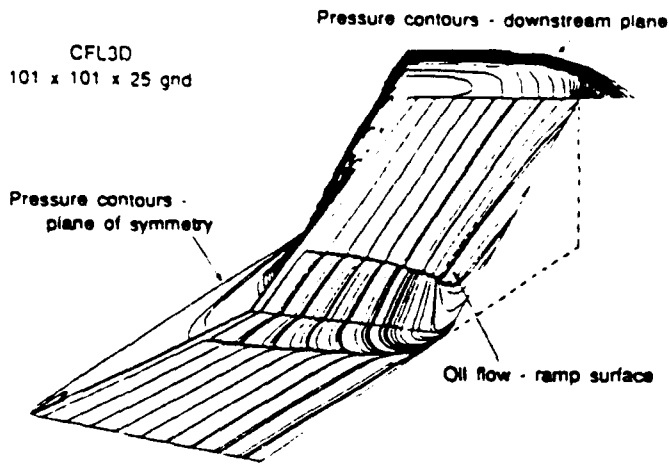


Fig. 8 3-D solution for 24° wedge. CFL3D.

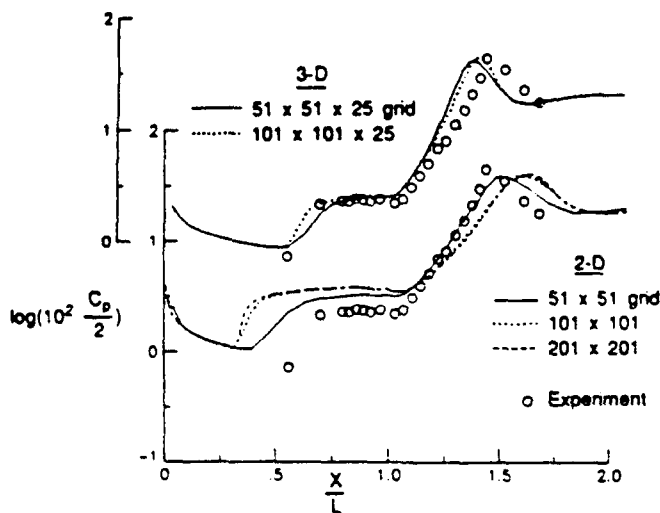


Fig. 9 Comparison of CFL3D computations and experiment for 24° wedge.

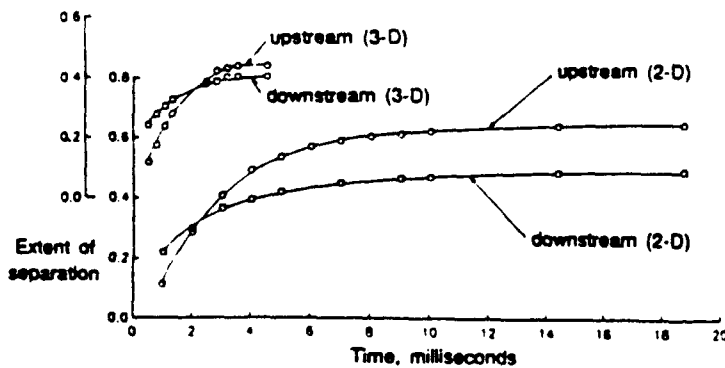


Fig. 10 Time history of separation extent for 24° wedge from CFL3D solutions.

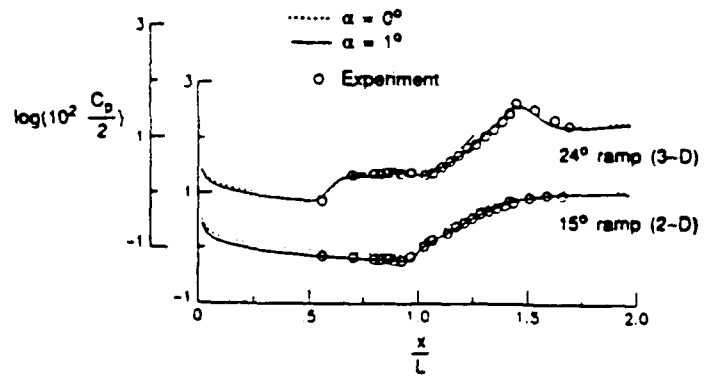
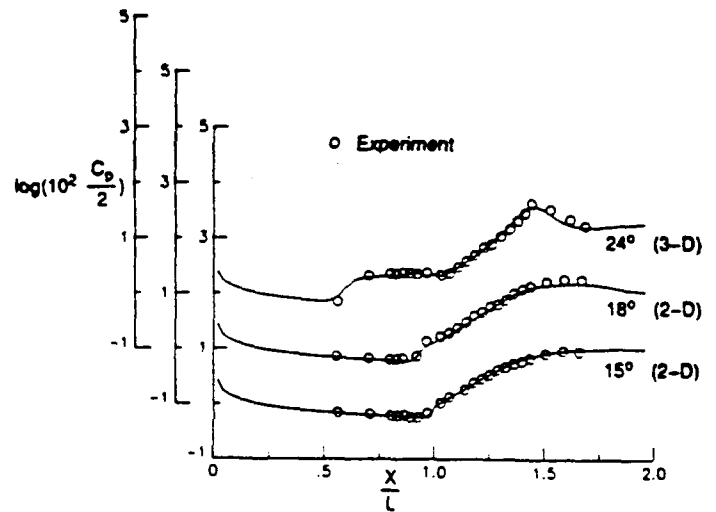
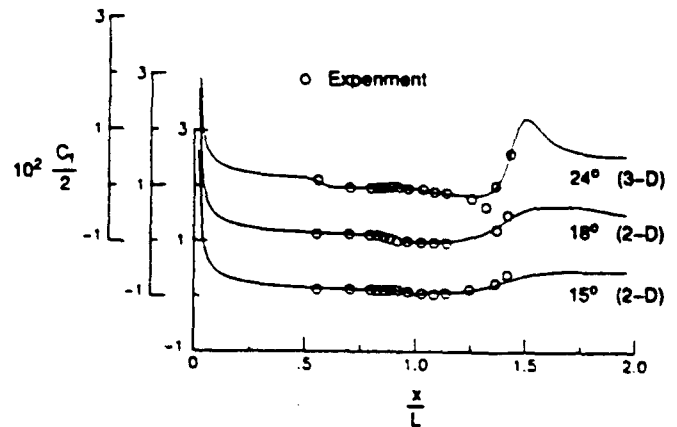


Fig. 11 Effect of angle of attack on surface pressure. CFL3D solutions.

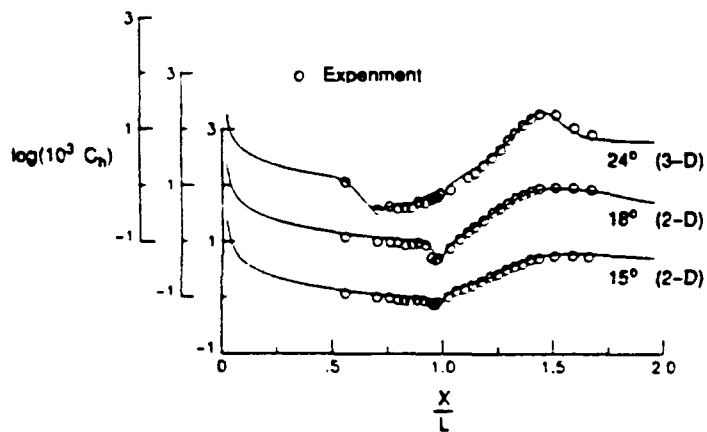


(a.) Surface pressure



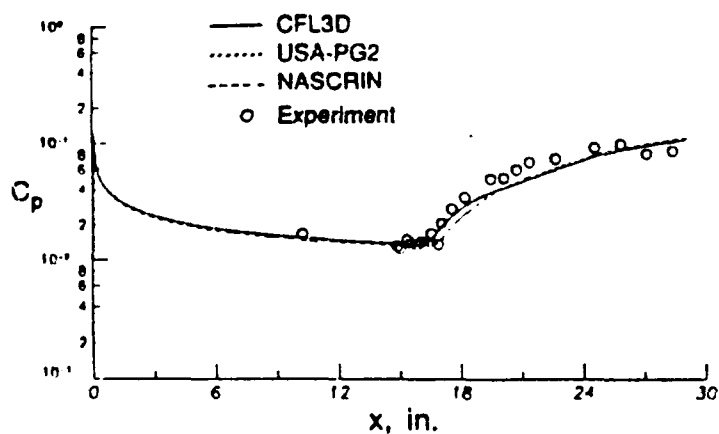
(b.) Skin friction

Fig. 12 Summary comparison of CFL3D computations and experiment.

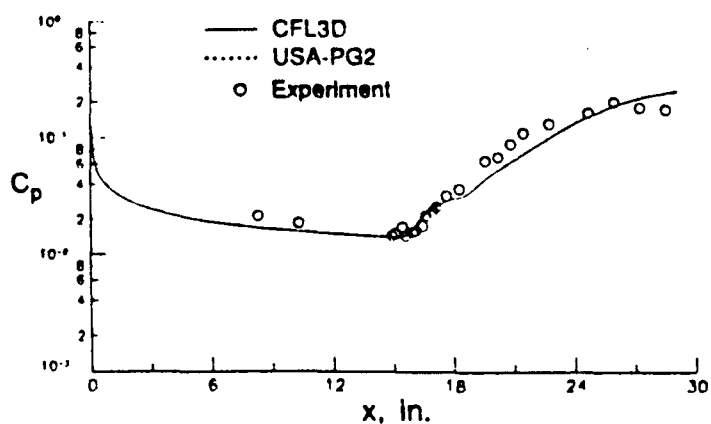


(c.) Surface heat transfer

Fig. 12 Concluded.

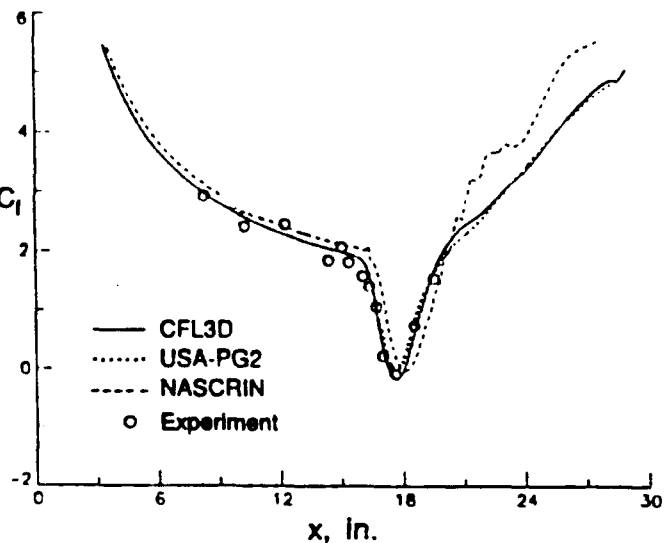


(a.) $\theta = 4.017^\circ$

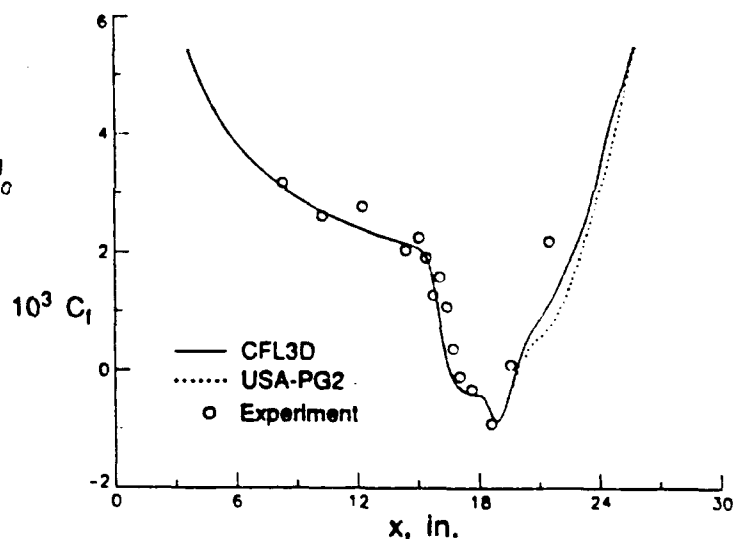


(b.) $\theta = 6.45^\circ$

Fig. 13 Comparison of computed and experimental surface pressure for shock-boundary layer interaction.

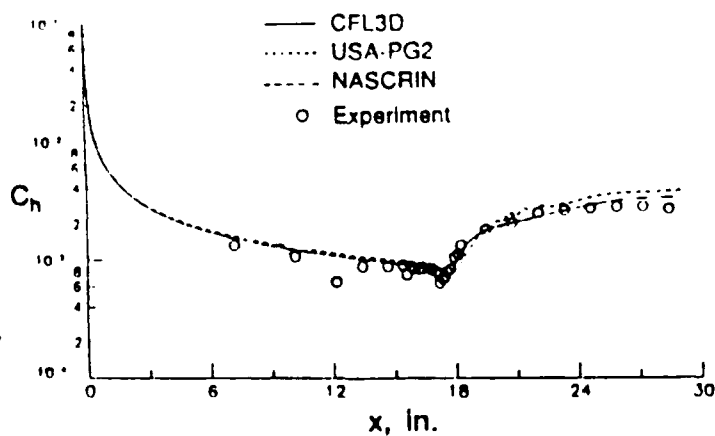


(a.) $\theta = 4.017^\circ$

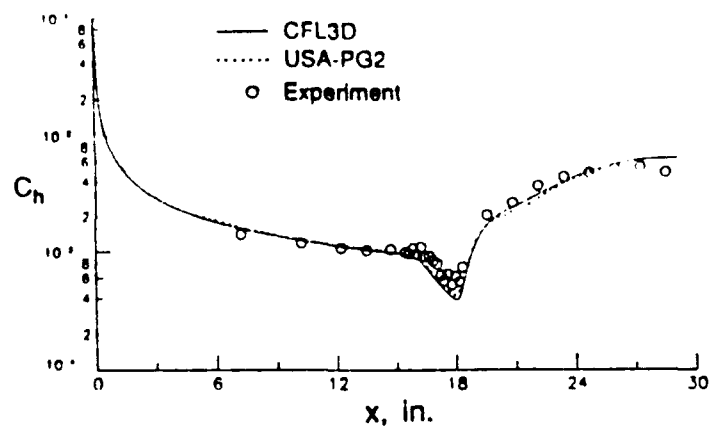


(b.) $\theta = 6.45^\circ$

Fig. 14 Comparison of computed and experimental skin friction for shock-boundary layer interaction.



(a.) $\theta = 4.017^\circ$

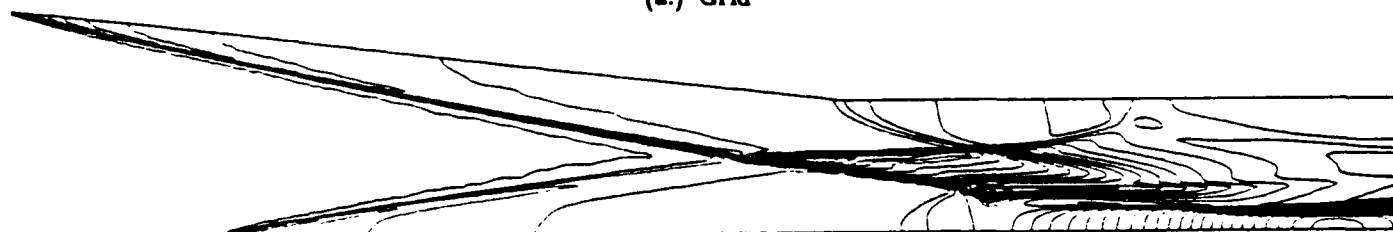


(b.) $\theta = 6.45^\circ$

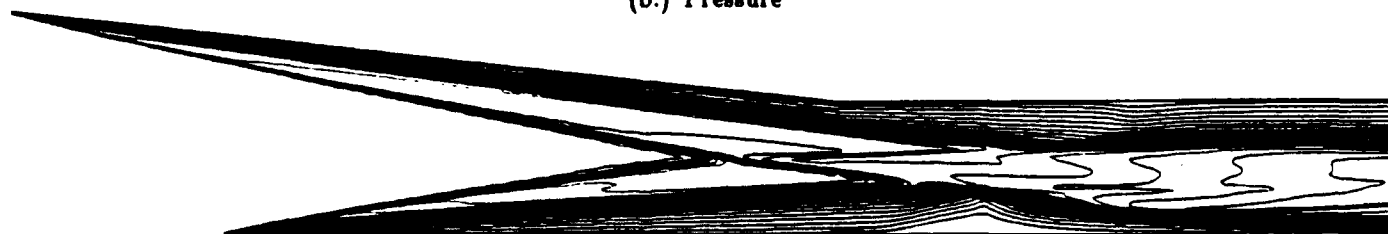
Fig. 15 Comparison of computed and experimental surface heat transfer for shock-boundary layer interaction.



(a.) Grid

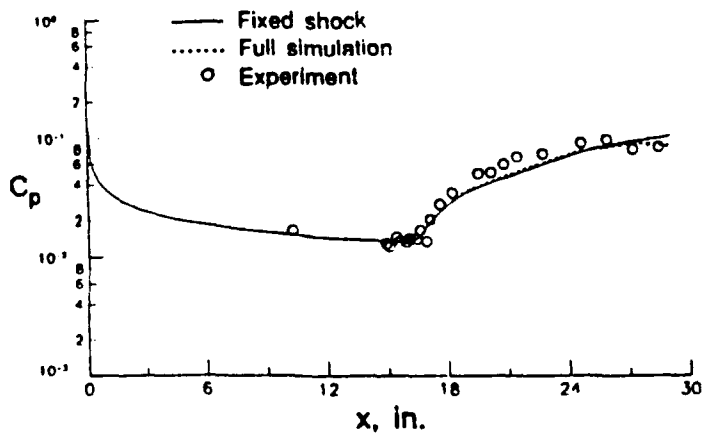


(b.) Pressure

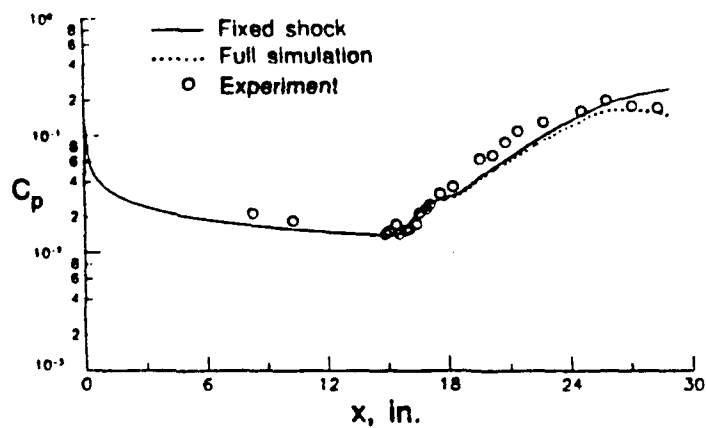


(c.) Mach number

Fig. 16 Grid and computed flow field for CFL3D simulation of complete configuration. $\theta = 6.45^\circ$.



(a.) $\theta = 4.017^\circ$



(b.) $\theta = 6.45^\circ$

Fig. 17. Comparison of fixed-shock and complete flow-field CFL3D computations.